Multi-Fidelity Numerical Methods for Aircraft and Wind Turbines
Aerodynamics, Aeroelasticity, and Aeroacoustics

Ribeiro, André F.P.

DOI
10.4233/uuid:5914f8f9-1d79-4b92-a77b-7cbf7c5e749f

Publication date
2025

Document Version
Final published version

Citation (APA)
Ribeiro, A. F. P. (2025). *Multi-Fidelity Numerical Methods for Aircraft and Wind Turbines: Aerodynamics, Aeroelasticity, and Aeroacoustics*. [Dissertation (TU Delft), Delft University of Technology]. https://doi.org/10.4233/uuid:5914f8f9-1d79-4b92-a77b-7cbf7c5e749f

Multi-Fidelity Numerical Methods for Aircraft and Wind Turbines

Aerodynamics, Aeroelasticity, and Aeroacoustics

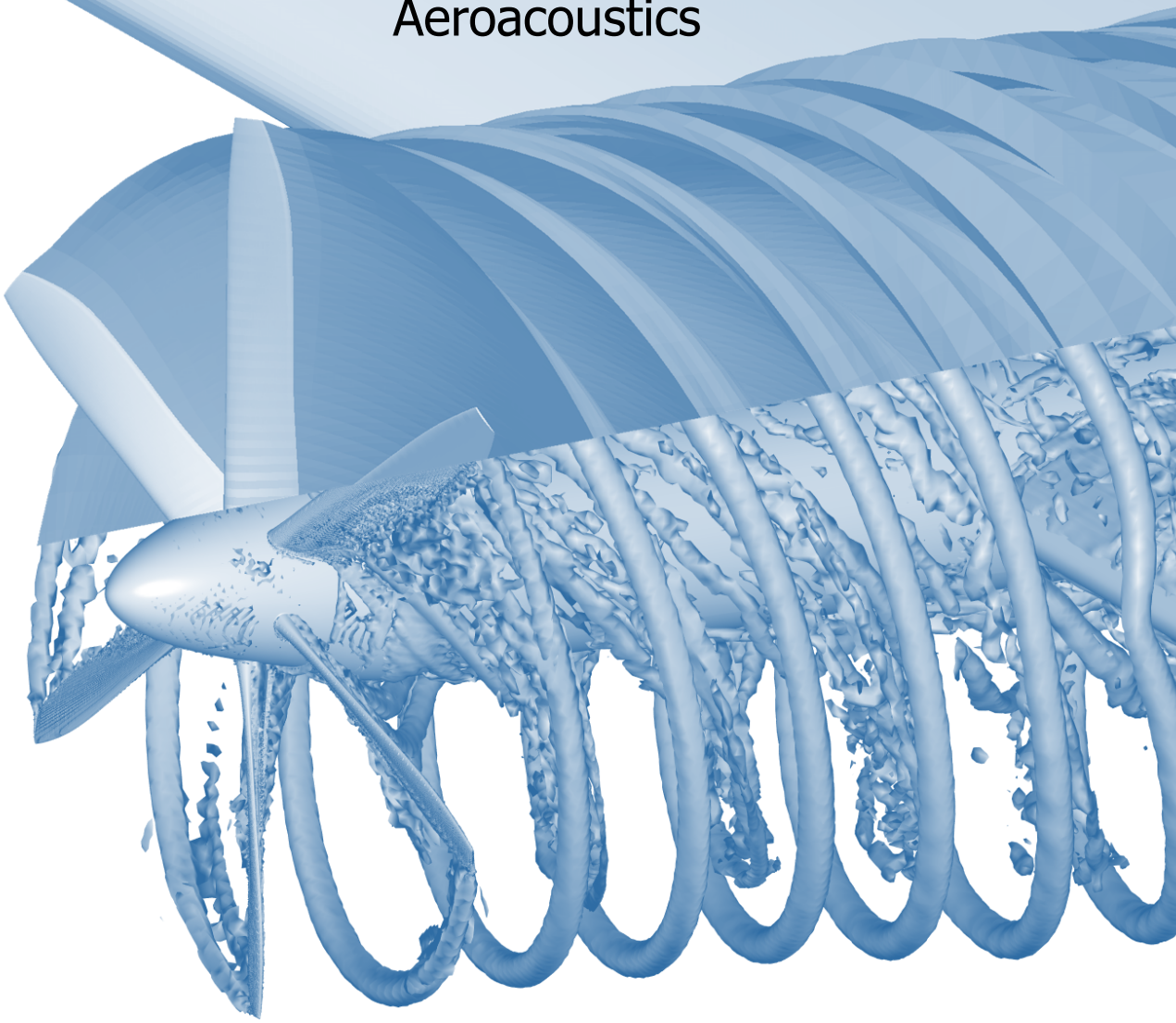

André PINTO RIBEIRO

Multi-Fidelity Numerical Methods for Aircraft and Wind Turbines

Aerodynamics, Aeroelasticity, and Aeroacoustics

Dissertation

for the purpose of obtaining a degree of doctor
at Delft University of Technology,
by the authority of Rector Magnificus Prof. dr. ir. T.H.J.J. van der Hagen,
chair of the Board of Doctorates,
to be defended publicly on Monday 14, April 2025 at 10:00 o'clock

by

André PINTO RIBEIRO

Master of Science in Mechanical Engineering,
Universidade Federal do Rio Grande do Sul, Brazil,
born in Porto Alegre, Brazil.

This dissertation has been approved by the promotors

Composition of the doctoral committee:

Rector Magnificus,	chairperson
Prof.dr. D. Casalino,	Delft University of Technology, promotor
Prof.dr.ir. C.J. Simao Ferreira,	Delft University of Technology, promotor
Independent members:	
Dr.ir. A. van Garrel	University of Twente
Prof.dr. M. Gennaretti	Roma Tre University
Prof.dr.-ing.habil S. Hickel	Delft University of Technology
Dr. D. Ragni	Delft University of Technology
Prof.dr. J.N. Sørensen	Technical University of Denmark

Keywords: offshore wind energy, panel method, highly flexible wing, fluid structure interaction, propeller-wing interaction, vertical axis wind turbine, actuator line, airfoil noise

Printed by: Gildeprint

Front & Back: Propeller-wing configuration simulated with a free wake panel method (top) and a lattice-Boltzmann code (bottom).

ISBN 978-94-6518-021-2

An electronic version of this dissertation is available at
http://repository.tudelft.nl/.

To my girls.

Contents

Summary

The aerospace and wind energy markets are going through dramatic changes. The first, due to the rise of electric aircraft with multiple rotors in various complex configurations that are incompatible with traditional design methods. The latter, due to the quick growth in wind turbine size and the move to floating offshore installations, which are more complex than their fixed-base onshore counterparts. Hence, there is a clear necessity for fast tools for aerodynamic and aeroelastic design of these new configurations, along with highly accurate methods for late stage verification of aerodynamics and aeroacoustics. The first objective of this thesis is to develop and validate a free wake panel code, exploring its capabilities and applicability to model complex problems relevant to the wind energy and aerospace market. The second objective is to develop methodologies for a high-fidelity lattice-Boltzmann code, also to evaluate the capabilities of such method for problems in wind energy and aerospace that mainstream tools struggle to solve.

The first half of the work focuses on the development and applications of the free wake panel method. After several fundamental verification and validation studies, the method is used to study the nonlinear aerodynamics of an offshore wind turbine undergoing surge, sway, and yaw motions. The method is able to reproduce experimental results and is then used to go beyond the range of motion available in the literature, showing where nonlinear effects start playing a role. The free wake panel method is then used on a highly flexible wing undergoing flutter. The method compares very well with the experimental flutter onset range and is also used on a case with gusts, where corrections to the experiments are proposed. The use of blade and strut pitching on vertical axis wind turbines is investigated next, with a novel combination of pitched elements is proposed, leading to more efficient wake steering. Finally, the free wake panel method is used to investigate propeller-wing interactions on a wing in cruise conditions, showing good agreement with reference cases, and good computational efficiency, due to a mixed fixed/free wake formulation.

The second half of the thesis focuses on high-fidelity lattice-Boltzmann simulations, using the commercial software PowerFLOW®. The first implementation of a sliding mesh actuator line method is explored, with the advantages and disadvantages quantified. This actuator line method is used, along with blade-resolved simulations, to investigate rotor tip vortex instabilities. Then, the method is validated on a propeller-wing interaction case in cruise and high-lift conditions, with good agreement with experimental data and a deeper flow analysis of slipstream deformation and tip vortex instabilities than what was possible in the experiments. Next, trailing-edge noise of a full wind turbine with serrations is performed and compared to field test data, with good agreement and run times that are compatible with industrial expectations. Finally, a detailed study of leading-edge noise, with a

focus on turbulence distortion is performed, where the effects of airfoil thickness on turbulence and noise are investigated in detail.

The conclusion of this work is that free wake panel methods can contribute to wind turbine and aircraft design, but there are cases where lifting line methods for wind turbines and vortex lattice methods for aircraft are sufficiently accurate while being faster. For wake steering studies, the panel method was shown to be useful for finding new solutions, but simulation of wind farms require more stable wakes, such as those obtained with actuator line or vortex particle methods. The scale-resolving lattice Boltzmann method was shown to be very accurate for applications in wind turbine wake dynamics, propeller-wing interaction, trailing and leading-edge noise, making such tool effective for design, able to reduce the amount of experimental campaigns. Several physical insights from the simulations are given throughout the work.

I

Prologue

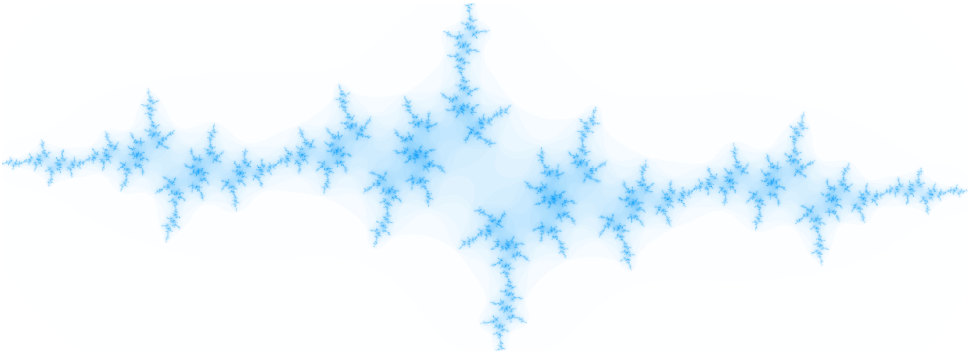

1

Introduction

The struggle itself to the heights is enough to fill a man's heart.
One must imagine Sisyphus happy.

Albert Camus

This chapter summarizes the motivation behind the work conducted in this thesis. The state-of-the-art for aerodynamics simulations of rotors is discussed and the main goals of the work are described.

1.1. Context

The aerospace and wind energy markets are both currently going through revolutions. In wind energy, the shift in focus from the well established onshore turbines to the offshore market, and in particular to floating offshore wind turbines (FOWTs), increased the complexity of the aerodynamics of the turbines substantially. Concurrently, the enormous effort to shift from fossil fuels to renewable energy has also led to less traditional wind turbine configurations, such as vertical axis wind turbines (VAWTs) and airborne wind energy solutions. In the aerospace market, recent developments in electric batteries and, yet again, an effort to shift from fossil fuels to renewable energy, have led to the rise of aircraft with numerous small electric propellers, instead of the traditional one to four large engines. Additionally, in lieu of a few large aircraft manufacturers designing aircraft that are topologically similar to their previous products, there are now hundreds of start-ups developing never-before tested configurations in the new electric vertical take-off and landing (eVTOL) segment.

Among the several risks introduced by these new concepts is the introduction of many unsteady aerodynamics problems. FOWTs do not behave like their fixed-foundations counterparts. Besides the blade spinning through a turbulent atmospheric boundary layer, the entire rotor can move in six degrees of freedom, introducing uncertainties regarding traditional design methods [1]. Onshore wind turbines also have construction and transportation constraints regarding the length of the blades, which offshore turbines do not have, meaning blades are becoming much longer and more susceptible to aeroelastic phenomena [2]. VAWTs are inherently unsteady in their operations [3], with the angle of attack of the blades varying drastically over each rotations. Building wind farms composed of VAWTs means that the interactions among turbines and wakes are paramount, again introducing more unsteady problems, as VAWTs have very complex wakes [4].

Installation effects, i.e. the performance of an isolated aircraft and an isolated engine compared to the performance of an engine installed on an aircraft, have historically been relatively small. This is because propellers usually cover a small portion of the frontal area of wings, with modern turbofans being mounted under the wings or on the tail, avoiding the direct impingement of wakes on the aircraft itself. The advent of distributed propulsion, with many small (typically electric) propellers placed along the leading-edge of aircraft wings [5], changes this entirely, making the design of the engine and aircraft as two separate efforts unreliable, and making aeroacoustic interactions more relevant [6]. The wakes of these propellers are unsteady in nature, putting into question the traditional assumptions of steady flow around wings. These wings are also becoming more flexible, making their design more complex and prone to aeroelastic phenomena [7].

Vertical flight was traditionally reserved for helicopters and some fighter jets, with the first having a large rotor that, in most flight conditions, ingests undisturbed free-stream flow. Many eVTOL configurations being designed at the moment have at least four, sometimes more than eight small propellers [8]. They are often placed in a pusher configuration, ingesting the wake of upstream propellers and lifting surfaces. These wakes make the unsteady flow around tilted propellers more complex

and prone to noise, which is a crucial part of designing a vehicle that is supposed to operate in urban environments [9].

With all of these unsteady aerodynamic problems in mind, we need to critically examine the state-of-the-art of aerodynamics for rotor design, including aeroelasticity and aeroacoustics.

1.2. Aerodynamic Simulations of Rotors

The simulation of aircraft and wind turbine rotors is typically conducted, in order of cost, using blade element momentum theory (BEMT), vortex methods, actuator models, and blade-resolved computational fluid dynamics (CFD). Comprehensive state-of-the-art reviews can be found in [10–12]. Comparisons of several methods for simulating a wind turbine in the wake of another turbine can be found in [13]. A brief overview of the most common methods is given in the following sections.

1.2.1. Blade Element Momentum Theory

BEMT is based on assuming the flow through a rotor behaves like a streamtube, with flow properties varying radially, but being constant around the circumference. Forces on the blade are computed based on flow properties for different radial sections and tabular airfoil data. BEMT has been the workhorse of wind turbine design for decades and simulations are very fast. Many improvements to BEMT have been made over the years in order to achieve more accurate results, including unsteady flows. For an introduction to the method see [14].

The use of tabular data comes with advantages and disadvantages. The main advantage is the accuracy of blade sectional data can be higher than blade resolved simulations. This is because the tabular data can come from experiments and can include effects that are difficult to simulate, such as boundary layer transition, flow separation, surface roughness, vortex generators, ice accretion, and other real-world effects. The disadvantage of using tabular data is that the blade section design cannot be arbitrarily changed in an optimization loop. Sectional data is also limited with regards to 3D flow separation. Finally, highly flexible blades or swept blades are difficult to simulate with BEMT [15] and, in general, with tabular data, as the airfoil cross section can effectively change in time [16]. As these configurations become more relevant, improvements and alternatives to BEMT continue to be developed [17, 18].

While BEMT is used for most of wind turbine design, it is limited in scope for aircraft, as it tends to deal with isolated rotors.

1.2.2. Vortex Methods

Here we refer to potential flow methods using vortices to describe the rotor wake as vortex methods. This includes lifting line, vortex lattice methods, and panel methods, with prescribed or free wakes. A thorough history of vortex methods can be found in [19]. Here we describe the three main forms of vortex methods.

Lifting line methods represent rotor blades as discretized lines, with each section representing a vortex. The vortex strength is computed with the local flow

properties and airfoil tabular data, as in BEMT. Wake filaments or particles are shed from the lifting line and their induction also affects the flow field.

Vortex lattice methods (VLM) work in a similar way, but instead of simulating the blades as lines, they are modelled as surfaces, discretized into panels, which run through the camber line of the airfoil sections. Instead of adapting the vortex strength based on tabular data, they are adapted to achieve impermeability on certain locations on the wing. Wakes are shed from the trailing-edges of the panels, in a similar fashion to the lifting line method.

Source and doublet panel methods describe the entire outer shell of the blades, hence capturing thickness effects more accurately than VLM. Each panel contains a source, which is imposed to achieve impermeability on the panel center, and a doublet, which is solved for by imposing the Kutta condition on the trailing-edges, where vortex wakes are shed. Aeroelastic simulations of highly flexible wings have shown some accuracy advantages of panel methods over VLM, while having similar cost [20].

Prescribed or free wakes can be used for all of these methods. Prescribed wakes are defined by the user based on knowledge of the configuration being simulated, while free wakes adapt to the flow and can capture unsteady effects, such as blade-vortex-interaction (BVI) [21]. Prescribed wakes are significantly cheaper to simulate, as the effects of wake filaments on each other can be ignored. Both methods are substantially cheaper than CFD [16].

Free wake methods, including the vortex particle method (VPM) [22], present an important advantage of properly capturing the wake motion and its unsteady interaction with bodies. The advantage of these methods over CFD is that the Lagrangian approach allows wakes to persist without the numerical dissipation of Eulerian methods or the enormous costs of unsteady, wake-resolving CFD simulations. The importance of rotor wake interaction in the eVTOL industry has led to recent developments of free wake VPM codes specifically targeting such applications [23, 24]. Filaments-based codes have also been applied to configurations with propellers [25, 26]. Free wakes have been used to solve unsteady aerodynamics of wind turbines with lifting line [27], VLM [28], and 3D panel methods [29]. A review of free wake methods developed for helicopters can be found in [30] and a comparison of different wake methods for eVTOL are shown in [31].

All of these methods are significantly more expensive than BEMT. The panel-based methods have the disadvantage of having to resolve the flow around the blades. This means that capturing real world effects, such as flow separation and vortex generators is difficult. Laminar to turbulent transition can be captured, but requires the inclusion of a boundary layer model.

The main advantage of panel-based methods is that they can handle arbitrary geometry changes, as seen on highly flexible blades under fluid structure interactions (FSI). As the pressure is directly computed on the surface of the blades, source and doublet panel methods have the additional advantage of being able to capture local flow effects, such as the pressure field induced by two bodies passing each other, as seen in counter rotating rotors, or BVI.

1.2.3. Actuator Models

Actuator models are typically split into two categories: actuator disk and actuator line models. Actuator disk models can be useful for modelling rotors to study the effects of their wakes. This can be done to simulate the slipstream of an aircraft propeller or wind turbine wake effects within a wind farm. Actuator disks can be seen as a combination of BEMT and CFD, where the flow velocity on an annulus of the disk is extracted from CFD and a blade element approach is used to compute the forces on this annulus, which is then applied in the CFD simulation as body forces. The loads can also vary along the azimuth of a given annulus [32], in non axisymmetric flow. This is the cheapest method to include the effects of a rotor in a CFD simulation, as blades are not resolved and the mesh can be quite coarse around the disk. Steady state solvers can be used, as no real rotations are performed, reducing the cost compared to other CFD-based approaches substantially. Tabular data is used for the blade element stage, with the advantages and disadvantages associated with this type of input which were discussed in the previous sections.

Actuator line models [33] can be imagined as a combination of actuator disk and lifting line. Unlike actuator disks, actuator lines act as individual blades, which rotate in the simulation, requiring unsteady simulations. Body forces are applied along the blades, with a smearing function. The CFD simulations often use large eddy simulations (LES), as a low dissipation scheme that can accurately preserve the rotor wake.

Actuator disk models are popular for aircraft design [34] and wind turbine siting [35] with the moderate computational resources associated with steady CFD. Actuator models have limitations in accuracy near blade tips and have the same issues as BEMT and lifting line methods regarding the tabulated data. Actuator line models are increasingly popular in simulations of wind farm controls, as the focus of those simulations are wake interactions, rather than blade design. Advanced applications of the actuator line models can be seen in [36–38]. Although rare, there has been some research on using actuator line models for aircraft design [39, 40].

1.2.4. Computational Fluid Dynamics

Here we refer to blade-resolved CFD simulations, i.e., not using actuator models. A very detailed summary of CFD simulations of wind turbines over the last decades is outlined in [12]. Summaries of CFD use for wind farms can be found in [41, 42]. CFD and in particular steady Reynolds-averaged Navier-Stokes (RANS) simulations have become the standard in aircraft detailed design, including transonic flows, which the aforementioned methods are not capable of simulating accurately. However, when separations are present, results are often unreliable [43, 44]. Unfortunately, complex phenomena such as flow transition and separation are quite common in wind turbines.

CFD simulations are orders of magnitude more expensive than the methods summarized in the previous sections. Aircraft rotor aeroacoustics, which is highly linked to the interaction between the wakes of the rotors and other components, requires unsteady solvers, which are even more expensive than the aforementioned steady RANS simulations.

The cost and complexity of CFD grows even further when more accuracy is required and hybrid RANS-LES methods are used [45]. The accuracy of these high-fidelity simulations can be quite high [46], potentially higher than all of the aforementioned methods. However, accurately capturing transition, separation, roughness effects, and wakes is still challenging and the cost of being able to achieve this makes the use of high-fidelity CFD quite limited in rotor design. Progress in hardware capabilities, including the rise of graphics cards use for simulations, is making unsteady, scale-resolved CFD more relevant and industrially achievable.

1.2.5. Summary of Aerodynamics Methods

Table 1.1 contains a summary of the advantages and disadvantages of the different aerodynamic methodologies described in the previous sections. The "Run Time" column shows the order of magnitude that can be expected for these methods to simulate a simple rotor. The "Transition" column refers to laminar to turbulent transition. "Separations" refer to flow detachment, which is partially addressed by many methods, but general 3D separations would only be truly captured by unsteady CFD. "Shocks" refers to supersonic flow, which most of these methods are not designed for. Although some of them could include some effects from shocks (e.g. panel methods, especially using a full potential flow approach [47]), CFD is usually used for designs where shocks are critical. "BVI", or blade vortex interaction is only captured by free wake panel methods and unsteady CFD. Large scale motion, as seen in the "FSI/Motion" column can only be captured by a few methods as well, with small displacements being possible with others. "VGs" stands for vortex generators, which tabular methods can capture partially, they can only be designed using CFD, and even then, unsteady simulations might be needed for high accuracy. Finally, the "Time to Setup New Rotor" column indicates the time to run a brand new case, with new airfoil geometry. Methods using tabular data would require building a database for the airfoils used, while the actuator disk approach would require a database for the full rotor, depending on the formulation used. If those databases exist, the time to setup a case is very short for tabular methods.

Table 1.1: Capabilities summary for aerodynamic methods.

	Run Time	Transition	Separations	Shocks	BVI	FSI/Motion	VGs	Time to Setup New Rotor
BEMT	<1 second	Yes	Partially	No	No	Partially	Indirectly	Medium
Lifting Line (prescribed wake)	10 seconds	Yes	Partially	No	No	Partially	Indirectly	Medium
Lifting Line (free wake)	10 minutes	Yes	Partially	No	Partially	Partially	Indirectly	Medium
VLM (prescribed wake)	10 seconds	Potentially	Potentially	No	No	Partially	No	Very Short
VLM (free wake)	10 minutes	Potentially	Potentially	No	Partially	Yes	No	Very Short
Panel Method (prescribed wake)	10 seconds	Potentially	Potentially	Potentially	No	Partially	No	Short
Panel Method (free wake)	10 minutes	Potentially	Potentially	Potentially	Yes	Yes	No	Short
Actuator Disk	1 hour	Yes	Partially	No	Partially	Partially	Indirectly	Medium
Actuator Line	100 CPUh	Yes	Partially	No	Partially	Partially	Indirectly	Medium
CFD (RANS)	1000 CPUh	Yes	Partially	Yes	Partially	No	Yes	Very High
CFD (unsteady)	10000 CPUh	Yes	Yes	Yes	Yes	Yes	Yes	Very High

It is easy to see why BEMT is so popular for wind turbine design, as it has the

capabilities needed for wind turbine simulations with extremely short run time. The vortex methods costs depend mostly on the wake approach, with small differences among them regarding supported features. Actuator disk is quite limited in scope, while actuator line can partially achieve many of the listed features. CFD is the clear winner in terms of potential to solve different problems, but it is also more expensive than other methods by orders of magnitude.

One important aspect of unsteady aerodynamics is its link to aeroacoustics. All of the methods described in Table 1.1 can handle aeroacoustics to some extent, but that extent is limited to either using analytical or empirical methods to compute the noise based on many assumptions, or it is limited to tonal noise. The only way to produce broadband noise from flow simulations in a generalized fashion is to use high-fidelity unsteady CFD.

As the activities required from this thesis involve FSI, rotor motion, and aeroacoustics, the methods of choice turn out to be the free wake panel method, the actuator line method, and unsteady CFD.

1.3. Aeroelastic Simulations of Rotors

FSI simulations require, at the very least, a structural and an aerodynamics solver. These are typically segregated and weakly coupled for wind turbine and aircraft simulations. One can distinguish FSI applications into quasi-steady cases, where the incoming flow is homogeneous and the interest is in a "final" blade/wing shape, which does not change with time, and truly unsteady cases, where there is no "final" blade/wing shape and the interest is in the statistics obtained from several timesteps, e.g., the maximum deflection. For realistic wind turbines simulations, as the incoming flow is the atmospheric boundary layer, even if the incoming flow is simulated under steady conditions, the blades encounter different flow conditions along throughout their rotations, meaning that quasi-steady simulations are limited in scope.

As FSI simulations require the aerodynamic solution at various time steps, they are typically orders of magnitude more expensive than a single steady aerodynamics simulation, even neglecting the time required for the structural solver. Hence, simulation time becomes even more critical for FSI cases, in particular for truly unsteady cases. Typical aeroelastic simulations of wind turbines are performed with BEMT [48, 49], with a few exceptions of applications of vortex methods [50] or CFD [49, 51], which incur significant cost. A detailed review of the state-of-the-art of wind turbine FSI can be found in [11]. In the aerospace market, different types of vortex methods have been the industrial solution of choice [52], with the rise of eVTOL having lead to renewed interest in free wake methods, in particular the VPM [53].

The structural solver, which is orders of magnitude cheaper than free wake or CFD-based methods, also varies in its complexity for different rotors simulations. Blades can be described by beam models, 2D finite element method (FEM) models, and 3D FEM models. These can be simulated in various degrees of complexity. For quasi-steady cases, they can be calculated as static deformation. Blade vibration can be achieved by linear analysis using modal decomposition, or non-linear un-

steady FEM simulations. Finally, blades can be studied individually or multi-body dynamics (MBD) methods can be used to simulate entire configurations. For wind turbines, this can include tower vibrations and even the motion of the platform the turbine is mounted on, in the case of floating offshore wind turbines [54]. For aircraft, this can include the deformations of the wings and blades [53].

Most simulations of wind turbine FSI use code-to-code validation, as not much experimental data on flexible rotors have been made public. Instead, most research organizations focus on theoretical turbines, designed to serve as references [55]. For aircraft, large efforts have been made to perform experiments that were made public and then used as part of large benchmark studies [56].

1.4. Aeroacoustic Simulations of Rotors

Noise produced by rotors impacts social acceptance of wind turbines and is important for aircraft certification purposes. Traditionally, rotor noise was computed based on analytical, semi-empirical, or empirical methods [57, 58]. These methods are very fast, often requiring simple geometry and flow properties, but are limited to simple configurations, with many assumptions that restrict their applicability to novel configurations and non-linear interactions. CFD-based noise computation can be performed from direct noise computation in an unsteady simulation, or by performing steady simulations in conjunction with stochastic methods to predict noise [59], again with some assumptions and limitations in terms of non-linear effects. The first approach is by far the most expensive of the available methods, but also the most general. Unsteady CFD is able to directly capture tonal sources [60], while scale-resolved unsteady CFD allows for broadband and tonal rotor noise to be computed [61], and can capture complex geometry effects that cannot be obtained from traditional methods [62]. In recent years, panel methods have also been applied to compute the tonal component of some aeroacoustic problems [6, 21], as a medium-fidelity approach between traditional and CFD-based methods.

The wind energy industry relies heavily on fast, traditional methods [58], while using higher fidelity approaches when these methods are inadequate [63]. The main interest is in reducing trailing-edge noise [62] by means of serrations and other devices that can be retrofitted to existing turbines to address excess noise. Trailing-edge noise is a broadband noise source which occurs around frequencies that are particularly annoying for humans. It occurs due to the turbulence in the blade boundary layer suction and pressure sides meeting on the trailing-edge. Leading-edge noise is typically the second highest aeroacoustic source and as trailing-edge noise is continuously reduced, it may become more important. It is also a broadband noise source, occurring at lower frequencies due to the interaction of the blades with the incoming turbulence.

Aircraft noise is typically divided into airframe noise (slat, flap, landing gear) and engine noise (rotors, stators, jet). Here we focus on the latter, with a focus on open rotors. Unlike for wind energy, tonal noise sources are the main issue with aircraft rotors, as they tend to be much higher than the broadband sources. However, as tonal noise is reduced, broadband noise starts becoming critical. The design of rotorcraft and propellers has heavily relied on analytical, semi-empirical,

and empirical methods, which were developed over the 1970s and 1980s (for a thorough history on these methods, see [64]). These methods evolved over the years and can include fairly complex conditions [65] and geometries [66, 67]. They require very little computational effort and have been the industry standard for design. However, the broadband noise capabilities are just as limited as in wind energy and CFD (typically URANS) is often used in late stage design due to its higher accuracy and ability to resolve complex 3D features [68–70]. As eVTOL aircraft have a large number of rotors that interact with the airframe components, the line between engine and airframe noise becomes more blurry. The noise from the tip vortices interacting with the airframe are expected to play a large role in public approval of these aircraft. Non-linear interaction between these parts is likely to require advances in the use of methods of various levels of fidelity.

1.5. Objectives

This thesis is focused on problems related to unsteady aerodynamics, in particular of rotors for wind energy and aerospace applications. Unsteady aerodynamics is a broad field and one that cannot be fully tackled with a single approach, as shown in Table 1.1. Hence, the objectives of this thesis are:

- Developing a free wake panel code for use in complex problems for wind turbines and aircraft, in order to understand the applicability of the tool for such cases and to advance the state-of-the-art in unsteady aerodynamics.
- Developing methodologies in an existing high-fidelity CFD solver in order to expand the capabilities of the method to tackle unsteady aerodynamics problems that currently rely extensively on experimental methods.

Hence, the studies in this work use two complementary methods: a free wake panel method developed for this thesis and a high-fidelity commercial CFD solver using the lattice-Boltzmann method (LBM), which will cover unsteady, scale-resolved simulations using blade-resolved meshes and the actuator line method. These methods correspond to the two main parts of this work: the first dealing with inviscid flow simulations and the second with viscous flow simulations. The common theme throughout the thesis is on expanding the use of higher-fidelity numerical simulations relative to the state-of-the-art. In order to do so, we must find problems that are relevant to the industry and that current standard methods do not address in a fully satisfactory manner.

The inviscid simulations were done with a code written from scratch during the PhD. Accordingly, the applications using the panel code are done in increasing degree of complexity, as each application serves as a building block for the next, with rigid moving geometries leading to FSI, and cases with some wake interaction leading to cases with lifting bodies inside of a rotor wake. While the source code of the LBM code was not modified for this work, advances were made via scripting and methodology development, in order to perform new kinds of simulations using the existing software.

The problems tackled in this work are illustrated in Fig. 1.1. First, unsteady aerodynamic phenomena linked to the dynamic motion (surge, sway, yaw) of offshore wind turbines, which are an active area of research as the technology is still in its early days. Second, the aeroelastic phenomena associated with long and flexible blades and wings, which are also a trend in the current wind and aerospace markets. Third, the study of wakes, which are critical for wind farm optimization and for rotor-wing interaction in modern aircraft. Fourth, the steering of these wakes for wind farm layout optimization. Fifth, the interaction of blades with upstream turbulence, leading to noise. Sixth, the unsteady boundary layer fluctuations that lead to trailing-edge noise, a major concern for wind turbine acceptance.

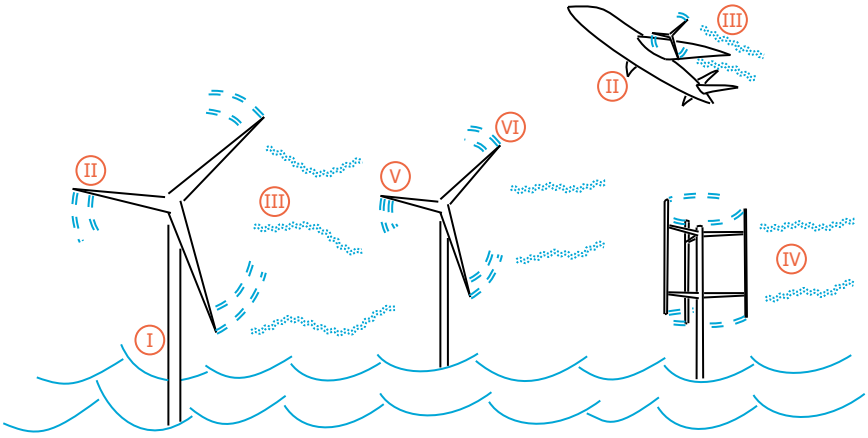

Figure 1.1: Unsteady aerodynamics problems associated with rotors. I: unsteady rotor motion on offshore wind turbines. II: aeroelastic phenomena linked to flexible blades and wings. III: wake interaction, including induction effects on the rotor and slipstream-wing interaction. IV: wake steering. V: inflow turbulence or leading-edge noise. VI: trailing-edge noise.

These problems can be tackled with a number of methods with their advantages and disadvantages. In this work, the inviscid panel code will have strong advantages in terms of moving geometries, while the viscous LBM simulations will allow for accurate capturing of boundary layer fluctuations and wake turbulence.

1.6. Publications During the Period of the PhD

The PhD documented in this thesis was developed in parallel to my day-to-day activities working full-time at Dassault Systèmes. Therefore, a large portion of the activities conducted in the past four years is not documented here. Summaries of all the works published during the PhD period are given in the next two subsections.

1.6.1. Publications Included in this Thesis

Studies that were published and that are related to this thesis are also part of the thesis itself. Hence, this list serves as a reference to the publications and as a

summary of the chapters of this thesis where the major scientific contributions can be found.

- Simulations of floating offshore wind turbine motion and their nonlinear aerodynamic effects, which are shown in Chapter 4, are documented in [71] and [72].
- Fluid structure interaction simulations of a highly flexible wing, part of the 3^{rd} Aeroelasticity Prediction Workshop, under flutter and gusts, which are shown in Chapter 5, were published in [73] and [74]. A summary of all contributions to the Workshop can be found in [75].
- The potential for wake steering in vertical axis wind turbines by means of blade and strut pitching is shown in Chapter 6 and was published in [76].
- A study on interaction between a propeller slipstream and a wing with a flap using a free wake panel method, shown in Chapter 7, was published in [77], whereas high-fidelity simulations were published in [78] and are the focus of Chapter 11.
- The first implementation of an actuator line model using a sliding mesh is shown in Chapter 9 and was published in [79].
- Blade-resolved and actuator line simulations of helical vortex instabilities due to an asymmetric rotor are shown in Chapter 10 and were submitted for publication in [80].
- Validation of an approach using 2.5D scale-resolved simulations against full-scale field test data of full wind turbine trailing-edge noise, including serrations, is shown Chapter 12 and was published in [81].
- Analyses of numerical simulations of inflow turbulence distortion near the leading-edges of airfoils of different thicknesses, along with the thickness effect on noise propagation shown in Chapter 13 were documented in [82].

1.6.2. Publications Not Included in this Thesis

- An extensive computational campaign to accurately predict full-scale landing gear noise for a Boeing 777 is documented in [83].
- Computational studies of the aerodynamics and aeroacoustics of a generic low boom concept aircraft (a version of the NASA X-59) flying at subsonic speeds are shown in [84–86].
- High-fidelity simulations seeking to contribute to the vortex ingestion case of the 5^{th} Propulsion Aerodynamics Workshop are documented in [87].
- Sensitivity studies showing the aeroacoustic effects of changes in slat tracks and the inboard slat tip geometry of a JAXA research aircraft are shown in [88].

- The experience accumulated over several years and projects on high-fidelity aeroacoustics simulations of airframe noise, with specific focus on far-field noise propagation from near-field data surfaces is documented in [89].
- A study on airfoil leading-edge defects aerodynamic categorization by means of machine learning is documented in [90].
- A subset of an experimental campaign of a wind turbine with straight and swept blades is documented in [91].
- A continuation of the work in propeller-wing interaction in [78], where a thorough analysis of the slipstream deformation is performed, is documented in [92].

References

[1] J. M. Jonkman, *Dynamics of offshore floating wind turbines—model development and verification,* Wind Energy **12**, 459 (2009).

[2] P. Veers, K. Dykes, E. Lantz, S. Barth, C. L. Bottasso, O. Carlson, A. Clifton, J. Green, P. Green, H. Holttinen, *et al.*, *Grand challenges in the science of wind energy,* Science **366**, eaau2027 (2019).

[3] M. M. Aslam Bhutta, N. Hayat, A. U. Farooq, Z. Ali, S. R. Jamil, and Z. Hussain, *Vertical axis wind turbine – a review of various configurations and design techniques,* Renewable and Sustainable Energy Reviews **16**, 1926 (2012).

[4] G. Tescione, D. Ragni, C. He, C. Simão Ferreira, and G. van Bussel, *Near wake flow analysis of a vertical axis wind turbine by stereoscopic particle image velocimetry,* Renewable Energy **70**, 47 (2014).

[5] K. A. Deere, J. K. Viken, S. Viken, M. B. Carter, M. Wiese, and N. Farr, *Computational analysis of a wing designed for the X-57 distributed electric propulsion aircraft,* in *35th AIAA Applied Aerodynamics Conference* (2017).

[6] C. Poggi, G. Bernardini, and M. Gennaretti, *Aeroacoustic analysis of wing-mounted propeller arrays,* in *AIAA AVIATION FORUM* (2021).

[7] T. E. Noll, J. M. Brown, M. E. Perez-Davis, S. D. Ishmael, G. C. Tiffany, and M. Gaier, *Investigation of the Helios prototype aircraft mishap. Volume I. Mishap report,* (2004), accessed: May 10 2023.

[8] Y. Zhou, H. Zhao, and Y. Liu, *An evaluative review of the vtol technologies for unmanned and manned aerial vehicles,* Computer Communications **149**, 356 (2020).

[9] T. Edwards and G. Price, *eVTOL Passenger Acceptance*, Contractor Report 20200000532 (National Aeronautics and Space Administration, 2020).

[10] M. Hansen, J. Sørensen, S. Voutsinas, N. Sørensen, and H. Madsen, *State of the art in wind turbine aerodynamics and aeroelasticity,* Progress in Aerospace Sciences **42**, 285 (2006).

[11] L. Wang, X. Liu, and A. Kolios, *State of the art in the aeroelasticity of wind turbine blades: Aeroelastic modelling,* Renewable and Sustainable Energy Reviews **64**, 195 (2016).

[12] J. O'Brien, T. Young, D. O'Mahoney, and P. Griffin, *Horizontal axis wind turbine research: A review of commercial CFD, FE codes and experimental practices,* Progress in Aerospace Sciences **92**, 1 (2017).

[13] H. Asmuth, G. P. Navarro Diaz, H. A. Madsen, E. Branlard, A. R. Meyer Forsting, K. Nilsson, J. Jonkman, and S. Ivanell, *Wind turbine response in waked inflow: A modelling benchmark against full-scale measurements,* Renewable Energy **191**, 868 (2022).

[14] T. Burton, N. Jenkins, D. Sharpe, and E. Bossanyi, *Wind Energy Handbook*, 2nd ed. (John Wiley & Sons, Ltd, 2011).

[15] R. B. de Luna, D. Marten, T. Barlas, S. G. Horcas, N. Ramos-García, A. Li, and C. O. Paschereit, *Comparison of different fidelity aerodynamic solvers on the IEA 10 MW turbine including novel tip extension geometries,* Journal of Physics: Conference Series **2265**, 032002 (2022).

[16] J. G. Leishman, *Challenges in modelling the unsteady aerodynamics of wind turbines,* Wind Energy **5**, 85 (2002).

[17] A. Li, M. Gaunaa, G. R. Pirrung, and S. G. Horcas, *A computationally efficient engineering aerodynamic model for non-planar wind turbine rotors,* Wind Energy Science **7**, 75 (2022).

[18] A. Li, G. R. Pirrung, M. Gaunaa, H. A. Madsen, and S. G. Horcas, *A computationally efficient engineering aerodynamic model for swept wind turbine blades,* Wind Energy Science **7**, 129 (2022).

[19] E. Branlard, *Wind Turbine Aerodynamics and Vorticity-Based Methods*, 1st ed., Research Topics in Wind Energy (Springer, 2017).

[20] L. Yang, C. Xie, and C. Yang, *Geometrically exact vortex lattice and panel methods in static aeroelasticity of very flexible wing,* Proceedings of the Institution of Mechanical Engineers, Part G: Journal of Aerospace Engineering **234**, 742 (2020).

[21] M. Gennaretti, G. Bernardini, J. Serafini, and G. Romani, *Rotorcraft comprehensive code assessment for blade-vortex interaction conditions,* Aerospace Science and Technology **80**, 232 (2018).

[22] D. J. Willis, *An unsteady, accelerated, high order panel method with vortex particle wakes*, Ph.D. thesis, Massachusetts Institute of Technology (2006).

[23] M. Tugnoli, D. Montagnani, M. Syal, G. Droandi, and A. Zanotti, *Mid-fidelity approach to aerodynamic simulations of unconventional VTOL aircraft configurations,* Aerospace Science and Technology **115**, 106804 (2021).

[24] E. J. Alvarez and A. Ning, *Modeling multirotor aerodynamic interactions through the vortex particle method,* in *AIAA Aviation Forum* (2019).

[25] B. Sandoz, V. Ahuja, and R. J. Hartfield, *Longitudinal aerodynamic characteristics of a V/STOL tilt-wing four-propeller transport model using a surface vorticity flow solver,* in *AIAA Aerospace Sciences Meeting* (2018).

[26] V. Ahuja and B. L. Litherland, *Comparison of aerodynamic analysis tools applied to a propeller-blown wing,* in *AIAA SCITECH Forum* (2023).

[27] R. Farrugia, T. Sant, and D. Micallef, *A study on the aerodynamics of a floating wind turbine rotor,* Renewable Energy **86**, 770 (2016).

[28] H. Lee and D.-J. Lee, *Numerical investigation of the aerodynamics and wake structures of horizontal axis wind turbines by using nonlinear vortex lattice method,* Renewable Energy **132**, 1121 (2019).

[29] L. Greco and C. Testa, *Wind turbine unsteady aerodynamics and performance by a free-wake panel method,* Renewable Energy **164**, 444 (2021).

[30] W. McCroskey, *Vortex wakes of rotorcraft,* in *33rd Aerospace Sciences Meeting and Exhibit* (1995).

[31] R. M. Erhard and J. J. Alonso, *A comparison of propeller wake models for distributed electric propulsion and evtol aircraft in complex flow conditions,* in *AIAA SCITECH Forum* (2022).

[32] P.-E. Réthoré, P. van der Laan, N. Troldborg, F. Zahle, and N. N. Sørensen, *Verification and validation of an actuator disc model,* Wind Energy **17**, 919 (2014).

[33] J. N. Sørensen and W. Z. Shen, *Numerical modeling of wind turbine wakes,* Journal of Fluids Engineering **124**, 393 (2002).

[34] A. Rosen and O. Gur, *Novel approach to axisymmetric actuator disk modeling,* AIAA Journal **46**, 2914 (2008).

[35] A. R. M. Forsting, A. Bechmann, and N. Troldborg, *A numerical study on the flow upstream of a wind turbine in complex terrain,* Journal of Physics: Conference Series **753**, 032041 (2016).

[36] P. Jha, M. Churchfield, P. Moriarty, and S. Schmitz, *Accuracy of state-of-the-art actuator-line modeling for wind turbine wakes,* in *51st AIAA Aerospace Sciences Meeting including the New Horizons Forum and Aerospace Exposition* (2013).

[37] J. N. Sørensen, R. F. Mikkelsen, D. S. Henningson, S. Ivanell, S. Sarmast, and S. J. Andersen, *Simulation of wind turbine wakes using the actuator line technique,* Philosophical Transactions of the Royal Society A: Mathematical, Physical and Engineering Sciences **373**, 20140071 (2015).

[38] M. J. Churchfield, S. J. Schreck, L. A. Martinez, C. Meneveau, and P. R. Spalart, *An advanced actuator line method for wind energy applications and beyond,* in *35th Wind Energy Symposium* (2017).

[39] C. Casses, C. Courtin, M. Drela, T. A. Fitzgibbon, J. Runda, M. Skarysz, P. Spalart, and Q. Wang, *Impact of propulsion modeling approach on high-lift force prediction of propeller-blown wings,* in *AIAA AVIATION Forum* (2022).

[40] Y. Delorme, R. Stanly, S. H. Frankel, and D. Greenblatt, *Application of actuator line model for large eddy simulation of rotor noise control,* Aerospace Science and Technology **108**, 106405 (2021).

[41] B. Sanderse, S. van der Pijl, and B. Koren, *Review of computational fluid dynamics for wind turbine wake aerodynamics,* Wind Energy **14**, 799 (2011).

[42] S.-P. Breton, J. Sumner, J. N. Sørensen, K. S. Hansen, S. Sarmast, and S. Ivanell, *A survey of modelling methods for high-fidelity wind farm simulations using large eddy simulation,* Philosophical Transactions of the Royal Society A: Mathematical, Physical and Engineering Sciences **375**, 20160097 (2017).

[43] E. N. Tinoco, O. Brodersen, S. Keye, and K. Laflin, *Summary of data from the sixth AIAA CFD drag prediction workshop: CRM cases 2 to 5,* in *55th AIAA Aerospace Sciences Meeting* (2017).

[44] C. L. Rumsey, J. P. Slotnick, and A. J. Sclafani, *Overview and summary of the third AIAA high lift prediction workshop,* Journal of Aircraft **56**, 621 (2019).

[45] J. Thé and H. Yu, *A critical review on the simulations of wind turbine aerodynamics focusing on hybrid rans-les methods,* Energy **138**, 257 (2017).

[46] G. Bangga and T. Lutz, *Aerodynamic modeling of wind turbine loads exposed to turbulent inflow and validation with experimental data,* Energy **223**, 120076 (2021).

[47] M. Gennaretti, U. Iemma, and L. Morino, *BEM for aerodynamics and aeroacoustics of rotors in subsonic/transonic forward flight,* in *2nd AIAA and CEAS Aeroacoustics Conference* (1996).

[48] T. Kim, A. M. Hansen, and K. Branner, *Development of an anisotropic beam finite element for composite wind turbine blades in multibody system,* Renewable Energy **59**, 172 (2013).

[49] C. Grinderslev, S. González Horcas, and N. N. Sørensen, *Fluid-structure interaction simulations of a wind turbine rotor in complex flows, validated through field experiments,* Wind Energy **24**, 1426 (2021).

[50] M. Sessarego, N. Ramos-García, and W. Shen, *Development of a fast fluid-structure coupling technique for wind turbine computations,* Journal of Power and Energy Engineering **3**, 1 (2015).

[51] Y. Li, A. Castro, T. Sinokrot, W. Prescott, and P. Carrica, *Coupled multi-body dynamics and CFD for wind turbine simulation including explicit wind turbulence,* Renewable Energy **76**, 338 (2015).

[52] J. Murua, R. Palacios, and J. M. R. Graham, *Applications of the unsteady vortex-lattice method in aircraft aeroelasticity and flight dynamics,* Progress in Aerospace Sciences **55**, 46 (2012).

[53] A. Savino, A. Cocco, A. Zanotti, M. Tugnoli, P. Masarati, and V. Muscarello, *Coupling mid-fidelity aerodynamics and multibody dynamics for the aeroelastic analysis of rotary-wing vehicles,* Energies **14**, 6979 (2021).

[54] Y. Liu, Q. Xiao, A. Incecik, and C. Peyrard, *Aeroelastic analysis of a floating offshore wind turbine in platform-induced surge motion using a fully coupled CFD-MBD method,* Wind Energy **22**, 1 (2019).

[55] E. Gaertner, J. Rinker, L. Sethuraman, F. Zahle, B. Anderson, G. E. Barter, N. J. Abbas, F. Meng, P. Bortolotti, W. Skrzypinski, G. N. Scott, R. Feil, H. Bredmose, K. Dykes, M. Shields, C. Allen, and A. Viselli, *IEA Wind TCP Task 37: Definition of the IEA 15-Megawatt Offshore Reference Wind Turbine*, Technical Report NREL/TP-5000-75698 (International Energy Agency, 2020).

[56] J. Heeg, *Overview of the aeroelastic prediction workshop,* in *51st AIAA Aerospace Sciences Meeting including the New Horizons Forum and Aerospace Exposition* (2013).

[57] R. K. Amiet, *Acoustic radiation from an airfoil in a turbulent stream,* Journal of Sound and Vibration **41**, 407 (1975).

[58] T. F. Brooks, P. D. Pope, and M. A. Marcolini, *Airfoil self-noise and prediction*, Reference Publication 89N25673 (National Aeronautics and Space Administration, 1989).

[59] R. Ewert and M. Bauer, *Towards the prediction of broadband trailing edge noise via stochastic surface sources,* in *10th AIAA/CEAS Aeroacoustics Conference* (2004).

[60] J. de Laborderie, L. Soulat, and S. Moreau, *Prediction of noise sources in axial compressor from urans simulation,* Journal of Propulsion and Power **30**, 1257 (2014).

[61] D. Casalino, G. Romani, R. Zhang, and H. Chen, *Lattice-Boltzmann calculations of rotor aeroacoustics in transitional boundary layer regime,* Aerospace Science and Technology **130**, 107953 (2022).

[62] F. Avallone, W. C. P. van der Velden, D. Ragni, and D. Casalino, *Noise reduction mechanisms of sawtooth and combed-sawtooth trailing-edge serrations,* Journal of Fluid Mechanics **848**, 560 (2018).

[63] S. Buck, S. Oerlemans, O. H. Mascarell, P. Joseph, W. N. Alexander, and S. Letica, *Active control of trailing edge noise,* in *AIAA AVIATION FORUM* (2021).

[64] K. S. Brentner and F. Farassat, *Modeling aerodynamically generated sound of helicopter rotors,* Progress in Aerospace Sciences **39**, 83 (2003).

[65] D. B. Hanson and D. J. Parzych, *Theory for noise of propellers in angular inflow with parametric studies and experimental verification*, Contractor Report 4499 (NASA, 1993).

[66] D. B. Hanson, *Noise of counter-rotation propellers,* Journal of Aircraft **22**, 609 (1985).

[67] D. B. Hanson, *Theory for broadband noise of rotor and stator cascades with inhomogeneous inflow turbulence including effects if lean and sweep*, Contractor Report 210762 (NASA, 2001).

[68] C. Nardari, D. Casalino, F. Polidoro, V. Coralic, P.-T. Lew, and J. Brodie, *Numerical and experimental investigation of flow confinement effects on uav rotor noise,* in *25th AIAA/CEAS Aeroacoustics Conference* (2019).

[69] M. Pestana, M. Sanjose, S. Moreau, M. Roger, and M. Gruber, *Assessment of the impact of a heterogeneous stator on the noise of an axial-flow low mach-number stage,* in *25th AIAA/CEAS Aeroacoustics Conference* (2019).

[70] H. Zhang, Y. Yang, P. Li, Y. Liu, Q. Li, and B. Noack, *Optimal rotation speed combination of contra-rotating rotors for multicopters,* in *AIAA AVIATION Forum* (2023).

[71] A. F. P. Ribeiro, D. Casalino, and C. S. Ferreira, *Surging wind turbine simulations with a free wake panel method,* Journal of Physics: Conference Series **2265**, 042027 (2022).

[72] A. F. P. Ribeiro, D. Casalino, and C. S. Ferreira, *Nonlinear inviscid aerodynamics of a wind turbine rotor in surge, sway, and yaw motions using a free-wake panel method,* Wind Energy Science **8**, 661 (2023).

[73] A. F. P. Ribeiro, D. Casalino, and C. Ferreira, *Free wake panel method simulations of a highly flexible wing at flutter,* in *AIAA AVIATION Forum* (2022).

[74] A. F. P. Ribeiro, D. Casalino, and C. Ferreira, *Free wake panel method simulations of a highly flexible wing in flutter and gusts,* Journal of Fluids and Structures **121**, 103955 (2023).

[75] M. Ritter, J. Hilger, A. F. P. Ribeiro, A. E. Öngüt, M. Righi, D. E. Raveh, A. Drachinsky, C. Riso, C. E. Cesnik, B. Stanford, P. Chwalowski, R. K. Kovvali, S. Duessler, K. C. Cheng, R. Palacios, J. P. dos Santos, F. D. Marques, G. R. R. Begnini, A. A. Verri, J. J. Lima, F. B. de Melo, and F. L. Bussamra, *Collaborative Pazy wing analyses for the third aeroelastic prediction workshop,* in *AIAA SCITECH 2024 Forum* (2024).

[76] A. F. P. Ribeiro, C. S. Ferreira, and D. Casalino, *Vertical axis wind turbine wake steering by pitched struts and blades,* Journal of Physics: Conference Series **2767**, 092004 (2024).

[77] A. F. P. Ribeiro, C. Ferreira, and D. Casalino, *On the use of filament-based free wake panel methods for preliminary design of propeller-wing configurations,* Aerospace Science and Technology **144**, 108775 (2024).

[78] A. F. P. Ribeiro, R. Duivenvoorden, and D. Martins, *High-fidelity simulations of propeller-wing interactions in high-lift conditions,* in *AIAA AVIATION Forum* (2023).

[79] A. F. P. Ribeiro and C. Muscari, *Sliding mesh simulations of a wind turbine rotor with actuator line lattice-Boltzmann method,* Wind Energy **27**, 1115 (2024).

[80] A. F. P. Ribeiro, T. Leweke, A. Abraham, J. N. Sørensen, and R. F. Mikkelsen, *Blade-resolved and actuator line simulations of rotor wakes,* Computers & Fluids **287**, 106477 (2025).

[81] A. F. P. Ribeiro, W. C. van der Velden, D. Casalino, and G. Wang, *Aeroacoustic simulations of a wind turbine: Validation with field tests, including trailing-edge serrations,* in *30th AIAA/CEAS Aeroacoustics Conference* (2024).

[82] A. F. P. Ribeiro, F. L. dos Santos, K. Venner, and L. D. de Santana, *Numerical study of inflow turbulence distortion and noise for airfoils,* Physics of Fluids **35**, 115112 (2023).

[83] M. R. Khorrami, B. Konig, E. Fares, A. F. P. Ribeiro, M. Czech, and P. A. Ravetta, *Airframe noise simulations of a full-scale large civil transport in landing configuration,* in *AIAA AVIATION FORUM* (2021).

[84] R. Ferris, M. Sacks, D. Cerizza, A. F. P. Ribeiro, and M. R. Khorrami, *Aeroacoustic computations of a generic low boom concept in landing configuration: Part 1 - aerodynamic simulations,* in *AIAA AVIATION FORUM* (2021).

[85] A. F. P. Ribeiro, R. Ferris, and M. R. Khorrami, *Aeroacoustic computations of a generic low boom concept in landing configuration: Part 2 - airframe noise simulations,* in *AIAA AVIATION FORUM* (2021).

[86] M. R. Khorrami, P. Shea, C. S. Winski, P. A. Ravetta, A. F. P. Ribeiro, R. Ferris, and M. Sacks, *Aeroacoustic computations of a generic low boom concept in landing configuration: Part 3 - aerodynamic validation and noise source identification,* in *AIAA AVIATION FORUM* (2021).

[87] A. F. P. Ribeiro, *Unsteady analysis of ground vortex ingestion with LBM-VLES,* in *AIAA SCITECH Forum* (2022).

[88] A. F. P. Ribeiro, M. Murayama, Y. Ito, K. Yamamoto, and T. Hirai, *Effect of slat tracks and inboard slat tip geometry on airframe noise,* in *28th AIAA/CEAS Aeroacoustics Conference* (2022).

[89] A. F. P. Ribeiro, M. R. Khorrami, R. Ferris, B. Koenig, and P. A. Ravetta, *Lessons learned on the use of data surfaces for Ffowcs Williams-Hawkings calculations: Airframe noise applications,* in *28th AIAA/CEAS Aeroacoustics Conference* (2022).

[90] A. F. P. Ribeiro and A. M. Forsting, *Machine learning categorization of a large CFD data set of airfoil leading-edge defects,* in *12th International Conference on Computational Fluid Dynamics – ICCFD12* (2024).

[91] E. Fritz, A. Ribeiro, K. Boorsma, and C. Ferreira, *Aerodynamic characterisation of a thrust-scaled IEA 15 MW wind turbine model: Experimental insights using PIV data,* Wind Energy Science **9**, 1173 (2024).

[92] R. Duivenvoorden, A. F. P. Ribeiro, T. Sinnige, and L. Veldhuis, *Slipstream deformation in propeller-wing-flap aerodynamic interaction,* submitted to Journal of Aircraft (2024).

II

Inviscid Flow Simulations

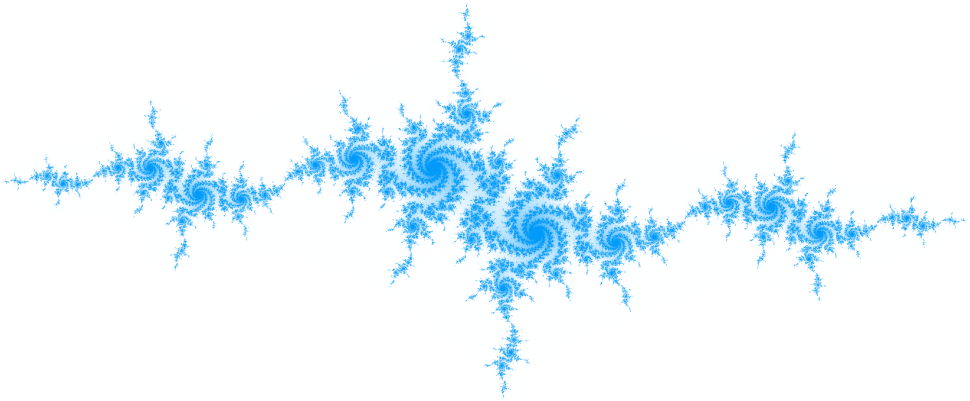

2

Numerical Methods

$$\rho \partial \vec{u}/\partial t + \rho(\vec{u} \cdot \nabla)\vec{u} = -\nabla p + \mu \nabla^2 \vec{u}$$

Incompressible Navier-Stokes equations

$$\vec{u} = -\nabla \Phi$$

Potential flow equation

A panel code with free wakes is developed from scratch for this work, named Code for Enhanced Loads and Interactions Simulations for Aerodynamics, or Code ELISA. It is written entirely in Julia, a modern, fast, dynamically-typed, functional programming language. This chapter contains descriptions of the numerical methods used in the code, along with details on their implementation.

2

2.1. Panel Method

The basic assumptions made for typical panel methods are that the flow is incompressible and inviscid, the latter having the consequence that the flow is also irrotational. This allows us to assume that there is a potential function Φ defined in space such that:

$$\vec{u} = -\nabla\Phi \tag{2.1}$$

where $\vec{u}$ is the velocity field. With basic properties of gradients, we arrive at the main equation of potential flow, which is a Laplace equation:

$$\nabla^2\Phi = 0 \tag{2.2}$$

The panel method employed in this work is based on the book of Katz and Plotkin [1] and the report by Maskew [2]. The method uses surface panels with constant strength doublets and sources with intensities μ and σ, respectively, and wake panels with constant strength vortex rings with intensities γ. By applying Green's theorem to Eq. 2.2, we obtain:

$$\frac{1}{4\pi}A_{ij}\mu_j + \frac{1}{4\pi}B_{ij}\sigma_j + \frac{1}{4\pi}C_{iw}\gamma_w = 0 \tag{2.3}$$

where A_{ij} and B_{ij} are elements of square matrices containing the influence coefficients of surface panel j on surface panel i and C_{iw} is composed of the influence of the wake panel w on surface panel i.

The influence coefficients are purely geometric and depend on the relative position of the two panels in question. For cases where there is no relative motion between solid surfaces (e.g., a set of rotating blades without a nacelle), A_{ij} and B_{ij} only need to be calculated once, while C_{iw} needs to be computed at every timestep if the wake is in motion.

A common way to close Eq. 2.3 is to set σ and γ, while leaving μ as the only unknowns. The source strengths are defined in a way to enforce surface impermeability, using:

$$\sigma = -(\vec{U}_\infty - \vec{u}_{body}) \cdot \hat{n} \tag{2.4}$$

where $\vec{U}_\infty$ is the freestream velocity, $\vec{u}_{body}$ is the kinematic velocity of the surface panel itself, and $\hat{n}$ is the unit vector normal to the panel. The strength of the wake vortex rings can be calculated as the jump in potential over the trailing edge, which enforces the Kutta condition. This is computed based on the adjacent top and bottom panels. The equation for γ is often shown in an incomplete, incorrect form, not including $\Phi_\infty = \vec{U}_\infty \cdot \vec{x}$, which is the freestream potential at an arbitrary location $\vec{x}$. The correct equation is [3]:

$$\gamma = \mu_{top} - \mu_{bottom} - (\Phi_{\infty top} - \Phi_{\infty bottom}) \tag{2.5}$$

Once a wake panel is created, γ is preserved, such that only the wake panel that is created in a given timestep has an unknown strength. This is handled by adding

the elements of C_{iw} corresponding to the new wake panels to A_{ij} in the position of the top and bottom trailing edge panels. The linear system can then be solved, and the surface velocities can be computed:

$$\vec{u} = \vec{U}_\infty - \vec{u}_{body} + \vec{u}_p = \vec{U}_\infty - \vec{u}_{body} - \nabla\mu + \sigma\hat{n} \tag{2.6}$$

where $\vec{u}_p$ is the perturbation velocity, which is the velocity on the panels caused by the doublet and source intensities. The velocities outside the surface are computed as a linear superposition of the velocity induced by each surface and wake panels on the point of interest:

$$\vec{u} = \frac{1}{4\pi}\sum_{j=1}^{N}\vec{A}_{ij}\mu_j + \frac{1}{4\pi}\sum_{j=1}^{N}\vec{B}_{ij}\sigma_j + \frac{1}{4\pi}\sum_{w=1}^{N_w}\vec{C}_{iw}\gamma_w + \vec{U}_\infty \tag{2.7}$$

where N is the number of surface panels, N_w the number of wake panels, $\vec{A}_{ij}$ and $\vec{B}_{ij}$ are the velocities that surface panel j induces on point i due to a unit strength doublet and source, respectively, and $\vec{C}_{iw}$ is the velocity that wake panel w induces on point i due to a unit strength vortex ring. Equation 2.7 is used to compute the velocity at each wake vertex, which in turn is used to convect the wake panels to their new position every timestep.

2.1.1. Influence Coefficients

In order to define the influence coefficients, we first need to define all the geometric properties of a panel. Surface panels are composed of three or four vertices ($\vec{v}_n$) and edges ($\vec{e}_n$). If they contain three, then they are triangles (tris) and are perfectly flat. If they contain four, then they are quadrangles (quads) and may not be perfectly flat. Wake panels are always quads. A panel center ($\vec{c}$) is defined as the average of its vertices. A local coordinate system is used on each surface panel, as shown in Fig. 2.1.

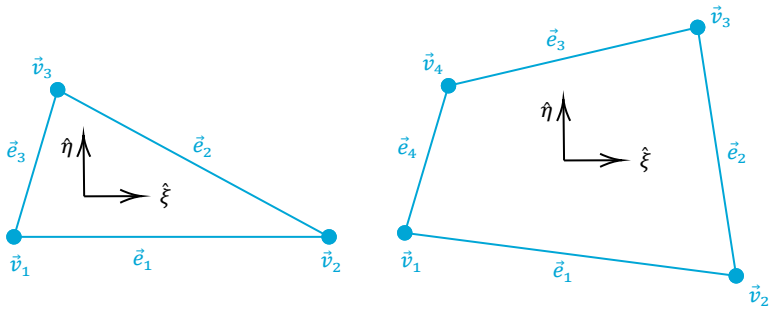

Figure 2.1: Panels and their local coordinate systems.

The unit vector $\hat{\xi}$ is parallel to the first edge of a tri and aligned with an imaginary line connecting the mid points of edges 2 and 4 of a quad. Initial tests on skewed

and warped quads showed that this is more accurate than using a vector parallel to edge 1 or a diagonal. The unit vector $\hat{\eta}$ is perpendicular to $\hat{\xi}$ and belongs to the plane of the panel (or the approximate plane of the panel, in the case of warped quads). Finally, the unit vector $\hat{n}$ is perpendicular to the panel itself, pointing outwards to the fluid.

The influence coefficients of a panel j on a point i, in their integral form, are:

$$A_{ij} = C_{ij} = \iint_j \hat{n} \cdot \nabla \frac{1}{\vec{r}} ds \tag{2.8}$$

$$B_{ij} = \iint_j \frac{1}{\vec{r}} ds \tag{2.9}$$

$$\vec{A}_{ij} = \vec{C}_{ij} = -\iint_j \nabla_i \left(\hat{n} \cdot \nabla \frac{1}{\vec{r}} \right) ds \tag{2.10}$$

$$\vec{B}_{ij} = -\iint_j \nabla_i \left(\frac{1}{\vec{r}} \right) ds \tag{2.11}$$

where $\vec{r}$ is the distance vector from panel j to panel i and the gradient ∇_i is taken with respect to the coordinates of i. Due to the equivalence of a doublet panel and a vortex ring [1], $A_{ij} = C_{ij}$ and $\vec{A}_{ij} = \vec{C}_{ij}$. Some authors choose to derive the algebraic expressions of the coefficients in the local coordinate system [1], however Maskew [2] derived formulations using the global coordinate system, which still require the definition of the unit vectors, but does not require computing all relevant quantities in the local coordinate system. The influence coefficients are calculated on each panel edge and their sum is the total influence a panel has on a point.

Here we take $\vec{e}_1$ as an example, which is defined as $\vec{v}_2 - \vec{v}_1$. The influence of other edges is computed in an analogous form. The influence of $\vec{e}_1$ on an arbitrary point $\vec{p}$ is calculated with the following equations:

$$\vec{a} \equiv \vec{p} - \vec{v}_1 \tag{2.12}$$

$$\vec{b} \equiv \vec{p} - \vec{v}_2 \tag{2.13}$$

$$A_l \equiv (\vec{a} \cdot \hat{\xi})(\vec{e}_1 \cdot \hat{\eta}) - (\vec{a} \cdot \hat{\eta})(\vec{e}_1 \cdot \hat{\xi}) \tag{2.14}$$

$$P_N \equiv (\vec{p} - \vec{c}) \cdot \hat{n} \tag{2.15}$$

$$P_A \equiv P_N^2 (\vec{e}_1 \cdot \hat{\eta}) + A_l (\vec{a} \cdot \hat{\xi}) \tag{2.16}$$

$$P_B \equiv P_A - A_l (\vec{e}_1 \cdot \hat{\xi}) \tag{2.17}$$

$$A_1 = C_1 = tan^{-1} \frac{(\vec{e}_1 \cdot \hat{\xi}) P_N \left(\left\| \vec{b} \right\| P_A - \|\vec{a}\| P_B \right)}{P_A P_B + P_N^2 \|\vec{a}\| \left\| \vec{b} \right\| (\vec{e}_1 \cdot \hat{\xi})^2} \tag{2.18}$$

$$B_1 = \frac{A_l}{\|\vec{e}_1\|} ln \left(\frac{\|\vec{a}\| + \left\| \vec{b} \right\| + \|\vec{e}_1\|}{\|\vec{a}\| + \left\| \vec{b} \right\| - \|\vec{e}_1\|} \right) - P_N A_1 \tag{2.19}$$

A proper `atan2()` function is able to deal with all the cases for A, with the only special case being the self-influence of a panel, in which the values of A for each edge are ignored in building the matrix A_{ij} and a value of -2π is used instead. The expression for B is singular for points lying on the edge, but as these influences are computed from panel center to panel center, this does not happen on a high quality, closed mesh. The velocity influence coefficients are given by:

$$\vec{A}_1 = \vec{C}_1 = \frac{(\vec{a} \times \vec{b})(\|\vec{a}\| + \left\|\vec{b}\right\|)}{\|\vec{a}\| \left\|\vec{b}\right\| (\|\vec{a}\| \left\|\vec{b}\right\| + \vec{a} \cdot \vec{b}) + d^2} \tag{2.20}$$

$$\vec{B}_1 = \frac{1}{\|\vec{e}_1\|} ln\left(\frac{\|\vec{a}\| + \left\|\vec{b}\right\| + \|\vec{e}_1\|}{\|\vec{a}\| + \left\|\vec{b}\right\| - \|\vec{e}_1\|}\right)[(\vec{e}_1 \cdot \hat{\xi})\hat{\eta} - (\vec{e}_1 \cdot \hat{\eta})\hat{\xi}] + A_1\hat{n} \tag{2.21}$$

The velocity influence coefficients are used for post-processing the velocity field, but more importantly, to compute the velocity on the wake vertices. Since wakes can cross surface panels, the singularities occur for $\vec{A}$ when $\vec{p}$ is on a panel vertex and for $\vec{B}$ when $\vec{p}$ is on a panel edge. In order to avoid these singularities, two measures are taken. The first is the term d^2, which is the only difference between Eq. 2.20 and the Biot-Savart law. This term avoids $0/0$ singularities and is an empirical value [4]. For this work, we set $d = 0.008\,\|\vec{e}_1\|$. The second measure is to set the natural logarithm in Eq. 2.21 to zero in case its denominator is zero. A representation of the velocity potential and velocity field created by source and doublet panels is shown in Fig. 2.2.

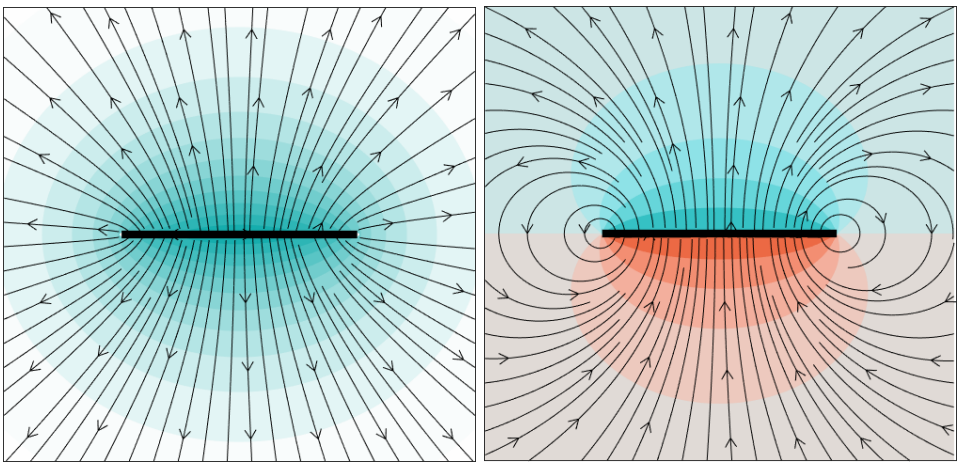

(a) Source panel. (b) Doublet panel or vortex ring.

Figure 2.2: Contour on center plane of square panels colored by the velocity potential created by the panels, with the associated streamlines showing the induced velocity field.

It is tempting to work exclusively using edges (or filaments, as they are usually referred to for wake panels) instead of panels, as some of the previous equations

allow this. In fact, computing $\vec{C}_{iw}$ requires calculating the vast majority of filaments twice, once for a given panel, and once on the neighbor panel that shares the filament. Steady cases often have neighbor panels with identical γ, meaning that the filaments shared by them can be skipped or erased. Iterating over the filaments seems like a much more efficient approach than iterating over panels. However, there is another formulation which is even more efficient than that. Assuming that $\vec{p}$ is distant from the panel, a far-field formulation can be used, which calculates the influence coefficients in a simplified approach and yields the following:

$$A = C = P_N S / \|\vec{p} - \vec{c}\|^3 \tag{2.22}$$

$$B = S / \|\vec{p} - \vec{c}\| \tag{2.23}$$

$$\vec{A} = \vec{C} = S[3P_N(\vec{p} - \vec{c}) - \hat{n}\|\vec{p} - \vec{c}\|^2] / \|\vec{p} - \vec{c}\|^5 \tag{2.24}$$

$$\vec{B} = S(\vec{p} - \vec{c}) / \|\vec{p} - \vec{c}\|^3 \tag{2.25}$$

where S is the surface area of the panel. These equations can be used if the distance between the panel and $\vec{p}$ is over 5 times the size of the panel [1]. For typical applications, such a condition is satisfied for the vast majority of the times the influence coefficients need to be computed. Hence,this approach is significantly faster than iterating over the wake filaments, unless the case is steady and a large number of filaments are erased. Since the focus of this thesis is on unsteady cases, the panel approach was chosen over the filament approach.

Further investigation led to another finding: the complex wakes of rotors result in wake panels warping and stretching dramatically. In particular, the panels that are at the end of the wake become extremely deformed. These panels are quite strong, as they are part of the startup vortex, and quite distant from the blades. Hence they are switched to the far-field formulation, which assumes that the panel is flat. Early simulations showed large fluctuations in blade forces, which started when the wake was sufficiently developed for the startup vortex to switch to the far-field formulation, and disappeared when the near-field (filament-based) formulation was used in the entire domain. This forces us to use the filament formulation for cases with complex wakes, such as rotors, restricting the far-field formulation to cases with simple wakes, such as wings, and to the solid surfaces, which are expected to have good mesh quality.

2.1.2. Vortex Core Model

The induction generated by the wake $\vec{C}_{iw}$ requires special attention, as wake edges cross each other and the surface quite often. The limitations of using an irrotational formulation to model a vortex lead to very high velocities near the wake edges, which can easily create meaningless results. Hence, instead of the d^2 term in Eq. 2.20, a vortex core model can optionally be used, which multiplies $\vec{C}_{iw}$ by a factor K [5].

$$K = 1 - a_1 e^{-b_1(h/r)^2} - a_2 e^{-b_2(h/r)^2} - a_3 e^{-b_3(h/r)^2} \tag{2.26}$$

where h is the distance between $\vec{p}$ and the infinite line that $\vec{e}_1$ lies on, r is the vortex core radius, and a_n and b_n are empirical constants. These constants are a function of the vortex Reynolds number $Re_\nu \equiv \gamma/\nu$, where ν is the fluid kinematic viscosity. Their value is defined for several Re_ν [5] and linear interpolation is used between these values. The vortex core radius is defined as:

$$r = \sqrt{r_0^2 + 4\alpha\nu\Delta t(1 + a' Re_\nu)/(1 + \epsilon)} \tag{2.27}$$

where r_0 is the radius in the previous timestep, $\alpha = 1.25643$ is Lamb's constant, Δt is the timestep, $a' = 0.000065$ is an empirical constant, and ϵ is the strain on $\vec{e}_1$, i.e. the ratio between its length in the current and previous timesteps. On the first timestep, r_0 can be set empirically to an estimate of the local boundary layer thickness, the airfoil thickness (if the filament is at the tip of a wing or blade), or any other empirical value. A value for r_0 between 60 and 70% of the blade chord was found to be accurate for wind turbine power prediction [6]. The purely inviscid Biot-Savart induced velocities on a line x running through the vortex core is shown in Fig. 2.3, along with results for the vortex core model, using a radius r and for several values of γ/ν.

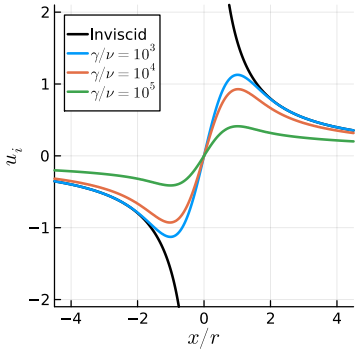

Figure 2.3: Velocity induced by a unit vortex along a line going through its center.

2.1.3. Symmetries

Two major cases of symmetries occur in aerodynamic simulations: symmetry across a plane and symmetry around an axis, or axisymmetry. When the incoming flow is aligned with the symmetry plane or axis, the simulation size can be drastically reduced by simulating only a part of the geometry. For panel codes, a case with one symmetry plane means being able to reduce the panel count in half.

Symmetry boundary conditions can be achieved by modifying the calculation of the influence coefficients. The influence of a starting panel j on a target point i simply needs to be calculated for every virtual position of panel j. Then, those values are added to the original influence coefficient and this new coefficient can

be used in the matrices of the linear system or to compute the velocity of a wake vertex. With this method, the large matrices are reduced significantly and fewer wake vertices need to be updated. The only assumption being made is that all virtual panels are identical to their real counterparts, including source and doublet strengths for solids and vortex strengths for wakes.

An example of axisymmetry is shown in Fig. 2.4a, which represents a simple rotor with three blades, where only one needs to be modelled. Figure 2.4b can be imagined as a simplified quadcopter with three blades on each rotor, where only one rotor needs to be simulated. This example only works if there is no asymmetric fuselage and the rotors are perfectly clocked. Note that, in the case of two perpendicular symmetry planes, it is not enough to have virtual panels behind the planes, but a third virtual copy is also needed. In the actual code, it is cheaper and simpler to displace the target i instead of the starting panel j and, in the case of a velocity influence, rotate the resulting vector back to its original position [1]. This way, fewer variables require recomputing, but the theory of the process is the same.

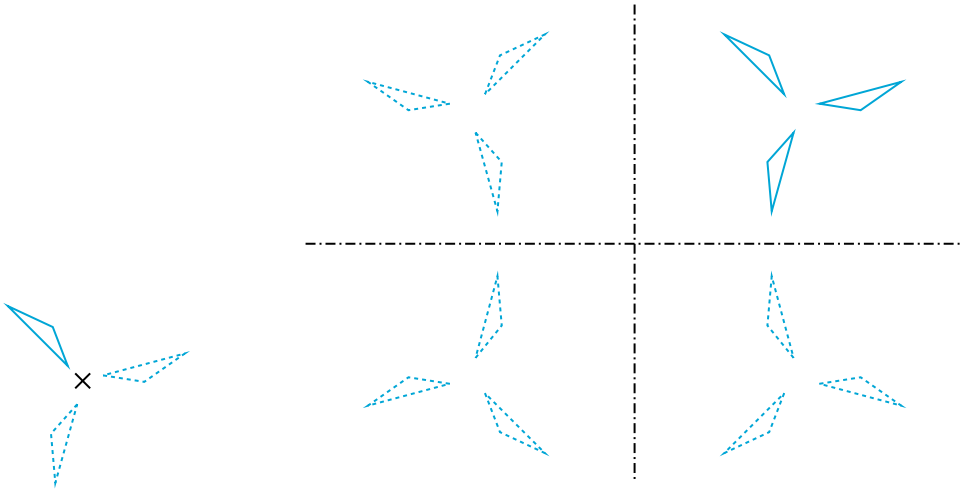

(a) Axial symmetry (b) Symmetry planes

Figure 2.4: Example of using symmetries in a panel code. Black dash-dotted lines are symmetry planes, black cross is a symmetry axis, blue triangles are geometries to be simulated, with dashed lines representing virtual solids.

Different parts of the panel code will benefit in different ways from the virtual panels. Reducing a case with N bodies to 1 means $1/N$ the memory required for the arrays storing panel properties, but $1/N^2$ the memory required for the influence coefficient matrices, which are generally far larger than all the other arrays combined. The construction of the influence matrix will still require iterating over all virtual bodies as influencing panels, but not as target panels. Hence, the time for building these matrices should be reduced by about $1/N$. Solving the linear system, which for unsteady cases needs to be done at every time step and is a significant part of the simulation time, scales with $O(N^2)$ using iterative methods. Hence, for

the basic panel code, not accounting for the wakes, it can be said that the case in Fig. 2.4, where the panel count is reduced by $1/4$, the cost will be reduced by up to $1/16$.

The wake adds two steps to the unsteady panel code which have significant cost: computing the velocities of all wake vertices and the influence of all the wake panels on the surface panels. Once again, as all the virtual panels still need to be used as influencing panels, but not target panels, the problem is reduced by a factor of $1/N$, not $1/N^2$. For long simulations, this drives the simulation cost. Every other part of the panel code, such as computing surface properties, convecting the wake, etc., will also be reduced by $1/N$, but their cost is negligible. Hence, symmetries are expected to reduce the cost of large simulations with rigid bodies by $1/N^2$ in the beginning of the run while the wake is small, gradually changing to $1/N$.

The memory footprint being reduced by $1/N^2$ is critical to ensure such cases can fit on the memory of a GPU, if one is being used. An early test on a wind turbine with three blades was 6.3 times faster by using two virtual blades, which falls near the average of $1/N$ and $1/N^2$.

2.1.4. First Wake Panels

At every timestep, Eq. 2.7 is used on each wake vertex and they are convected by $\vec{u}\Delta t$. The wake point that coincides with the surface trailing edge requires special attention, since calculating the velocity in that location is not trivial, as that is theoretically a stagnation point. In the first timestep, when the wake panels are first built, it is assumed that the flow travels at $\vec{U}_\infty - \vec{u}_{body}$. Using this instead of geometrical properties (say assuming that the wake is aligned with the trailing edges) makes the wake more homogeneous and avoids any geometry-induced discontinuities. The first wake vertex is placed $0.3(\vec{U}_\infty - \vec{u}_{body})\Delta t$ away from the trailing edge. The factor of 0.3 accounts for the body "dragging" the wake with it [1] and can be modified by the user.

After the initial timestep, the wake vertices that are not on the trailing edge are free to travel with the velocity given by Eq. 2.7. The trailing edge points still require special treatment. Instead of assuming their velocity, we instead assume that their new position lies between the trailing edge and previously shed wake vertex. This is achieved by drawing a parabola between the previously shed wake vertex and the trailing edge. This parabola is tangent to the trailing edge bisection plane.

Figure 2.5 shows the wake panels in the first two timesteps of a simulation. Subsequent timesteps behave the same way, with the wake vertices traveling with their calculated velocity and the first point after the trailing edge being interpolated. The spanwise position of point $\vec{w}_2$ on the right side of Fig. 2.5 lies on the straight line between $\vec{w}_1$ and $\vec{w}_3$, when seen from the top of the bisection plane.

In spite of the first streamwise wake filaments being significantly stretched when they are convected for the first time (by a factor of $1/0.3$), the strain correction in Eq. 2.27 is ignored in the first two wake rows, since this vortex stretching is simply an artifact of the special treatment of the first wake row.

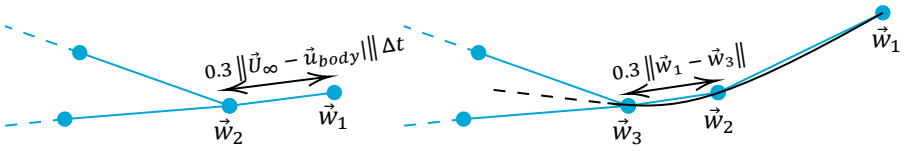

Figure 2.5: Trailing edge wake panels in the first and second timesteps.

2.1.5. Far Wake Treatment

The formulation described so far fails when wake panels impinge on surface panels, as their interactions lead to unphysical results. A solution to this problem [7] is to change formulations after a few wake panels rows from velocity potential wake panels to velocity wake panels, as shown in Fig. 2.6. The first row of wake panels after the trailing edge is dealt with by adding their C_{iw} coefficients to A_{ij}. The next few wake panels rows (the exact number is a user input, but initial tests suggest that only a couple of rows are needed) are dealt with normally, by calculating C_{iw}, multiplying it by γ_w and subtracting it from the right hand side of the linear system of equations.

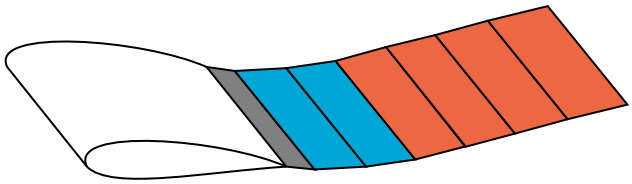

Figure 2.6: The three types of wake panels behind an airfoil. First row after trailing edge in grey, near wake panels in blue, far wake panels in orange.

The value of $\vec{C}_{iw}\gamma_w$ is computed for the subsequent wake panels (the far wake, from the trailing edge perspective) on each surface panel, i.e. we calculate the velocity $\vec{u}_{fw}$, which is a velocity induced on the surface panels by the far wake panels. We can then enforce surface impermeability by adding this additional velocity to Eq. 2.4:

$$\sigma = -(\vec{U}_\infty + \vec{u}_{fw} - \vec{u}_{body}) \cdot \hat{n} \tag{2.28}$$

The new values of σ can then be multiplied by their influence coefficients and $B_{ij}\sigma_j$ can be subtracted from the right hand side of the linear system of equations. Hence, the near wake affects the left hand side of the linear system in Eq. 2.3 and the far wake affects the right hand side. This stabilizes the problem and allows for cases of strong wake-body interaction to be computed, as a vortex core model can be added to the Biot-Savart equation.

2.1.6. Surface Velocity

We now focus on the calculation of Eq. 2.6, i.e. the surface gradient of μ. Figure 2.7 shows two very different surface meshes. On the left is the ideal case: a mesh

where all elements are perfect squares. On the right is a poor quality mixed mesh of tris and quads. The neighbors of an arbitrary panel are labeled in three levels: level 1 are panels that share an edge with the panel of interest, level 2 are panels that share a vertex with the panel, and level 3 are panels that share a vertex with a level 2 panel.

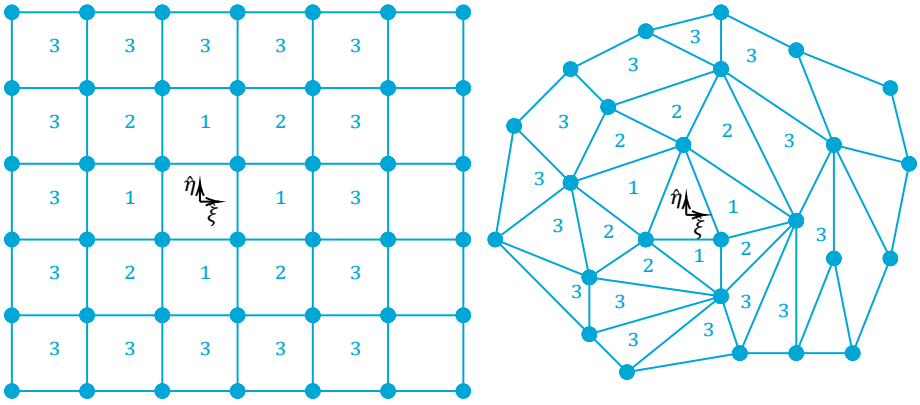

Figure 2.7: Examples of structured and unstructured surface meshes, with edge neighbors labeled as 1, vertex neighbors labeled as 2, and indirect vertex neighbors labeled as 3.

Calculating $\nabla\mu$ on the mesh with the structured squares is trivial with finite differences. The gradient can be computed in the $\hat{\xi}$ direction by using the panels labeled as 1 left and right of the panel of interest and central differences, while the gradient in the $\hat{\eta}$ direction can be computed with the top and bottom neighbors. On a perfect mesh, this solution has no drawbacks and is the method of choice for panel methods that are not general purpose (i.e., require a structured mesh and make some assumptions about the shape of the geometry). On an unstructured mesh with tris, this method is less than ideal, as using the 1 neighbors will not be very accurate. Another choice [8, 9] is to use a larger stencil (say the vertex neighbors 2) and build a linear system with two unknowns (the derivative of μ on each axis, $\partial\mu/\partial\xi$ and $\partial\mu/\partial\eta$) and as many equations as there are neighbors. The optimal solution for this system can then be calculated using the least-squares method. Each equation has the following form:

$$[(\vec{c}_i - \vec{c}_0)\cdot\hat{\xi}]\partial\mu/\partial\xi + [(\vec{c}_i - \vec{c}_0)\cdot\hat{\eta}]\partial\mu/\partial\eta = \mu_i - \mu_0 \tag{2.29}$$

where the subscript 0 indicates the panel of interest, and i are the neighbors. This method is implemented in this work in the following manner:

- If the user so desires, only the edge neighbors 1 are used. This will only apply to quads and will only be accurate if the mesh is of high quality and the panel does not border a sharp edge.
- Otherwise, and on tris, vertex neighbors 2 are located. Only neighbors that are approximately co-planar with the panel of interest are included. This is

achieved by checking that the two panels have normals that are within $60°$ of each other.
- If there are at least 6 neighbors, stop looking for neighbors. Fewer than 4 can easily lead to cases where the linear system will not have a unique solution. When a quad is on an edge, it has 5 node neighbors, but it needs an extended stencil in order for proper gradient computation.
- Extend the stencil to vertex neighbors of vertex neighbors 3.
- If there are still fewer than 6 co-planar neighbors, extend the stencil once again.

Panels near sharp edges with low resolution, such as wing tips, often require the two stencil extensions. The linear system can be solved for each panel before starting the simulations, unless the geometry is flexible and the distance between neighbors changes over time. If the number of neighbors is still under 6 or the linear system leads to very large numbers, infinities, or NaNs, the freestream and relative velocities are projected onto the surface as a rough approximation [10].

2.1.7. Surface Pressure

Once the surface velocity is known, the surface pressure p can also be calculated using the following equation, which is derived from the unsteady Bernoulli equation [11]:

$$\frac{p - p_\infty}{\rho} = -\frac{\left\|\vec{u}_p\right\|^2}{2} + (\vec{u}_{body} - \vec{U}_\infty) \cdot (\vec{u}_p) + \frac{\partial \mu}{\partial t} \tag{2.30}$$

where p_∞ is the freestream pressure and ρ is the fluid density. The time derivative is computed with standard backwards Euler. An option is also given for the user to select panels that are purposefully at very coarse resolution and should not affect the global forces (such as the tips of wings and blades) to be ignored. Their velocity is set to a projection of the freestream and their pressure is set to p_∞. This means they do not contribute to the integrated forces.

When the far wake treatment is added, the unsteady Bernoulli equation requires additional terms [12]:

$$\frac{p - p_\infty}{\rho} = -\frac{\left\|\vec{u}_p + \vec{u}_{fw}\right\|^2}{2} + (\vec{u}_{body} - \vec{U}_\infty) \cdot (\vec{u}_p + \vec{u}_{fw}) + \frac{\partial \mu}{\partial t} - \frac{\partial \phi_{fw}}{\partial t} \tag{2.31}$$

where the velocity induced by the far wake $\vec{u}_{fw}$ needs to be added to the perturbation velocity $\vec{u}_p$ and the time derivative of the potential induced by the far wake ϕ_{fw} needs to be included. This time derivative is composed of three terms: one related to the wake velocity, one related to the wake deformation, and one related to the flux of wake points through the near wake/far wake boundary. The second term can usually be neglected [12], leading to:

$$\frac{\partial \phi_{fw}}{\partial t} = \sum_{w=1}^{N_{fw}} (\vec{u}_{body} - \vec{w}_w) \cdot \vec{u}_{fw,w} - \sum_{w=1}^{N_{TE}} C_{w,1}\gamma_w \tag{2.32}$$

where N_{fw} is the number of far wake panels, $\vec{w}_w$ is the velocity of wake panel w, and $\vec{u}_{fw,w}$ is the velocity induced by the far wake panel w on the surface panel where p is being computed. The last term is a line integral of the induced potential of the first filament of the first far wake panel (i.e., the filament shared with the last near wake panel). Hence, it is integrated over a number of filaments equal to the number of trailing edge filaments on the bodies (N_{TE}). During testing, this term seemed to play a negligible role in pressure, but its computation is also very quick in comparison to the wake velocity term, and hence it was not removed.

2.1.8. Surface Motion

The surface motion and velocity are critical components of the panel code and the methods used herein were chosen after many tests on different configurations. The motion is critical to ensure the body is at the correct position at every timestep, while the velocity is crucial for the accuracy of Eq. 2.30. The user can define body motions as functions of time and space. If an aeroelastic simulation is performed, the body also moves due to the structural deformation.

If a time-dependent body velocity is used, then it is applied to the panel vertices at timestep t with the velocity value at time $t - \Delta t/2$, which is a first order interpolation. Once the body is moved and deformed, from the kinematics and structural deformation, the value of $\vec{u}_{body}$ can be computed from second order backward differentiation [13], using the center of the panel $\vec{c}$:

$$\vec{u}^t_{body} = \frac{3\vec{c}^t - 4\vec{c}^{t-\Delta t} + \vec{c}^{t-2\Delta t}}{2\Delta t} \tag{2.33}$$

where the superscripts represent the timestep when the coordinate is measured. This formula ensures that the kinematic velocity includes all forms of panel motion, while the second order formulation provides enough accuracy for relatively large timesteps.

2.2. Structural Model

The blades and wings are simulated as geometrically exact beam models, based on the works by [14], [15], and [16]. This allows for nonlinear, time domain calculations with large deflections, anisotropic deformation couplings, and curved beams. The open source Julia module GXBeam [17, 18] is used with nonlinear time marching solutions for coupling to the aerodynamics solver, and for nonlinear engenvalue analysis for the initial validation of wing vibration modes.

GXBeam was selected as the structural solver for three main reasons. First, it is written in Julia, as is the aerodynamics solver used for the simulations, which facilitates the coupling of the two codes. Second, it is a fast solver, being faster than the Fortran code GEBT [15], which GXBeam was originally based on. Lastly,

it can simulate rotating structures composed of arbitrary numbers of connected composite beams in large deformations, which is not important for wings, but will be useful for aeroelastic simulation of wind turbines. GXBeam also supports automatic differentiation, has native support for unsteady adjoint sensitivity analysis, and performs rotation parameterization with an extension to Wiener-Milenković parameters, avoiding singularities [19]. It uses the mixed variational formulation of geometrically exact beam theory [20], which can avoid numerical integration if the lowest possible order shape functions are used.

Other similar open source geometrically exact beam models available are GEBT [15] and BeamDyn [21]. Both codes are written in Fortran. GEBT is slower than GXBeam, and BeamDyn cannot handle beam assemblies, which is something that could be useful for simulating wings with pods and full wind turbines. GXBeam also has advantages over ASWING [22] in terms of solution smoothness [19]. Validation and examples of GXBeam can be found in [23].

The beam elements are modelled as Timoshenko beams, requiring 6×6 symmetric stiffness matrices, which for our cases follow the form:

$$\text{Stiffness Matrix} = \begin{bmatrix} K_{11} & 0 & 0 & K_{12} & K_{13} & K_{14} \\ 0 & GA & 0 & 0 & 0 & 0 \\ 0 & 0 & GA & 0 & 0 & 0 \\ K_{12} & 0 & 0 & K_{22} & K_{23} & K_{24} \\ K_{13} & 0 & 0 & K_{23} & K_{33} & K_{34} \\ K_{14} & 0 & 0 & K_{24} & K_{34} & K_{44} \end{bmatrix} \tag{2.34}$$

where K is the stiffness, the indices 1, 2, 3, and 4 correspond to the axial, torsion, out of plane bending (flapping), and in plane bending (horizontal, or edge-wise) displacements, G is the shear modulus, and A is the cross-section area. Elements set to zero in the stiffness matrix are equivalent to no coupling between the shear and the beam axial, bending, and torsion deformations. The inertial effects are accounted for with 6×6 symmetric node-based mass matrices, defined as:

$$\text{Mass Matrix} = \begin{bmatrix} m & 0 & 0 & 0 & mc_3 & -mc_4 \\ 0 & m & 0 & -mc_3 & 0 & mc_1 \\ 0 & 0 & m & mc_4 & -mc_1 & 0 \\ 0 & -mc_3 & mc_4 & I_{22} & -I_{32} & I_{24} \\ mc_3 & 0 & -mc_1 & -I_{32} & I_{33} & -I_{34} \\ -mc_4 & mc_1 & 0 & I_{24} & -I_{34} & I_{44} \end{bmatrix} \tag{2.35}$$

where m is the lumped mass, i.e. the mass around the node, modeled as concentrated on the node, c is the distance of the lumped mass to the beam node, as the nodes are not necessarily located on the section center of mass, and I the inertia, with indices consistent with the stiffness matrix.

2.3. Fluid Structure Interaction

The coupling of the aerodynamics and structural solvers is performed to allow for fluid structure interaction (FSI) simulations. A loosely-coupled approach [24] is

used. Each surface panel i is associated with a structural node j, which is part of a beam model. This is done by nearest neighbor. Then, the force acting on each panel $\vec{F}_i = -p_i \hat{n} S$ is added to the corresponding nodes. The torque associated with each force $\vec{T}_i = (\vec{x}_i - \vec{x}_j) \times \vec{F}_i$, where $\vec{x}_i$ is the panel center and $\vec{x}_j$ is the node coordinates vector, is also added to each node. These forces and torques are inputs to the structural solver, which in turn computes the displacement and rotation of each node of the beam model.

The geometry involved in the FSI coupling is shown in Fig. 2.8. Each structural node n_j has an associated direction $\vec{d}_j$, which is constructed as the difference between the next and previous nodes coordinates. Each surface vertex i is projected onto the beam by $d_i = (\vec{x}_i - \vec{x}_j) \cdot \vec{d}_j$, where d_i is the projected distance to the structural nodes. Splines [25] are constructed to interpolate the displacements and rotations along the beam element, so that smooth distributions are available along the span. Then, each surface point is rotated and translated around the beam model, based on those splines. This morphs the geometry into its new shape, while preserving a smooth panel distribution.

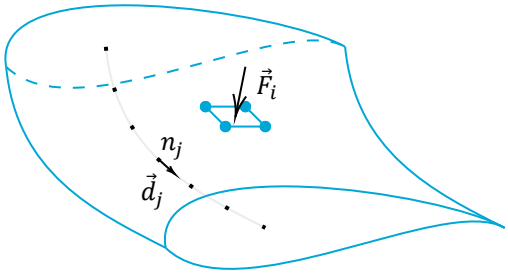

Figure 2.8: Example of an aerodynamic section and panel (in blue) and the beam model nodes (black).

2.4. Workflow of Unsteady Panel Code

The unsteady panel method applied in this thesis starts by solving the steady-state problem with the following steps:

1. Set solver options such as the timestep, fluid properties and conditions, empirical constants, etc.
2. Load surface mesh and compute its properties, such as panel neighbors, size, area, normals, etc. Initialize the large vectors and matrices and solve the least squares problems for surface velocity calculations in this step as well.
3. Compute the influence coefficient matrices and build the main linear system of equations.
4. Solve the linear system of equations.
5. Compute the surface properties. Calculating the surface forces, velocities, and pressures is theoretically optional for non-FSI simulations, as they are

used for post-processing only, not playing a role in solving the equations at all.

After running the steady-state solver, which can be used on its own for non-lifting bodies, the unsteady solver is initialized:

1. Create first row of wake panels.
2. Add wake to the linear system.
3. Solve the linear system of equations.
4. Compute the surface properties.

Finally, the unsteady loop can begin:

1. If a vortex core model is used, update the core radius of each wake filament.
2. Calculate the velocity of each wake vertex.
3. If body motion is imposed, move the geometry.
4. If FSI is being used, interpolate loads from the panel method to the structural solver, compute the deformation of the beam models, and deform the points of the panels accordingly.
5. Update geometry properties as needed. Static cases can skip this step altogether, while a rigid body rotation needs to recompute some properties. If panels move relative to each other, the influence coefficients need to be updated. If significant mesh deformation is present, the least squares problem for the surface velocity calculation needs to be updated.
6. Convect the wake and add a new row of wake panels to the trailing edges.
7. Add wake to the linear system.
8. Solve the linear system of equations.
9. Compute the surface properties.

This loop is repeated as many times as needed. For problems with many surface panels, the linear system solution can be a bottleneck. For long simulations with many wake panels, computing the wake velocities is the most expensive part of the simulation, followed by adding the wake to the linear system of equations. If a far wake is also included, then computing the time derivative of the induced potential can be as expensive as adding the wake to the linear system of equations.

In order to accelerate these steps, they can all be performed on the GPU, which in early tests led to a speed-up of $2\times$ over the CPU (8GB GPU against a 20 cores CPU). Large linear systems are difficult to fit on GPU memory, so different approaches are used to accelerate this step. The solution can be done using direct matrix inversion or an iterative method, namely the generalized minimal residual method (GMRES), depending on user input. Direct inversion can be much faster for small problems, but is not feasible for large matrices. An option to use a preconditioner, namely the lower-upper (LU) decomposition of the left hand side matrix is available. As this matrix does not change dramatically throughout the computation, this only needs to be done once and can accelerate GMRES by an order of magnitude.

References

[1] J. Katz and A. Plotkin, *Low-Speed Aerodynamics*, 2nd ed., Cambridge Aerospace Series (Cambridge University Press, 2001).

[2] B. Maskew, *Program VSAERO Theory Document: A Computer Program for Calculating Nonlinear Aerodynamic Characteristics of Arbitrary Configurations*, Contractor Report 4023 (National Aeronautics and Space Administration, 1987).

[3] H. Youngren, E. Bouchard, R. Coopersmith, and L. Miranda, *Comparison of panel method formulations and its influence on the development of QUADPAN, an advanced low-order method,* in *Applied Aerodynamics Conference* (1983).

[4] C. R. Satterwhite, *Development of CPANEL, An Unstructured Panel Code, Using a Modified TLS Velocity Formulation*, Master's thesis, California Polytechnic State University, San Luis Obispo (2015).

[5] M. Ramasamy and J. G. Leishman, *A Reynolds number-based blade tip vortex model,* Journal of the American Helicopter Society **52**, 214 (2007).

[6] B. Xu, B. Liu, X. Cai, Y. Yuan, Z. Zhao, and Y. Wang, *Accuracy of the aerodynamic performance of wind turbines using vortex core models in the free vortex wake method,* Journal of Renewable and Sustainable Energy **11**, 053307 (2019).

[7] M. Gennaretti and G. Bernardini, *Novel boundary integral formulation for blade-vortex interaction aerodynamics of helicopter rotors,* AIAA Journal **45**, 1169 (2007).

[8] W. K. Anderson and D. L. Bonhaus, *An implicit upwind algorithm for computing turbulent flows on unstructured grids,* Computers & Fluids **23**, 1 (1994).

[9] E. Sozer, C. Brehm, and C. C. Kiris, *Gradient calculation methods on arbitrary polyhedral unstructured meshes for cell-centered CFD solvers,* in *52nd Aerospace Sciences Meeting* (AIAA, 2014).

[10] D. Kinney, *Aero-thermodynamics for conceptual design,* in *42nd AIAA Aerospace Sciences Meeting and Exhibit* (AIAA, 2004).

[11] J. Katz and D. Weihs, *Hydrodynamic propulsion by large amplitude oscillation of an airfoil with chordwise flexibility,* Journal of Fluid Mechanics **88**, 485 (1978).

[12] G. Bernardini, J. Serafini, M. Molica Colella, and M. Gennaretti, *Analysis of a structural-aerodynamic fully-coupled formulation for aeroelastic response of rotorcraft,* Aerospace Science and Technology **29**, 175 (2013).

[13] E. Süli and D. F. Mayers, *An Introduction to Numerical Analysis* (Cambridge University Press, 2003).

[14] D. Hodges, *Nonlinear Composite Beam Theory*, Progress in Astronautics and A (American Institute of Aeronautics and Astronautics, 2006).

[15] W. Yu and M. Blair, *GEBT: A general-purpose nonlinear analysis tool for composite beams,* Composite Structures **94**, 2677 (2012).

[16] Q. Wang and W. Yu, *Geometrically nonlinear analysis of composite beams using wiener-milenković parameters,* Journal of Renewable and Sustainable Energy **9**, 033306 (2017).

[17] T. McDonnell and A. Ning, *GXBeam: A pure Julia implementation of geometrically exact beam theory,* Journal of Open Source Software **7**, 3997 (2022).

[18] T. McDonnell and A. Ning, *Geometrically exact beam theory for gradient-based optimization,* Computers & Structures **298**, 107373 (2024).

[19] T. G. McDonnell, *Gradient-Based Optimization of Highly Flexible Aeroelastic Structures*, Ph.D. thesis, Brigham Young University (2023), accessed: October 4 2022.

[20] D. H. Hodges, *A mixed variational formulation based on exact intrinsic equations for dynamics of moving beams,* International Journal of Solids and Structures **26**, 1253 (1990).

[21] Q. Wang, M. A. Sprague, J. Jonkman, N. Johnson, and B. Jonkman, *BeamDyn: a high-fidelity wind turbine blade solver in the FAST modular framework,* Wind Energy **20**, 1439 (2017).

[22] M. Drela, *Integrated simulation model for preliminary aerodynamic, structural, and control-law design of aircraft,* in *40th Structures, Structural Dynamics, and Materials Conference and Exhibit* (1999).

[23] T. McDonnell, *GXBeam.jl,* (2022), accessed: October 4 2022.

[24] Y. Bazilevs, K. Takizawa, and T. E. Tezduyar, *Computational fluid-structure interaction: methods and applications* (John Wiley & Sons, 2013).

[25] P. Dierckx, *Curve and Surface Fitting with Splines*, Monographs on numerical analysis (Clarendon Press, 1995).

3

Verification and Validation

If it disagrees with experiment, it's wrong.
In that simple statement is the key to science.

Richard Feynman

This chapter contains several simulations used to verify and validate the free wake panel method against analytical, numerical, and experimental data.

Parts of this chapter have been published in Journal of Physics: Conference Series **2265**, 042027 (2022) [1].

3.1. Introduction

Verification refers to checking whether a certain methodology is implemented correctly. This can be achieved by comparing results of a code to values that should be identical to it, such as other software using the same methods or analytical solutions of the same equations solved by the code. Validation refers to checking whether a certain methodology represents reality. This is achieved by comparing to experimental data or other already validated data.

During the processes of verification and validation, three main types of errors, which are intrinsic to any numerical solution need to be kept in mind, along with an additional type of error linked to iterative and unsteady problems:

1. *"Am I using enough digits?"*, or **truncation** errors. These are caused by the finite floating point precision of computers. It is tempting to use 32 bit precision for panel methods, as they use half the memory required for 64 bit floats. However, early simulations showed that for large geometries with high aspect ratio panels this was not satisfactory. Hence, 64 bit floats are used, which offer much higher precision than required from standard aerodynamics applications. Hence, truncation errors are assumed to not play a role in this work.
2. *"Is my mesh fine enough?"*, or **discretization** errors. They are caused by the fact that numerical methods do not solve continuous equations, instead discretizing them into a finite number of elements. These come from two sources for our code: the mesh used to represent geometries and the timestep chosen for the simulations. These errors can play a very large role in almost any numerical solver and will be carefully examined in this work by performing grid and timestep convergence studies.
3. *"Am I solving the right equations?"*, or **modelling** errors. These are related to the equations chosen to represent the physical phenomenon being modelled. In the case of a panel method, the assumptions intrinsic to the potential flow equation can play a big role. We assume incompressible flow, hence cases with moderate to high Mach numbers will result in large modelling errors. The assumption of inviscid flow is also critical in low to moderate Reynolds numbers cases or any cases with flow separation.
4. *"Were my equations solved?"*, or **convergence** errors. These occur in two forms for our cases: the residuals of the iterative solver for the linear system of equations and the physical time the unsteady simulations are run for, or time convergence. Errors in the iterative solver can be set to arbitrarily low numbers, which simply makes the solution process slower. Time convergence needs to be checked by the user and in most cases consists of monitoring certain flow properties, such as the integrated forces acting on a body and checking if they have stabilized to a quasi-steady value or periodic regime.

We use a large number of test cases to verify and validate the panel code in the next sections. We do this with cases of incremental complexity, in order to ensure different features of the code are implemented properly.

3.2. Sphere

The sphere is an excellent test case for early stages of panel code development, as it has a simple geometry, no wakes, and an analytical solution, at least in potential flow theory. Three separate aspects of the code can be examined: the basics of the panel method can be checked with the surface potential, the gradient computation can be checked with the surface velocity, and the velocity influence can be checked with the off-body flow velocities.

In order to have a single value for the error throughout the sphere, the L^2 norm of the error (or root mean square of the error) is used:

$$L^2 = \sqrt{\frac{\sum_{i=1}^{N}(\varphi_i - \varphi_{i,ref})^2}{N}} \tag{3.1}$$

where N is the number of panels and φ is an arbitrary variable, computed at each i panel center for the numerical case and the analytical case ref.

The potential on the surface panels can be computed as $\Phi = \Phi_\infty - \mu$, where $\Phi_\infty = \vec{x} \cdot \vec{U}_\infty$ for a surface point at location $\vec{x}$, μ is the doublet strength, $\vec{U}$ is the flow velocity, and ∞ denotes a freestream quantity. The analytical equations for the potential and velocity field for a sphere with radius R in spherical coordinates (r, θ, ψ) are:

$$\Phi = -U_\infty R(r/R + 0.5R^2/r^2)cos(\theta) \tag{3.2}$$

$$U_r = U_\infty(1 - R^3/r^3)cos(\theta) \tag{3.3}$$

$$U_\theta = -U_\infty(1 + 0.5R^3/r^3)sin(\theta) \tag{3.4}$$

$$U_\psi = 0 \tag{3.5}$$

We start by testing different meshing strategies for the sphere. Meshes comprised exclusively of triangles are compared to full quad or quad dominant meshes. We also compare a structured approach with an unstructured isotropic approach. The meshes are shown in Fig. 3.1.

The results of the runs based on these meshes are summarized in Table 3.1. All cases have similar number of panels. The structured tri case is by far the least accurate, indicating that isotropic panels are more accurate and splitting quads into tris is detrimental to the accuracy. From the errors on the velocity potential, we see that quad meshes are superior to tri meshes, from a pure panel method accuracy point of view. Finally, we see that a structured quad mesh produces much better surface gradients than other mesh types. The surface velocity is a derived quantity, hence the structured quad case producing better surface velocities than the isotropic quad case, in spite of having slightly worse results for the potential, is remarkable. The takeaway from this part of the study is to prioritize quads over tris, and to try to have isotropic, structured panels.

Another information present in table 3.1 is the velocity error based on least squares for the surface gradient, instead of the simple finite differences approach that is easy to perform in quads (as explained in section 2.1.6). Here we see the

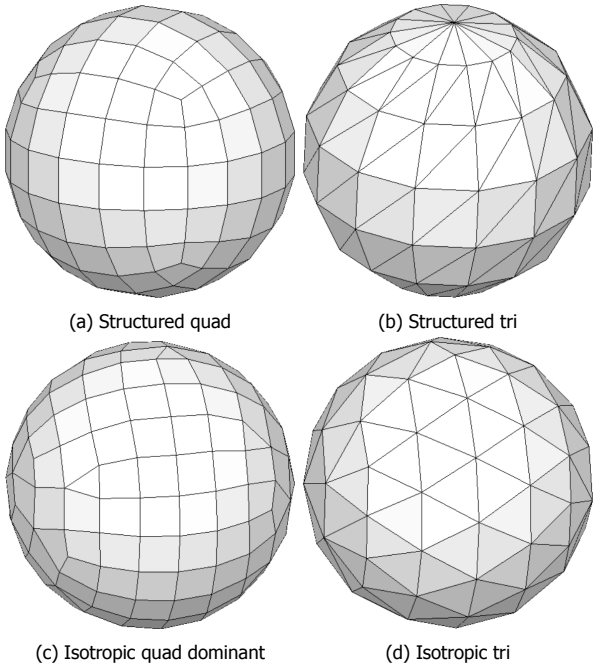

(a) Structured quad (b) Structured tri

(c) Isotropic quad dominant (d) Isotropic tri

Figure 3.1: Surface meshes for the sphere.

Table 3.1: Errors on different meshes for the sphere.

Case	Panels	$L^2(\Phi)$	$L^2(U)$
Structured Tri	168	0.022	0.714
Isotropic Tri	156	0.019	0.682
Isotropic Quad	172	0.009	0.680
Isotropic Quad Least Squares	172	0.009	0.685
Structured Quad	150	0.011	0.669
Structured Quad Least Squares	150	0.011	0.667

least squares approach being marginally more accurate than the simple finite differences for the structured quad mesh, while producing marginally worse results for the isotropic quad mesh. We keep both options in the code, as the finite differences approach is very accurate for quasi-2D meshes, such as present in extruded airfoils and simple wings, and the least squares approach should be more accurate in cases with worse mesh quality.

Next, we can use the sphere to investigate the grid convergence behavior of the code. We start from the isotropic tri and structured quad cases and progressively refine the surface meshes. We calculate the error $\Delta\Phi = \Phi - \Phi_{ref}$, where ref is the analytical result. Here we use the mean (or L^1 norm) of the absolute value $|\Delta\Phi|$

over the panels. The results in Fig. 3.2 show first order convergence behavior, as expected for the method. We can also observe that the quads produce smaller errors than the tris for the same number of panels, as seen in Table 3.1.

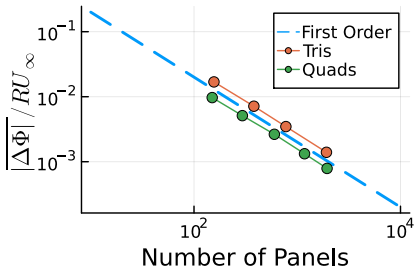

Figure 3.2: Grid convergence with the isotropic tri and structured quad mesh topologies.

Finally, we investigate the off-body velocity calculation. Figure 3.3 shows the grid convergence behavior of a velocity profile perpendicular to the flow for the quad structured meshes. The off-body velocities match the analytical solution nearly perfectly, until $r/R \approx 1.05$, which can be observed more clearly in the sub plot. Between this point and the body we observe two distinct behaviors: the cases with 150 and 294 panels are approaching the analytical results from below, while the other cases slightly overpredict the velocity near the body, then reach velocities also slightly below the analytical solution at $r/R = 1$. They approach from above, not from below. These two behaviors represent two different cases: points near panel centers (the cases with 150 and 294 panels) and points near panel vertices (other cases).

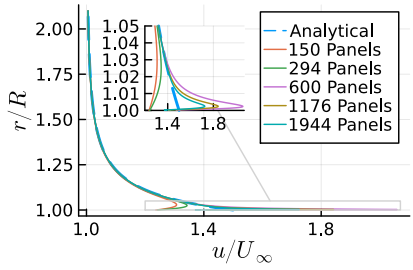

Figure 3.3: Velocity profile on a line perpendicular to the flow for various quad structured meshes.

For both cases velocities on the surface are slightly underpredicted, but points near nodes (or edges, in general) have a less benign behavior, as they tend to have their velocities overpredicted in regions just off the surface. These velocities would tend towards infinity, if not for the d^2 term in equation 2.20, which can be interpreted as a vortex core and could be fine-tuned to achieve lower overshoots around $r/R = 1.05$, with the consequence of causing more undershoots around $r/R = 1$.

With a real, viscous fluid, velocities at the wall should be zero for this case, hence, a slight underprediction is not completely undesirable, but an overprediction is. One way to avoid this issue is to compute velocities close to the surface by interpolating between the off-body velocities in accurate regions (for this case at $r/R \approx 1.05$) and the surface velocities. This would require an empirical factor to define where the "accurate" off-body region is, and adding expensive steps of finding nearest panels to the (already expensive) wake velocities calculation. Keeping in mind that approaching edges is less common than approaching panels and that the over and under prediction effects are counter-acting, we choose to accept this limitation without further corrections.

3.3. Static Airfoil

For a first verification of a lifting case, i.e., a case with a wake, we examine a NACA 0012 airfoil in static conditions. This can be compared with XFOIL [2], which is the de-facto industry standard tool for low speed airfoil simulation. XFOIL can be run in inviscid mode and also uses a source doublet formulation, albeit a higher order one. This case is used to define meshing best practices for airfoils, which will be necessary for the following cases.

As all other lifting bodies simulated hereafter, the trailing-edge of the airfoil is modelled as a cusp. Even though this is a 2D case, the code is written in 3D, hence a very large span is used and only a small section in the center is post-processed, in order to approximate a 2D case. The effect of the span length will be discussed in this section. The angle of attack is set to $5°$, which should fall within the limitations of an inviscid model.

A surface mesh is built using a cosine spacing or Chebyshev nodes, meaning the panels are finer in the chordwise direction near the leading and trailing-edges, which are the regions where higher gradients are expected. The results we examine in this section are the pressure coefficient $Cp = (p-p_\infty)/(0.5\rho_\infty U_\infty^2)$ and lift coefficient $C_L = L/(0.5\rho_\infty U_\infty^2)$, where p is the static pressure, ρ is the density, and L is the integrated lift force, or the force perpendicular to the freestream velocity on the 2D plane.

We start with a grid convergence study. We simulate the airfoil with a timestep of $\Delta t = 400c/U_\infty$ a total run time of $T = 800c/U_\infty$, and a span of $300c$. Figure 3.4 shows Cp along the streamwise coordinate x, normalized by the airfoil chord c. Comparison are shown for four resolutions and XFOIL results, itself run at a very fine resolution. Based on these results, between 100 and 200 panels per chord appears to be an accurate resolution for airfoil simulations.

We use the case with 200 panels per chord to evaluate the impact of time on the simulations. Figure 3.5 shows the time convergence of C_L with different choices of timestep compared to XFOIL. Lift is slightly underpredicted. The timestep plays a very small role on the results, with small timesteps showing no advantage for this case over very large ones. The total simulation time is critical for accuracy, with around 200 flow passes being needed to achieve converged results. We can conclude that for steady cases the physical simulation time should be quite long, but a very large timestep can be used, hence simulations costs remain low.

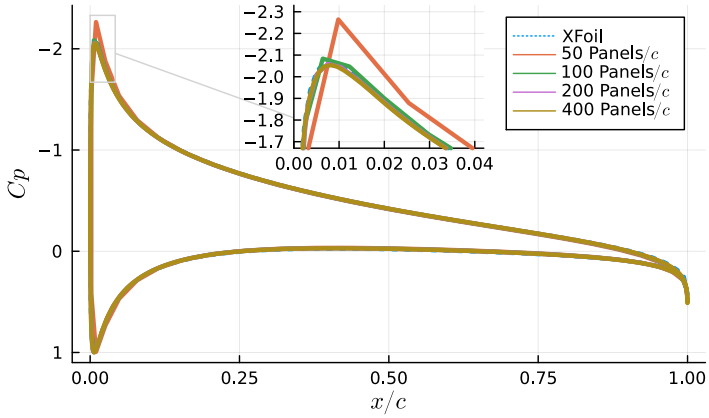

Figure 3.4: Pressure coefficient for various meshes.

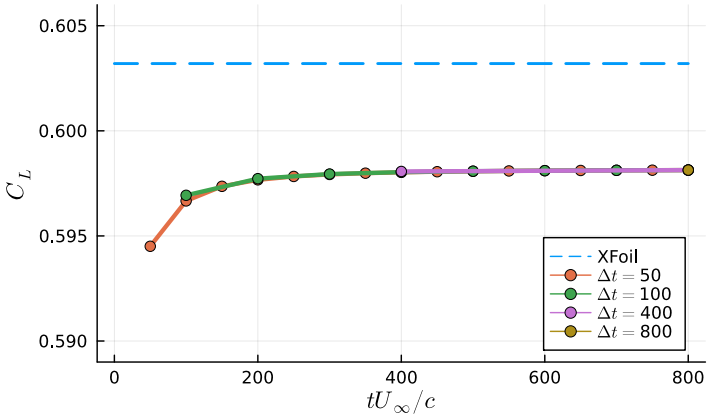

Figure 3.5: Time convergence of the lift coefficient.

Finally, we investigate the airfoil span length S and spanwise discretization effects. The question we seek to answer is how large a finite wing needs to be in order to behave as a 2D airfoil in its center. Figure 3.6 compares several span lengths, all using a spanwise element size of about $\Delta z = 6c$, and one case testing the spanwise grid spacing, where $\Delta z = 50c$. The results show that 2D flow is obtained with a span somewhere between $100c$ and $200c$ and that the spanwise discretization is not a critical parameter, with very large Δz values being accurate, while reducing computational time significantly.

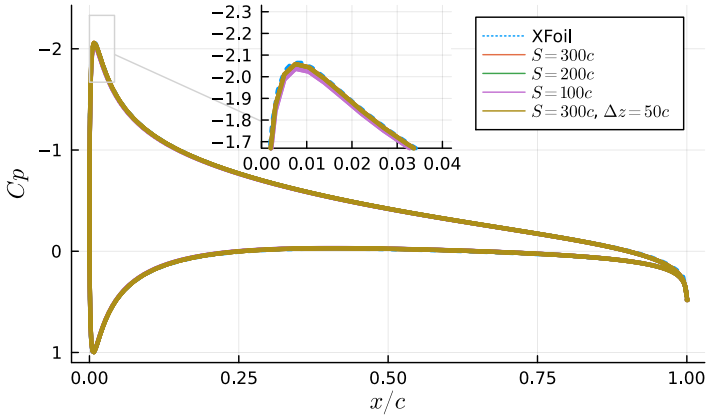

Figure 3.6: Span length and spanwise panel size effect on Cp. Spanwise element size $\Delta z \approx 6c$ unless stated otherwise.

3.4. Dynamic Airfoils

The unsteady features of the code are tested with dynamic airfoils simulations. We simulate four scenarios: a sudden change in airfoil angle of attack, a sudden change in flow vertical velocity, a harmonic oscillation of the angle of attack, and harmonic gusts. Analytical solutions are available for all conditions.

For the sudden change in airfoil angle of attack α, we use the Wagner function [3], which can be expressed as [4]:

$$\frac{C_L(s)}{2\pi\alpha} = \frac{1}{2} + \frac{2}{\pi}\int_{k=0}^{\infty} \frac{1}{k}\left(C(k)^R - \frac{1}{2}\right) sin(ks)\mathrm{d}k \tag{3.6}$$

where $s = tU_\infty/b$, t is time, $b = c/2$, and $C(k)^R$ is the real part of the Theodorsen function (see Eq. 3.9). If integrated numerically, this equation allows us to calculate the development of lift over time due to an infinitely fast change of α, as C_L approaches the steady value of $2\pi\alpha$.

For a sharp vertical gust, we use the Küssner function [5]. This solution considers the gust as it moves along the airfoil, hence the wind velocity at the leading-edge can be different from the velocity at the trailing-edge, meaning U_∞ is a function of time and space. The solution to this problem can be expressed as [6]:

$$\frac{C_L(s)}{2\pi\alpha} = \frac{2}{\pi}\int_{k=0}^{\infty} \frac{S^*(k)^R}{k} sin(ks)\mathrm{d}k \tag{3.7}$$

where $S^*(k)^R$ is the real part of the complex conjugate of the Sears function (see Eq. 3.11). Again, numerical integration allows us to obtain the time history of lift from this expression.

For an airfoil with a harmonic oscillation of α of the type $\alpha = \Delta\alpha e^{i\omega t}$, and vertical position h of the type $h = \Delta h e^{i\omega t}$, where $\omega = 2\pi f$ is the angular frequency and f is

the pitching frequency. Using the reduced frequency $k = \omega b/U_\infty$, Theodorsen [7] found the solution:

$$\frac{C_L(t)}{2\pi} = b^2\left(\ddot{h} + U_\infty\dot{\alpha} - ab\ddot{\alpha}\right) + 2U_\infty C(k)\left[\dot{h} + U_\infty\alpha + b\,(0.5 - a)\,\dot{\alpha}\right] \tag{3.8}$$

where a is the distance from the center of the airfoil to the center of rotation, normalized by b, positive towards the trailing-edge (e.g., for pitching around the quarter chord, which is used throughout this section, $a = -0.5$), and $C(k)$ is the Theodorsen function, computed using Bessel functions:

$$C(k) = \frac{J_1(k) - iY_1(k)}{[J_1(k) + Y_0(k)] + i\,[J_0(k) - Y_1(k)]} \tag{3.9}$$

For harmonic gust simulations, we use the vertical sinusoidal gust solution derived by Sears [8]. The streamwise velocity U_∞ is constant and the vertical velocity $w = We^{i\omega(t-x/U_\infty)}$, where W is the gust amplitude and x is the streamwise coordinate, centered on the half chord. Assuming that for small angles, $\alpha = W/U_\infty$:

$$\frac{C_L(t)}{2\pi\alpha} = e^{i\omega t}S(k) \tag{3.10}$$

where $S(k)$ is the Sears function, which also uses Bessel functions and the Theodorsen function:

$$S(k) = [J_0(k) - iJ_1(k)]\,C(k) + iJ_1(k) \tag{3.11}$$

Figure 3.7 illustrates the naming conventions described in the previous paragraphs. The analytical solutions obtained by these authors is achieved under the assumption of a thin airfoil with small angles of attack, hence, all cases are simulated with a NACA 0001 airfoil with 200 panels per chord, and amplitude of motion set to 1° (not depicted in Fig. 3.7, which uses a thick airfoil and larger α for clarity). The center of rotation, represented by the cross, corresponds to the case where $a = -0.5$, or rotation around the quarter-chord which is the case we use for Theodorsen. For the Wagner function, $a = 0.5$, or rotation around three-quarter-chord.

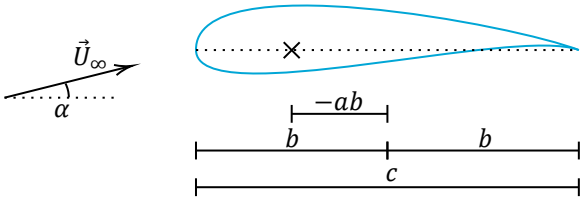

Figure 3.7: Conventions used for equations used in this section. The black cross marks the center of rotation.

Figure 3.8 shows a convergence study on the timestep for the validation of the Wagner function. Unlike static cases, dynamic cases are clearly strongly affected by the timestep. This case in particular involves instantaneous changes in the flow. Therefore, the smaller the timestep, the larger the acceleration imposed on the body, which means the spikes in transient forces seen at the beginning of the simulations become more pronounced. The analytical results do not present such spikes, as they do not include the non-circulatory component of lift (added-mass effect). Looking past the initial fluctuations, good agreement is observed between simulations and theory.

Figure 3.9 shows the same type of study, but focusing on the Küssner function. For this case, the choice of the timestep seems to affect the very early stages of the simulation, as the gust is still travelling over the airfoil. For the case of $\Delta t = 1.6c/U_\infty$, the gust travels more than the length of the airfoil in a single timestep, creating a peak, which fades in the following timestep. This peak reduces substantially as the timestep becomes smaller and soon after these initial inaccuracies, the simulations and theory agree very well.

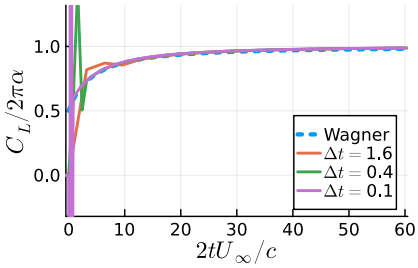

Figure 3.8: Effect of sudden change in angle of attack on lift. Values of Δt normalized with U_∞/c.

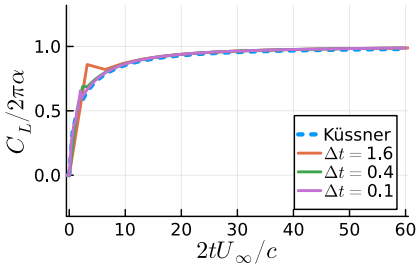

Figure 3.9: Effect of a sudden vertical gust on lift. Values of Δt normalized with U_∞/c.

We now examine the Theodorsen case. Oscillating an airfoil with a sinusoidal function for the angle of attack will create lift which, for small amplitudes, also follows a similar sinusoidal function, with amplitude ΔC_L (which can be normalized with the static lift corresponding to the maximum α, or $2\pi\Delta\alpha$) and phase ϕ, which is the angular difference between applying α and the resulting C_L. These results are summarized in Figures 3.10 and 3.11, which again contain a timestep study. The timestep Δt is defined as a fraction of the oscillating period $T = 1/f$. The same study is conducted for plunging motion, with vertical displacement amplitude $\Delta h = 0.01c$, and the results are summarized in Figures 3.12 and 3.13.

A very good agreement is observed for both ΔC_L and ϕ for all values of k. While ΔC_L is quite insensitive to Δt, ϕ shows some sensitivity, in particular for small values of k. For $k = 0.25$, $T/\Delta t = 80$ is equivalent to $T/\Delta t = 20$ for $k = 1$, in terms of the physical timestep or wake panels length. This is reflected in Figures 3.11 and 3.13, leading to the conclusion that for this case, the physical timestep is a more relevant parameter than the number of timesteps per oscillation cycle.

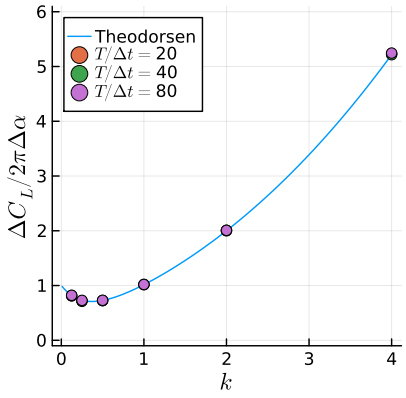

Figure 3.10: Amplitude of lift coefficient oscillations vs reduced frequency. Airfoil pitching around quarter chord.

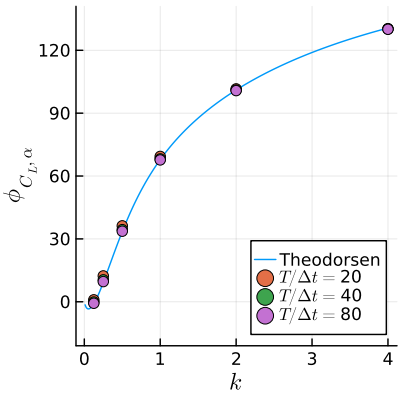

Figure 3.11: Phase (in degrees) of lift coefficient oscillations with respect to the angle of attack vs reduced frequency. Airfoil pitching around quarter chord.

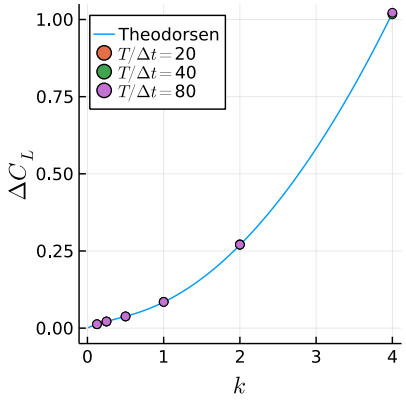

Figure 3.12: Amplitude of lift coefficient oscillations vs reduced frequency. Plunging airfoil case.

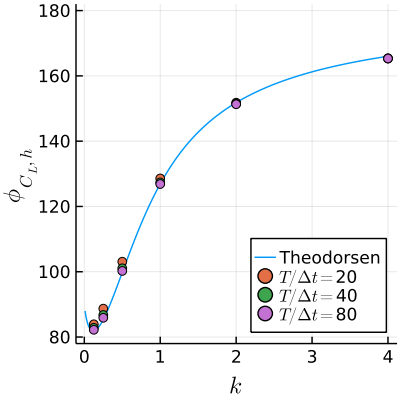

Figure 3.13: Phase (in degrees) of lift coefficient oscillations with respect to the vertical position vs reduced frequency. Plunging airfoil case.

Interestingly, a good value of Δt seems to be around $0.3c/U_\infty$ (corresponding to $T/\Delta t = 40$ for $k = 0.25$), which is similar to the results of the Wagner and Küssner functions. This corresponds to wake panels that have a length of 30% of the chord.

Finally, we turn to the Sears case. Figures 3.14 and 3.15 show the amplitude of lift fluctuations and phase with respect to the gust velocity w, respectively. The results are more sensitive to the timestep than the Theodorsen case, but seem to converge towards the analytical methods around $T/\Delta t = 80$ as well. Interestingly,

at $k=2$ the phase shows more resolution dependence, while at $k=1$, the amplitude shows more sensitivity. Overall, the results match the analytical data very well and we consider the code well verified against all the airfoil cases examined here.

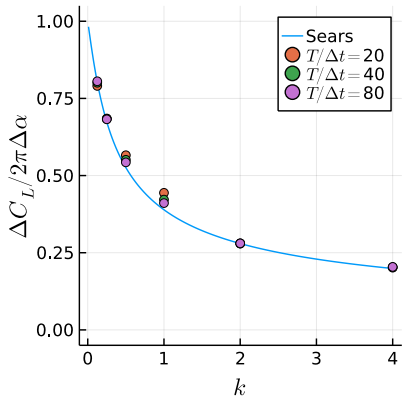

Figure 3.14: Amplitude of lift coefficient oscillations vs reduced frequency. Harmonic gust case.

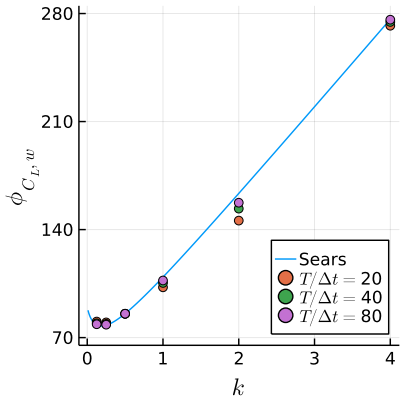

Figure 3.15: Phase (in degrees) of lift coefficient oscillations with respect to the vertical velocity at mid chord vs reduced frequency. Harmonic gust case.

3.5. Rotor in Hover

The Caradonna-Tung [9] rotor in hover conditions is chosen as the first truly 3D validation case with complex wakes. This is a simple rotor using two NACA 0012 straight blades at 8° pitch, and hence can be seen as an additional step of complexity on top of the previous airfoil simulations. The rotor diameter is 2.286 m and the current simulations are at 1250 RPM, which corresponds to tip Mach number of around 0.4, which is at the edge of what the subsonic assumptions can handle.

The tip vortices give us a chance to investigate spanwise discretization effects. The hover condition introduces another degree of complexity: during the initial transient, blade-vortex-interaction occurs, with part of the rotor wake impinging on the blades themselves, as seen in 3.16. This persists for a significant time, with the self induction of the wake pushing the root vortex up during the first 5 rotations, as shown in Fig. 3.17. After this, the wake in the root starts moving downwards, only escaping the blades entirely after about 5 further revolutions. Traditional free wake panel methods do not handle this well, for reasons discussed in 2.1.1. Computing wake panels as a velocity influence, instead of a potential influence [10] solves instabilities that would arise otherwise.

Figure 3.18 shows the spanwise mesh resolution effects on Cp, plotted on the normalized local x axis, running from the leading to the trailing-edge. We use 150 panels in the chordwise direction and compare 10, 20, and 80 panels in the spanwise direction. Effects are relatively small and all results compare favorably with

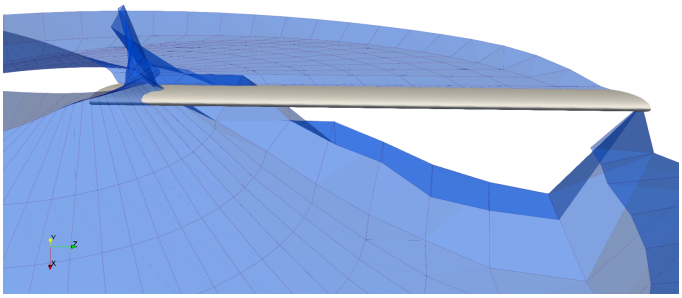

Figure 3.16: Blade intersecting its own wake after one rotation. Wake from other blade not shown for clarity. The root vortex continues to rise for several revolutions due to self induction of the wake.

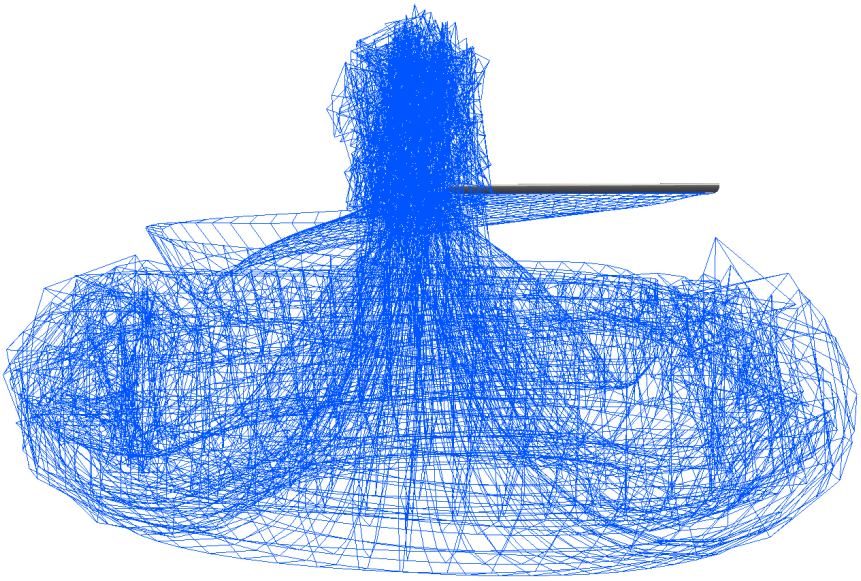

Figure 3.17: Startup wake being inducted through the rotor. Second blade and its wake are modelled with axial symmetry.

experiments. The suction peak reduces with coarsening at the outboard leading-edge. In order to keep simulations cost low, 20 spanwise panels seem adequate.

Figure 3.19 shows the cylindrical coordinate system used to locate the wing tip vortex. The angle ψ is the wake age angle, or the angle a certain point in the wake has travelled since it was shed from the blade tip (in the rotating reference frame). The radius r is the distance between the vortex and the axis of rotation (i.e., the wake contraction), and z is the vertical distance the vortex has travelled. Note that

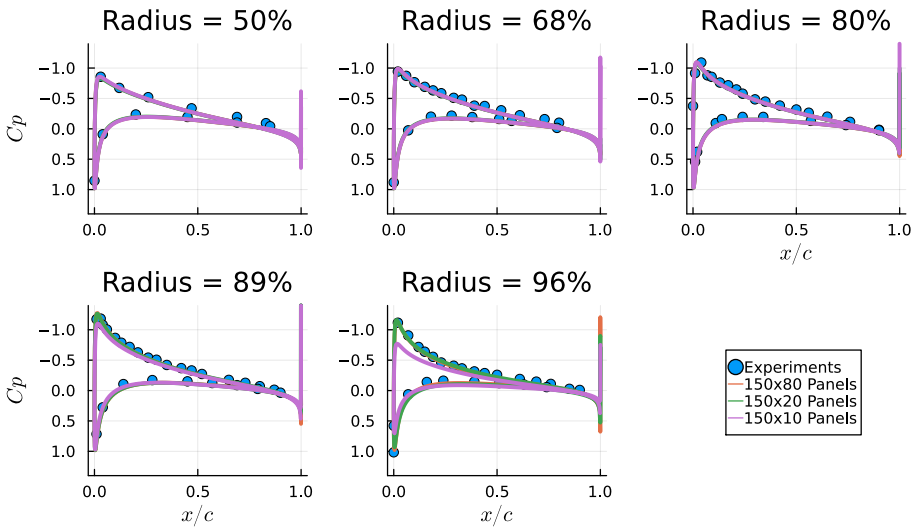

Figure 3.18: Pressure coefficient in different planes along the blade for different resolutions compared to experiments.

ψ and r are calculated as projected on the $z = 0$ plane and for our purposes, ψ is zero at the blade trailing-edge and is not limited to $360°$.

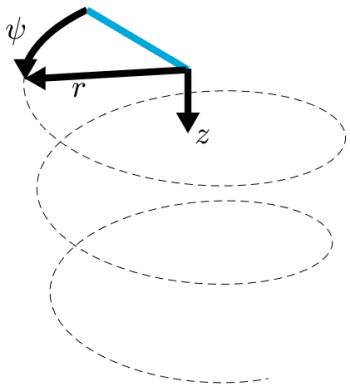

Figure 3.19: Cylindrical coordinate system used to represent wake position. The blue line represents a blade and the helix its tip vortex.

Figure 3.20 shows the tip vortex location along the wake age angle. The top of the figure shows the distance from the vortex to the axis of rotations and the bottom shows the vertical distance travelled from the trailing-edge. The slope change in the z/R curve at $\psi = 180°$ corresponds to the region where the wake passes under the second blade. Results agree fairly well with experiments and with each other, again indicating grid convergence with 20 spanwise panels. Interestingly, the coarsest results match better with experiments for z/R. The inviscid assumptions of the

method tend to lead to overprediction of sectional lift, which would cause the airfoil induction to be higher, moving the wake vortex further away from the blade than in reality. As seen in Fig. 3.18, the coarsest case is reducing the suction peak, and hence, the sectional lift in the outboard section. This is effectively moving the wake closer to experimental values, even though it is doing so due to discretization errors.

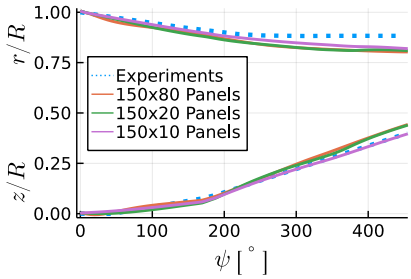

Figure 3.20: Tip vortex position for different resolutions compared to experiments.

Figures 3.21 and 3.22 show results for a timestep study for the rotor. The study is conducted with 20 spanwise panels. The pressure coefficient does not change dramatically with the timestep, with only minor changes in the suction peak. The wake position, on the other hand, changes with the timestep and only converges up to $\psi = 360°$ around $\Delta\psi = 6°$, or with 60 timesteps per rotation. At this stage, the results match the experimental data very well for z/R. With these results, we see that for reasonable accuracy of Cp, relatively large timesteps can be used, while converging the wake position in hover requires very small timesteps.

One way to improve results for larger timesteps is to use higher order wake filaments, which can be parabolas [11] or circular arcs [12], which improve the filament self induction [13]. The drawback of these methods is that the complexity for calculating the filament influence coefficient increases dramatically and special care needs to be taken with the ratio of vortex core size and filament curvature [14]. Hence, the vast majority of free wake methods uses simple straight filaments.

3.6. Wind Turbine

The NREL Phase VI 15 kW turbine [15][16] is used for validation of the method for wind turbines, as a large amount of experimental data are available for this case. This case presents a much more realistic blade geometry, with variable pitch and chord distributions and is more challenging for a fully inviscid panel code than the previous ones, as it deals with a highly loaded thick airfoil, with significant flow separations in the root, along with a curved tip. Therefore, some inaccuracies are to be expected.

Simulations are run at 7 m/s, 72 RPM. The rotor radius is 5.029 m and the turbine has two blades. A very fine structured surface mesh with about $42,000$ elements, used in several CFD studies in the past [17, 18], is employed for this

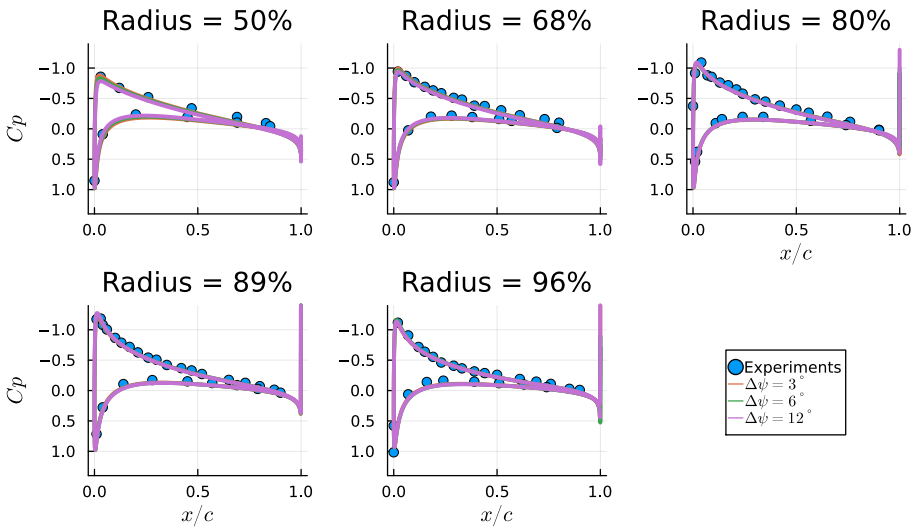

Figure 3.21: Pressure coefficient in different planes along the blade for different timesteps compared to experiments.

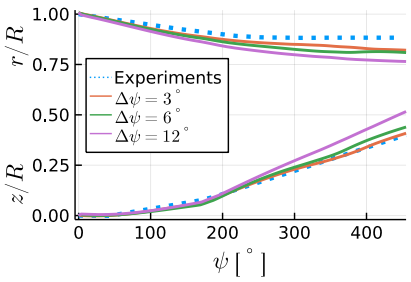

Figure 3.22: Tip vortex position for different timesteps compared to experiments.

case, allowing us to bypass mesh studies altogether. This also serves as a stress test for the code, as it is a much larger case than the previous ones. We use 60 timesteps per revolution, simulating 20 revolutions total. Only one of the two blades is simulated, with axial symmetry being used to speed up the simulations. This can be observed in Fig. 3.23, which also shows the large number of rotations simulated and entanglement of the wake panels at the very end of the wake, which is a common issue with free wake methods [19]. This entanglement forces us to avoid the far-field wake treatment, as described in section 2.1.1. Using the far-field formulation for this case, although significantly cheaper, led to unphysical fluctuations on the wake and on the blade surface.

Figure 3.24 shows the Cp distribution at various planes along the blade, showing very good agreement with experimental data. Some differences are seen in the root section, near the trailing-edge, which occur due to the separated flow that

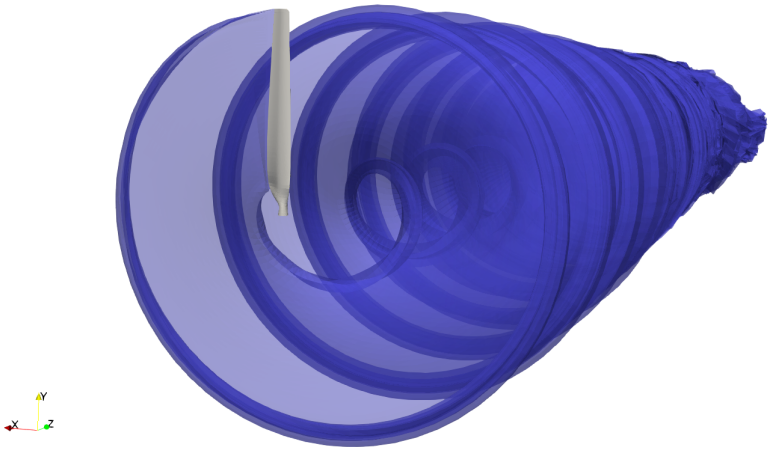

Figure 3.23: Blade and wake of the NREL Phase VI simulation. Second blade and its wake are modelled with axial symmetry.

occurs in the root region, where there is a transition from a circular cross-section to the S809 airfoil. As shown in Fig. 3.23, this region is simulated without a wake or nacelle, which is not physical, but should play only a small role in the overall turbine aerodynamics. In other parts of the blade, suction peaks are generally slightly overpredicted, as expected from a fully inviscid simulation.

Results for this wind turbine are also available at higher freestream velocities. However, even small increases to the velocity create large separations on the blade, which would not be captured with the current method. This is the main limitation of an inviscid tool for wind turbine simulations, as regions with separated flow are common for many flow conditions.

3.7. Conclusions

This chapter summarized verification and validation efforts for the panel code developed for this thesis. The verification phase focused on cases with analytical solutions, where the panel code should provide very accurate solutions. For all cases, the results adequately reproduced the theory. The validation phase focused on rotors, where the accuracy of the method was also adequate. The test cases were limited to flow conditions that are within the capabilities of potential methods. In the presence of separated flows, shocks, or very low Reynolds numbers, panel codes are not suitable tools and should be avoided.

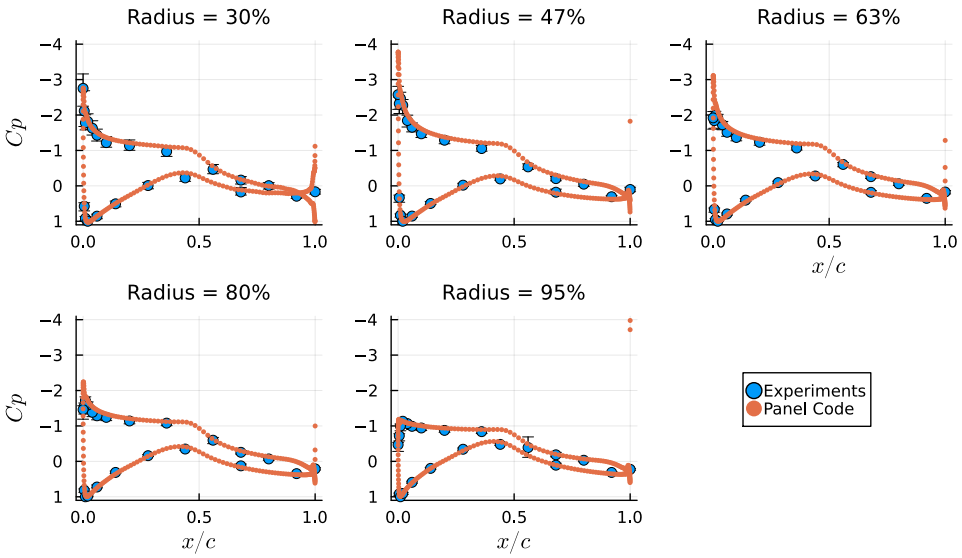

Figure 3.24: Pressure coefficient in different planes along the blade compared to experiments.

References

[1] A. F. P. Ribeiro, D. Casalino, and C. S. Ferreira, *Surging wind turbine simulations with a free wake panel method,* Journal of Physics: Conference Series **2265**, 042027 (2022).

[2] M. Drela, *XFOIL: An analysis and design system for low Reynolds number airfoils,* in *Low Reynolds Number Aerodynamics*, edited by T. J. Mueller (Springer Berlin Heidelberg, Berlin, Heidelberg, 1989) pp. 1–12.

[3] H. Wagner, *Über die Entstehung des dynamischen Auftriebes von Tragflügeln,* ZAMM - Journal of Applied Mathematics and Mechanics / Zeitschrift für Angewandte Mathematik und Mechanik **5**, 17 (1925).

[4] S. T. M. Dawson and S. L. Brunton, *Improved approximations to Wagner function using sparse identification of nonlinear dynamics,* AIAA Journal **60**, 1691 (2022).

[5] H. G. Küssner, *Zusammenfassender Bericht über den instationären Auftrieb von Flügeln,* Luftfahrtforschung **13**, 410 (1936).

[6] A. Kayran, *Küssner's function in the sharp edged gust problem—A correction,* Journal of Aircraft **43**, 1596 (2006).

[7] T. Theodorsen, *General Theory of Aerodynamic Instability and the Mechanism of Flutter*, Tech. Rep. 496 (NACA, 1934).

[8] W. R. Sears, *Some aspects of non-stationary airfoil theory and its practical application,* Journal of the Aeronautical Sciences **8**, 104 (1941).

[9] F. Caradonna and C. Tung, *Experimental and analytical studies of a model helicopter rotor in Hover*, Technical Memorandum 81232 (NASA, 1981).

[10] M. Gennaretti and G. Bernardini, *Novel boundary integral formulation for blade-vortex interaction aerodynamics of helicopter rotors,* AIAA Journal **45**, 1169 (2007).

[11] D. B. Bliss, M. E. Teske, and T. R. Quackenbush, *A new methodology for free wake analysis using curved vortex elements*, Contractor Report 3958 (National Aeronautics and Space Administration, 1987).

[12] F. Beyer, D. Matha, T. Sebastian, and M. Lackner, *Development, validation and application of a curved vortex filament model for free vortex wake analysis of floating offshore wind turbines,* in *50th AIAA Aerospace Sciences Meeting including the New Horizons Forum and Aerospace Exposition* (AIAA, 2012).

[13] M. J. Bhagwat and J. G. Leishman, *Self-induced velocity of a vortex ring using straight-line segmentation,* Journal of the American Helicopter Society **59**, 1 (2014).

[14] B. M. Govindarajan and J. G. Leishman, *Curvature corrections to improve the accuracy of free-vortex methods,* Journal of Aircraft **53**, 378 (2016).

[15] M. Hand, D. Simms, L. Fingersh, D. Jager, J. Cotrell, S. Schreck, and S. Larwood, *Unsteady Aerodynamics Experiment Phase VI: Wind Tunnel Test Configurations and Available Data Campaigns*, Tech. Rep. TP-500-29955 (NREL, 2001).

[16] C. Masson, J. Johansen, N. Sørensen, F. Zahle, C. Bak, H. Madsen, E. Politis, G. Schepers, K. Lindenburg, H. Snel, R. Rooij, E. Arens, G. van Bussel, G. Kuik, F. Meng, T. Sant, A. Knauer, G. Moe, X. Munduate, and S. Schreck, *IEA Wind Annex XX: HAWT Aerodynamic and Models from Wind Tunnel Measurements - Final Report*, Tech. Rep. TP-500-43508 (NREL, 2008).

[17] M. A. Potsdam and D. J. Mavriplis, *Unstructured mesh CFD aerodynamic analysis of the NREL phase VI rotor,* in *47th AIAA Aerospace Sciences Meeting including The New Horizons Forum and Aerospace Exposition* (2009).

[18] A. F. P. Ribeiro, *Otimização e dinâmica dos fluidos computacional aplicadas a turbinas eólicas*, Master's thesis, Universidade Federal do Rio Grande do Sul (2012).

[19] D. R. Houck, N. deVelder, and C. L. Kelley, *Comparison of a mid-fidelity free vortex wake method to a high-fidelity actuator line model large eddy simulation for wind turbine wake simulations,* Journal of Physics: Conference Series **2265**, 042044 (2022).

4

Nonlinear Aerodynamics of Floating Wind Turbines

I have yet to see any problem, however complicated,
which, when you looked at it the right way,
did not become still more complicated.

Poul Anderson

We investigate the aerodynamics of a surging wind turbine with numerical simulations based on the free wake panel method described in the previous chapters. We focus on the UNAFLOW case: a surging wind turbine which was modelled experimentally and with various numerical methods. Good agreement with experimental data is observed for amplitude and phase of the thrust with surge motion, as well as for the wind turbine wake. We then extend our simulations beyond the frequency range of the UNAFLOW experiments and reach results that do not follow a quasi-steady response for surge. Finally, simulations are done with the turbine in yaw and heave motion, and the impact of the wake motion on the blade thrust is examined. This chapter seeks to contribute a different method to the pool of results for the UNAFLOW case, while extending the analysis to conditions that have not been simulated before, and providing insights into nonlinear aerodynamic effects of wind turbine motion.

Parts of this chapter have been published in Wind Energy Science **8** (4), p. 661-675 (2023) [1].

4.1. Introduction

With the wind energy market leaning heavily towards offshore turbines in recent years, floating offshore wind turbines (FOWT) have become the focus of numerous research groups. One of the many challenges of such configurations is that, due to oceanic waves, the turbine is subjected to large amplitude motions, making its aerodynamics even more complex than that of onshore turbines. Turbines can translate horizontally perpendicular (surge) or parallel (sway) to the rotor plane. They can translate vertically (heave). They can rotate around the tower axis (yaw), or around the two horizontal axes (roll and pitch). These degrees of freedom are illustrated in Figure 4.1.

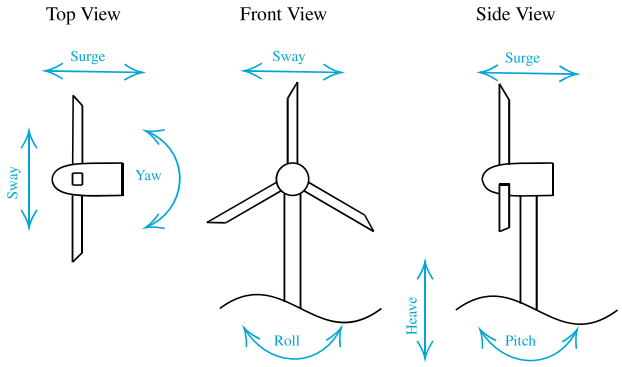

Figure 4.1: Degrees of freedom of a FOWT.

The sway and heave motion are, from a rotor aerodynamics perspective, equivalent. Rolling moves the rotor in a very similar way to sway, with an added in-plane rotation, equivalent to a change in rotation velocity. Pitching can be thought of as a combination of surge, yaw, and heave. Hence, for rotor aerodynamics, we can consider the surge, yaw, and sway as the fundamental forms of rotor motion, from which the others can be derived. For this reason, in this study, we focus on these three degrees of freedom. While these rotor motions have been studied experimentally [2], the frequencies and amplitudes of the motion are typically limited and inertial effects can affect the accuracy of the results. Hence, numerical studies are needed to investigate FOWT motion.

The UNAFLOW [3, 4] project provided a simplified test case for a non-stationary rotor, by simulating a surging wind turbine in a wind tunnel, without any tilting of the tower. Several groups have simulated the UNAFLOW case with different methodologies including blade element momentum theory (BEM), lifting line, and computational fluid dynamics (CFD), with fairly good results being achieved [5–7]. Furthermore, vortex methods have shown promising results for FOWT in surge and other degrees of freedom for other turbines [8, 9].

While BEM simulations have successfully captured dynamic inflow conditions [10], most of the research has focused on dynamic blade pitch, streamwise velocity

fluctuations, or surge. Recent developments have been made to extend BEM to general wind turbine motion [11] but, to our knowledge, validation of these models for sway conditions have not been extensive. Dynamic yaw and sway motion have the potential to be more difficult to capture than surge, as the wake moves from side to side and the assumptions of momentum theory may lead to large errors.

Here, we seek to contribute to the pool of UNAFLOW results by simulating the UNAFLOW case with a source and doublet free wake panel method. Unlike BEM and lifting line, panel methods directly model the blades, free from table look ups, while still being a fraction of the cost of a CFD simulation [12]. Blade thickness effects are included, by simulating the entire blade surface, rather than the camber surface or a single line, which can lead to better accuracy [13]. Panel methods have also been shown to accurately model full rotors, including aeroelastic effects [14–16]. The free wake allows for complex scenarios, such as blade vortex interaction [17], which could happen in extreme surge conditions.

With these characteristics in mind, this is an important stepping stone towards the ultimate goal of this research: aeroelastic simulations of FOWT through a fully-coupled transient aerodynamic/structural fluid-structure interaction (FSI). To our knowledge, only experimental and CFD results have been used to investigate the wake of the UNAFLOW turbine [5]. CFD adds significant diffusion to the tip vortices, making comparisons to experiments difficult. Hence, in this work we also show how the free wake panel method compares to experimental measurements of the wake.

The next objective of this work is to extend the surge analysis to sway and yaw motion. We use the UNAFLOW rotor to perform such investigations, in order to contribute to the knowledge of the physics of these motions. Finally, we seek to understand the impact of the wake motion on surge, sway, and yaw. We do this by employing unique features of the free wake panel method, allowing us to include rotor motion effects indirectly. The analysis of wake motion effects seeks to clarify mechanisms of turbine motion that will need to be accounted for when simulating FOWT motion with methods without true wake motion, such as BEM and prescribed wake vortex methods.

4.2. Surging Wind Turbine Simulations

The UNAFLOW turbine case [4] consists of a 3 blade rotor with a diameter of 2.38 m, rotating at 150 to 265 RPM, with U_∞ between 2.5 and 6 m/s. The entire rotor surges upwind and downwind at a frequency (f) ranging from 0.125 to 2 Hz and amplitude (A) from 2.5 to 125 mm, with the rotor center axial position following $A\sin(2\pi f t)$, where t is time. In non dimensional terms, for the case with freestrean velocity $U_\infty = 4$ m/s, this corresponds to reduced frequencies $f_r = fD/U_\infty$ between 0.07 and 1.2 and normalized amplitude $A_r = A/D$ between 0.001 and 0.05. This motion is performed such that the rotation axis is always aligned with the freestream, meaning no yawed flow occurs. As the majority of the experimental data are for $U_\infty = 4$ m/s and RPM of 241, these are the conditions we simulate in this work. We use different values of f and A for our simulations, based on availability of experimental data, while giving a preference to cases with high surge velocity $U_S = 2\pi f A$. For details on full scale values for these quantities see [18].

The blades are based on the SD7032 airfoil section, transitioning into a circle in the root region. For the simulations in this work, the blade geometry was constructed based on chord and twist distributions provided in the experimental data set [19]. However, this led to small differences in the geometry. In particular, the blade chord approaches zero at the tip [20], which is inconsistent with the geometry description [19], and can lead to some differences in results. Figure 4.2 shows the UNAFLOW wind turbine, along with its wake, as simulated by the methods described in this work. The blades are simulated without the hub and tower for simplicity.

Figure 4.2: Panel method simulation results of the UNAFLOW rotor and its wake.

The blades are discretized with 100 chordwise panels, using a cosine distribution, and 50 equally spaced spanwise panels each, with a total of about $15,000$ panels. The panel distribution is shown in Figure 4.3. This panel distribution was chosen as it provided grid converged results for several preliminary studies on airfoils and rotors, not included here for brevity. The blade tips and roots are closed to enforce impermeability. Wake panels are only shed from the trailing edges, meaning no vorticity can be shed from the 90° edges at the tips and roots. The timestep is set to $1/36$ of a revolution unless otherwise stated, which corresponds to a rotation angle of $\Delta\psi = 10^\circ$. Simulations are run for at least 40 revolutions, leading to about $216,000$ wake panels. This time discretization corresponds to 72 timesteps per surging period for $f = 2$ Hz, which is the highest surge frequency available in the experimental data set.

For a demonstration of the accuracy of the chosen timesteps, simulation duration, and validation of the mean flow properties, refer to [18]. Here, we focus on the main results for surge, while normalizing the plots in a different way than in the original publication, as this will help with comparisons to the other rotor motions. The main parameter we will use throughout this work is the thrust coefficient C_T:

$$C_T = \frac{T}{\frac{1}{2}\rho\pi R^2 U_\infty^2} \tag{4.1}$$

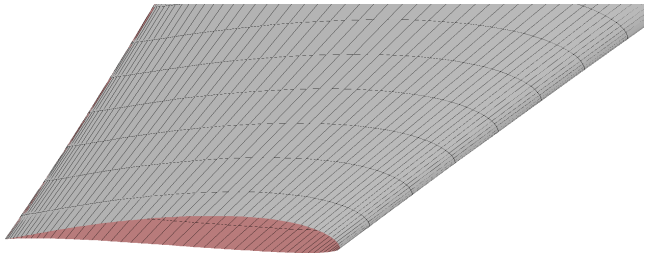

Figure 4.3: Surface mesh used for the UNAFLOW blade, cut by a clipping plane.

where T is the thrust force, ρ is the air density, and R is the turbine radius.

4.2.1. Surge velocity effects

We examine the fluctuating component of C_T, while keeping $A = 15$ mm ($A_r = 0.006$), and varying f between 0 and 2 Hz (f_r between 0 and 1.2). Figure 4.4 shows the effect of f_r on the amplitude of the fluctuations of thrust (ΔC_T), normalized by A_r. Note that ΔC_T is the amplitude that would multiply a sine function to represent the time history of C_T, or $(C_{Tmax} - C_{Tmin})/2$, assuming a time history of C_T that is perfectly sinusoidal. Figure 4.5 shows the effect of f_r on the phase shift ϕ between the rotor position and the fluctuations of C_T. The experimental data shown throughout this chapter were filtered at the surge frequency. The lowest surge frequency, $f_r = 0.3$ Hz was run for twice as long as other cases, to obtain meaningful statistics from the simulations.

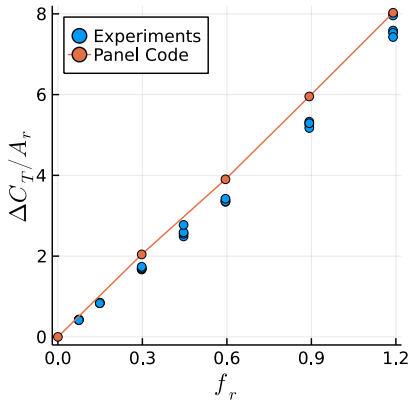

Figure 4.4: Surge frequency effect on the amplitude of the fluctuation of the thrust coefficient. Simulations at constant A, experiments at various A shown.

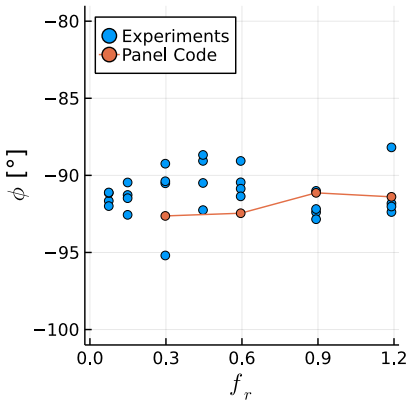

Figure 4.5: Surge frequency effect on the phase between the rotor position and its thrust. Simulations at constant A, experiments at various A shown.

The values of $\Delta C_T/A_r$ agree well with experimental data, with an approximately linear relation between the surge velocity and the thrust fluctuations. This confirms

the quasi-steady nature of the results, which is likely due to the relatively small values of U_S [21]. The average slope of $\Delta C_T/A_r$ as a function of f_r in the simulations is 15% higher than in the experiments, likely due to the inviscid approach. The values of ϕ fall within the experimental scatter, being within 3° of -90° for all cases, which corresponds to the quasi-steady response.

4.2.2. Rotor wake

We now focus on the rotor wake. The UNAFLOW experiments included particle image velocimetry (PIV) on a vertical plane in the rotor wake, aligned with the center of the nacelle. Measurements were made at several stages of the surging motion and averaged over several snapshots, with the rotor always being in the same azimuth [4]. We focus on two rotor positions, which the experiments refer to as steps 1 and 5. Both steps correspond to the rotor being in its central position ($x = 0$), with the rotor moving with maximum velocity against the wind in step 1 ($\dot{x} = -U_S$) and maximum velocity with the wind in step 5 ($\dot{x} = U_S$). As the rotor is in the same position and same azimuth for both steps, any change in the wake is caused by unsteady effects of the surging motion.

Simulations are done with $f = 1$ Hz and $A = 35$ mm, which correspond to $f_r = 0.6$, $A_r = 0.015$, and $U_S/U_\infty = 0.055$. This configuration was selected since it contains PIV data for all steps, while also having a high value of U_S. Figure 4.6 shows the UNAFLOW rotor, along with the wake panels and the PIV plane, as a reference for the results discussed in the following paragraphs. When the rotor crosses steps 1 and 5, the bottom blade is rotated 187° away from the PIV plane.

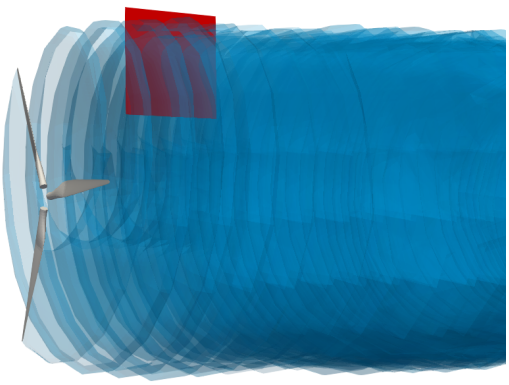

Figure 4.6: UNAFLOW wind turbine (grey), wake panels (blue), and PIV plane (red).

Figures 4.7 and 4.8 show experimental and numerical results on the PIV plane. Both steps 1 and 5 are shown in each figure, in order to better see the difference between them. The precise location of the tip vortices in the simulation is highlighted as pink points in both figures, for comparisons. Consistent with expectations, during step 1 the tip vortices are further downstream than in step 5. The horizontal distance between the vortices in steps 1 and 5 is very well captured by the simulation, being about 6 cm in both simulations and experiments. The vortices

radial and streamwise positions are noticeably different between simulations and experiments, likely in large part due to the blades tip geometry not being identical to the experimental blades, as they are not described in details in the documentation. The blades in the simulations are slightly longer and have a larger chord on the tip. It should be noted that the PIV data indicate the wake is shrinking in radius, which should not be the case and is likely an effect of experimental uncertainty. The expanding wake in the simulations is more realistic.

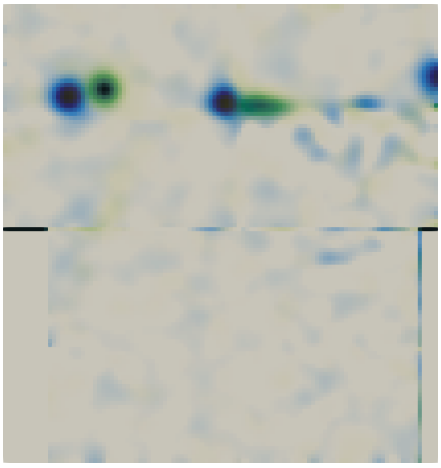

Figure 4.7: Experimental tip vortex position on steps 1 (green) and 5 (blue). Vorticity perpendicular to the plane shown from 0 to 300 1/s.

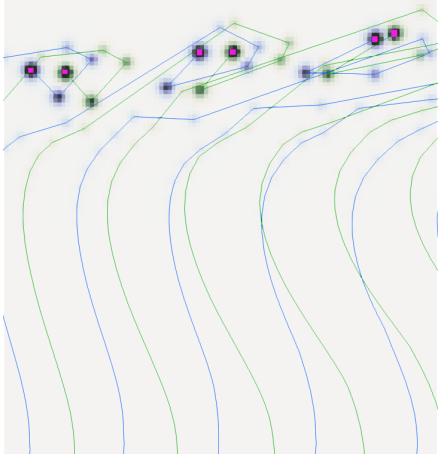

Figure 4.8: Numerical wake on steps 1 (green) and 5 (blue). Vorticity perpendicular to the plane shown from 0 to 300 1/s. Lines represent a cut through the wake panels. Pink dots highlight the tip vortices.

CFD simulations conducted for the UNAFLOW turbine [5] were able to capture the horizontal displacement of the first tip vortex in Figures 4.7 and 4.8 to some extent. However, the second tip vortex displacement was inverted, that is, the vortex from step 1 was upstream of the position in step 5. To our knowledge, no other studies have been made where the wake of a surging wind turbine was simulated numerically and the results were validated with experiments. Hence, we believe this is the first time that a surging wind turbine simulation shows results that agree well with experimental data in terms of wake dynamics.

It is worth noting that the wind turbine wake is folding upon itself on the right side of Figure 4.8. This is a common consequence of using an inviscid free wake method, as complex wakes tend to become tangled as they develop, which can be partially observed on the right side of Figure 4.2. Using a vortex core model [22] can stabilize the wake for a longer time if the vortex core radius is large enough, but has small effects on the location of the tip vortices in the plane investigated here. The simulations shown here employed the aforementioned vortex core model and achieved better wake stability with it. Without a vortex core model, the wakes became entangled at earlier locations.

4.2.3. Beyond the UNAFLOW Results

In this Section, we seek to expand our simulations beyond the limitations of the UNAFLOW experiments. Due to the relatively small reduced frequencies involved in wind turbine surge motion [23] and the assumptions of inviscid flow in the simulations, we do not expect superlinear increases in ΔC_T. Based on Theodorsen [24] results on airfoil sections, we expect first to see nonlinear behavior in the phase, and then a sublinear change in ΔC_T. For more details, see [18].

Results for simulations beyond the experimental data are shown in Figures 4.9 and 4.10. The orange circles represent the data shown in Section 4.2.1, with $A = 0.015$ mm and f varying between 0.5 and 2 Hz. The green circles show an extension of the orange data, with the same A, but with f varying from 2 to 8 Hz. The grey dashed line in Figure 4.9 is a linear extension of the orange circles. The grey region in Figure 4.10 represents the quasi-steady regime, which we set around $-90° \pm 3°$, as this contains most of the experimental data.

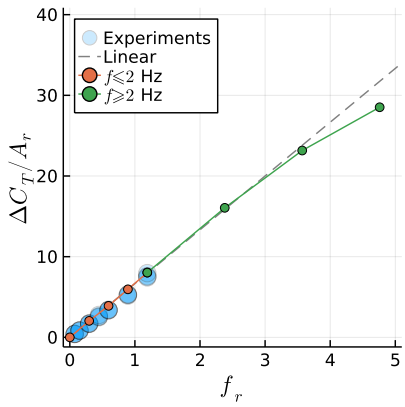

Figure 4.9: Maximum surge velocity effect on the amplitude of the fluctuation of the thrust coefficient.

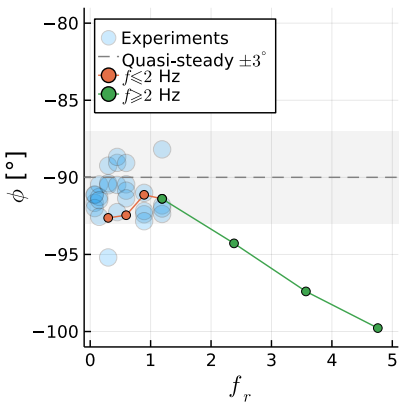

Figure 4.10: Maximum surge velocity effect on the phase between the rotor position and its thrust.

We can now find where $\Delta C_T / A_r$ breaks from a linear trend and when ϕ leaves the quasi-steady regime. At $f_r = 3.6$, we observe a noticeable deviation from the linear relation between $\Delta C_T / A_r$ and f_r. Increasing f_r leads to a reduction in ΔC_T, instead of the increase seen in 2D. In contrast ϕ moves away from the quasi-steady regime at an earlier point, near $f_r = 2$.

Normalizing ΔC_T with the surge amplitude and plotting results against the frequency is sufficient to collapse the experimental data here, as demonstrated in previous studies. For a discussion on how to normalize surging rotor data, see [21]. However, the normalization used herein for f_r might not be sufficient to collapse nonlinear data with different flow conditions. If the nonlinear effects occur due to Theodorsen effects as is the case here, the rotor RPM should likely be taken into account, as it is an important factor for the value of k along the blades.

4.3. Swaying and Yawing Wind Turbine Simulations

We now move on to simulations of the two other degrees of freedom of interest for FOWT in this work: sway and yaw. We continue to use the UNAFLOW turbine, in spite of no experimental data being available for the cases investigated in this Section. Although not shown, some of the simulations in Section 4.2 used symmetry conditions, with only a single blade of the rotor being simulated. This is no longer possible, as the introduction of lateral wind makes the loads on the blades asymmetric. Hence, all simulations in this Section include all three blades.

4.3.1. Fixed Turbine with Side Wind

In order to identify the dynamic effects of sway and yaw, we first need to understand the static effects of side wind. Hence, we simulate a fixed UNAFLOW rotor with side wind. This is usualy referred to as a yaw case, but to avoid confusion between static and dynamic yaw cases, we refer to the static yaw cases as side wind throughout this chapter and use the word yaw to refer to dynamic rotation around the tower axis.

We perform side wind simulations by rotating the wind vector around the vertical axis by a side slip angle β varying between 0 and $40°$, see Figure 4.11. Even though this is a static simulation, results can not converge to a steady state, as the blades experience different wind vectors during a rotation, making cases with side slip intrinsically unsteady. However, as there are three blades, the dynamic loads on the blades mostly cancel each other out, leading to negligible fluctuations of rotor thrust. This occurred in our simulations for side wind, sway and yaw. Hence, instead of investigating C_T on the entire rotor, we instead look at it on a single blade, or C_{Tb}. This value becomes periodic as the simulation progresses and its fluctuation amplitude ΔC_{Tb} will be investigated in this and the following Sections.

Figure 4.12 shows the effect of β on ΔC_{Tb}. We see a linear trend, with the thrust fluctuations increasing as β increases up to about $10°$. After that, the results are nonlinear and, as in surge, fall below the linear trend. For the high values of β we investigate here, flow separations would likely occur in real turbines, increasing C_{Tb}. We highlight that for side wind, C_{Tb} varies periodically as a sine wave, with the frequency of the rotor rotation. This serves as a baseline for the results that follow.

4.3.2. Swaying Turbine

We impose a swaying motion on the turbine using the same conventions of Section 4.2. We set $A_r = 0.05$ and conduct simulations at f between 1 and 5 Hz. Again we use ΔC_{Tb} to measure the sensitivity of the blades to the unsteady loads. In this and the next Sections, we start the rotor motion with one blade pointing straight up, and refer to this as "blade 1". The other blades are numbered in clockwise direction, looking downwind. The choice of the blade can affect the results, as will be shown.

The sway motion introduces a side velocity, which at its maximum value (when the rotor is at the center of the motion) $V_S = 2\pi f A$, introduces a maximum side

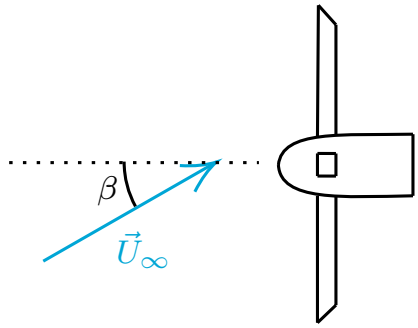

Figure 4.11: Top view of turbine with definition of side slip angle β. Dotted line represents the rotor axis.

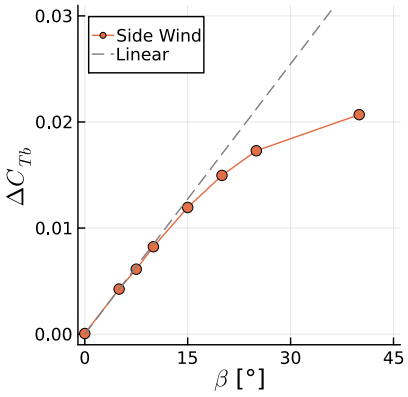

Figure 4.12: Axial force fluctuation amplitude of single blade during rotation for different side wind angles.

wind angle $\beta_{max} = \tan^{-1}(V_S/U_\infty)$, see Figure 4.13. We can use β_{max} to compare the sway results to the static results of the previous Section. Note that the sway velocity adds to U_∞, meaning C_{Tb} must be scaled with a higher incoming velocity, or multiplied by $cos(\beta_{max})^2$ for a fair comparison with the side wind case, which we do.

Figure 4.14 shows the time history of C_{Tb} for blade 1 at different values of f. The signals repeat periodically and we show one period for clarity. The mean values of C_{Tb} reduce with frequency due to the scaling explained in the previous paragraph. The forces on the blades actually increase with f. We see that, unlike the surge and side wind results, more than one frequency is involved in the response to sway motion. Figure 4.15 shows the amplitude of each sway frequency, as a function of the maximum β experienced during sway, along with the side wind results of the previous Section. The effects become nonlinear for values of β_{max} similar as seen in the side wind results. A substantial discontinuity appears for $\beta_{max} = 40°$, where f is equal to the rotation frequency, making the response in Figure 4.14 a simple sine wave and reducing ΔC_{Tb}.

By scaling ΔC_{Tb} with $cos(\beta_{max})^2$, we are able to match the linear regions of the sway cases with the side wind results. Note that without this scaling, ΔC_{Tb} grows in a superlinear fashion, instead of the sublinear trend seen in Figure 4.15. Different studies may or may not include such a factor, which would potentially lead to conflicting conclusions.

We now take a closer look at one of the curves of Figure 4.14, to explain their behavior. We take the case at $f = 2$ Hz because it is relatively simple, due to its sway frequency being half of the rotation frequency, but complex enough that it can serve as an example to explain all the other curves. Figure 4.16 shows a zoomed in view of C_{Tb} as a function of time, where the blade azimuth is shown as vertical lines. Figure 4.17 shows the horizontal rotor sway velocity projected onto the blade chord

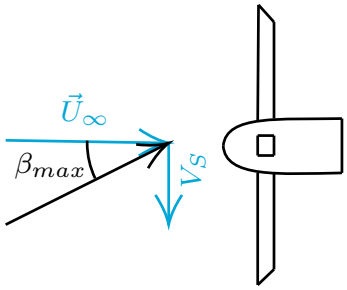

Figure 4.13: Top view of turbine with definition of maximum side wind angle β_{max}.

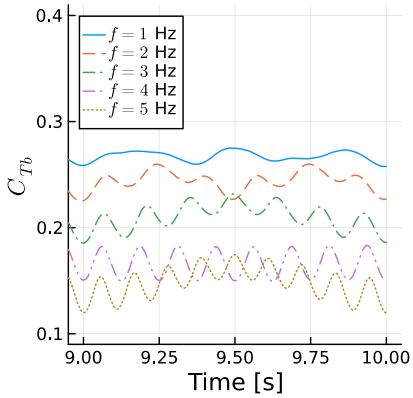

Figure 4.14: Time history of single blade thrust coefficient for various sway frequencies. Thrust normalized with maximum rotor velocity magnitude.

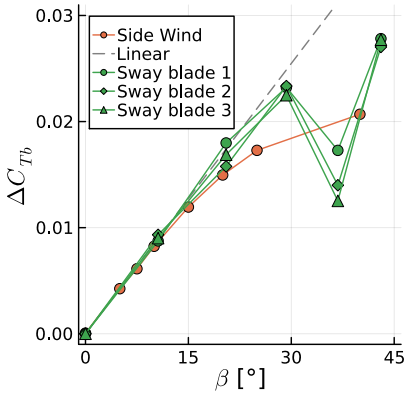

Figure 4.15: Amplitude of single blade thrust coefficient fluctuation for various side wind angles and various maximum side wind angles achieved during sway motion. Thrust normalized with maximum rotor velocity magnitude.

$V_{S,c}$ in the same intervals and with the same vertical lines. The color conventions for the azimuth ψ are shown in Figure 4.18.

The horizontal rotor sway velocity varies with the cosine of the sway frequency f, while the projection onto the chord varies with the cosine of the rotational frequency f_Ω. When both functions are at their maxima with opposite signs, the maximum blade thrust is achieved, as seen at 9.75 s. When they are at their maxima with the same sign, the blade thrust is minimized, as seen at 9.5 s. The equation for the horizontal sway velocity projected onto the blade chord is:

$$V_{S,c} = -2\pi f A \cos(2\pi f t) \cos(2\pi f_\Omega t) \tag{4.2}$$

We can see that the thrust fluctuations in Figure 4.16 are nearly directly proportional to $V_{S,c}$, as seen in Figure 4.17, other than some differences that we will

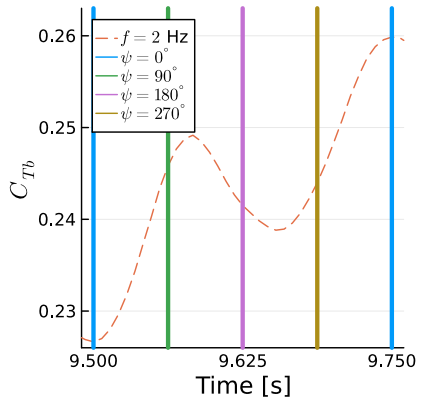

Figure 4.16: Time history of blade 1 thrust coefficient for a sway case. Vertical lines show blade azimuth.

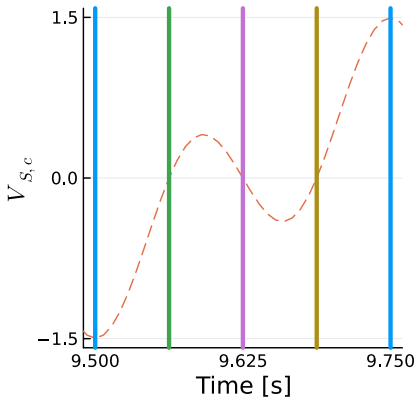

Figure 4.17: Time history of horizontal sway velocity projected on airfoil chord at the tip of blade 1. Vertical lines show blade azimuth.

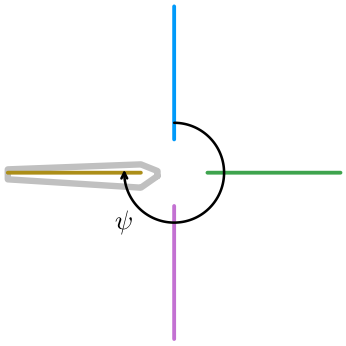

Figure 4.18: Azimuth convention used. Blade shown at $\psi = 270^\circ$.

address in Section 4.3.4. All the other curves in Figure 4.14 can be interpreted in similar ways. They are all at $\psi = 0^\circ$ at multiples of 0.25 s.

The general behavior for sway motion is as follows: when the blade is pointing to either side, the sway velocity projection onto the blade chord is zero, sway effects are minimal, and the thrust is near its mean value. When the blade is pointing up or down, the potential for sway effects is maximum and the thrust can reach its maximum or minimum, if this coincides with maximum sway velocity. Hence, the relationship between the rotation and sway frequencies, along with the phase between the trigonometric functions that represent those motions will dictate the behavior of the blade thrust.

4.3.3. Yawing Turbine

We impose a yawing motion on the turbine by rotating it around the vertical central axis using the same conventions of Section 4.2. This results in a dynamic angle between the freestream velocity and the rotor axis, as in Figure 4.11. The yaw amplitude is the maximum value of this angle, which we set to $A = 3°$. Once again, the simulations are conducted f varying between 1 and 5 Hz. The yawing motion introduces a velocity on the rotor relative to the rotation axis, which reaches its maximum at the tip radius R:

$$U_Y = 2\pi f A R \tag{4.3}$$

where A must be in radians. As U_Y can act with or against U_∞, we do not adjust the flow velocity in the calculation of C_{Tb}.

Figure 4.19 shows the time history of C_{Tb} for different values of f. Results are remarkably similar to Figure 4.14, with multiple frequencies involved and the pure sine response for $f = 4$ Hz. Figure 4.20 shows ΔC_{Tb} as a function of U_Y/U_∞ for the yaw cases. Results seem to indicate a linear trend throughout all cases, with some effects of blade choice and again a large decrease in thrust fluctuation when the yaw and rotation frequencies match, at $U_Y/U_\infty = 0.4$, as in sway. Surge cases are also included for reference, as a function of U_S. This is the main reason for using U_Y in Figure 4.20, as it allows us to compare surge and yaw in the same graph. If we used the reduced frequency, this would not account for the different motion amplitudes used in either case.

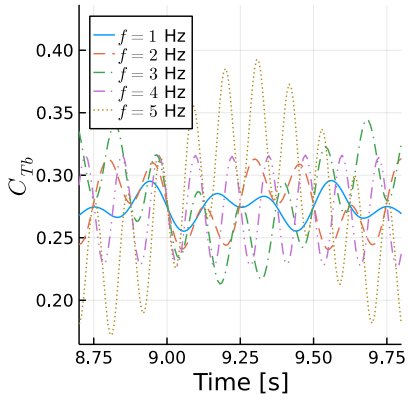

Figure 4.19: Time history of single blade thrust coefficient for various yaw frequencies.

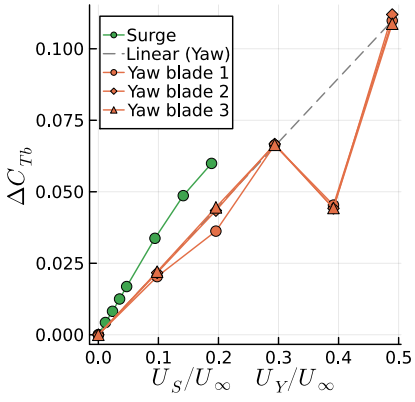

Figure 4.20: Amplitude of single blade thrust coefficient fluctuation for various maximum surge velocities and maximum tip yaw velocities.

Note that U_Y is not acting on the entire rotor plane. It acts mostly near the blade tips when they are horizontal. Hence we see that in spite of the more complex nonlinear behavior of the yaw motion, for comparable U_S and U_Y, the surging motion

is more critical for blade loading. Taking into account phase cancellation effects of the three blades for yawing motion, the rotor forces (but not necessarily the rotor moments) acting on the tower will be less critical in yaw versus a comparable surge motion as well. Also noteworthy is that yaw seems to remain linear even at $U_Y/U_\infty = 0.5$, whereas the surge becomes nonlinear around $U_S/U_\infty = 0.15$.

Similar to the previous Section, we now focus on a single yaw case, namely $f = 3$ Hz, and zoom into the time history of C_{Tb}. This is shown in Figure 4.21. The same conventions of Figure 4.18 are used. Figure 4.22 shows the streamwise component of the blade tip yaw velocity $U_{Y,R}$. The forces fluctuations are nearly proportional to $-U_{Y,R}$, as they are modulated by the yaw frequency f and rotational frequency f_Ω. Again, as in sway, the thrust fluctuation is nearly perfectly proportional to the velocity induced by the motion, although inversely proportional in this case. The blade tip velocity introduced by yaw as a function of time t is:

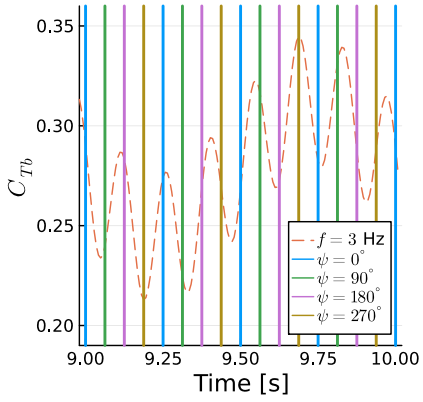

Figure 4.21: Time history of blade 1 thrust coefficient for a yaw case. Vertical lines show blade azimuth.

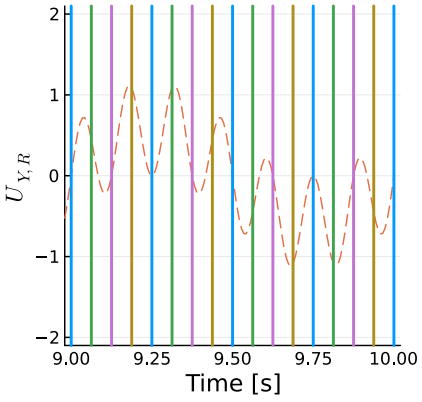

Figure 4.22: Time history blade 1 streamwise blade tip yaw velocity. Vertical lines show blade azimuth.

$$U_{Y,R} = 2\pi f A \cos(2\pi f t) R \sin(2\pi f_\Omega t) \tag{4.4}$$

where the cosine corresponds to the velocity change due to yaw and the sine is due to the blade tip distance to the yaw axis changing with the blade azimuth. A negative $U_{Y,R}$ is in the opposite direction as the freestream velocity, adding thrust.

The general behavior for yaw is as follows: when the blade is pointing up or down, the velocity introduced by the yaw force is zero and the thrust is near its mean value. This can be seen for all cases of $\psi = 0^\circ$ and $\psi = 180^\circ$. When the blade is at $\psi = 90^\circ$ or $\psi = 270^\circ$, there is a potential for high yaw effects, if this coincides with high yaw velocities. This can be seen near 9.2 and 9.3 s. In other words, the amplitude of the thrust fluctuations is linked to the phase between the trigonometric functions describing the blade rotation and the yaw motion.

4.3.4. Effect of Blade Azimuth

The results shown so far for sway and yaw are all for single blades, which had specific initial position, with blade 1 pointing up. The sway and yaw motions were all done with the rotor in neutral position at time equal to zero. The rotation frequency was 4 Hz and the sway and yaw frequencies were 1, 2, 3, 4, and 5 Hz. Hence, the rotor motion and blade position were locked in phase and this is not representative of all the possible loads blades can experience with different starting positions or with non-integer frequency ratios.

We can analyse Equations 4.2 and 4.4 to verify the amplitude of ΔC_{Tb} for arbitrary combinations of frequencies and phase. We can see that $V_{S,c}$ is a function of the product of two cosines and $U_{Y,R}$ a product of a sine and a cosine. Let us refer to these products as the phase-frequency amplitude, as they are linked to the phase of the trigonometric functions and the ratio of their frequencies. In both cases, the trigonometric products can vary in amplitude between 0.5 and 1, where 1 corresponds to the amplitude varying between -1 and 1. Hence, we can use the previous results, calculate the phase-frequency amplitude for each case, normalize the results by the phase-frequency amplitude, and then multiply them by 0.5 and 1. This will allow us to see the range of possible results for each sway and yaw amplitudes, for arbitrary combinations of frequencies and phase.

Figures 4.23 and 4.24 show the numerical results achieved for each blade in the previous simulations, along with the theoretical range of the results for arbitrary combinations of frequency ratios, and starting blade position. The dashed lines represent the possible range of results based on each blade result with corresponding colors. For the yaw motion, in Figure 4.24, we see that the range calculated based on each of the blades is always nearly identical. Hence, the thrust amplitude is behaving according to Equation 4.4. The same can be said for most of the sway motion in Figure 4.23, however at $\beta_{max} = 37°$, i.e. when the sway frequency is identical to the rotation frequency, all three curves are supposed to be at the bottom range of the prediction of Equation 4.2, but in reality they are at different levels. Hence, there is a mismatch between the three ranges, showing that the sway results are not simply following Equation 4.2, which is hinted at by the fact that the trends are nonlinear.

The thrust fluctuations start by scaling linearly with the surge, sway, and yaw motions, as these motions act on the blade sections, increasing and decreasing the relative flow velocity. The surge and yaw motions act on the axial velocity of a given blade section, while the sway motion changes the tangential velocity on the blade sections. As the tangential velocity is typically much higher than the axial velocity in wind turbines, the sway motion effects are small, compared to the surge and yaw. However, the sway motion moves the rotor out of the slipstream, leading to changes in axial velocity that are not due to simple changes in the kinematic velocities. This effect is quantified in the next Section.

4.4. Wake Motion Sensitivity Study

Methods such as BEM are unable to capture the detailed wake motion of wind turbines shown in Figure 4.7, while the numerical dissipation of CFD also introduces

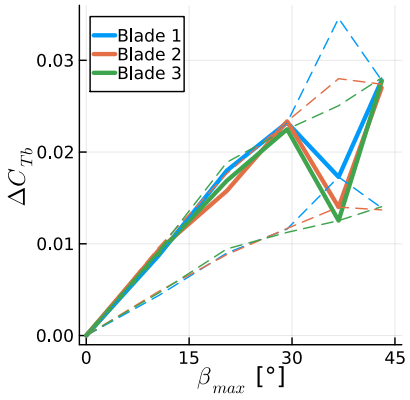

Figure 4.23: Amplitude of blade thrust coefficient fluctuation for various maximum side wind angles achieved during sway motion. Simulations results shown, along with the theoretical possible range of results in dashed lines. Thrust normalized with maximum rotor velocity magnitude.

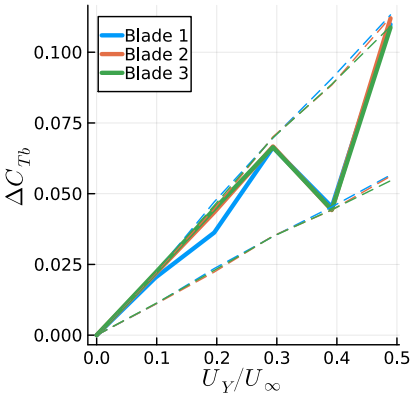

Figure 4.24: Amplitude of blade thrust coefficient fluctuation for various maximum tip yaw velocities. Simulations results shown, along with the theoretical possible range of results in dashed lines.

challenges for preserving tip vortices. However, such methods are able to achieve accurate results for rotor motion [21]. Hence, we seek to quantify the impact of the wake induction on the blades for moving rotors. We achieve this by comparing the simulations in the previous sections with cases where the rotor is not surging, swaying, or yawing, but the effects of these motions are still present. Throughout this section we refer to these simulations as having pseudo motion.

To do this, we take advantage of the properties of panel methods and model the rotor motion indirectly. The rotation of the rotor is still performed explicitly, but the surge, sway, and yaw motion are included not by displacing the turbine, but by modifying the equation for the sources σ and the unsteady Bernoulli equation, which computes the pressure p. In both equations, the panel kinematic velocity $\vec{U}_k$ is used. Hence, for the simulations with real motion in the previous sections, the rotors were displaced and their displacement was then included in σ and p as $\vec{U}_k$. For the pseudo motion simulations, we add the surge, sway, and yaw velocities to $\vec{U}_k$ for computing σ and p, while not surging, swaying, and yawing the rotor.

The pseudo motion method means that the wake panels are always released from the trailing edges in the fixed rotor position. The wakes are not identical to the wakes of a fixed rotating turbine, as changes in the circulation on the blades will affect how the wake is convected. However, the wakes are substantially different from the cases with real motion, while still being more realistic than a frozen or prescribed wake method. With this, we seek to quantify the effect of real motion and the associated realistic wake, compared to pseudo motion and the more simple wake that comes with it.

We select various frequencies from the previous Sections and simulate them in

pseudo motion. The results are summarized in Figures 4.25 and 4.26. The mean thrust on the blades is predicted very well with pseudo motion, staying within 5% of the real motion results. The thrust fluctuation, however, varies substantially, in particular for sway cases. The sway case behaves differently from the others because as the rotor moves to the side, the undisturbed flow is allowed to energize the wake, moving it further away from the rotor in the axial direction. Concurrently, the rotor moving to the side means it is moving away from the wake induction in the lateral direction, or moving outside of the stream tube and into the freestream flow. Thus a rotor in sway achieves lower axial induction and higher thrust, which is a counter intuitive combination. The variation in ΔC_{Tb} for sway in pseudo and real motion can also be explained by this interaction of the freestream flow and the wake. If we consider that on one side of the rotor the wake is stretched by the aforementioned interaction and on the other side the wake is compressed by the opposite effect, ΔC_{Tb} can be dampened or augmented by the real sway motion, depending on how the blade position is aligned with the lateral motion.

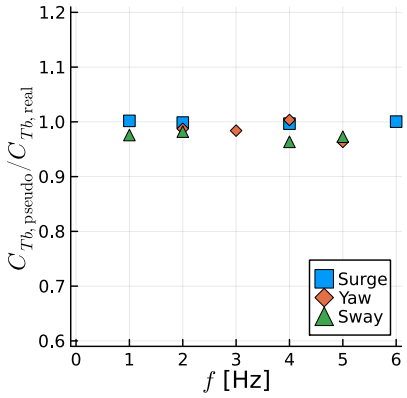

Figure 4.25: Ratio between mean blade thrust for pseudo motion and real motion simulations for various frequencies and motion types.

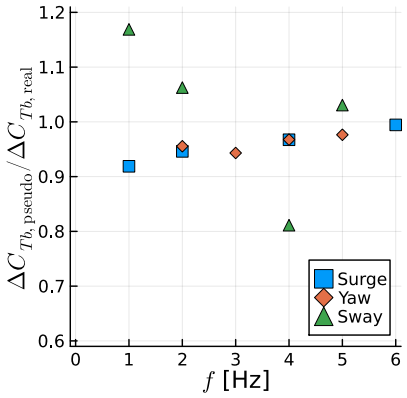

Figure 4.26: Ratio between amplitude of fluctuating blade thrust for pseudo motion and real motion simulations for various frequencies and motion types.

Figures 4.27, 4.28, and 4.29 show the wakes for real and pseudo surge, sway, and yaw, respectively. The surge case uses axial symmetry, hence only one blade is shown. The differences between real and pseudo motion in surge are subtle, while the yaw motion is more obvious, as the wake becomes more irregular in real motion, due to the lack of symmetry. The sway case is quite extreme, with the pseudo motion showing a very well behaved wake, almost identical to the other cases, while real motion makes the wake become chaotic very quickly.

The amplitudes and frequencies used in this chapter for surge are mostly related to the UNAFLOW experiment. For sway and yaw, we decided to use the same frequencies as in surge, adapting the amplitude to obtain values of ΔC_{Tb} in the same order of magnitude as the surge cases. While this is an arbitrary decision, we

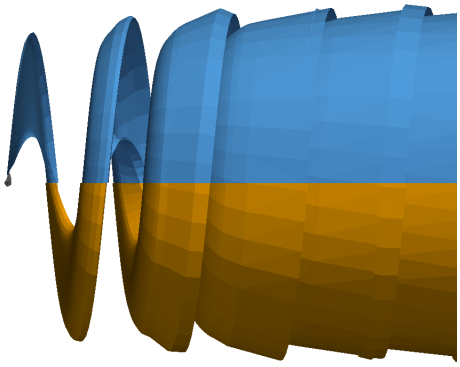

Figure 4.27: Wake for real (top, blue) and pseudo (bottom, orange) surge motion at $f = 1$ Hz. Only one blade shown.

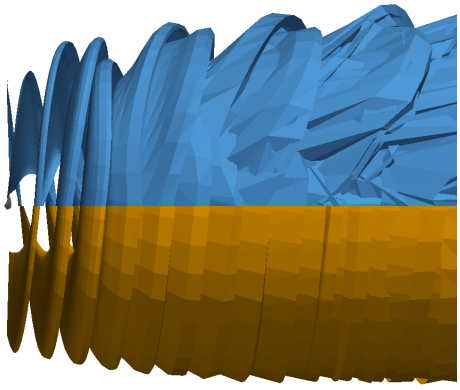

Figure 4.28: Wake for real (top, blue) and pseudo (bottom, orange) sway motion at $f = 4$ Hz.

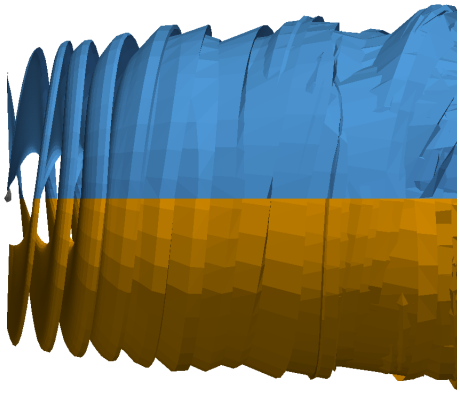

Figure 4.29: Wake for real (top, blue) and pseudo (bottom, orange) yaw motion at $f = 3$ Hz.

believe the results herein can be generalized. For surge, as long as the amplitude and frequencies do not lead to the wakes impinging on the blades, we have no reasons to believe the effect of wake motion will be severe. For sway, the amplitude chosen for this section is compatible with the turbine oscillating from side to side by less than $4°$, which seems realistic for a FOWT. This is sufficient for the thrust fluctuations to be severely affected by wake motion, leading to the conclusion that sway motion is heavily affected by wake motion effects. Finally, for dynamic yaw motion, with very high yaw amplitudes, a similar effect of wake motion as seen on sway could be encountered. However, we believe FOWT platforms do not tend to yaw dynamically at high amplitudes. Hence, we expect the wake motion effects for yaw to be small, in general.

4.5. Conclusions

We have shown that a free wake panel method can accurately capture mean and unsteady thrust of a surging wind turbine. The methodology used in this chapter slightly underpredicts the mean thrust and overpredicts the amplitude of thrust fluctuations, however results are comparable and in line with the state-of-the-art [21].

The effects of the rotor motion on the tip vortices was also shown to be accurately captured by the method in what we believe is the first simulation of surging wind turbine wakes that accurately reproduce experimental data. Wake vortices are particularly difficult to capture with CFD methods, as the Eulerian approach tends to dissipate them [5]. Lagrangian methods have a significant advantage in preserving the wake vortices near the body, with the disadvantage of wake entanglement far from the rotor, which in turn requires some dissipation for stabilization.

We found that the surge frequency had to be tripled from its maximum value in the experimental campaign to reach a nonlinear response in thrust. The current method allowed us to investigate this by isolating Theodorsen effects. This means that, in reality, the nonlinear response could happen earlier due to other phenomena, such as dynamic stall.

We then studied side wind, sway motion, and yaw motion of a rotor. We demonstrated the complexity of the forces acting on the blades during sway and yaw motions, even without flow separations. By comparing side wind results with sway results using the maximum sway angle and including the sway velocity in the thrust coefficient, we were able to show linear behavior for sway at low frequencies that matched the side wind trends. For the yaw motion, the blade tip surge effect was demonstrated by investigating the axial force on a single blade during a yaw cycle. For both sway and yaw, the blade forces fluctuations can vary by a factor of 2, depending on the ratio between the rotor motion and rotation, and the blade initial position.

Finally, we used an interesting feature of the current methodology to perform what we refer to as pseudo motion simulations, where we accounted for the surge, sway, and yaw motion on the rotor, without actually performing these motions on the turbine. With this we showed the sensitivity of wake deformation on the forces on the blades. It was found that the sway motion allows undisturbed air to enter

the wake, increasing the mean thrust and, in our case, reducing the dynamic loads. Surge and yaw were shown to be fairly insensitive to the wake motion, which explains the fact that methods that do not capture wake dynamics can still predict surge motion effects well.

References

[1] A. F. P. Ribeiro, D. Casalino, and C. S. Ferreira, *Nonlinear inviscid aerodynamics of a wind turbine rotor in surge, sway, and yaw motions using a free-wake panel method,* Wind Energy Science **8**, 661 (2023).

[2] A. Fontanella, A. Facchinetti, S. Di Carlo, and M. Belloli, *Wind tunnel investigation of the aerodynamic response of two 15 MW floating wind turbines,* Wind Energy Science **7**, 1711 (2022).

[3] I. Bayati, L. Bernini, A. Zanotti, M. Belloli, and A. Zasso, *Experimental investigation of the unsteady aerodynamics of FOWT through PIV and hot-wire wake measurements,* Journal of Physics: Conference Series **1037**, 052024 (2018).

[4] I. Bayati, M. Belloli, L. Bernini, D. Boldrin, K. Boorsma, M. Caboni, M. Cormier, R. Mikkelsen, T. Lutz, and A. Zasso, *UNAFLOW project: UNsteady aerodynamics of FLOating wind turbines,* Journal of Physics: Conference Series **1037**, 072037 (2018).

[5] I. Bayati, M. Belloli, L. Bernini, D. Boldrin, K. Boorsma, M. Caboni, M. Cormier, R. Mikkelsen, T. Lutz, and A. Zasso, *UNAFLOW project: UNsteady aerodynamics of FLOating wind turbines,* Journal of Physics: Conference Series **1037**, 072037 (2018).

[6] K. Boorsma and M. Caboni, *Numerical analysis and validation of unsteady aerodynamics for floating offshore wind turbines*, Tech. Rep. R11345 (TNO, 2020).

[7] M. Cormier, M. Caboni, T. Lutz, K. Boorsma, and E. Krämer, *Numerical analysis of unsteady aerodynamics of floating offshore wind turbines,* Journal of Physics: Conference Series **1037**, 072048 (2018).

[8] N. Ramos-García, S. Kontos, A. Pegalajar-Jurado, S. González Horcas, and H. Bredmose, *Investigation of the floating IEA wind 15 MW RWT using vortex methods part I: Flow regimes and wake recovery,* Wind Energy **25**, 468 (2022).

[9] N. Ramos-García, S. González Horcas, A. Pegalajar-Jurado, S. Kontos, and H. Bredmose, *Investigation of the floating iea wind 15-mw rwt using vortex methods part ii: Wake impact on downstream turbines under turbulent inflow,* Wind Energy **25**, 1434 (2022).

[10] S. Mancini, K. Boorsma, G. Schepers, and F. Savenije, *A comparison of dynamic inflow models for the blade element momentum method,* Wind Energy Science **8**, 193 (2023).

[11] S. Mancini, K. Boorsma, M. Caboni, K. Hermans, and F. Savenije, *An engineering modification to the blade element momentum method for floating wind turbines,* Journal of Physics Conference Series **2265**, 042017 (2022).

[12] J. G. Leishman, *Challenges in modelling the unsteady aerodynamics of wind turbines,* Wind Energy **5**, 85 (2002).

[13] L. Yang, C. Xie, and C. Yang, *Geometrically exact vortex lattice and panel methods in static aeroelasticity of very flexible wing,* Proceedings of the Institution of Mechanical Engineers, Part G: Journal of Aerospace Engineering **234**, 742 (2020).

[14] M. Gennaretti, G. Bernardini, J. Serafini, and G. Romani, *Rotorcraft comprehensive code assessment for blade-vortex interaction conditions,* Aerospace Science and Technology **80**, 232 (2018).

[15] M. Sessarego, N. Ramos-García, and W. Shen, *Development of a fast fluid-structure coupling technique for wind turbine computations,* Journal of Power and Energy Engineering **3**, 1 (2015).

[16] L. Wang, X. Liu, and A. Kolios, *State of the art in the aeroelasticity of wind turbine blades: Aeroelastic modelling,* Renewable and Sustainable Energy Reviews **64**, 195 (2016).

[17] M. Gennaretti and G. Bernardini, *Novel boundary integral formulation for blade-vortex interaction aerodynamics of helicopter rotors,* AIAA Journal **45**, 1169 (2007).

[18] A. F. P. Ribeiro, D. Casalino, and C. S. Ferreira, *Surging wind turbine simulations with a free wake panel method,* Journal of Physics: Conference Series **2265**, 042027 (2022).

[19] A. Fontanella, I. Bayati, R. Mikkelsen, M. Belloli, and A. Zasso, *UNAFLOW: UNsteady Aerodynamics of FLOating Wind turbines,* (2021).

[20] I. Bayati, M. Belloli, L. Bernini, R. Mikkelsen, and A. Zasso, *On the aero-elastic design of the DTU 10MW wind turbine blade for the LIFES50+ wind tunnel scale model,* Journal of Physics: Conference Series **753**, 022028 (2016).

[21] S. Mancini, K. Boorsma, M. Caboni, M. Cormier, T. Lutz, P. Schito, and A. Zasso, *Characterization of the unsteady aerodynamic response of a floating offshore wind turbine to surge motion,* Wind Energy Science **5**, 1713 (2020).

[22] M. Ramasamy and J. G. Leishman, *A Reynolds number-based blade tip vortex model,* Journal of the American Helicopter Society **52**, 214 (2007).

[23] T. T. Tran and D.-H. Kim, *A CFD study into the influence of unsteady aerodynamic interference on wind turbine surge motion,* Renewable Energy **90**, 204 (2016).

[24] T. Theodorsen, *General Theory of Aerodynamic Instability and the Mechanism of Flutter*, Tech. Rep. 496 (NACA, 1934).

5

Highly Flexible Wing in Flutter and Gusts

When nothing seems to help, I go and look at a stonecutter hammering away at his rock, perhaps a hundred times without as much as a crack showing in it. Yet at the hundred and first blow it will split in two, and I know it was not that last blow that did it, but all that had gone before.

Jacob Riis

This chapter presents fluid structure interaction simulations of a highly flexible wing at various flow conditions, including flutter regime and under sinusoidal gusts. Static and aeroelastic wing deflections are compared to experimental data, with good accuracy. Two regions of flutter onset are predicted within the experimental range. An analysis of the flutter modes is performed, showing that the second torsion mode plays a role in flutter, something that had not been published before. Limit cycle oscillations are achieved and are shown to compare well with reference data. Finally, gust simulations are compared to experiments and corrections for the wind tunnel measurements are proposed, which should facilitate future validation efforts. This chapter serves as a contribution to the Pazy wing dataset and is a step towards mid-fidelity simulations for more complex configurations, including fuselage effects and tail interactions.

Parts of this chapter have been published in Journal of Fluids and Structures **121**, 103955 (2023) [1].

5.1. Introduction

Aircraft wings have become more flexible in recent years, mostly due to high aspect ratio wings having favorable aerodynamic properties (such as lower induced drag) and lightweight structures helping improve fuel efficiency, but also because the flexibility of the wings can also have advantages for the dynamic response of the aircraft [2]. These factors have led to the very flexible wings that are present in modern commercial aircraft such as the Boeing 787 and in high-altitude long-endurance drones. As wing deflections increase, the assumptions of linear models are no longer valid and nonlinear methods need to be used. As large deflections and rotations on wings change their aerodynamics and structural characteristics, nonlinear aeroelastic models and analysis methods are on the rise [3]. Models that can accurately include the large deflections into stability calculations of these wings at low computational cost are needed to avoid late stage modifications in the development cycle [4]. In particular, the NASA Helios mishap led to the recommendation to develop more advanced multidisciplinary time domain methods appropriate for highly flexible aircraft [5].

In order to validate such models, the Pazy wing experiment [6] was conducted as part of the Aeroelastic Prediction Workshop (AePW) Large Deflection Working Group [2, 7, 8]. The Pazy wing was created at Technion with the intent to be used for validation of aeroelastic models. It is a rectangular, flexible wing which exhibits two flutter modes. This provides a simple, yet challenging test case, as the wing deformation has substantial effects on its structural and aeroelastic properties, such as its modal characteristics, with "some trends that are opposite to those obtained in the linear domain" [9].

Several groups have simulated the Pazy wing, typically using nonlinear static and linearized dynamic simulations [10], as adding both static and dynamic structural and aerodynamic nonlinearities concurrently is considered demanding [11]. The linearization needs to be done on the deformed configuration, i.e., after statically deforming the wing for certain flow conditions, to deal with the wing static nonlinearities [12]. High-fidelity, Navier-Stokes-based simulations using a detailed 3D structural model have the potential to perform such calculations in a structural and aerodynamic nonlinear framework [13], but the computational cost is still too high for the quick turnaround required during the design phase. The need to deform the volume mesh while supporting large deflections also complicates the use of methods that require off-body meshes.

Flexible wings can also go through large dynamic deformations outside of flutter, in the case of gusts. A modified version of the Pazy wing was constructed at the Delft University of Technology to perform wind tunnel analysis of its interactions with gusts [14]. This serves as an opportunity for validation of aeroelastic tools for the challenging case of sinusoidal gusts interacting with a highly flexible wing. To the authors knowledge, no numerical simulations of this configuration have been published.

Panel methods have shown good balance between accuracy and cost for the simulation of flexible wings [15]. Typically, the vortex lattice method (VLM) or doublet lattice methods (DLM) are employed for aeroelastic simulations of wings

[9, 12, 16]. These methods employ panel (doublet or vortex ring) sheets running through the wing chord line, hence thickness effects are neglected. A major drawback of using panel sheets is the difficulty in describing aircraft fuselages and other bodies that can have an effect on the wing aerodynamics, such as wing mounted pods.

An alternative to VLM and DLM is a full 3D panel method, where the complete surface of the aircraft is modelled. This allows for thickness effects to be captured, for boundary layer models to be included, and for a one-to-one correspondence with CFD results, in terms of surface data, so that corrections can be easily implemented in the panel code based on CFD simulations, which can capture transition effects and separations. Loads on fuselages can also be calculated more accurately, as their surfaces are represented. As VLM and DLM, full 3D panel methods are boundary element methods, and hence, only surface meshes are needed, simplifying the mesh deformation process.

VLM, DLM, and 3D panel methods simulations of wings can take several approaches to wake modeling [17]. The most simple approach is a flat prescribed wake, aligned with the flow or trailing edge. This can be used to simulate steady cases quickly, without iterating on the wake position and its effects on the wing. Alternatively, the wake position can be partially defined, with the vertical locations of the points being changed through an iterative procedure [18]. For unsteady simulations, the wake can be either simply convected with the freestream velocity or the wake velocity can be computed, based on the freestream and the induction of the panels in the simulation [17]. The latter approach is substantially more expensive, from a computational standpoint, but it allows for accurate wake motion and interactions [19].

In this work, we seek to contribute to the Pazy wing studies and the AePW by conducting structurally and aerodynamically nonlinear, time domain simulations. We focus on validating a 3D panel code with free wake coupled with a geometrically exact beam structural model. These results are compared to experimental data and can serve as reference for future code verification. We also seek to contribute to the analysis of the flutter behavior of the Pazy wing, showing for the first time that the second torsion mode contributes to the first flutter mode of the wing. Finally, we conduct the first gust simulations of the Pazy wing and show that the gust properties measured in the experiments are strongly affected by the wing induction, which can help future validations with experimental data.

5.2. Numerical Methods

5.2.1. Aerodynamic Model

The free wake panel code described in the previous chapters is used here, with the added complexity of the flexible wing, which requires a scructural model.

5.2.2. Structural Model

The structural properties of the beam model were computed based on a detailed 3D finite element method (FEM) wing model of the Pazy wing. The University of

Michigan's process to convert 3D FEM models to beam models [20] was used and the beam model was then used by their Nonlinear Aeroelastic Simulation Toolbox (UM/NAST), originally developed by [21]. The beam has 16 equally spaced nodes, which was shown to be sufficient to capture the same modal behavior of the detailed FEM wing model [8]. The elements are Timoshenko beams, requiring 6×6 symmetric stiffness matrices. As done by [12], we assume shear stiffness to be very large, as deflections due to shear are expected to be negligible compared to bending and torsion. UM/NAST provided node-based mass matrices, which are used in this work.

5.2.3. Fluid Structure Interaction

The influence coefficients are recomputed at every timestep, to account for relative motion between the panels. The main nonlinear effects that the current implementation neglects are related to flow separations, as the aerodynamic model is inviscid and hence unable to capture static or dynamic stall.

The current mapping scheme conserves total forces and moments, but does not ensure preservation of virtual work, due to the nearest neighbor interpolation. The error associated with this reduces with grid refinement. We can calculate the virtual work δW_a performed by the aerodynamic forces $\vec{F}$, based on the displacement of the surface panels $\vec{s}$:

$$\delta W_a = \sum_i \vec{F}_i \cdot \vec{s}_i \tag{5.1}$$

where the sum is performed over all surface panels i. We can also calculate the virtual work δW_s performed by the structural forces $\vec{F}$ and torques $\vec{T}$, based on the associated displacements $\vec{s}$ and rotations $\vec{\theta}$:

$$\delta W_s = \sum_j \vec{F}_j \cdot \vec{s}_j + \sum_j \vec{T}_j \cdot \vec{\theta}_j \tag{5.2}$$

where the sum is performed over all beam nodes j. In our simulations, the differences between δW_a and δW_s were typically well under 1% for most cases and around 2% for extreme cases, near the second flutter mode. Hence, we consider the current model appropriate for this work.

5.3. Test Case Description

The Pazy wing [6] is a highly flexible wing constructed at Technion specifically for validation of aeroelastic models. It is a simple cantilevered rectangular wing composed of a NACA0018 airfoil with chord $c = 0.1$ m and span $s = 0.558$ m (which could also be refferred to as the semispan). Tip deflections of approximately half of the span were reached in the experiments. Limit cycle oscillations (LCO) were encountered and measured in the experiments. They are caused by flutter involving the second out of plane bending mode and first torsion mode at relatively low speeds, while higher speeds develop flutter with the first out of plane bending mode and first torsion mode. Both flutter modes occur at high wing deflections, meaning

linearized dynamics methods must be used only after nonlinear static deflections, as at such deformation levels, influence coefficients need to be recomputed. The second flutter mode is difficult to reach experimentally without damaging the wing.

The wing skin, which is made of polyester shrink film, introduces pre-tension, deforming between the ribs. It also buckles at large wing deformations, adding some uncertainty to the aerodynamics of the wing and structural properties of the skin. While many simulations of the Pazy wing are computed using the structural model of the wing with and without the skin, as a way to estimate the experimental uncertainty [12], we focus on the experimental data with skin only. It is worth noting that given a stable and accurate 3D FEM model that could provide a very detailed surface geometry of the wing with the deformed skin, the 3D panel method used in this work could include the aerodynamic effects of the buckling, keeping in mind the limitations of the inviscid approach. Such a model is not available for the Pazy wing at the moment.

We model the Pazy wing using quadrilateral panels, with 150 panels in the chordwise direction with a cosine distribution (refining the leading and trailing edges), and 26 panels in the spanwise direction, with a uniform distribution. The surface mesh is shown in Fig. 5.1, along with the coordinate system definition used in this work. A symmetry plane is placed on the wing root to model the wind tunnel wall, mirroring the wing surface and wake panels. The timestep is set to $\Delta t = 0.25c/U_\infty$. The spanwise panel discretization and the timestep length are verified in Section 5.4.3. Wake panels are deleted once they reach the arbitrary location of $x = 10s$, as this saves computational time and does not affect the results noticeably. Simulations are run for at least 2000 timesteps, or 500 flow passes, where the first 4 timesteps are used to initialize the wake, with a rigid wing. Detecting the presence of flutter could be done early in the simulation, as will be shown in Section 5.4.2.

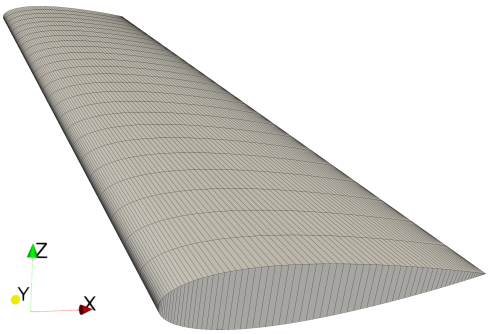

Figure 5.1: Surface mesh of the Pazy wing, seen from the root side.

5.4. Results

5.4.1. Structural Model Validation

We start by verifying and validating the structural model without the aerodynamics. The experimental data set includes static wing deformation, achieved by placing

a weight at the wing tip. Two cases are investigated: with the weight applied near the elastic center, and with a lever arm of 0.13 m, dubbed the bend and the torsion tests, respectively. The wing tip vertical displacement w is shown in Fig. 5.2, corresponding to the bend test. Note that the wing was built slightly bent, leading to a tip displacement of 18.8 mm at the tip even with zero tip mass, which we applied in the structural model. Gravity forces were applied o the corresponding lumped masses. The wing tip twist θ from the torsion test is shown in Fig. 5.3. Reference data for the beam model computed by DLR are shown for the bend test. Throughout this work, the wing displacement and θ are measured in beam node location, which is at 44% of the wing chord. Here, we measure θ by projecting the tip leading and trailing edges on a vertical plane, to approximate how it was done experimentally.

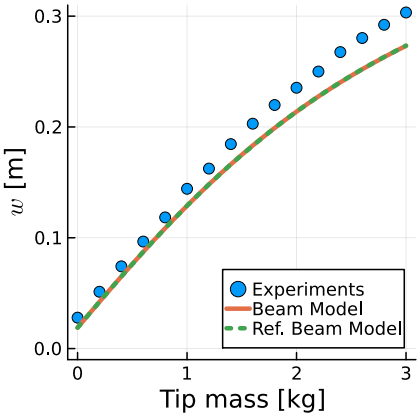

Figure 5.2: Static wing bend test results. Vertical tip displacement versus mass placed at wing tip.

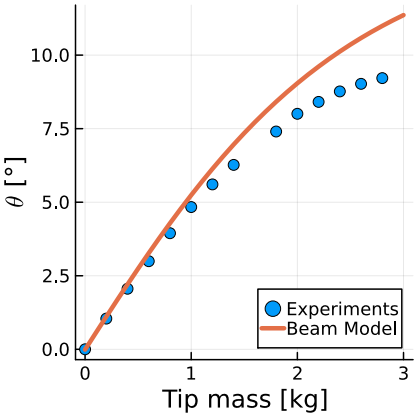

Figure 5.3: Static wing torsion test results. Tip twist angle versus mass placed at wing tip, behind the trailing edge.

Displacements are almost indistinguishable from the reference beam results, with discrepancies up to about 15% with experimental data for high values of tip mass. In the experiments, the skin of the wing buckled and behaved in a nonlinear way for large deflections, something the beam model does not capture. The twist behaves in a similar fashion, but with discrepancies closer to 20% for higher mass, with some uncertainty associated with twist angles for large values of w, as measuring the twist is more difficult to do with large deflections, since the wing cross section is no longer aligned with the horizontal axis. Overall we consider the results verified, as they reproduce the reference beam model, which is the most accurate geometrically nonlinear numerical representation available for the Pazy wing with skin, and agree with data shown in [8], which indicate the beam model is being used correctly. In terms of validation with the experiments, at the moment we are not aware of a more accurate structural representation of the Pazy wing (the FEM with skin fails in nonlinear solutions), hence while the agreement could be

improved, it seems to be at the state-of-the-art.

The natural frequencies of the undeformed model are shown in Table 5.1, where "bending" stands for the out of plane bending mode and "horizontal" stands for the in plane bending mode. The frequencies are compared with UM/NAST results [8], using the same stiffness and inertia matrices for the beam model used in this work. The two codes agree very well, providing confidence in the structural model used in this work. The difference between the current results and UM/NAST is shown in the Δ column, and is typically under 0.1%.

Table 5.1: Natural frequencies (Hz) of the undeformed wing beam model.

Mode	Description	Current Results	UM/NAST	Δ
1	1st bending	4.19	4.19	$< 0.1\%$
2	2nd bending	28.50	28.49	$< 0.1\%$
3	1st torsion	42.02	41.88	0.3%
4	3rd bending	83.11	83.06	$< 0.1\%$
5	1st horizontal	105.23	105.89	0.6%

5.4.2. Aeroelastic Simulations Validation

The Pazy flutter boundaries were measured by recent experiments [7] where two instability regions could be extracted: a smaller onset region and a larger offset region. For example, at static root angle of attack $\alpha = 3°$, if the flow speed was continuously increased, the wing would start vibrating at 49 m/s. Once the vibrations started, a hysteresis effect would mean that decelerating to 40 m/s was required to stop them. The onset region matched numerical predictions [9, 22] very well, which we will discuss in Section 5.4.5. These results correspond to the first flutter region, which is a hump mode that involves the first torsion and second bending modes. Increasing the flow speed made the vibrations disappear. At much higher flow speeds, a second flutter region appears, involving the first torsion and first bending modes. The experimental flutter boundary for the second flutter region is not yet available, hence numerical data is used for reference.

Aeroelastic simulations were conducted for $\alpha = 3$, 5, and $7°$, with U_∞ up to 80 m/s. Figures 5.4 and 5.5 show the time history of the wing tip twist angle θ for four simulations at different U_∞ and $\alpha = 3°$. At $U_\infty = 45$ and 75 m/s, oscillations appear early in the simulations ($tU_\infty/c = 100$), but they are damped and θ ultimately converges to a steady value. For $U_\infty = 50$ m/s, θ diverges as the wing encounters the first flutter mode. The same happens at $U_\infty = 80$ m/s for the second flutter mode. Oscillations for the second flutter mode clearly occur at much lower frequencies and higher amplitudes than the first, as the second flutter mode is linked to the first bending mode. Note that from here on, θ is simply the angle around the spanwise direction, or y axis, as computed by the structural model, hence without a projection to a vertical plane.

Figure 5.6 shows the vertical tip displacement of the wing w as a function of the freestream velocity U_∞ for $\alpha = 3$, 5, and $7°$. The blue diamonds represent the

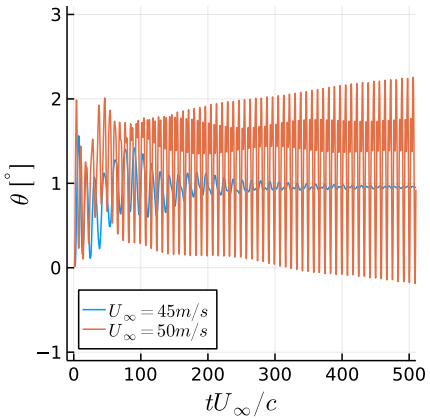

Figure 5.4: Time history of wing tip twist for $\alpha = 3°$ near and at the first flutter mode.

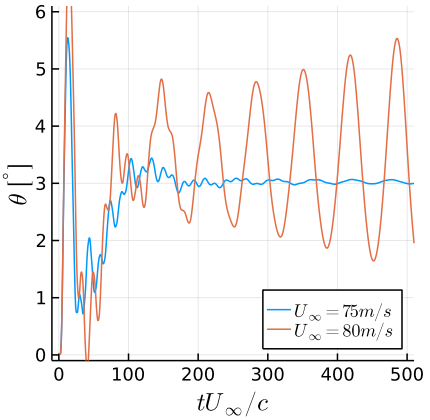

Figure 5.5: Time history of wing tip twist for $\alpha = 3°$ near and at the second flutter mode.

experimental first flutter onset region, i.e., the velocities in which the wing enters flutter. The area shaded in blue represents the experimental first flutter speed range, that is, once the wing starts to flutter, it needs to go outside that range of U_∞ for flutter to stop. The velocities at the edge of this range are the flutter offset velocities. Note that for $\alpha = 7°$ there was no experimental data for reducing U_∞, hence the upper range of the flutter onset and lower range of the flutter offset are unknown. The dashed blue lines represent the experimental static deformation of the wing. The green diamonds show the second flutter onset region found with SHARPy [12] for the Pre-Pazy wing, which is slightly different from the Pazy wing simulated here, but serves as the best current estimate of the second flutter onset. The orange circles represent simulations with the present panel method, while the stars highlight cases for which the simulations led to large vibrations, as shown in Figs. 5.4 and 5.5.

The current results in Fig. 5.6 are in line with the references. A quantitative comparison with the static deformation results is difficult to perform, as there are errors associated to those measurements, especially at low velocities, due to the wing being slightly bent and twisted. Qualitatively, results agree well. The numerical flutter range is within 1 m/s of the experimental flutter onset range for $\alpha = 3$ and $7°$ and within 3 m/s for $\alpha = 5°$. The second flutter onset points match the SHARPy results within 1 m/s. In this Section, the objective was to find the conditions that create flutter, rather than trying to characterize the LCO, which will be done in Section 5.4.5. Hence, the simulations here were run until it was clear that the fluctuations were growing, not until LCO was reached.

Note that in this Section we scale our velocities to better compare to experiments. Based on the dynamic pressure and velocities stated in [6], the fluid density in the experiments can be induced to be 1.19 kg/m^3, while our simulations and the ones by [12] use 1.225 kg/m^3. Hence, we scale all simulation velocities in this

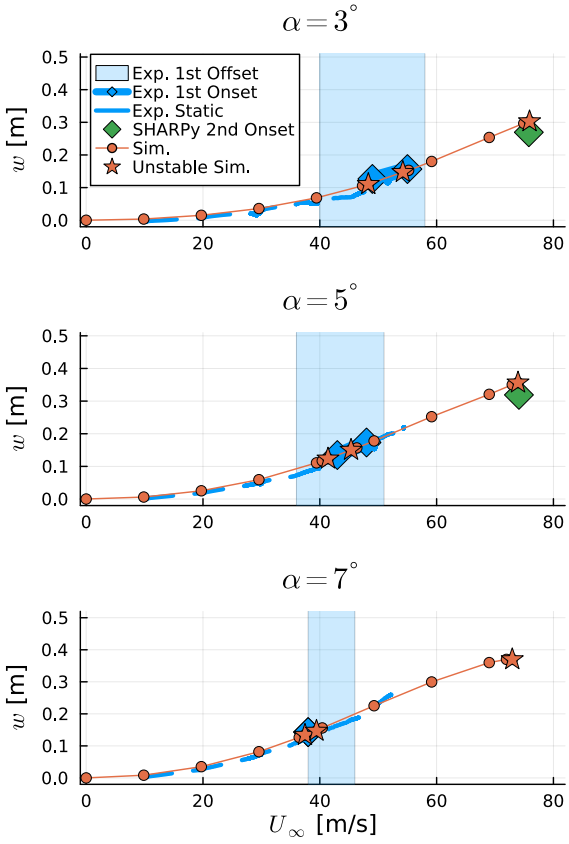

Figure 5.6: Vertical tip displacement range for various flow velocities at three angles of attack.

Section by $\sqrt{1.19/1.225}$, so that the same dynamic pressures can be compared.

5.4.3. Resolution Study

In order to verify that our aerodynamic surface mesh and timestep are adequate for our simulations, we perform resolution studies. The chordwise panel distribution of our aerodynamic surface mesh is consistent with previous studies [23] and will not be examined in this work. However, the spanwise discretization can be an important factor, as it influences interpolation mapping between the aerodynamic and structural models. Hence, we test two surface meshes in this Section: the baseline mesh with 26 spanwise sections, and a fine mesh with 39 spanwise sections. The refinement ratio of 1.5 between the two meshes was chosen because it is large enough to show potential differences, while forcing the spanwise discretization to be different from the baseline case, whereas a refinement ratio of 2 would have kept half of the spanwise panel nodes to be in the same position as in the baseline. The fine mesh simulations took approximately 70% more computational time than

the baseline simulations.

For determining if the timestep is adequate for our simulations, we compare the baseline simulations with timestep $\Delta t = 0.25c/U_\infty$ with two additional simulations with timesteps $2\Delta t$ and $\Delta t/2$. This changes the computational cost by a substantial amount for two reasons: first, halfing the timestep means the number of timesteps in a simulation need to be doubled to achieve the same physical time. Second, halfing the timestep doubles the number of wake panels present during the simulation. The first leads to a simple linear behavior, doubling the simulation time, while the latter doubles the number of some of the calculations, such as the induction from the surface panels on the wake panels, but increases with $O(N^2)$ the number of calculations on the wake interacting with itself. This made the simulations about three times faster for $2\Delta t$ and over three times more expensive for $\Delta t/2$.

We use the simulations at $\alpha = 5°$ and simulate the points before and after the first flutter mode, and before the second flutter mode. This is done to check if the wing tip displacements are consistent for a wide range of flow velocities. Results are shown in Fig. 5.7.

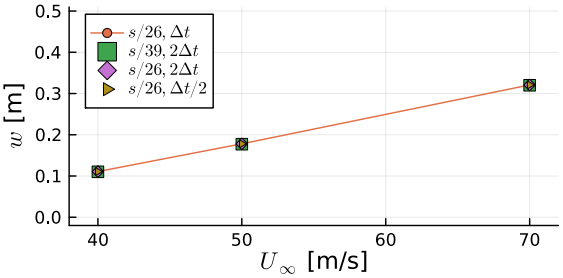

Figure 5.7: Vertical tip displacement for various flow velocities at $\alpha = 5°$. Baseline surface mesh, spanwise refined surface mesh, and simulations where the timestep is doubled and halved.

Fine mesh results are within 0.6% of the baseline results, indicating the discretization is appropriate for the mapping and subsequent coupling between the aerodynamic and structural models. Differences in tip displacement for the cases with doubled and halved timesteps are well within 0.05% of the baseline results, indicating the timestep used in the simulations is adequate. We now turn to the flutter onset itself. We simulate the different cases at intervals of 1 m/s near the first and second flutter modes, to determine the flutter range for each case. Results are shown in Table 5.2. Results are given with the simulation fluid density and hence should be scaled in order to compare to experiments.

Given our step in velocities of 1 m/s, the spanwise resolution does not affect the flutter velocities on its own. The largest timestep modifies the 1st flutter start speed by 1 m/s, but otherwise all results are identical. The reason we use the baseline timestep instead of the largest timestep used here is that the largest timestep was unable to achieve LCO. This will be further discussed in Section 5.4.5.

With the tip deformation results and the flutter speeds showing very little effects from spanwise refinement and timestep changes, we consider the resolution study

Table 5.2: Flutter speeds in m/s at $\alpha = 5°$. Cases with different spanwise resolutions and timesteps. Fluid density is 1.225 kg/m^3.

Panels/span	Timestep factor	1st start	1st end	2nd start
26	1/2	42	46	75
26	1	42	46	75
26	2	43	46	75
39	2	43	46	75

conducted in this Section sufficient to give us confidence in results using the baseline spanwise resolution of 26 panels per span and the timestep of $\Delta t = 0.25c/U_\infty$.

5.4.4. Flutter Characteristics

We turn our attention to two specific cases of the previous section: $U_\infty = 50$ and 80 m/s at $\alpha = 3°$. These cases produced the first and second flutter modes of the Pazy wing, respectively. We seek to characterize the flutter motion in Figs. 5.8 and 5.9. The second flutter mode, shown in Fig. 5.8 is displaying a vertical displacement that is in opposite phase with the wing twist, while being about $15°$ ahead of it. The entire wing is bending and twisting in the same direction, indicating this is indeed a combination of the first bending and first twisting modes.

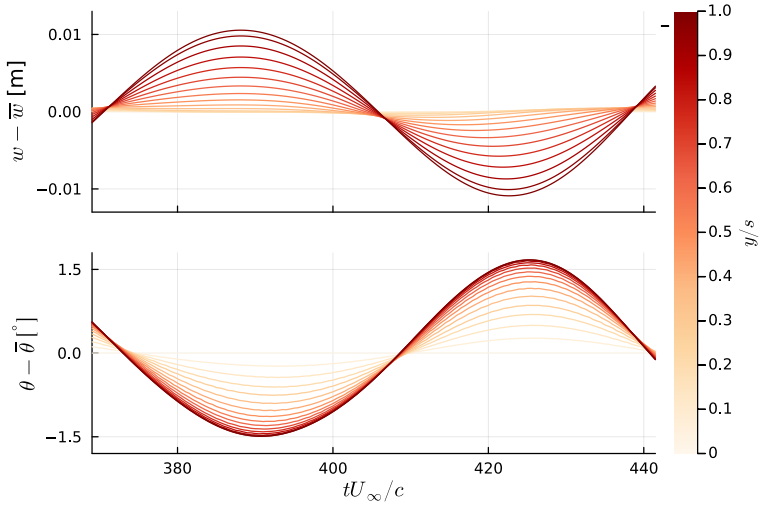

Figure 5.8: Vertical displacement fluctuation along the wing (top), and twist angle fluctuation along the wing (bottom) for $\alpha = 3°$, $U_\infty = 80$ m/s, at the second flutter mode. Colors represent the spanwise position.

Figure 5.9 shows the same analysis on the first flutter mode. Consistent with the experimental analysis [7], the vertical displacement (which is changing signs around 85% of the span) corresponds to the second bending mode and is in phase with the twist, and about $50°$ ahead of it (as evidenced by the trough for $w - \bar{w}$

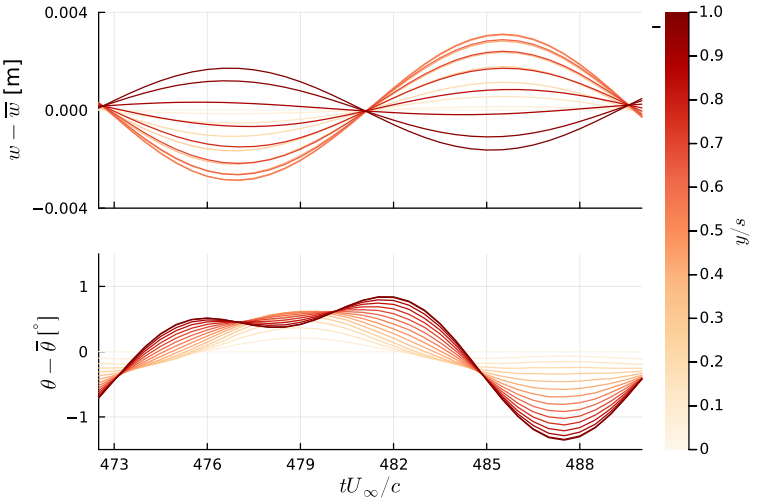

Figure 5.9: Vertical displacement fluctuation along the wing (top), and twist angle fluctuation along the wing (bottom) for $\alpha = 3°$, $U_\infty = 50$ m/s, at the first flutter mode. Colors represent the spanwise position.

near $tU_\infty/c = 486$ and the trough for $\theta - \bar{\theta}$ at $tU_\infty/c = 487$).

The second torsion mode seems to be present in the results, as seen by the θ curves. The structural model for this case was not validated for the second torsion mode, hence it is not obvious if this mode is correct or not. Similar curves from experimental data [7] show wiggles that could be due to the second torsion mode, but could also be noise from the measurements. The presence of this mode might be correct, as simulations using linearized models that require the eigenmodes as inputs have shown that including the second torsion mode was important for accuracy [24]. Also, experiments have shown that three sine waves are needed to represent the strain on the wing at LCO, which could indicate the presence of three modes [7].

The Pazy wing, along with its wake, is shown in Figs. 5.10 and 5.11 for the first and second flutter modes, respectively. The wakes are colored by the vortex strength γ, which is proportional to the sectional circulation, and hence, lift coefficient, at the time the wake panel is shed. The second flutter mode, shown in Fig. 5.11, occurs at very large levels of wing deformation. White regions on the wake indicate high sectional lift and we can see two white spots, one near the wing and one at 60% of the wake length, showing the low frequency of the wing oscillations. The first flutter mode, on Fig. 5.10, is clearly occurring at a much higher frequency. As the second bending mode is active, the color patterns on the wake are more complex, as the lift along the wing is not fluctuating in a synchronized fashion. We can also observe the wake structures becoming larger and more complex as they move downstream, as one would expect from a plunging airfoil [25].

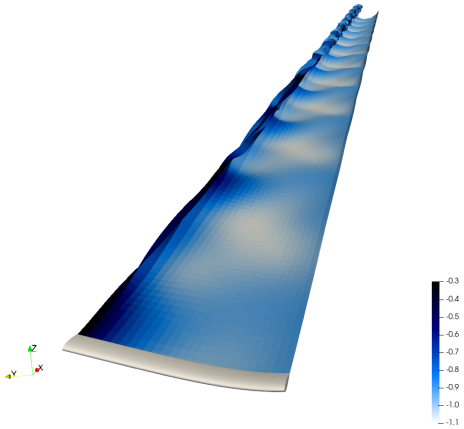

Figure 5.10: Pazy wing and its wake, colored by vortex strength, at $\alpha = 3^\circ$, $U_\infty = 50$ m/s. First flutter mode.

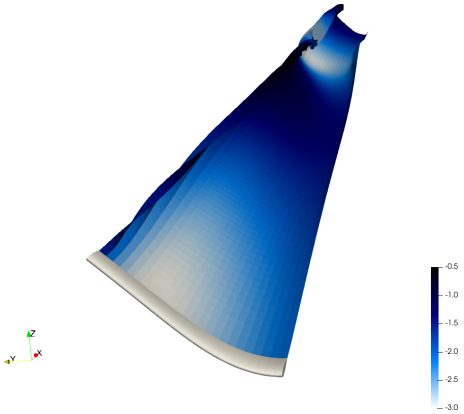

Figure 5.11: Pazy wing and its wake, colored by vortex strength, at $\alpha = 3^\circ$, $U_\infty = 80$ m/s. Second flutter mode.

5.4.5. Limit Cycle Oscillations

LCO refer to the oscillations of a vibrating system that have stabilized to a somewhat periodic behavior. Predicting the LCO response of a highly flexible wing introduces significant challenges on top of the flutter onset prediction. Not only must the flutter onset be accurately captured, but nonlinear mechanisms that limit the oscillations are required to avoid divergence.

Two types of flutter LCO are possible in flutter: supercritical and subcritical [26, 27]. In supercritical LCO, the oscillations appear at a certain flow speed (the flutter speed) and progressively increase as the speed increases. The oscillations disappear as the flow speed is brought back to the flutter speed. In subcritical LCO, flutter is more abrupt and large oscillations appear as soon as the flutter speed is reached. The flow speed must then be reduced to a value lower than the original flutter speed for the oscillations to disappear. Hence, hysteresis effects play an important role in the flutter offset.

Critically, flow separation, which can at times have a stabilizing role, in the sense that it can reduce the forces acting on the wing, can have a destabilizing role in flutter, leading to subcritical LCO [27]. For the Pazy wing, the first flutter mode clearly shows subcritical behavior in the experiments. Simulations that do not include flow separation, but include geometric nonlinear effects have been shown to capture the amplitude of the LCO associated with the first flutter mode of the Pazy wing [22], but not the subcritical effects. In the case of the present simulations, nonlinear geometry effects come from the structural model, while nonlinear inviscid aerodynamic effects [28], come from the panel code. Flow separation is missing, meaning capturing the subcritical LCO is likely not possible, but achieving LCO for the first flutter mode should be.

For the second flutter mode, above 70 m/s, we were not able to stabilize the simulations, as flutter initiates quickly and the oscillations are large, leading to nu-

merical instabilities in the solution. For the first flutter mode, achieving a stable solution was possible, as long as we use a timestep $\Delta t = 0.25c/U_\infty$ or lower. Doubling the timestep led to numerical instabilities.

We believe the reason for these instabilities at larger timesteps is that the larger timestep was not able to accurately represent the second torsion mode. The second torsion mode has a period of about $8c/U_\infty$, meaning the larger timestep was resolving it with 16 points per oscillation. Previous studies on plunging airfoils [23] have shown that a phase error of $O(5°)$ is made when using 20 timesteps per periods for reduced frequencies near 0.4 (which is the reduced frequency of the Pazy wing for the second torsion mode at the flow conditions for the first flutter mode). Using the smaller timesteps, the second torsion had half the period of the first torsion mode, making them synchronized throughout the simulations and reducing the θ peak in Fig. 5.9. With the larger timestep, the second torsion mode was not synchronized with the first torsion mode and eventually they had a constructive interference effect, making the θ peak even higher, leading to large deflections that would make the structural solver unstable.

Results for the LCO achieved with $\Delta t = 0.25c/U_\infty$ are shown in Fig. 5.12. The original run time of 500 flow passes has to be extended to about 1200 flow passes to quantify LCO. In this Section, our results are at $\alpha = 3°$ and $U_\infty = 50$ m/s. The first flutter mode LCO frequency for the Pazy wing shows little variation with α and U_∞ [7] and is between 25 and 30 Hz. Previous simulations [2] found a similar range, between 31 and 33 Hz. Our current results indicate LCO at 28.5 Hz, while the experiments show around 28.3 Hz at $\alpha = 3°$ and $U_\infty = 50$ m/s, making this an excellent agreement, within under 1%. The amplitude of the tip displacements was found to be about 2% of the span, which is in line with other numerical results [22]. The LCO amplitude also seems to have only small variations with α and U_∞.

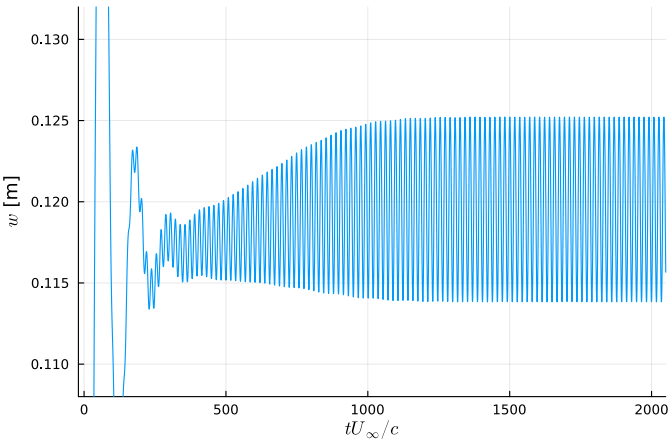

Figure 5.12: Time history of wing tip displacement for $\alpha = 3°$, $U_\infty = 50$ m/s.

5.4.6. Gust Interaction

A modified version of the Pazy wing, the Delft-Pazy wing, was experimentally tested with gusts at the Delft University of Technology [14]. This wing was made more flexible, to allow for large deflection under lower wind velocities. Externally, the wing is almost identical to the Technion built Pazy wing. The beam model developed by the University of Michigan for the original Pazy wing was updated to account for the lower stiffness of the Delft-Pazy wing [29], meaning a methodology identical to the one used in the previous sections can be applied to the Delft-Pazy wing.

Wind tunnel data are available for sinusoidal gusts interacting with the wing for two cases. The vertical velocity of the gust follows the form:

$$U_z(t) = A_G \sin(2\pi f_G t) \tag{5.3}$$

where U_z is the vertical component of the freestream velocity, A_G is the gust amplitude, f_G is the gust frequency, and t is time. The spanwise freestream velocity is zero and streamwise component of the freestream velocity can be adjusted to achieve a constant velocity magnitude of $U_\infty = 18.3$ m/s.

One of the advantages of the current panel method is that the freestream velocity can be an arbitrary user defined function, whereas CFD methods could smear sharp gusts before they reach the target object, due to numerical diffusion. For this case, this means we can create gusts that are functions of time and space, which for the Delft-Pazy wing corresponds to:

$$U_z(x,t) = A_G \sin\left(2\pi f_G \frac{U_\infty t - x}{U_\infty}\right) \tag{5.4}$$

where x is the streamwise coordinate. Here we have a gust that at a given instant in time has a wavelength of U_∞/f_G that is convected with U_∞.

The results of these gust experiments are tip deflections, defined as $w = \bar{w} + A_w sin(2\pi f_G + \phi_w)$, where A_w is the amplitude of the tip deflection motion and ϕ_w is the phase between the tip deflection and the gust velocity at the wing root quarter chord location. The two test conditions from the experiments of [14] are shown in Table 5.3. Here, α is the steady mean angle of attack of the wing root.

Table 5.3: Experimental conditions of the gust cases.

Case	α (°)	f_G (Hz)	A_G (m/s)
1	5	5.7	0.81
2	10	3.2	0.65

The wing tip deflection for simulations and experiments over a gust period $T = 1/f_G$ for cases 1 and 2 are shown in Fig. 5.13. Note that T is different for cases 1 and 2. The amplitudes of the tip displacement are over predicted (19% for case 1) and the phase difference is larger than expected (15° for case 2). The present method has been shown to capture amplitude and phase of moving geometries [23] and it should be accurate for the present case, barring low Reynolds effects being dominant. We believe there are two main reasons for the discrepancies.

The first is that experiments measured the gust $0.75c$ upstream of the wing center span and assumed negligible unsteady influence of the wing on the measurement location. The second is the assumption that the gust travels with U_∞ near the wing, ignoring the flow deceleration near the stagnation point. Both points could affect the amplitude and phase of the wing response.

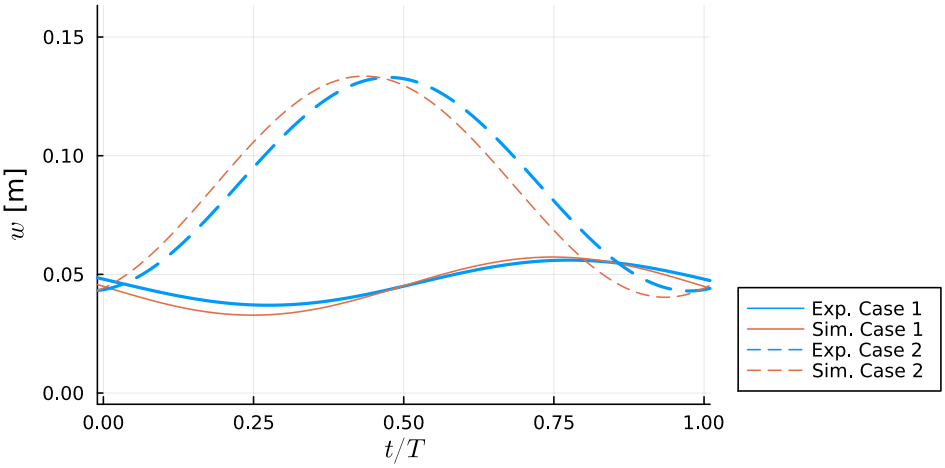

Figure 5.13: Vertical tip displacement of the Delft-Pazy wing under gusts.

The second point can be addressed by directly including the guide vanes of the wing tunnel in the simulations [30], which is beyond the scope of our work. The first can be addressed by using the present simulations to estimate the effect of the wing on the measurement. Another advantage of the present method is the potential to break down the velocity in a point in space into the freestream component and the induction by arbitrary sets of surface and wake panels. Hence, we measured the wing induction on the same location as the experiments. This location was a plane $0.75c$ upstream the unrotated wing leading edge, at spanwise coordinates 140 to 415 mm, where zero spanwise coordinate corresponds to the wing root, and transverse coordinates -80 to 140 mm for case 1, -60 to 160 mm for case 2, where a zero transverse coordinate is at the chord line. The wing was then rotated around its mid point, to achieve the correct angle of attack. The planes for cases 1 and 2 are shown in Fig. 5.14.

With these measurements, we can compare the measured $A_{G,\text{meas}}$ with the freestream $A_{G,\infty}$, which in the experiments were assumed to be the same. The objective is to achieve an $A_{G,\text{meas}}$ close to the experimental value by correcting $A_{G,\infty}$, which is unknown in the experiments. We can also check if there is a phase between the the imposed and measured gust, ϕ_G, caused by the wing induction. The results of this study are summarized in Tables 5.4 and 5.5. The difference Δ is always relative to the experimental value. For case 1 the wing deflection is smaller, putting it closer to the measurement plane. A freestream gust of 0.69 m/s leads to the measured gust of 0.81 m/s. Correcting for the gust amplitude does not change

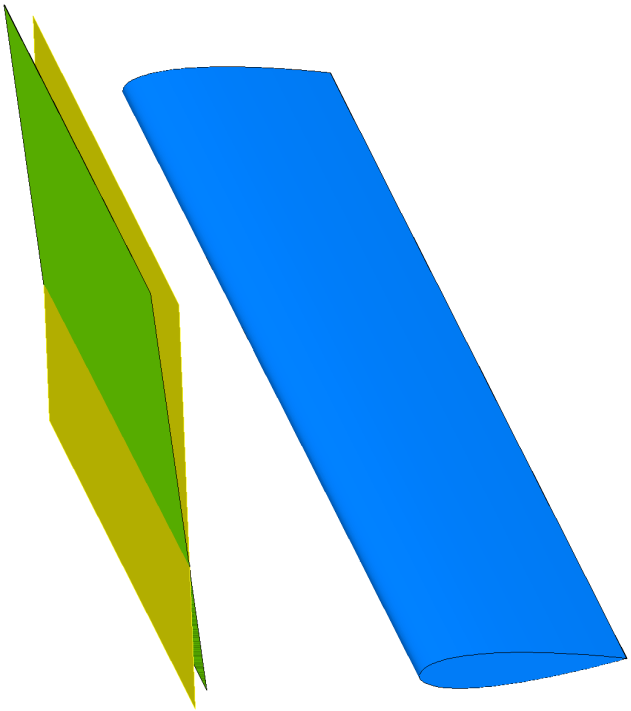

Figure 5.14: Delft-Pazy wing (blue), along with the experimental measurement planes for cases 1 (yellow) and 2 (green).

ϕ_w, but the wing introduces a phase error in the measurement plane of $\phi_G = 6°$, which can be used as a correction. For case 2 the wing is more deflected and hence further away from the measurement plane, leading to smaller effects of the wing on the measurement plane. The large phase differences for case 2 could be explained by the trailing edge separations on the wing seen in experiments [14].

Table 5.4: Case 1 results for experiments, simulations, and simulations with corrected gust.

	Exp.	Sim.	Δ	Sim. corr.	Δ
$A_{G,\infty}$ (m/s)	-	0.81	-	0.69	-
$A_{G,\mathrm{meas}}$ (m/s)	0.81	0.96	19%	0.81	0%
$\bar{w}$ (m)	0.0465	0.0451	-3%	0.0450	-3%
A_w (m)	0.0095	0.0123	29%	0.0104	10%
ϕ_G (°)	-	0	-	6	-
ϕ_w (°)	171	180	9°	174	3°

The corrections obtained in this study improved wing tip displacement correlations with experimental data by only using the flow velocities achieved in the simulations on the measurement plane. It is worth noting that, in the experiments,

Table 5.5: Case 2 results for experiments, simulations, and simulations with corrected gust.

	Exp.	Sim.	Δ	Sim. corr.	Δ
$A_{G,\infty}$ (m/s)	-	0.65	-	0.62	-
$A_{G,\text{meas}}$ (m/s)	0.65	0.69	6%	0.65	0%
$\bar{w}$ (m)	0.088	0.086	-2%	0.087	-2%
A_w (m)	0.045	0.046	2%	0.044	-2%
ϕ_G (°)	-	0	-	2	-
ϕ_w (°)	-81	-66	15°	-68	13°

the gusts were generated using guide vanes which oscillated in angle of attack. The amplitude of these oscillations was $5°$ for cases 1 and 2, meaning that A_G was expected to be quite similar for both cases, being different only due to the effects of changing f_G. Hence, the corrected values of $A_{G,\infty}$ of 0.69 and 0.62 m/s are more in line with expectations than the original wind tunnel values of 0.81 and 0.65 m/s.

5.5. Conclusions

Simulations of the highly flexible Pazy wing were conducted for different angles of attack and flow velocities. The structural model and the aeroelastic simulations were compared with experimental data, with good agreement being found. In particular, the flutter onset was predicted within 1 m/s of the experimental values for most angles of attack. No artificial displacement or velocity was applied to the wing for it to start vibrating in the simulations. These are the first published results for the Pazy wing using a time domain 3D panel method with a free wake.

An analysis of the flutter motion was done, in order to clarify the phenomena occurring at the first and second flutter modes. We found that the first flutter mode includes the second torsion mode of the wing. As described in Section 5.4.4, we have reasons to believe this is correct and, to our knowledge, this is the first time this behavior was clearly identified and documented. Previous publications describe the first flutter region of the Pazy wing as a combination of the first torsion mode and the second bending mode only. We also show that by reducing the timestep in the simulation, LCO were obtained for the first flutter mode, with the LCO frequency being within 1% of the experimental data.

Simulations of the wing under gusts were also conducted and validated with experimental data. To our knowledge, this work shows the first numerical validation of the Delft-Pazy wing gust experiments. It was shown that errors in amplitude and phase were related to the wing induction at the experimental measurement location. In the experiments, it was assumed that the wing induced a constant velocity at the measurement location and with our method we can isolate that effect from the incoming gust. We demonstrated that the current method can be used to correct this measurement error, leading the simulations to show a substantially better agreement with the tip displacement amplitude seen in the experiments. In the presence of flow separations, the current method loses accuracy and comparisons to experiments are less reliable.

The framework developed herein can be applied to other, more complex cases in the future, where the advantages of a full 3D panel method would be more evident. Such cases can include fuselage-mounted wings, wings with pods, or aircraft where the wing wake has strong interactions with the horizontal tail plane.

Each case simulated herein (i.e., each angle of attack and flow speed combination) was run in about 30 minutes on a desktop with 20 cores. This was sufficient to determine the shape of the wing and if flutter took place. Using the larger timestep, which produced results within 1 m/s of the baseline results for flutter onset, but could not achieve LCO, the run time was reduced to 5 minutes. In order to quantity the LCO, simulations with baseline timestep took about 70 minutes. Hence, the current methods are a fraction of the cost of CFD, but substantially more expensive than linearized methods. These run times can be reduced in the future by code and setup optimization. Changes that could substantially reduce the run time are: reducing the length of the wake, coarsening the surface mesh, increasing the timestep (as demonstrated), updating the influence coefficient matrices less often, and skipping the calculation of the wake velocity, letting it convect with the freestream.

Future simulations of the Pazy wing with the current method can include more geometrical details, such as the wing tip rod, and the deformed wing skin. A detailed structural model, including the deformation of the wing skin could be developed in the future and coupled with aerodynamic simulations. Such a model is not yet available, as knowing the structural properties of the skin is challenging, as is modelling its buckling. More analysis of the second flutter mode can also be done, as doing so experimentally has been difficult, due to the high dynamic pressures and deformations that can damage the wing. Finally, the guide vanes in the wind tunnel could be included to more accurately model the gust response.

References

[1] A. F. P. Ribeiro, D. Casalino, and C. Ferreira, *Free wake panel method simulations of a highly flexible wing in flutter and gusts,* Journal of Fluids and Structures **121**, 103955 (2023).

[2] M. Ritter and J. Hilger, *Dynamic aeroelastic simulations of the Pazy wing by UVLM with nonlinear viscous corrections,* in *AIAA SCITECH 2022 Forum* (2022).

[3] F. Afonso, J. Vale, E. Oliveira, F. Lau, and A. Suleman, *A review on non-linear aeroelasticity of high aspect-ratio wings,* Progress in Aerospace Sciences **89**, 40 (2017).

[4] C. E. Cesnik, R. Palacios, and E. Y. Reichenbach, *Reexamined structural design procedures for very flexible aircraft,* Journal of Aircraft **51**, 1580 (2014).

[5] T. E. Noll, J. M. Brown, M. E. Perez-Davis, S. D. Ishmael, G. C. Tiffany, and M. Gaier, *Investigation of the Helios prototype aircraft mishap. Volume I. Mishap report,* (2004), accessed: May 10 2023.

[6] O. Avin, D. E. Raveh, A. Drachinsky, Y. Ben-Shmuel, and M. Tur, *Experimental aeroelastic benchmark of a very flexible wing,* AIAA Journal **60**, 1745 (2022).

[7] A. Drachinsky, O. Avin, D. E. Raveh, Y. Ben-Shmuel, and M. Tur, *Flutter tests of the Pazy wing,* AIAA Journal **60**, 5414 (2022).

[8] C. Riso and C. E. Cesnik, *Low-order geometrically nonlinear aeroelastic modeling and analysis of the Pazy wing experiment,* in *AIAA SCITECH 2022 Forum* (2022).

[9] A. Drachinsky and D. E. Raveh, *Nonlinear aeroelastic analysis of highly flexible wings using the modal rotation method,* AIAA Journal **60**, 3122 (2021).

[10] M. Ritter, J. Hilger, and M. Zimmer, *Static and dynamic simulations of the Pazy wing aeroelastic benchmark by nonlinear potential aerodynamics and detailed FE model,* in *AIAA Scitech Forum* (2021).

[11] M. Righi, *Uncertainties quantification in flutter prediction of a wind tunnel model exhibiting large displacements,* in *AIAA Scitech Forum* (2021).

[12] N. Goizueta, A. Drachinsky, A. Wynn, D. E. Raveh, and R. Palacios, *Flutter predictions for very flexible wing wind tunnel test,* in *AIAA Scitech 2021 Forum* (2021).

[13] M. Fehrs, M. Ritter, S. Helm, and C. Mertens, *CFD simulations of the Pazy wing in support of the third aeroelastic prediction workshop,* in *International Forum on Aeroelasticity and Structural Dynamics (IFASD)* (2022).

[14] C. Mertens, J. L. Costa Fernández, J. Sodja, A. Sciacchitano, and B. W. van Oudheusden, *Integrated aeroelastic measurements of the periodic gust response of a highly flexible wing,* in *International Forum on Aeroelasticity and Structural Dynamics (IFASD)* (2022).

[15] L. Yang, C. Xie, and C. Yang, *Geometrically exact vortex lattice and panel methods in static aeroelasticity of very flexible wing,* Proceedings of the Institution of Mechanical Engineers, Part G: Journal of Aerospace Engineering **234**, 742 (2020).

[16] M. Patil and D. Hodges, *On the importance of aerodynamic and structural geometrical nonlinearities in aeroelastic behavior of high-aspect-ratio wings,* Journal of Fluids and Structures **19**, 905 (2004).

[17] J. Katz and A. Plotkin, *Low-Speed Aerodynamics*, 2nd ed., Cambridge Aerospace Series (Cambridge University Press, 2001).

[18] B. Maskew, *Program VSAERO Theory Document: A Computer Program for Calculating Nonlinear Aerodynamic Characteristics of Arbitrary Configurations*, Contractor Report 4023 (National Aeronautics and Space Administration, 1987).

[19] M. Gennaretti and G. Bernardini, *Novel boundary integral formulation for blade-vortex interaction aerodynamics of helicopter rotors,* AIAA Journal **45**, 1169 (2007).

[20] C. Riso, D. Sanghi, C. E. Cesnik, F. Vetrano, and P. Teufel, *Parametric roll maneuverability analysis of a high-aspect-ratio-wing civil transport aircraft,* in *AIAA Scitech 2020 Forum* (2020).

[21] W. Su and C. E. S. Cesnik, *Nonlinear aeroelasticity of a very flexible blended-wing-body aircraft,* Journal of Aircraft **47**, 1539 (2010).

[22] C. Riso and C. E. Cesnik, *Post-flutter dynamics of the Pazy wing geometrically nonlinear benchmark model,* in *International Forum on Aeroelasticity and Structural Dynamics (IFASD)* (2022).

[23] A. F. P. Ribeiro, D. Casalino, and C. S. Ferreira, *Surging wind turbine simulations with a free wake panel method,* Journal of Physics: Conference Series **2265**, 042027 (2022).

[24] M. Ritter, *October 13,* Personal communication (2022).

[25] J. Young and J. C. S. Lai, *Oscillation frequency and amplitude effects on the wake of a plunging airfoil,* AIAA Journal **42**, 2042 (2004).

[26] P. Marzocca, L. Librescu, and W. A. Silva, *Flutter, postflutter, and control of a supersonic wing section,* Journal of Guidance, Control, and Dynamics **25**, 962 (2002).

[27] E. Dowell, J. Edwards, and T. Strganac, *Nonlinear aeroelasticity,* Journal of Aircraft **40**, 857 (2003).

[28] A. F. P. Ribeiro, D. Casalino, and C. S. Ferreira, *Nonlinear inviscid aerodynamics of a wind turbine rotor in surge, sway, and yaw motions using a free-wake panel method,* Wind Energy Science **8**, 661 (2023).

[29] C. Riso, *AePW3-LDWG,* (2022), accessed: October 4 2022.

[30] A. V. Kassem, *Wind Gust Generation for Wind Turbine Testing via Numerical Methods*, Master's thesis, Delft University of Technology (2019).

6

VAWT Wake Steering by Pitched Struts and Blades

The greatest disaster one can encounter in computation is not instability or lack of convergence, but results that are simultaneously good enough to be believable, but bad enough to cause trouble.

Joel H. Ferziger

Vertical axis wind turbines (VAWTs) have been identified as a technology that, in association with wake steering, can increase power density of wind farms. In this chapter we validate the free wake panel code used throughout this thesis for VAWT wake prediction, which leads to satisfactory results. We then use this method to simulate wake steering by means of fixed pitched blades and struts. We demonstrate that combining pitched wakes and struts can lead to very advantageous wake behavior, but only when the interactions between the tip vortices are taken into account. The possibility to inject more high momentum flow into the wake while moving the vortex system away from the next turbine could make pitched blades and struts a powerful tool for future wind farms.

Parts of this chapter have been published in The Science of Making Torque from Wind (2024) [1].

6.1. Introduction

With the recent global shift towards renewable energy, the interest in wind energy is growing every year. Traditional horizontal axis wind turbines have been the preferred method for extracting energy from the wind. However, interest in vertical axis wind turbines (VAWTs) is on the rise, due to their advantages over traditional turbines. The main benefits of VAWTs are: the fact that the generator can be at ground level, leading to easier installation and maintenance; noise reduction, due to lower tip speeds; and the omnidirectional wind capture without the need for a yawing mechanism.

As onshore and offshore wind farms become larger, reducing the distance between the turbines without substantial loss to the power production of each turbine is an important research and industrial topic, as the interaction between the wakes becomes a critical phenomenon. Many research groups have investigated wake steering and other forms of control in order to increase the power densities of future wind farms [2]. Recent studies have investigated the effects of static and dynamic VAWT blades pitching [3], which besides potentially improving power production [4–6], can also be used to improve wake recovery [7]. Improving wake recovery with fixed blade pitching usually comes with a performance penalty on the first turbine and a performance gain on the downstream turbines. A study on the aerodynamic effects of the horizontal supports holding the blades (struts) has also shown promising results [8]. Fixed pitched struts could be structurally advantageous, as the moment of inertia around the horizontal axis is increased when using airfoil shaped struts. To the authors' knowledge, the combination of pitching blades and struts has not yet been investigated.

In this work, we perform numerical simulations of pitched VAWTs using a free wake panel method, which are validated with computational fluid dynamics (CFD) simulations performed by Ming [7], who used actuator line unsteady Reynolds-averaged Navier-Stokes (URANS), with the $k-\epsilon$ turbulence model. The free wake simulations allow us to examine the unsteady interaction of the vortices created by blade and strut pitching in a cost-effective manner. As the wake steering effects from pitching are dominated by advection effects (instead of diffusion or mixing effects) in the near-wake, Lagrangian methods are a promising approach to examine potential benefits from pitching. We then go beyond the previous studies and include pitched struts along with the pitched blades. The objectives of this work are to validate the free wake panel method for VAWT wake steering and to verify the potential gains in wake steering from combined pitching of blades and struts.

6.2. Case Description

In this work, we simulate the three-bladed VAWT that was used in the work of [7]. This is a high Reynolds VAWT, which is more suitable for the inviscid method used in this work than small scale VAWTs. A sketch of the top and side view of the VAWT is given in Fig. 6.1. The freestream velocity U_∞ is 10 m/s, the tip speed ratio $\lambda = \Omega R/U_\infty$ is set to 4.5, where Ω is the angular velocity, and R is the turbine radius. This condition was chosen as it is near the maximum power coefficient for

this turbine. The VAWT is square in cross section, meaning the height H is equal to the diameter D, which is 160 m. The blades have chord $c = D/40$ and can have zero pitch angle, or $\pm 10^\circ$, where a positive pitch means the nose points towards the center of the rotor. Struts are included in some of the simulations, which was not the case in the reference results. They are lifting surfaces with the same chord as the blades, with a starting radius of $0.13R$ and a maximum radius of $0.99R$. The struts can have the same pitch angle as the blades, where a positive pitch means the nose pointing away from the turbine horizontal symmetry plane. The blades and struts have NACA0025 cross sections.

For the discretization of the blades and struts, we use 50 panels over the blades height and 22 panels over the struts span, with homogeneous spacing. For the blades and struts we use 200 panels around the chordwise direction, with cosine spacing, i.e. refinement on the leading and trailing-edges. The timestep corresponds to 6° rotation of the turbine and simulations are run for at least 960 timesteps, i.e. 16 full rotations or over 11 flow passes over the rotor diameter. The simulated geometry, in correct proportions, is shown in Fig. 6.2.

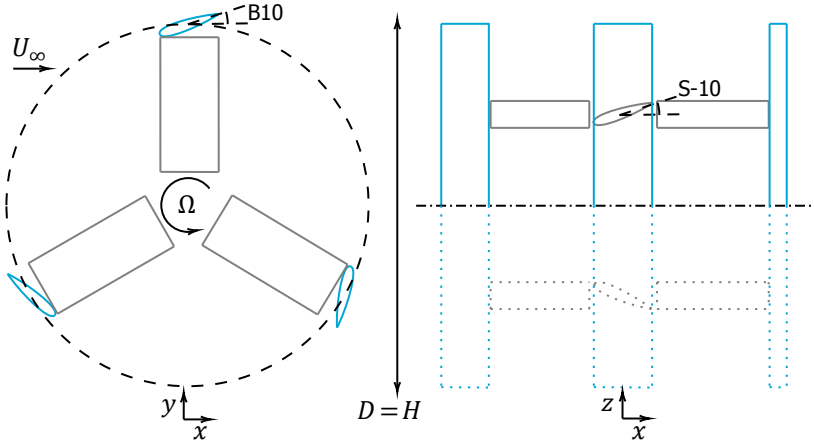

Figure 6.1: Sketch of the VAWT. Not to scale. Top view on the left, side view on the right. Symmetry plane shown as dash-dotted line. Blade path shown as dashed circle. Virtual panels shown in dotted lines. Positive blade pitch and negative strut pitch illustrated. Blades are in blue, struts in grey.

Early simulations with small values for the radius used in the vortex core model had very unstable wakes. Previous experience with this method [9] has shown that in order for complex wakes to be preserved, large values of the core radius are needed. We hence set the radius to about twice the chord of the blades and struts (or about $D/20$). This allowed us to preserve the wakes of the VAWTs while still obtaining reasonable values for the power coefficients when compared to reference CFD.

The nomenclature used throughout this paper describes cases based on the blade pitch angle and strut pitch angle. Cases with no struts and blades pitched at -10, 0, and 10° are named B-10, B0, and B10 respectively. Cases with the struts pitched at -10, 0, and 10° are named S-10, S0, and S10 respectively. Hence, the

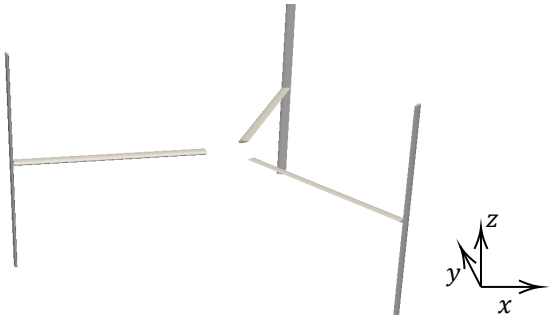

Figure 6.2: Top half of the VAWT as simulated in this work. To scale. Blades and struts are pitched as in Fig. 6.1.

case in Fig. 6.1 is referred to as B10S-10.

6.3. Results

6.3.1. Single Turbine with Pitched Blades and no Struts

We begin by comparing results from our simulations with reference CFD results [7]. Figure 6.3 shows the wakes of each of the three cases simulated in this section, along with the measurement planes at $x = 1D$, $3D$, and $5D$, which will be used for comparisons to reference data. Blade pitching clearly has strong wake steering effects, with positive pitching contracting the wake axially and spreading it laterally, while negative pitching (as we will see later) has the opposite effect. B0 is the only case where the wake is nearly symmetric, as the other cases have asymmetric vortices appearing at the corners of the turbine, which are responsible for the wake steering [10].

Figure 6.4 shows planes perpendicular to the streamwise direction, where the bottom halves of the nine squares show CFD data, while the top halves are the panel code results. The planes show time-averaged streamwise velocity u normalized by the freestream velocity. The grey squares at the center of the images are the outline of the VAWTs. The CFD and free wake results use similar resolutions in the planes, but the free wake vectors were drawn at lower density for clarity. Near the turbine, at $x = 1D$, results are very similar between both methods. Discrepancies increase at $x = 3D$, while at $x = 5D$ the results become quite different. Free wakes made of vortex filaments tend to become entangled over long distances and this leads to large errors. In addition, for all figures the CFD results show more diffusion of the wake than panel code results. This is expected, as CFD tends to cause too much dissipation and diffusion, while Lagrangian methods tend to have too little of both. In spite of such differences, the wake steering from the pitched blades is captured and the shapes of the wakes are very similar.

Throughout the work we use the power coefficient C_P to measure the effects of pitching on the turbine power production. It can be computed as:

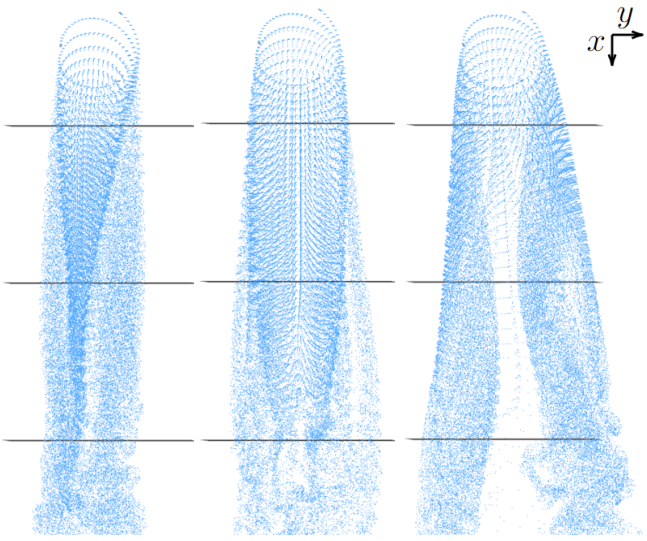

(a) B-10. (b) B0. (c) B10.

Figure 6.3: Top view of wakes generated by each blade pitch setting. Horizontal lines are the planes at $x = 1D$, $3D$, and $5D$, from top to bottom, where $x = 0$ is at the rotor axis.

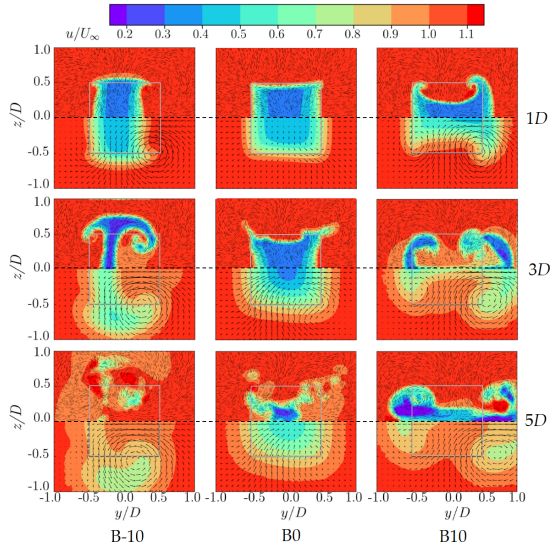

Figure 6.4: Planes perpendicular to the streamwise direction. The rows are, from top to bottom, $1D$, $3D$, and $5D$ downstream of the VAWT center. The columns correspond to different blade pitch angles. The top half of each square corresponds to free wake results, while the bottom halves are the reference CFD [7].

$$C_P = \Omega Q/(0.5\rho U_\infty^3 DH), \tag{6.1}$$

where Q is the turbine torque and ρ the air density. Table 6.1 shows the effect of blade pitching on C_P for the current simulations and the reference CFD. The inviscid methods used in this work have limitations in calculating C_P accurately [11], as the torque requires sectional drag to be accurate. Hence, we do not expect a perfect match. With viscous drag being neglected, the power calculated with the panel code is higher than in CFD. The losses due to blade pitching are also higher than the reference, but the qualitative agreement is fair, with both methods predicting B10 to have the worst performance, then B-10, and then B0. These results give some confidence to the method, but also serve as a warning that the effects of pitching obtained for the remainder of the paper are potentially overpredicted.

Table 6.1: Power coefficient for the VAWTs. Current results compared to the reference CFD. Values in red indicate the loss of power relative to B0 of the corresponding method.

	B-10	B0	B10
Panel Code	0.50 (-11%)	0.56	0.48 (-14%)
CFD [7]	0.46 (-8%)	0.50	0.44 (-12%)

As expected, pitching the blades leads to lower power for the VAWT. The expected benefit of blade pitching is in wake steering, trying to improve the power of the downstream turbines in a manner that compensates the power loss for the upstream turbine. The power available for the downstream turbine can be estimated by computing the average of u^3/U_∞^3 on a downstream plane the size of the frontal area of a potential downstream turbine. In a case with optimal wake steering, where the wake is moved completely outside of the grey squares representing the turbine outlines (which also represent the position of potential downstream turbines) in Fig. 6.4, this available power would be one. When the wake does not spread outside of the location of the downstream rotors, the available power is low. Streamwise vortices can energize the wake by advecting high speed flow from the surrounding area into the downstream rotor locations.

For completeness, we also examine the streamwise (x) and lateral (y) thrust coefficients for these cases:

$$C_{Tx|y} = F_{x|y}/(0.5\rho U_\infty^2 DH), \tag{6.2}$$

where F is the force acting on the rotor and $x|y$ represents that the force and corresponding coefficient can be taken in the x or y directions. Results for C_T are shown in Table 6.2. While the lateral thrust is in fair agreement with the CFD, the streamwise thrust is substantially overpredicted. This is not surprising given the very high angles of attack found in the flow conditions studied here, which can potentially lead to inaccuracies due to excess flow separation in CFD and certainly cause inaccuracies in the inviscid panel method, which has no flow separations. Hence, these results highlight some of the limitations of the method employed in this work.

Table 6.2: Thrust coefficients for the VAWTs. Current results compared to the reference CFD.

	B-10	B0	B10
C_{Tx} Panel Code	0.88	0.81	0.88
C_{Tx} CFD [7]	0.69	0.68	0.64
C_{Ty} Panel Code	-0.46	0.02	0.38
C_{Ty} CFD [7]	-0.37	0.02	0.34

The available power for potential downstream rotors at $x = 3D$ is shown in Table 6.3. The differences between CFD and panel code in available power for B0 is far larger than for B-10 and B10, since the wake at B0 is diffusion dominated, while the other case have strong advection effects. As mentioned before, diffusion is likely overestimated in the CFD results and certainly underestimated in the free wake results. Other potential sources of differences are the interactions between the vortices, as the free wake simulations do not account for merging and breakup of the vortical structures.

Table 6.3: Power available for a VAWT at $x = 3D$. Blue values in parentheses indicate gain over B0 for the respective method.

	B-10	B0	B10
Panel Code	0.63 (5.9×)	0.11	0.61 (5.7×)
CFD [7]	0.64 (2.6×)	0.25	0.72 (2.9×)

6.3.2. Two Turbines with Pitched Blades and no Struts

We now investigate an array of two turbines: the first with pitched blades and the second, placed at $x = 3D$, without blade pitching (B0). This was also simulated in [7] and here serves to validate the use of free wake panel methods for VAWT wake interaction. The time histories of C_P for the three cases are shown in Fig. 6.5. Whereas integrating the available power in the wake of B0 led to substantial differences between free wake and CFD simulations (see Table 6.3), the agreement of simulating two turbines is very good. This could be due to the presence of the downstream turbine creating more local advection effects, that compensate for the errors in diffusion. For the three cases we can observe reasonably good agreement, but also very slow convergence. This is because the wake of the first turbine needs to travel a distance of $3D$, then interact with the second turbine, and then propagate further to remove the startup vortex effects from both turbines.

Top and side views of the three simulations are shown in Fig. 6.6. As soon as the wakes reach the second turbine, they become extremely tangled and the flow downstream of that region is not meaningful, which indicates that even if the current free wake simulations are fast and accurate enough compared to the CFD, adding another downstream turbine is unfeasible.

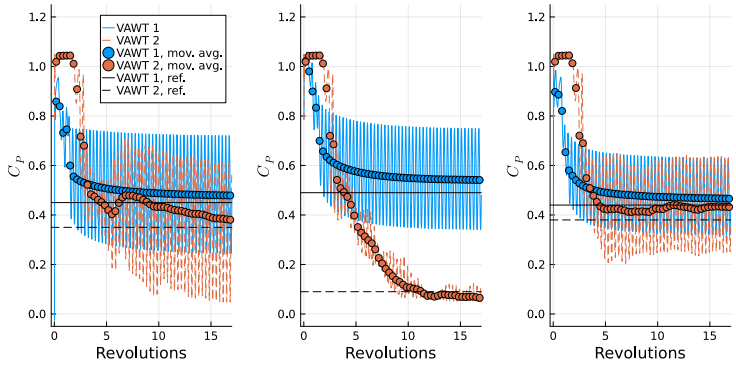

(a) B-10. (b) B0. (c) B10.

Figure 6.5: Time history of the power coefficient for the two turbine arrays. Reference results are CFD from [7].

6

6.3.3. Combining Blade and Strut Pitching

We now investigate the effects of including and pitching the struts of the blades. The top and bottom struts are always pitched in opposite directions, making the case symmetric around the $z = 0$ plane. The power coefficient C_P for all cases is shown in Table 6.4. Comparing these results with Table 6.1, we can see that adding the struts at zero pitch has a small effect of about 2% on C_P. Blade or strut pitching seems to decrease C_P by nearly 10%, with the exception of B0S-10, which has minor effects. Combining blade and strut pitching tends to have a cumulative effect, reducing power by almost 20%, with the exception of B10S10, which has a much larger power loss.

Table 6.4: Power coefficient for the VAWT. Percentage decrease in power relative to B0S0 shown in red.

	B-10	B0	B10
S10	0.45 (-19%)	0.50 (-9%)	0.39 (-30%)
S0	0.51 (-8%)	0.55	0.47 (-15%)
S-10	0.45 (-19%)	0.55 (-1%)	0.48 (-14%)

The wake planes at $x = 3D$ for the nine configurations are shown in Fig. 6.7. The center row is similar to the center row of Fig. 6.4, with small differences due to the presence of the struts, even though they are at zero pitch angle. By looking at the center column, we can observe pitching the struts has similar effects to pitching the blades, with a positive pitch leading to the wake being stretched to the sides and a negative pitch pushing the wake to the top and bottom. The four corner images show the effects of combining blade and support pitching, which seems to be favorable for B10S-10 and less effective for B-10S10. These results are not intuitive, as if blade and strut pitching tend to move the wake in the same direction, one would expect B10S10 and B-10S-10 to be the optimum cases.

Again, we evaluate the available power in the wake of the turbines, at a distance

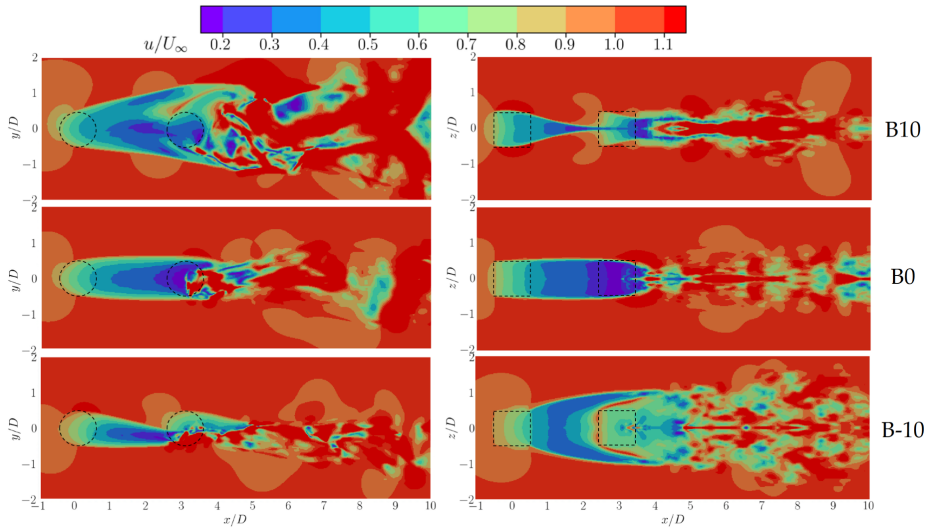

Figure 6.6: Top (left) and side (right) views of the turbine pairs. The downstream turbine is always B0 and is at $x = 3D$.

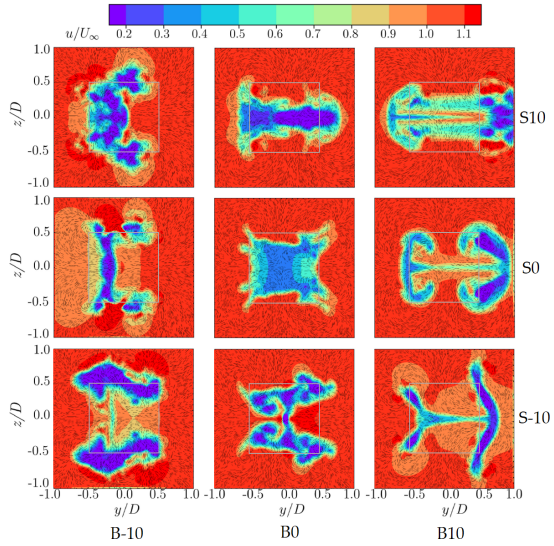

Figure 6.7: Planes perpendicular to the streamwise direction at $x = 3D$. The rows correspond to different horizontal supports pitch angles. The columns correspond to different blade pitch angles.

of $3D$. This location is selected due to being close enough to avoid excessive wake entanglement, but far enough that it could potentially be used in a high-density turbine array. Results are summarized in Table 6.5. Given the inaccuracies seen in Section 6.3.1, the computed trends could be misleading, but, assuming the trends

are reasonable, the gains with strut pitching are substantially lower than with blade pitching, which is consistent with the fact that the blades are longer and translate faster than the struts. However, a few cases are noteworthy: first, B0S-10 provides fair improvement over the baseline ($2.4\times$), with very little penalty to the upstream turbine (-1%), although other cases can lead to overall higher power output (sum of power for the two turbines) due to superior wake recovery. Second, B10S-10 is the only case where combined pitching is more effective than blade pitching. Finally, B-10S0 and B10S0 show that the struts at zero pitch have a noticeable effect in the downstream power, compared to the cases in Table 6.3.

Table 6.5: Power available for a VAWT at $x = 3D$. Blue values in parentheses indicate gain over B0S0.

	B-10	B0	B10
S10	0.42 (2.9×)	0.46 (3.2×)	0.50 (3.5×)
S0	0.56 (3.9×)	0.14	0.64 (4.5×)
S-10	0.46 (3.3×)	0.35 (2.4×)	0.70 (4.9×)

In order to investigate the physics of the vortex system acting on the wake, we now focus on the wake filaments coming from the tips of the blades and struts in the near wake of the VAWTs. An isometric representation of what we will investigate here is shown in Fig. 6.8 for clarity. The actual analysis is shown in Fig. 6.9, which has vertical cuts of the wakes seen from donwstream of the turbines, where only the top halves of the VAWTs are shown, along with circles indicating the direction of the vorticity generated by the wake filaments. The blade wakes are blue and the strut wakes are red. We can now understand the effects of the cases of combined strut and blade pitching. Cases B-10S-10 and B10S10 theoretically should work well, as both the blade and struts are trying to pull high momentum flow into the wake from the same direction (the sides and the top/bottom, respectively). However, we see that in these cases the vortices created by the struts and blades are close together and spinning in the same direction, working against each other in the region between them. Case B-10S10 has counter rotating vortex pairs, but they are working to expand the wake in all directions, only pulling flow into the wake in the small region between the vortices.

The case that works best based on previous analyses is B10S-10 and Fig. 6.9 clarifies the reason for this. The vortex pairs are counter rotating, working together to move the wake to the outside diagonals. They are also arranged in ways that allow them to propel themselves outwards, moving the vortex cores away from the wake, which the other cases do not achieve well, allowing for strong wake steering. Finally, the vortices are pulling high momentum flow into the wake from the sides and top/bottom, energizing the flow in a more effective way.

6.4. Conclusions

In this study, we have explored various VAWT configurations with pitched blades and struts in an attempt to model wake steering with a free wake panel method. The key findings from this research are:

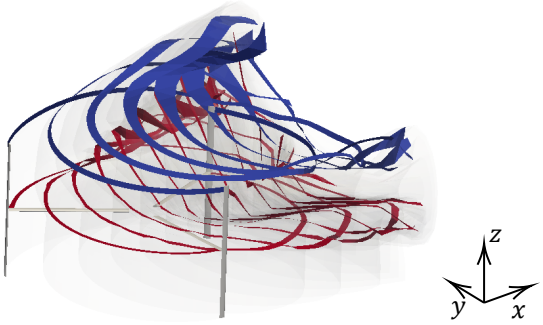

Figure 6.8: Isometric view of the data shown in Fig. 6.9. Top half of case B10S-10. The wake panels are trimmed at $x = 0.8D$ and colored in transparent grey. The blade tip vortices are shown as blue ribbons. The strut tip vortices are shown in red ribbons.

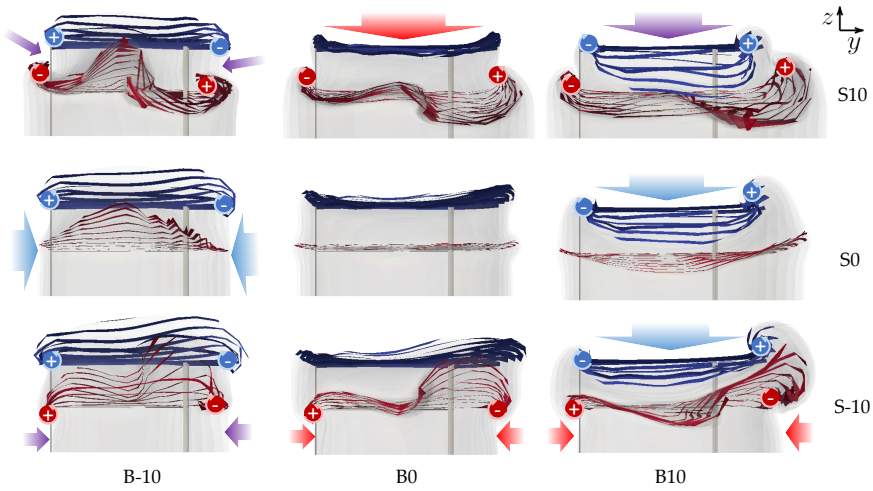

Figure 6.9: View towards upstream of all cases with struts. Tip wake filaments of the struts shown in red, and in blue for the blades. Remaining filaments shown in transparent grey. Positive (counter-clockwise) and negative (clockwise) vorticity regions highlighted with circles. Large arrows indicate flow being injected into the wake by the vortices, with colors indicating which vortices are inducing the airflow (red: struts, blue: blades, purple: both). Only top half of the VAWTs shown due to symmetry.

- Simulating an isolated VAWT with a free wake panel method leads to reasonable power prediction. Estimating power available for the next turbine is limited to short distances (three diameters in our case, but increasing vortex cores can stabilize wakes further) and is inaccurate in cases that are dominated by diffusion.

- Simulating sets of turbines downstream from each other showed good accuracy in power prediction, but is limited to two turbines, as the wakes become entangled after the second turbine. Such simulations take over a day in a desktop computer with 20 cores and a GPU with 8 GB of RAM. This time could

likely be substantially reduced with acceleration techniques, such as the fast multipole method.

- For the cases studied here, strut pitching was less effective than blade pitching for wake steering. Combining strut and blade pitching can be very effective, but only if the interaction between the tip vortices are well accounted for.

The design that we investigated was symmetric around the horizontal plane, which might be necessary for good interaction between the strut and blade vortices to be achieved. Results from previous strut pitching studies investigated wake steering by pitching the upper and lower struts in the same direction [8] need to be reconsidered when combining blade and strut pitching.

While the lack of dissipation and diffusion in the current method tends to over-predict the power reduction in the wake of the turbine, combined with the fact that the inviscid approach does not include potential dynamic stall effects, the reported results reveal, for the first time, the potential of combining blade and strut pitching to achieve a higher wind-farm power density. In this respect, the present low-fidelity method can provide useful preliminary qualitative information about the vortical wake structure, but do not replace the usage of higher fidelity approaches to calculate the true benefits of blade and strut pitching in VAWTs, taking also into account wind shear, incoming turbulence from the atmospheric boundary layer, and ground effects.

References

[1] A. F. P. Ribeiro, C. S. Ferreira, and D. Casalino, *Vertical axis wind turbine wake steering by pitched struts and blades,* Journal of Physics: Conference Series **2767**, 092004 (2024).

[2] D. R. Houck, *Review of wake management techniques for wind turbines,* Wind Energy **25**, 195 (2022).

[3] B. LeBlanc and C. Ferreira, *Estimation of blade loads for a variable pitch vertical axis wind turbine from particle image velocimetry,* Wind Energy **25**, 313 (2022).

[4] M. Elkhoury, T. Kiwata, and E. Aoun, *Experimental and numerical investigation of a three-dimensional vertical-axis wind turbine with variable-pitch,* Journal of Wind Engineering and Industrial Aerodynamics **139**, 111 (2015).

[5] B. K. Kirke and B. Paillard, *Predicted and measured performance of a vertical axis wind turbine with passive variable pitch compared to fixed pitch,* Wind Engineering **41**, 74 (2017).

[6] B. Chen, S. Su, I. M. Viola, and C. A. Greated, *Numerical investigation of vertical-axis tidal turbines with sinusoidal pitching blades,* Ocean Engineering **155**, 75 (2018).

[7] M. Huang, *Wake and wind farm aerodynamics of vertical axis wind turbines*, Ph.D. thesis, Delft University of Technology (2023).

[8] V. Mendoza and A. Goude, *Improving farm efficiency of interacting vertical-axis wind turbines through wake deflection using pitched struts,* Wind Energy **22**, 538 (2019).

[9] A. F. P. Ribeiro, D. Casalino, and C. S. Ferreira, *Nonlinear inviscid aerodynamics of a wind turbine rotor in surge, sway, and yaw motions using a free-wake panel method,* Wind Energy Science **8**, 661 (2023).

[10] D. D. Tavernier, C. Ferreira, U. Paulsen, and H. Madsen, *The 3D effects of a vertical-axis wind turbine: rotor and wake induction,* Journal of Physics: Conference Series **1618**, 052040 (2020).

[11] A. F. P. Ribeiro, D. Casalino, and C. S. Ferreira, *Surging wind turbine simulations with a free wake panel method,* Journal of Physics: Conference Series **2265**, 042027 (2022).

7

Inviscid Free Wake Method for Propeller-Wing Interaction

If the only tool you have is a hammer,
it is tempting to treat everything
as if it were a nail.

Abraham H. Maslow

With distributed propulsion and electric vertical take-off and landing aircraft on the rise, fast and accurate methods to simulate propeller slipstreams and their interaction with aircraft components are needed. In this chapter, we compare results obtained with the panel method developed in the thesis to experimental and previously validated numerical data. In particular, we study a propeller-wing configuration at zero angle of attack and the aerodynamics of the blade-resolved slipstream interaction with the wing. We use a prescribed wake on the wing and a free wake on the propeller, which greatly accelerate the computations. Results indicate that, while forces are overpredicted due to the inviscid nature of the panel method, the free wake is able to capture the slipstream deformation and shearing with remarkable success. We find that a filament-based free wake panel method can be a useful tool for propeller-wing interaction in preliminary aircraft design.

Parts of this chapter have been published in Aerospace Science and Technology **144**, 103955 (2024) [1].

7.1. Introduction

Aircraft design is currently undergoing a paradigm shift. While most aircraft flying today follow the classic tube and wing concept, with wing or tail-mounted turbofans or front-mounted propellers, the vast majority of aircraft being designed are for the electric vertical take-off and landing (eVTOL) market, where configurations are more varied and less traditional. These configurations are blurring the lines between rotorcraft and aircraft, usually with several propellers that have slipstreams going over the wings, fuselage, and tail. For flight mechanics and noise, the trajectories of these slipstreams and their interactions with other rotating and non-rotating components are critical. In parallel, aircraft with distributed propulsion, where a large number of propellers are mounted on the wing, are also being designed and studied [2]. Such wings require a deeper integration of the propulsion and wing during design than traditional aircraft, as a much larger portion of the wing is inside slipstreams.

Many experimental studies are being conducted on propellers with a focus on eVTOL and distributed propulsion [3–6]. These help understand the physics involved in these new configurations, while providing validation data for numerical studies [7] using computational fluid dynamics (CFD), which can then be applied to aircraft design and analysis. An alternative to lattice-Boltzmann method (LBM) and Navier-Stokes simulations of these aircraft is to use vortex methods [8], which allow for blade resolved simulations of propellers, wings, and their wakes. With the complex physics of slipstream-wing interaction, some research is being done on using the vortex particle method approach to the wakes [9, 10]. These methods can accurately predict many physical aspects of wakes, including leapfrogging and vortex breakup [11].

A more traditional approach to simulating wakes in potential flow is to use panel-based or filament-based wakes [12]. Such approach is less accurate than particle-based methods for wake-body interactions, but it is also simpler to implement and requires fewer equations to be solved. Filament-based wakes have been heavily used over the past 60 years to simulate steady cases for aircraft [13] and unsteady cases for rotorcraft [14–17]. However, their use for complex eVTOL configurations has been more limited [18]. In particular, studies verifying the feasibility of this method for propeller-wing interactions are not common and, to the authors knowledge, no detailed attempt at validating these methods with experimental data on slipstream deformation has been made.

In this work, we make use of experimental [6] and validated high-fidelity simulation data [7] (detailed in Chapter 11) of a propeller-wing interaction case to investigate the potential use of a filament-based free wake panel method for preliminary design of aircraft with complex slipstream interactions. We use an inviscid panel method to model the wing and propeller surfaces directly. Our focus is on understanding the accuracy of such a method and its limitations in assessing the aerodynamic characteristics of propeller-wing configurations.

7.2. Test Case Description

The geometry used in this work is a straight wing based on the NLF-Mod22(B) airfoil [19], with a nested chord $c = 300$ mm, a span of 1.248 m. We focus on results at an angle of attack of $0°$ and nested flap (i.e. the flap is not deployed). The wing is equipped with a TUD-XPROP-S reference propeller [5, 20], with 6 blades, diameter $D = 203.2$ mm, and a blade pitch at 70% of the radius of $30°$. The propeller is installed 173.5 mm ($\approx 0.858D$) ahead of the leading-edge, with the axis of rotation angled $5°$ with respect to the wing chord line. The flow conditions are freestream velocity $U_\infty = 30$ m/s, resulting in a wing chord Reynolds number $Re \approx 600{,}000$, a freestream Mach number $M \approx 0.09$, and a propeller advance ratio of $J = U_\infty/(Dn) = 0.8$, where n is the rotational speed in rotations per second. A view of the geometry is shown in Fig. 7.1, where the planes where surface pressure were measured are also highlighted.

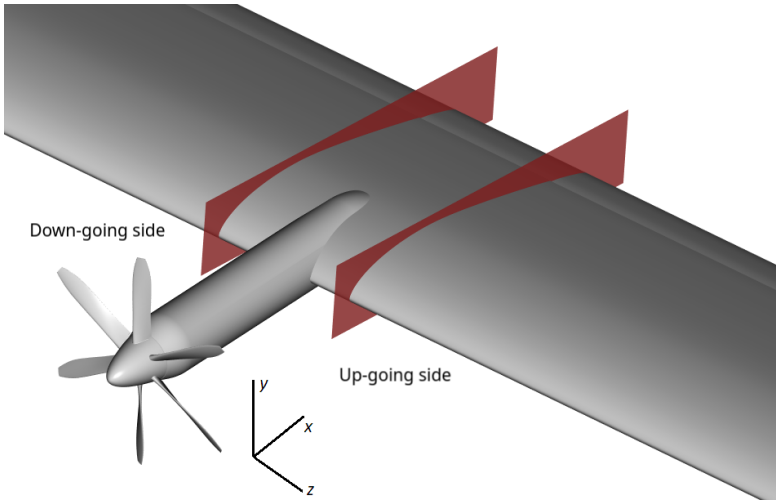

Figure 7.1: Geometry of the simulated propeller and wing. Red planes are where surface pressure was measured. Up and down-going refer to the direction of the propeller rotation. Coordinate system used throughout the work also shown.

7.2.1. Numerical Setup - Lattice-Boltzmann

Simulations are run with PowerFLOW 6-2021-R7, using the subsonic isothermal solver, as the blade tip Mach number due to the propeller rotation is 0.35. A Cartesian mesh is used, with cubic cells ranging from 0.03 mm on the propeller blades leading-edges to 61 mm far from the wing. An average y^+ of 40 was used on the wing, which is compatible with the wall function used. The simulations are similar in setup to previous works on wing sections [21, 22]. The wind tunnel walls are included to account for blockage effects, but are simulated as free slip walls. The surfaces of the propeller and wing are modelled as fully turbulent. The boundary conditions used in the upstream and downwind faces of the numerical wind tunnel

are a velocity inlet and a pressure outlet, respectively. More details on the setup can be found in [7], where a resolution study and validation with experimental data are available.

7.2.2. Numerical Setup - Free Wake Panel Method

The panel code used in this work can handle surface meshes composed of triangles and quads, which means that including the propeller nacelle, boom, and pylon is not difficult. However, as this study focuses on using this method for preliminary design, we remove these components for simplicity and simulate floating blades spinning in front of the wing. This is common practice for vortex lattice methods [23], due to limitations of such methods, but also for panel codes [18] for simplicity. This is illustrated in Fig. 7.2, where the detailed geometry used in the LBM simulation is compared to the surface mesh used by the panel method.

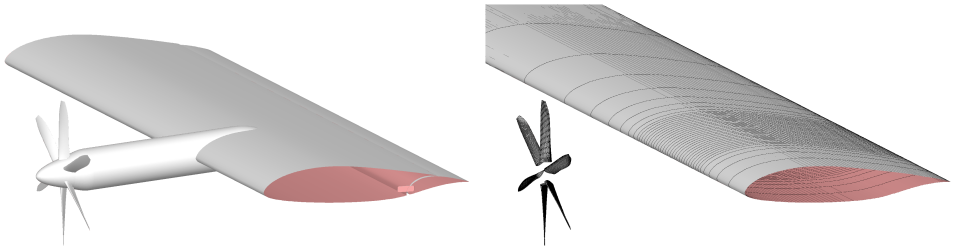

(a) Geometry used in LBM simulation. (b) Surface panels used in the free wake simulations.

Figure 7.2: Geometries used for the two numerical methods. Clip plane present on the port side, to visualize the flap gap and bracket on the LBM model.

The wing itself is also simplified for the panel code, with the removal of the gap between the main element and the flap, along with the flap brackets. Another simplification is that in the free wake formulation used here, trailing-edges must be sharp. Hence, sharp trailing-edges were used on the wing and blades. Finally, we changed the wing aspect ratio from about 4 to nearly 15. This was done because in the LBM simulations free slip boundary conditions were used on the sides of the numerical domain, which can be done with the panel method with symmetry conditions [12], but would add to the cost without substantially affecting the results. Hence, we simply extend the wing span to avoid strong effects from the tip vortices. As shown in Section 7.4.3, the outboard pressure distribution using both methods is very similar, indicating the different approaches to the wing tip are equivalent.

The wing is discretized with 150 panels along the chord with cosine spacing and 50 panels along span, with a spanwise spacing of about $c/40$ in slipstream, growing with a geometric progression to over $2c$ at the edges. The blades are discretized with 100 panels along chord with cosine spacing and 50 panels along the span, with constant spacing. The timestep was chosen to achieve a propeller rotation between 2.5 and $20°$ per timestep. The space and time discretizations were selected based on previous experience with the code [24, 25], while attempting to keep simulation

costs compatible with preliminary design, with the finer mesh on the wing chord (compared to the blades) being selected due to the wing leading-edge interaction with the propeller wake.

The vortex core model used an initial vortex age of $1/12n$, where n is the propeller rotation frequency. This corresponds to a vortex core radius of 0.45 mm at the propeller trailing-edge, or about 3% of the blade chord. As the propeller wake develops and the vortex cores grow, the vortex core radius of the filaments coming from the propeller are about 1.5 mm as they reach the wing trailing-edge. The standard constants described in the original article for the vortex core model were used [26].

7.3. Discretization Effects on Isolated Components

7.3.1. Wing Wake

The timestep used in the free wake simulations is directly linked to the number of wake panels that must be calculated during the simulation. Every timestep a new row of wake panels is added to the wing and propeller blades. The timestep required for simulating a wing can be quite large, typically several times larger than a flow pass $t_w = c/U_\infty$, while rotors cannot have timesteps that would lead to corresponding azimuthal rotations $\Delta\psi$ that are excessive. Hence, we have a conflict between the propeller rotation period $t_p = 1/n$ and t_w. In the case of the present simulations, to achieve a $\Delta\psi$ of about $20°$, we require the timestep to correspond to $t_w/33$.

For the forces on the wing to converge to a steady state solution, the startup vortex (i.e., the last filament in the wake) needs to convect to a large distance, $O(10c)$ or even $O(100c)$. This means that the simulation with the propeller resolved at $\Delta\psi = 20°$ requires hundreds of timesteps, increasing the cost dramatically, as calculating the wake self induction is an N^2 problem.

A different issue with the wake that appeared in our simulations was due to the far wake formulation. In order for the propeller wake panels to switch to the far wake formulation before impinging on the wing leading-edge, we start using such formulation after about $\Delta\psi = 200°$, or 10 wake rows when $\Delta\psi = 20°$. From the blade airfoil sections point of view, this is a substantial distance, but from the wing point of view, this means the far wake formulation starts on the wing wake after a distance of about $c/3$. Hence, the wing far wake formulation starts close to its trailing-edge, leading to inaccurate results.

One possible solution to the problem of the far wake formulation being used too close to the wing trailing-edge would be to change the code to allow for different wakes to use different formulations, i.e. using the far wake formulation on the propeller only. This would solve this problem, but would still leave us with the issue of the long time required to converge the forces on the wings.

Hence, we use a different approach that solves both problems concurrently: we employ a prescribed wake for the wing and a free wake for the propeller. Wake panels on the wing still appear at every timestep, but they are forced to be aligned with the freestream and are stretched to an arbitrary length of 1 m. This is done

for all wake panels, regardless of the formulation (see Fig. 2.6).Hence, the wing wake quickly becomes very long, moving the startup vortex away, while also making the far wake formulation only take place after a distance of more than $30c$. The assumptions here are that the wing is converging to a steady circulation, meaning the unsteady effects of vortex strengths being created at the trailing-edge are negligible. This was verified with a purely free wake simulation, where we observe that at the wing tips the wing circulation is converging to steady results and behind the propeller the fluctuations in circulation are around $\pm 1\%$.

The impact of the distance between the start of the far wake and the wing trailing-edge (fw_s), the timestep (Δt), and the use of the prescribed wake on the lift coefficient ($C_L = F_y/(q_\infty cS)$, where F_Y is the force in the vertical direction, $q_\infty = 0.5\rho_\infty U_\infty^2$ is the freestream dynamic pressure, ρ_∞ is the freestream air density, and S is the wing span) are shown in Fig. 7.3. The blue, orange, and green lines show that reducing fw_s can have an effect on C_L, as when $fw_s = 3c$, C_L is reduced by a small amount (about 0.2%), while the effect at $fw_s = 1c$ is about four times larger. As mentioned previously, with the propeller in place, $fw_s = c/3$, which would lead to even larger errors. We can also see in Fig. 7.3 the effect of increasing Δt, by comparing the blue and purple lines. An increased timestep is very advantageous for the computational cost, as we can observe much fewer iterations are needed for C_L to stabilize when a larger timestep is used. Finally, the prescribed wake results are also shown, in gold. While the results do not match the blue and purple lines perfectly, the difference is small (again about 0.2%), and the number of iterations required to reach convergence is similar to using a large timestep. Hence, the prescribed wake for the wing is the approach we choose for the simulations in this work, solving the problems of the near wake effects and the slow convergence due to the small timestep required by the propeller concurrently.

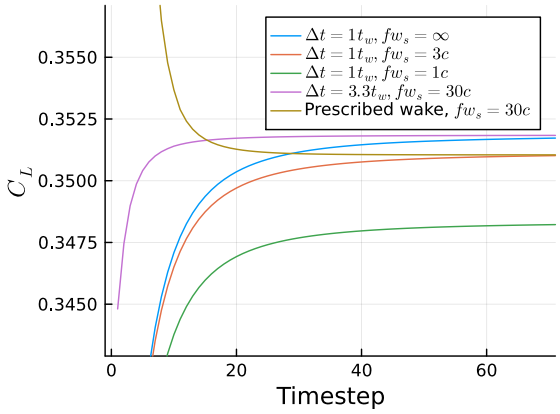

Figure 7.3: Effect of far wake start distance, timestep length, and prescribed wake on the lift coefficient of the standalone wing.

7.3.2. Propeller Wake

As mentioned before, the timestep for the propeller is more stringent than that of the wing and ultimately drives the simulation cost. Here, we simulate the isolated propeller aligned with the freestream, which can be done with six-fold axisymmetry, meaning we only simulate one blade. We measure the thrust coefficient $T_c = T/(q_\infty A)$ and the torque coefficient $Q_c = Q/(q_\infty AR)$, where T is the thrust acting on the propeller, Q is the torque, $R = D/2$ is the propeller radius, and $A = \pi R^2$ is the propeller disk area. These coefficients can be compared with experimental values [5].

Results for the propeller are shown in Fig. 7.4. The timestep varies to obtain $\Delta\psi$ between 2.5 and $20°$. The time is normalized in flow passes over the wing (which is not included here, but will be included later and understanding how many flow passes we need is important to estimate the cost of the simulations) and simulations are run for two flow passes, or 3.7 propeller rotations. The fact that the propeller forces converge in few flow passes is encouraging, regarding the convergence of the propeller-wing assembly, as it is an indicator that simulations will not have to run for a very long time. Two flow passes is nearly 70 timesteps for $\Delta\psi = 20°$, which, as shown in Fig. 7.3, is enough for the isolated wing to converge as well. The blue and orange lines indicate that the far wake formulation works well for the propeller, as using it causes marginal changes in the thrust and torque. A grid convergent behavior can be seen for T_c and Q_c, with differences between the simulations becoming smaller as the timestep is decreased. The differences between $\Delta\psi = 5$ and $2.5°$ are under 0.5% and, hence, we consider $\Delta\psi = 5°$ a converged result. While T_c nearly matches experimental results for $\Delta\psi \leq 5°$, Q_c is about 5% lower than the experiments for the same simulations, which is not surprising given that very accurate torque predictions require accurate sectional drag values, which the current inviscid method cannot achieve. Overall, we consider these results satisfactory for preliminary design.

7.4. Propeller-Wing Simulations Results

7.4.1. Convergence

Figure 7.5 shows the convergence of the total streamwise (F_x) and vertical (F_y) forces acting on the propeller-wing assembly, for each of the previously used values of $\Delta\psi$. Simulations use a prescribed wing wake unless stated otherwise. The prescribed wake on the wing leads to a fast and consistent force convergence of F_y, which is a major advantage over a full free wake approach. The timestep effects on F_x are very similar to the isolated propeller results, with $\Delta\psi = 5°$ appearing sufficient for grid convergence, from a mean force perspective. As $\Delta\psi$ is reduced, the unsteady effects of the propeller wake on the wing start becoming more apparent and higher frequencies are captured in the forces. After around 2 flow passes over the wing (which again, corresponds to 3.7 propeller rotations), the forces are statistically converged, whereas the full free wake approach requires about 25 flow passes. The peak in forces around $tU_\infty/c = 0.3$ corresponds to the propeller wake first reaching the wing leading-edge.

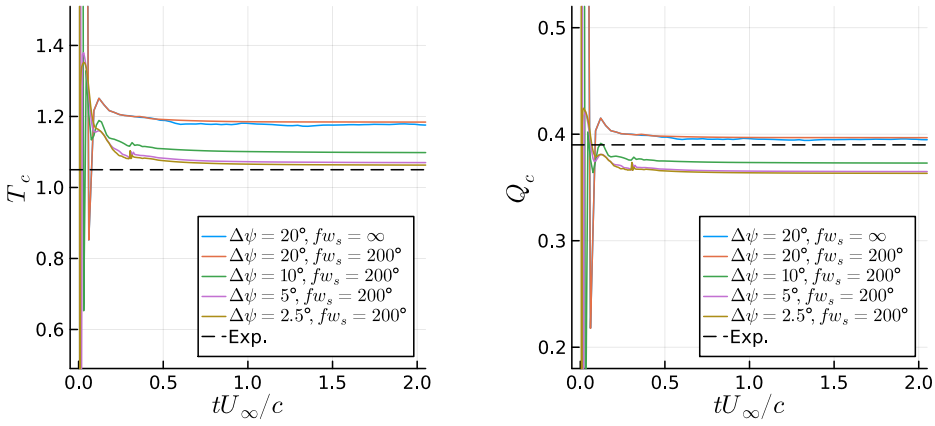

(a) Thrust coefficient.

(b) Torque coefficient.

Figure 7.4: Time history of integral coefficients of the isolated propeller. Far wake and timestep effects.

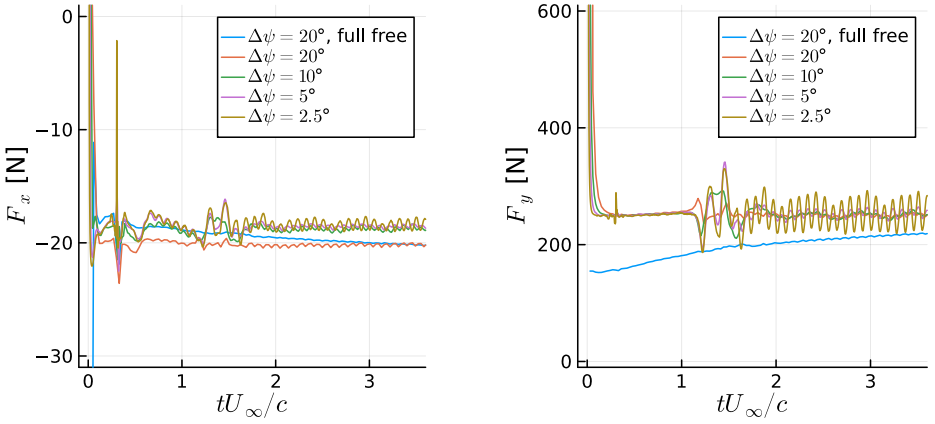

(a) Streamwise force component.

(b) Vertical force component.

Figure 7.5: Time history of forces on wing-propeller assembly. Perscribed wing wake and timestep effects.

Figure 7.6 illustrates the difference between the two wing wake approaches. On the left side, the full free wake approach is used and we can observe that all 200 rows of wake panels are very close together and still near the wing trailing-edge. On the right side, we see the prescribed wake approach on the wing combined with the free wake approach on the propeller. This forces the wing wake to move far from the trailing-edges very quickly, while still having a high resolution on the propeller, which as seen in Fig. 7.4, is necessary. Unless stated otherwise, for the

remainder of this work "free wake simulations" refer to the mixed wake approach, with prescribed wing wake and free propeller wake.

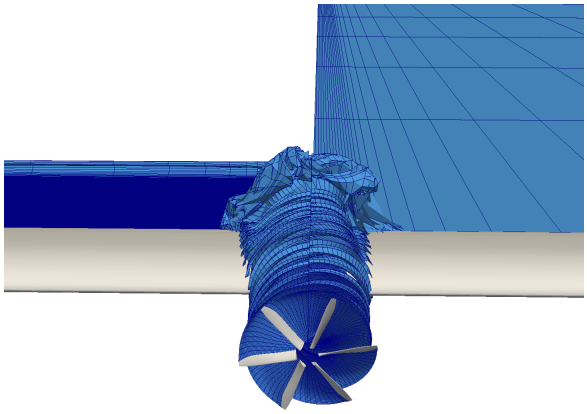

Figure 7.6: Different wake approaches used in this work. Full free wake approach on the left, prescribed wake on the wing and free wake on the propeller on the right. Results after 200 timesteps, with $\Delta\psi = 5°$.

7.4.2. Force Development

Here, we focus on the forces acting on the wing sections along the span. Early XFOIL [27] simulations showed that the aerodynamic forces on the NLF-Mod22(B) airfoil are very sensitive to viscosity. For example, C_L in inviscid mode was nearly 70% higher than the one computed in viscous mode. Hence, we can expect that forces acting on the wing according to the inviscid free wake simulations are different from the LBM simulations. However, it would be useful if the effect of the propeller on the wing is captured in spite of these differences.

We take spanwise sections of 16 mm from both the LBM and free wake simulations. Here we focus on $\Delta\psi = 5°$, as these are considered converged results, based on Section 7.4.1. The lift, drag ($C_D = F_x/(q_\infty cS)$), and pitching moment ($C_m = M/(q_\infty cSc)$, where M is the moment around the spanwise direction at the quarter chord location, with a positive value meaning nose up) coefficients along the wing span are shown in Fig. 7.7, where the forces and moments acting on the propeller are removed. Note that the LBM forces include the nacelle. For the results in this section, the reference span S is changed to the corresponding fraction of the wing span (16 mm), so that the development plots show quasi 2D results for each spanwise position. The orange and green lines show two possible approaches for correcting the inviscid data: shifting or scaling the curves. The values used for shifting and scaling are shown on the plots. For C_L, shifting the forces provides good agreement, but an overshoot of about 10% in the peak value, while scaling the forces make them match LBM data fairly well, with the down-going side (negative z) showing more discrepancies. For C_D both approaches are mostly inaccurate, due to the viscosity playing a large role in drag, i.e., as expected, drag forces obtained from an inviscid approach cannot be relied on. Shifting or scaling C_m seem

to produce reasonably good results on the down-going side ($z<0$), but the trends on the up-going side are not captured.

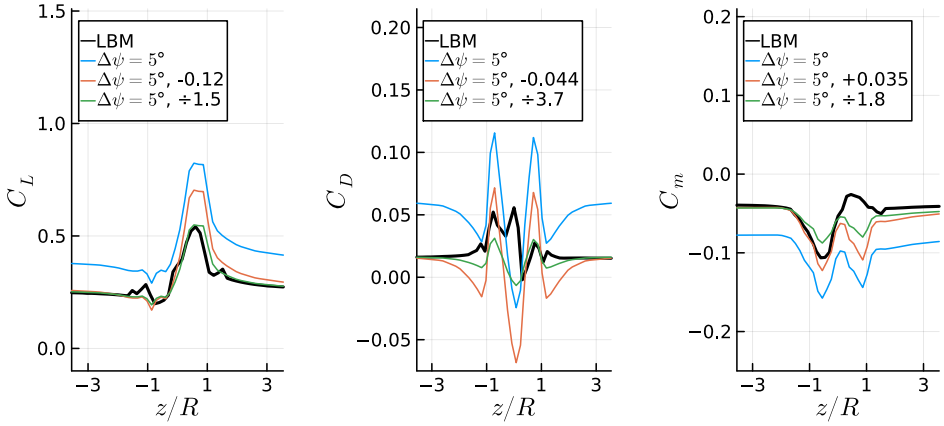

(a) Lift coefficient. (b) Drag coefficient. (c) Pitching moment coefficient.

Figure 7.7: Wing force development along the span.

7

7.4.3. Pressure Distribution

Pressure coefficient $Cp = (p - p_\infty)/q_\infty$, where p is the static pressure and p_∞ is the freestream static pressure, is computed on two planes on each side (up-going and down-going) of the propeller axis, at 70% of the propeller radius (71.12 mm), as shown in Fig. 7.1. Pressure at these locations is available in the experimental data. We also select a plane further away from the slipstream, at $z/R = 3$, which is mostly outside of the effect of the slipstream as seen in Fig. 7.7. This plane serves to examine how the flow around the wing behaves without strong slipstream effects. The results are shown in Fig. 7.8.

We first focus on the Cp cut outside of the slipstream in Fig. 7.8a. Viscous and inviscid XFOIL results of the isolated wing section are also included. The XFOIL results assume no propeller effects. The viscous XFOIL results are very close to the LBM results, while the inviscid XFOIL data are very close to the free wake results, indicating that the small differences between the LBM and free wake simulations are mostly due to viscous boundary layer effects, in this plane. The viscous effects reduce the suction in the first three quarters of the chord and decrease the trailing edge pressure. The bump in the panel methods results near $x/c = 0.85$ is due to a discontinuity in the surface tangent on the suction side where the main element ends and the flap begins. The LBM simulation includes the actual flap gap, leading to a discontinuity in Cp. A similar effect appears in smaller magnitude on the pressure side near $x/c = 0.7$, where the pressure side flap gap is.

In the presence of the slipstream, in Figs. 7.8b and 7.8c, the results are qualitatively similar to the references, but as in Fig. 7.8a the trailing edge pressure is lower when viscosity is present. Over the entire airfoil, the slipstream seems to create

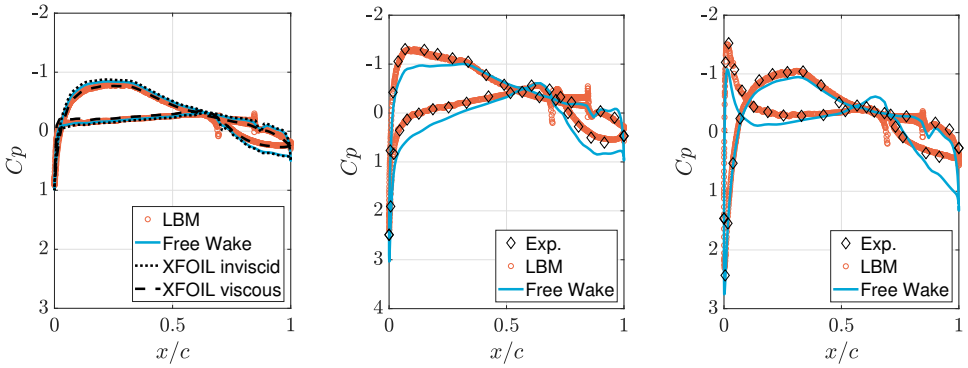

(a) Outside of slipstream (b) Up-going side (c) Down-going side

Figure 7.8: Pressure coefficient along the wing chord.

more differences between the viscous and inviscid results. This is partially due to the propeller producing more thrust with the panel method, leading to higher total pressure and different wing section angle of attack. Another possible reason for the discrepancies is that the slipstream shearing is imperfect when using filament-based free wakes. We investigate this in Fig. 7.9, where we compare the experimental and LBM results at $z/R = \pm 0.7R$ to results obtained from the free wake simulations at $z/R = \pm 0.5R$. The agreement is excellent, indicating that the free wake-based slipstream has weaker shearing than in reality, which will be investigated more in Section 7.4.5.

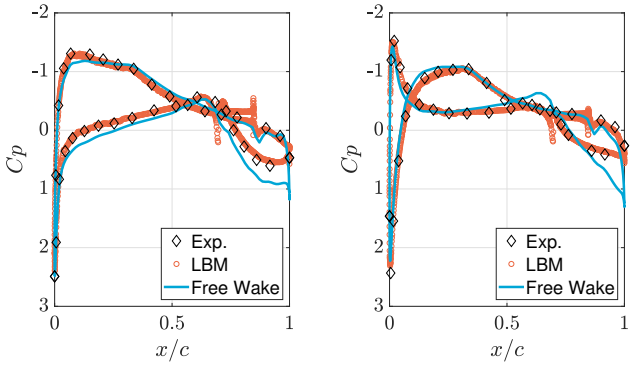

(a) Up-going side (b) Down-going side

Figure 7.9: Pressure coefficient along the wing chord. Experiments and LBM at $\pm 0.7R$ of the center axis, results using the free wake approach at $\pm 0.5R$.

7.4.4. Forces

We now look at the integrated forces on the propeller and wing in a quantitative manner. Table 7.1 shows the propeller thrust coefficient, and the lift, drag, and

moment coefficients integrated over the wing. We compare the results obtained with the panel method (using $\Delta\psi = 5°$) with the LBM simulations and experiments. Integrated forces on the wings were not available from experiments. The wing forces are computed over an arbitrary span of 0.4 m, or about twice the propeller diameter.

Table 7.1: Propeller thrust coefficient, along with 0.4 m span drag, lift, and moment coefficients.

	Exp.	LBM	Free Wake
T_c	1.05	1.04	1.10
C_D	-	0.025	0.054
C_L	-	0.32	0.41
C_m	-	-0.056	-0.078

The free wake results for T_c are less comparable to the reference values than they were for the case of the isolated propeller. The propeller is tilted with regards to the incoming free stream, which could lead to higher angles of attack along the blades, which tend to generate excess sectional lift with inviscid methods. The differences between the forces are substantial, as expected, due the the large differences between viscous and inviscid XFOIL results for this wing. Hence, for practical use in preliminary design, corrections are needed.

7.4.5. Slipstream Deformation

The previous sections showed some of the limitations of the inviscid free wake approach for forces and pressure on the wing and propeller. Away from the body, the viscous effects are expected to be smaller and the free wake approach is likely to be more accurate. The experimental campaign conducted for this propeller-wing configuration only included a total pressure plane at a distance of c downstream of the wing trailing-edge. In order to validate the free-wake method, including slipstream-wing interaction, we use the LBM results on planes at various streamwise locations. These planes are illustrated in Fig. 7.10.

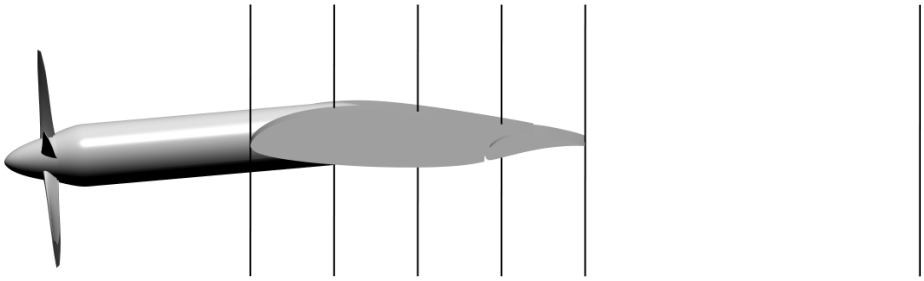

Figure 7.10: Planes used throughout this section at $x/c = [0, 0.25, 0.5, 0.75, 1, 2]$.

In Fig. 7.11 and 7.12 we compare the numerical results for the planes shown in Fig. 7.10. In this section, we use $\Delta\psi = 2.5°$ to achieve maximum detail in the figures, although $\Delta\psi = 5°$ results are very similar. The figures show instantaneous (i.e., not

time-averaged) velocity magnitude. At $x/c = 0.00$, we see very good agreement of the slipstream and stagnation region near the wing leading-edge. The main difference that can be observed in this and all subsequent planes is that the LBM results have sharper gradients, while the free wake results are more smeared. This is expected, as the LBM simulations are using a scale-resolving scheme, with a very fine space and time discretization, able to capture more complex and smaller flow structures than a free wake method.

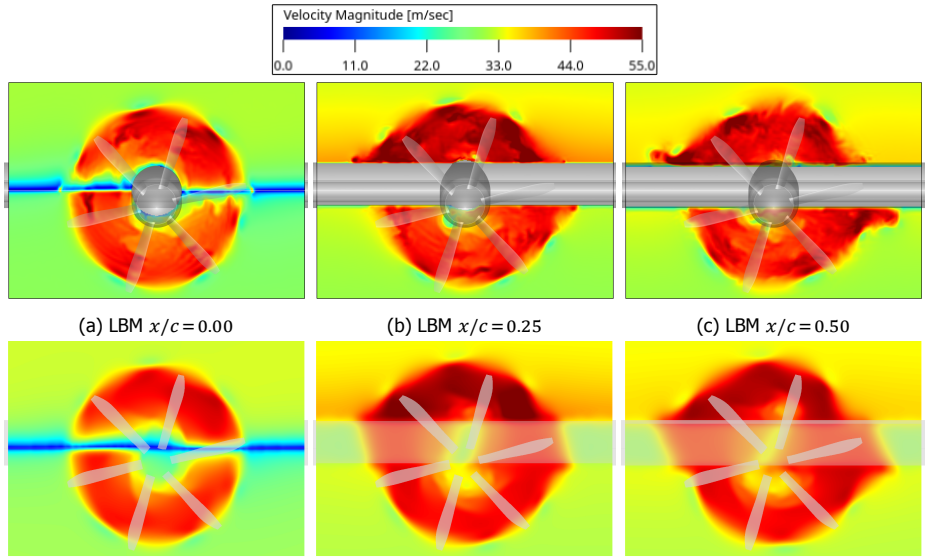

(a) LBM $x/c = 0.00$ (b) LBM $x/c = 0.25$ (c) LBM $x/c = 0.50$

(d) Free wake $x/c = 0.00$ (e) Free wake $x/c = 0.25$ (f) Free wake $x/c = 0.50$

Figure 7.11: Velocity magnitude on planes along the slipstream. First half of the wing. Results using $\Delta\psi = 2.5°$.

As we move to $x/c = 0.25$, it is apparent that the free wake simulations create a velocity field inside the wing, which is not physically meaningful, but allows us to see an artefact of this method. Inside solid bodies, the flow velocity should be equal to the freestream in the formulation we use [28], but here the filaments from the propeller wake are crossing through the wing, inducing a velocity field. In order to correct for this, one would need to disable the filaments inside the bodies or cut the filaments as they pass over the wing. This would add cost and complexity to the code and could be implemented in the near future.

At $x/c = 0.50$ and $x/c = 0.75$, we see secondary flow structures forming on the far left and right sides, on the suction and pressure sides of the wing, respectively. Remarkably, the free wake is able to reproduce these flow structures to some extent. Even at $x/c \geq 1.00$ the shearing of the slipstream seems to be captured very well by the free wake simulations, in spite of the presence of the wing wake in this region, which is prescribed as flat. This indicates that the motion of the wing wake is not playing a large role in the near wake deformation. We can also observe that the geometry simplifications in the free wake simulations did not introduce

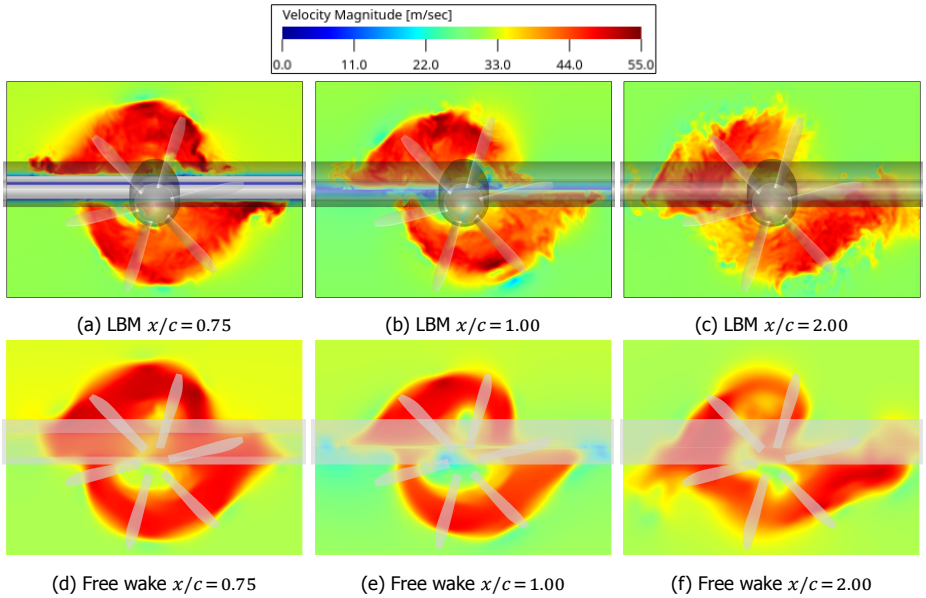

(a) LBM $x/c = 0.75$ (b) LBM $x/c = 1.00$ (c) LBM $x/c = 2.00$

(d) Free wake $x/c = 0.75$ (e) Free wake $x/c = 1.00$ (f) Free wake $x/c = 2.00$

Figure 7.12: Velocity magnitude on planes along the slipstream. Second half of the wing and downstream plane. Results using $\Delta\psi = 2.5°$.

major differences. Overall, the agreement between the free wake and LBM results is remarkable, both from a qualitative (shape of the slipstream) and quantitative (colors in the figures) point of view.

The 3D features of the slipstream are shown in Fig. 7.13. The breakup of the tip vortices in the LBM simulation can be seen at the top left of the image. The secondary vortical structure, where the slipstream edge touches the suction side of the wing, previously shown in the planes, can be seen in both simulations, with good agreement between them. The slipstream filaments from the free wake penetrating the wing can also be observed. Finally, the deformation of the tip vortices as they reach the wing leading-edge can also be seen in both simulations, although this deformation is more pronounced in LBM, as the free wake penetrates through the wing.

A close-up of the interaction between the propeller slipstream and wing leading-edge is shown in Fig. 7.14. In the free wake simulations, the velocity field induced by the wake filaments contributes to the sources on the wing surface, which attempt to enforce impermeability. However, in spite of the wake accumulating in front of the wing leading-edge at first, the finite timestep allows for filaments perpendicular to the wing to penetrate it. These filaments are highly stretched, as the wing sources attempt to push the wake nodes near the surface away from it, keeping most filaments parallel to the surface outside. The LBM results show that as impermeability is enforced, the tip vortices become extremely stretched over the leading-edge. In both cases, we can see the tip vortices lagging behind near center of the suction side of the wing, meaning this effect is due to the leading-edge

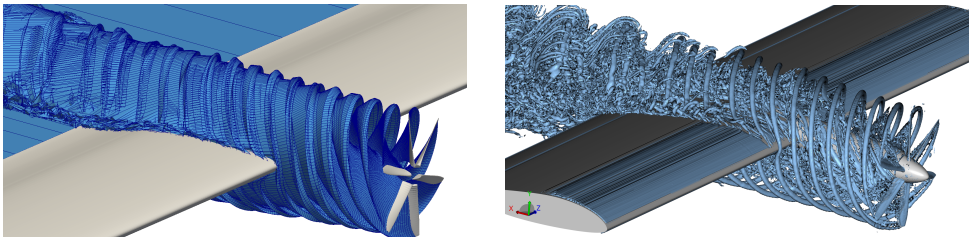

(a) Free wake results.

(b) LBM results. Isosurfaces of $\lambda_2 = -50U_\infty^2/c^2$.

Figure 7.13: Visualisation of the slipstream deformation as it moves along the wing.

interaction with the vortices, not a viscous effect in the boundary layer. Inside the slipstream, we can also observe more complex 3D flow structures that form concentric cylinders around the propeller axis for both simulations. Again the similarities are remarkable. The most apparent shortcoming of the free wake simulation is the lack of vortex break-up, which is evident in the LBM results. The geometry simplifications clearly have some effect in the wakes of the blades roots, yet we believe a detailed design of the nacelle would require viscous effects to be accounted for and hence do not focus on this here.

7.4.6. Computational Cost

The cost of each simulation used in this work is summarized in Table 7.2. Simulating of the wing by itself is very quick, as large timesteps or a prescribed wake can be used. The isolated propeller benefits tremendously from the axisymmetry of the problem, with only one blade and its wake requiring real panels, with the other five being represented by virtual panels [12]. The propeller-wing assembly requires more time, especially given the relatively small timestep needed for convergence results. However, the time of 8 hours, which corresponds to 160 CPU hours is orders of magnitude lower than the time required for an unsteady CFD simulation, which in the case of the LBM simulation referenced in this work cost $O(10000)$ CPU hours.

Table 7.2: Approximate time required to perform each simulation on a desktop computer with 20 CPU cores and a GPU with 8 GB VRAM.

Case	Time	Notes
Wing	2 minutes	Prescribed wake or large timestep
Propeller	30 minutes	Axisymmetric, $\Delta\psi = 5°$
Propeller + Wing	8 hours	Mixed wake approach, $\Delta\psi = 5°$

The times reported here can be reduced further in a number of ways. The setup can be optimized, to try to minimize the number of panels used in the simulations. Further code optimization can be done to accelerate the computations. An obvious potential improvement is to skip the calculation of the flow velocity at all the wake points where the wake is prescribed, which was not done in this work. Finally, more parts of the code could be performed on the GPU, as for the current simulations,

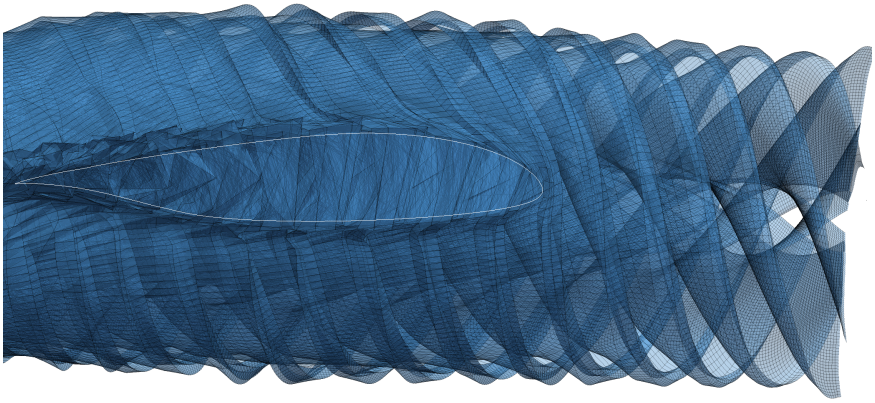

(a) Free wake results. Wake filaments penetrating through wing.

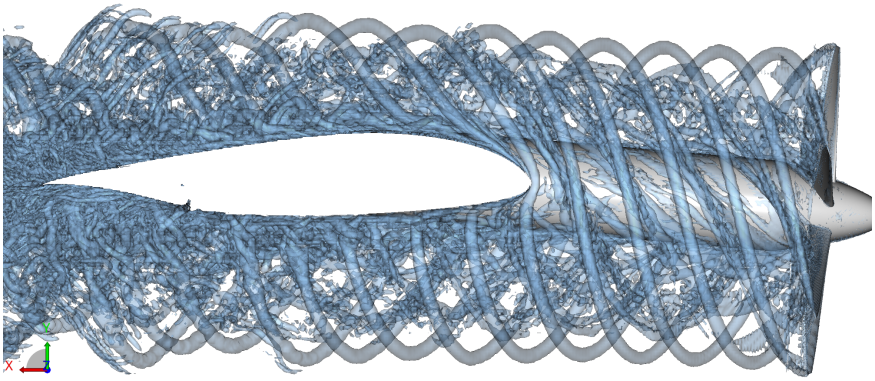

(b) LBM results. Isosurfaces of $\lambda_2 = -50U_\infty^2/c^2$.

Figure 7.14: Close-up view of slipstream going over the wing leading-edge. Wakes are shown with transparency, in order to see inside the slipstream.

only the computation of the wake velocities was performed on the GPU, as the linear system solution exceeded the GPU memory and other parts of the code were only written for CPUs.

7.5. Conclusions and Outlook

In this work we employed lattice-Boltzmann simulations that were previously validated with experiments to evaluate the feasibility of using a filament-based free wake panel method for preliminary design of propeller-wing configurations. The experimental data was limited to a few flow properties in certain locations and therefore the lattice-Boltzmann solution allowed for a detailed validation of the free

wake simulations.

A mixed prescribed-free wake approach is used, with the wing wake being prescribed and the propeller wake free. This allowed for convecting the startup vortex away from the wing in few iterations, while keeping a small enough timestep to accurately model the propeller, and avoided issues with using the far wake formulation near the wing trailing-edge. Such mixed approach would have issues in a pusher configuration, but with a traditional upstream propeller, it was shown to be adequate, while changing the wing lift by less than 0.2%.

On the isolated propeller, the thrust obtained by the free wake simulations matched experimental data very well, while torque was not as accurate. This is expected, standing the inviscid nature of the free wake panel methodology, and has been seen before in wind turbines [25].

The force development on the wing showed that with a simple scaling of the forces, lift changes caused by the slipstream were well captured , while the pitching moment was less accurate and drag was inaccurate, as expected from an inviscid approach. Interestingly, the value for scaling the lift was selected to match the lift outside the slipstream and it seemed valid inside the slipstream as well. This means that a simple 2D XFOIL simulation can be used to estimate the scaling factor. The extend of the applicability of such scaling would need to be verified in a future study with more reference data. Such empirical scaling affects the reliability of such a method as a predictive tool, but is standard practice in aircraft design.

The pressure distribution showed that the small differences in viscous and inviscid isolated airfoil simulations become much larger in the presence of the slipstream, partially due to inaccuracies in angle of attack and flow velocity, but also because of underprediction of the slipstream shearing. Comparing the free wake pressure distribution closer to the propeller axis to reference data further away from the propeller axis led to very similar results. This means the free wake results need to be used with care, as relying on sectional forces without applying some sort of correction can lead to very overpredicted forces.

The propeller slipstream deformation as it travelled over the wing was remarkably similar to the reference simulations. There will always be differences when comparing to a scale-resolved simulation, with results appearing more smeared, but these wakes are relatively difficult and expensive to obtain with CFD. This could be the main use of a free wake method for eVTOL design: predicting and understanding wake interactions in complex configurations. The main shortcoming of the filament-based free wake approach here is the lack of vortex break-up and the upper and lower slipstreams always being connected, which is likely linked to the underprediction of the slipstream shearing.

The time required for the simulation of the propeller-wing assembly was two orders of magnitude faster than LBM, which could be suitable for preliminary design, but future work can be applied to accelerating the simulations further.

We believe that this work demonstrates that filament-based free wake panel code simulations are indeed able to provide some value in preliminary design phases of aircraft with propellers. There are severe limitations linked to the inviscid approach used in this work, but the method is also able to capture very complex flow

physics which are generally difficult to capture. Future work can focus on extending the validation of the method, to verify the possibility of using simple corrections to account for viscous effects. More complex configurations can also be studied, such as multiple propellers, stability and control, as well as aeroelastic and aeroacoustic simulations.

References

[1] A. F. P. Ribeiro, C. Ferreira, and D. Casalino, *On the use of filament-based free wake panel methods for preliminary design of propeller-wing configurations,* Aerospace Science and Technology **144**, 108775 (2024).

[2] K. A. Deere, J. K. Viken, S. Viken, M. B. Carter, M. Wiese, and N. Farr, *Computational analysis of a wing designed for the X-57 distributed electric propulsion aircraft,* in *35th AIAA Applied Aerodynamics Conference* (2017).

[3] T. Sinnige, R. Nederlof, and N. van Arnhem, *Aerodynamic performance of wingtip-mounted propellers in tractor and pusher configuration,* in *AIAA AVIATION FORUM* (2021).

[4] T. C. A. Stokkermans, D. Usai, T. Sinnige, and L. L. M. Veldhuis, *Aerodynamic interaction effects between propellers in typical evtol vehicle configurations,* Journal of Aircraft **58**, 815 (2021).

[5] R. de Vries, N. van Arnhem, T. Sinnige, R. Vos, and L. L. Veldhuis, *Aerodynamic interaction between propellers of a distributed-propulsion system in forward flight,* Aerospace Science and Technology **118**, 107009 (2021).

[6] R. R. Duivenvoorden, N. Suard, T. Sinnige, and L. L. M. Veldhuis, *Experimental investigation of aerodynamic interactions of a wing with deployed fowler flap under influence of a propeller slipstream,* (2022).

[7] A. F. P. Ribeiro, R. Duivenvoorden, and D. Martins, *High-fidelity simulations of propeller-wing interactions in high-lift conditions,* in *AIAA AVIATION Forum* (2023).

[8] E. Branlard, *Wind Turbine Aerodynamics and Vorticity-Based Methods*, 1st ed., Research Topics in Wind Energy (Springer, 2017).

[9] M. Tugnoli, D. Montagnani, M. Syal, G. Droandi, and A. Zanotti, *Mid-fidelity approach to aerodynamic simulations of unconventional VTOL aircraft configurations,* Aerospace Science and Technology **115**, 106804 (2021).

[10] E. J. Alvarez and A. Ning, *Modeling multirotor aerodynamic interactions through the vortex particle method,* in *AIAA Aviation Forum* (2019).

[11] E. J. Alvarez and A. Ning, *High-fidelity modeling of multirotor aerodynamic interactions for aircraft design,* AIAA Journal **58**, 4385 (2020).

[12] J. Katz and A. Plotkin, *Low-Speed Aerodynamics*, 2nd ed., Cambridge Aerospace Series (Cambridge University Press, 2001).

[13] J. L. Hess, *Panel methods in computational fluid dynamics,* Annual Review of Fluid Mechanics **22**, 255 (1990).

[14] W. Johnson, *Influence of wake models on calculated tiltrotor aerodynamics,* American Helicopter Society Aerodynamics, Acoustics, and Test and Evaluation Technical Specialists' Meeting (2002).

[15] M. Gennaretti and G. Bernardini, *Novel boundary integral formulation for blade-vortex interaction aerodynamics of helicopter rotors,* AIAA Journal **45**, 1169 (2007).

[16] G. Bernardini, J. Serafini, M. Molica Colella, and M. Gennaretti, *Analysis of a structural-aerodynamic fully-coupled formulation for aeroelastic response of rotorcraft,* Aerospace Science and Technology **29**, 175 (2013).

[17] B. M. Govindarajan and J. G. Leishman, *Curvature corrections to improve the accuracy of free-vortex methods,* Journal of Aircraft **53**, 378 (2016).

[18] V. Ahuja and B. L. Litherland, *Comparison of aerodynamic analysis tools applied to a propeller-blown wing,* in *AIAA SCITECH Forum* (2023).

[19] L. Boermans and P. Rutten, *Two-dimensional aerodynamic characteristics of airfoil NLF-MOD22 with fowler flap*, Technical Report (Delft University of Technology, 1995).

[20] N. van Arnhem, R. de Vries, T. Sinnige, and L. Veldhuis, *TUD-XPROP-S propeller geometry,* (2022).

[21] A. F. P. Ribeiro, D. Casalino, and E. Fares, *Lattice-boltzmann simulations of an oscillating NACA0012 airfoil in dynamic stall,* in *Advances in Fluid-Structure Interaction*, edited by M. Braza, A. Bottaro, and M. Thompson (Springer International Publishing, 2016) pp. 179–192.

[22] A. F. P. Ribeiro, D. Singh, B. Konig, and E. Fares, *On the stall characteristics of iced wings,* in *55th AIAA Aerospace Sciences Meeting* (2017).

[23] C. N. Sheridan, D. D. Pham, and S. Whiteside, *Evaluation of vspaero analysis capabilities for conceptual design of aircraft with propeller-blown wings,* in *AIAA AVIATION FORUM* (2021).

[24] A. F. P. Ribeiro, D. Casalino, and C. Ferreira, *Free wake panel method simulations of a highly flexible wing at flutter,* in *AIAA AVIATION Forum* (2022).

[25] A. F. P. Ribeiro, D. Casalino, and C. S. Ferreira, *Surging wind turbine simulations with a free wake panel method,* Journal of Physics: Conference Series **2265**, 042027 (2022).

[26] M. Ramasamy and J. G. Leishman, *A Reynolds number-based blade tip vortex model,* Journal of the American Helicopter Society **52**, 214 (2007).

[27] M. Drela, *XFOIL: An analysis and design system for low Reynolds number airfoils,* in *Low Reynolds Number Aerodynamics*, edited by T. J. Mueller (Springer Berlin Heidelberg, Berlin, Heidelberg, 1989) pp. 1–12.

[28] B. Maskew, *Program VSAERO Theory Document: A Computer Program for Calculating Nonlinear Aerodynamic Characteristics of Arbitrary Configurations*, Contractor Report 4023 (National Aeronautics and Space Administration, 1987).

III

Viscous Flow Simulations

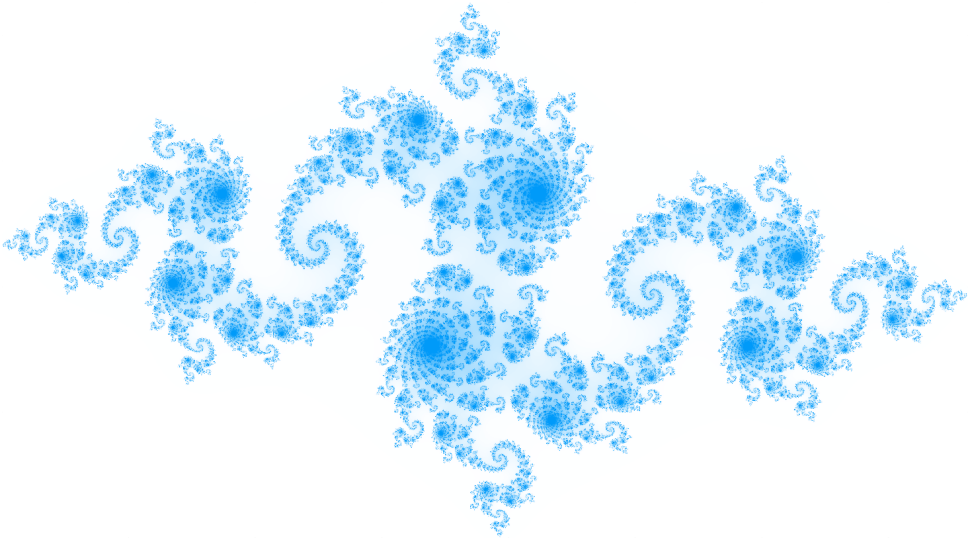

8

Numerical Methods for Computational Fluid Dynamics

How can less be more? It's impossible. More is more.

Yngwie Malmsteen

This chapter shifts focus from the inviscid free wake panel method to high-fidelity computational fluid dynamics. Here, the lattice-Boltzmann method, which is used for the next chapters, is described, along with methods for noise propagation and actuator line simulations.

8.1. The Lattice-Boltzmann Method

The numerical simulation of viscous fluids has historically been carried out using the Navier-Stokes equations. In its incompressible form, the equations can be written as so:

$$\rho \frac{\partial \vec{u}}{\partial t} + \rho(\vec{u} \cdot \nabla)\vec{u} = -\nabla p + \mu \nabla^2 \vec{u} \tag{8.1}$$

where ρ is the fluid density, t is the time, $\vec{u}$ is the velocity vector, p is the pressure, and μ is the dynamic viscosity. These equations are combined with the continuity equation:

$$\nabla \cdot \vec{u} = 0 \tag{8.2}$$

With the solution to these equations, one would be able to describe the three components of velocity and the fluid pressure in any point in space and time. However, as analytical solutions to the Navier-Stokes equations are only available for a small number of simple cases, numerical methods, collectively described as computational fluid dynamics (CFD) are used for most cases. This is usually carried out by discretizing the continuum space into a mesh and the continuum time into finite timesteps. Then, finite difference, finite volume, or finite element methods are employed to solve the equations numerically. See [1] for a comprehensive description of traditional CFD.

In the last two decades, the Lattice-Boltzmann method (LBM) [2] has been growing in popularity as an alternative to the Navier-Stokes equations. The objective is the same: to have a description of the velocity and pressure fields over time, based on a certain mesh and timesteps. However, instead of using continuum mechanics as the foundation for describing fluid flow, statistical mechanics are used, considering the fluid as particles that interact with each other and the boundary conditions. A thorough description of the LBM can be found in [3].

We first need to consider that a particle can be in a certain spatial coordinate $\vec{x}$. Then, we consider that the particle has a certain velocity $\vec{c}$. These quantities change as a function of time t. As dealing with individual particles quickly becomes too expensive, we instead work with the distribution function $f(\vec{x}, \vec{c}, t)$, which represents the probability that particles at position $\vec{x}$ and time t have the velocity $\vec{c}$. This can also be interpreted as the number of particles in a certain location and time that are travelling with a certain velocity. Fluid properties can be extracted from the moments of the distribution function. For example, density and momentum are simply:

$$\rho(\vec{x}, t) = \int f(\vec{x}, \vec{c}, t) d\vec{c} \tag{8.3}$$

$$\rho(\vec{x}, t)\vec{u}(\vec{x}, t) = \int f(\vec{x}, \vec{c}, t)\vec{c} d\vec{c} \tag{8.4}$$

The distribution of f is governed by the Boltzmann equation:

$$\frac{d}{dt}f(\vec{x},\vec{c},t) = \frac{\partial}{\partial t}f(\vec{x},\vec{c},t) + \vec{c}\nabla f(\vec{x},\vec{c},t) = C \tag{8.5}$$

where C is the collision operator, which defines how particles interact. As the Navier-Stokes equations, this can be discretized in time and space, but additionally, the velocity space must also be finite, so that the Boltzmann equation can be solved numerically. These assumptions lead to the Lattice-Boltzmann equation, which, including a body force F, takes the form:

$$f_i(\vec{x} + \vec{c}_i\Delta t, t + \Delta t) = f_i(\vec{x},t) + C_i(\vec{x},t) + \Delta t F_i(\vec{x},t) \tag{8.6}$$

where the subscript i denotes one of the velocities that particles are assumed to be able to travel in and Δt is the timestep. As in the Navier-Stokes equations, body forces are added to the Lattice-Boltzmann equations, in order to simulate the effect of gravity, Coriolis forces, or other fields that affect the flow. Equation 8.6 can be interpreted as such: the particle density function for discrete $\vec{x}$, $\vec{c}$, t is computed based on two processes, the advection and the collision steps. In the advection step, a particle is streamed from one cell to another by $\vec{c}\Delta t$. One key factor of this step is that no interpolation is needed to compute fluxes, as in the advection of the Navier-Stokes equations. This makes this step very inexpensive, computationally, while also making it have little numerical dissipation. The physical duration of a timestep in isothermal LBM is given by:

$$\Delta t = \frac{\Delta}{\sqrt{3}c} \tag{8.7}$$

where Δ is the mesh size and c is the speed of sound. Therefore, decreasing the speed of sound allows the simulations to be conducted at larger physical timesteps, which is advantageous for performance and can be done as long as compressibility effects are not important.

The collision step accounts for the interaction between particles with different velocities in the same cell. This is usually computed with the Bhatnagar-Gross-Krook (BGK) [4] approximation, given by:

$$C_i(\vec{x},t) = -\frac{1}{\tau}\left[f_i(\vec{x},t) - f_i^{eq}(\vec{x},t)\right] \tag{8.8}$$

where τ is the relaxation time and f_i^{eq} is the equilibrium particle distribution function. We can compute τ based on the kinematic viscosity $\nu = \mu/\rho$, the speed of sound c, and Δt as:

$$\tau = \frac{\nu}{c^2} + \frac{\Delta t}{2} \tag{8.9}$$

and f_i^{eq} is:

$$f_i^{eq} = \rho w_i e^{\vec{c}_i\cdot\vec{u}/T - \vec{u}\cdot\vec{u}/(2T)} \tag{8.10}$$

where w_i are the weighting factors for each velocity direction and T is the temperature. We can approximate f_i^{eq} by a third order expansion [5] as:

$$f_i^{eq} \approx \rho w_i \left[1 + \frac{\vec{c}_i \cdot \vec{u}}{T} + \frac{1}{2}\left(\frac{\vec{c}_i \cdot \vec{u}}{T}\right)^2 + \frac{1}{6}\left(\frac{\vec{c}_i \cdot \vec{u}}{T}\right)^3 - \frac{\vec{u} \cdot \vec{u}}{2T}\left(1 + \frac{\vec{c}_i \cdot \vec{u}}{T}\right)\right] \quad (8.11)$$

The BGK equation can be interpreted as the particle distributions converging towards an equilibrium state with a certain relaxation factor which is proportional to the fluid viscosity. The more viscous the fluid, the faster the particles attempt to reach an equilibrium. Here, the Boussinesq approximation can be used in order to add a certain eddy viscosity to the fluid viscosity [6], analogous to what is done in Navier-Stokes turbulence modelling. Finally, with f_i computed, the fluid density and momentum can be calculated by:

$$\rho = \sum f_i \quad (8.12)$$

$$\rho\vec{u} = \sum \vec{c}_i f_i \quad (8.13)$$

And pressure can be computed from the ideal gas law:

$$p = \rho R T \quad (8.14)$$

where R is the specific gas constant. Note that pressure is not needed during the computations and is calculated only as a post-processing step. This is advantageous when working with compressible air flow, where the large number of digits in the fluid pressure often require double precision in numerical computations.

The choice of the discretization of the velocity space is a critical part of the LBM. In general, the fewer directions particles can travel into, the less physics are captured by the method. However, the more directions, the higher the computational cost. For isothermal, quasi-incompressible cases, particles only need to travel to adjacent cells for mass and momentum conservation to be achieved. A cost-effective option is to use the D3Q19 formulation, i.e., a 3D 19-states model. This means that particles can travel to 18 adjacent cells, or stay in their current cell. This is shown in Figure 8.1, where the circles denote the directions particles can travel in, for a lattice of cubic cells. For this arrangement, the value of w_i is $1/3$ for the particles that stay in the same cell, $1/18$ for particles that travel in the six directions perpendicular to the cell faces, and $1/36$ for the remaining twelve diagonal directions.

All quantities are computed in so-called lattice units, where $\Delta t = 1$, $\Delta x = 1$, and the norm of $\vec{c}_i$ is zero, one, or $\sqrt{2}$. With these assumptions, the model is closed by arbitrarily setting $T = 1/3$ [7], leading to $c = \sqrt{T}$ and, assuming the simulation is of an ideal gas, $p = \rho T$. Using the Chapman-Enskog expansion [8], the Euler and Navier-Stokes equations can be obtained from the LBM [9].

Body forces are generally simple to apply in Navier-Stokes solvers, but LBM requires some corrections. A simple approach [10] is to apply body force components F_i in Eq. 8.6 as computed from a general body force per cell volume $\vec{F}$ using:

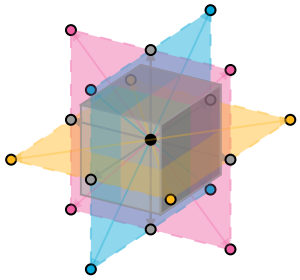

Figure 8.1: Discretization of the velocity space into 19 vectors.

$$F_i = \left(1 - \frac{1}{2\tau}\right)\omega_i \left(\frac{\vec{c}_i - \vec{u}}{c^2} + \frac{\vec{c}_i \cdot \vec{u}}{c^4}\vec{c}_i\right) \cdot \vec{F} \tag{8.15}$$

This formulation also requires a correction to Eq. 8.13:

$$\rho\vec{u} = \sum \vec{c}_i f_i + \frac{\Delta t}{2}\vec{F} \tag{8.16}$$

Throughout this thesis, the commercial software PowerFLOW is used. A unique feature of PowerFLOW is how it deals with boundary conditions. At solid walls, LBM traditionally has two simple boundary conditions: specular reflection and bounce-back. Specular reflection is equivalent to a free-slip boundary condition, where the wall tangential component of the particles are preserved, whereas bounce-back is equivalent to no-slip, with the tangential components being reflected back. For both cases, particle components normal to the wall are reflected back into the cells. The normal momentum exchange between particles and solids corresponds to pressure, while the tangential exchange corresponds to friction. This means velocity gradients do not need to be computed in LBM for friction calculation.

A combination of specular reflection and bounce-back can be used to achieve a fluid velocity near the wall that is larger than zero, but smaller than the equivalent inviscid velocity. This is needed for the use of wall models, which are typically needed for Cartesian grids. PowerFLOW uses the log-law as a wall model [11]. Let us define $u_+ = u/u_\tau$ and $y_+ = yu_\tau/\rho$, where u_+ is a non-dimensional velocity, u is the wall tangential velocity, $u_\tau = \sqrt{\tau/\rho}$ is the friction velocity, τ is the shear stress, y_+ is the non-dimensional wall distance, and y is the wall-normal distance, usually measured half a cell from the wall. Hence, the velocity can be computed for the sub-laminar and turbulent regions as:

$$u_+ = \begin{cases} y_+, & \text{if } y_+ < 5 \\ \frac{1}{\kappa} ln(y_+) + C, & \text{if } y_+ > 35 \end{cases}$$

where $\kappa \approx 0.41$ is the von Kármán constant and C is an empirical constant, typically equal to 5.5, but here also includes proprietary pressure gradient corrections. Between these well defined regions, where $5 < y_+ < 35$, u_+ is not well defined

and different codes use different methods. In PowerFLOW, an additional logarithmic equation is fitted between the sub-laminar and turbulent regions. The wall treatment has been recently improved to capture resolved turbulence in sufficiently resolved boundary layers, which allows for laminar separation bubbles to be captured [12, 13].

For velocity inlet and pressure outlet boundary conditions, the formulation of Zou and He [14] is used. This formulation is used to define f_i that point from the inlet and outlet faces into the fluid domain. This is achieved by imposing a certain velocity or density (derived from a user-imposed pressure by using the ideal gas law) at the cells adjacent to the boundaries in Eqs. 8.12 or 8.13, respectively. Then, we assume that the non-equilibrium part of the particle distributions (the first term in the square brackets in Eq. 8.8) performs a bounce-back at the boundaries. This gives us a closed system of equations, allowing the values of f_i entering the domain to be computed.

All the boundary conditions described so far assume the domain boundaries are flat surfaces adjacent to cell faces. For complex geometries, PowerFLOW uses surface elements with second order accuracy, dubbed surfels [15]. Surfels are flat elements generated by the intersection between the fluid mesh and surface facets. Figure 8.2 shows a 2D representation of how surfels are formed. Note that some cells have more than one surfel. During the discretization of the domain, surfels and their associated Pgrams (simple parallelograms in 2D) are created. The Pgrams define which cells interact with a given surfel, both sending and receiving particles to and from that surfel. They are formed by extruding the surfel along the velocity space directions i.

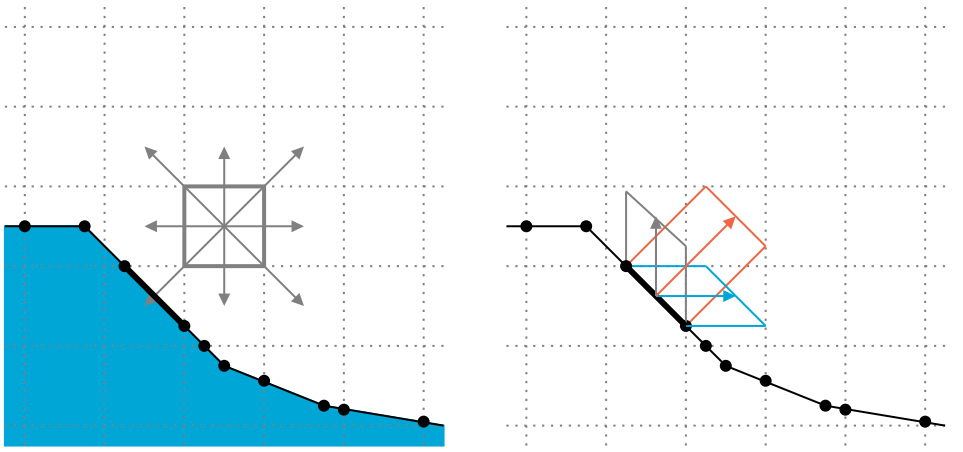

(a) Solid geometry (blue) with a highlighted surfel (bold black line) interacting with the highlighted cell (bold grey box).

(b) Pgrams associated with the highlighted surfel. Grey and blue Pgrams interact with two cells each, orange Pgram interacts with four cells.

Figure 8.2: Two-dimensional representation of surfels (black lines split by black circles) and their interaction with the particle velocity space (grey arrows) of a lattice (dotted grey lines).

The computations start with the gathering step, where the volume fraction of

each cell covered by Pgram i defines the fraction of f_{i*} that will interact with the surfel, where $*$ denotes the direction opposite of the Pgram extrusion. In Fig. 8.2, that means that for the orange Pgram, around 60% of f_i traveling towards the bottom left diagonal of the grey cell is advected to the highlighted surfel, and 40% of the same f_i is advected to the cell where the surfel is. The second step is surfel collision, where all the particles that reach the surfel interact and the outgoing values of f_i become:

$$f_i = f_i^{eq} + \left(1 - \frac{1}{\tau}\right)(f_{i*} - f_{i*}^{eq}) \tag{8.17}$$

where again $*$ denotes the incoming particle distribution functions, τ is computed with Eq. 8.9 with $\nu = 0$, effectively making this a specular reflection (which will be corrected), and f_i^{eq} is computed with Eq. 8.11, by using the Pgram weighted volume averaged surfel density and tangential velocity as ρ and $\vec{u}$ respectively. Finally, the scattering step is performed, with the particles being redistributed to nearby cells based on the fraction of the volume of the Pgram that they occupy. This step needs a few corrections. The first is a mass flux correction, to ensure the method is conservative and the number of particles coming in match the number of particles coming out. Then, a friction correction can be added to avoid a full specular reflection, allowing for wall functions to be used. Finally, a velocity gradient correction is added to make the scheme second order, avoiding the first order piece-wise constant assumption of the method described so far. The method is thus conservative and lacks the lattice alignment issues of first order methods. A thorough explanation of surfels and all the corrections is provided in the thesis of Li [16].

For rotations, PowerFLOW uses a sliding mesh approach [17]. This is achieved by rotating the geometry inside an axisymmetric region of the mesh, which is separated from the inertial domain by an interface made of surfels. Inside the sliding mesh, effects of inertial forces due to rotations are accounted for by a second order method, using Eq. 8.15. The velocities in the sliding mesh are shifted based on Eq. 8.16.

At the interface between the rotating (internal) and inertial (external or fixed) domains, surfels are used on both sides. They coincide in the first time step and, after that, one external surfel will overlap with one or two internal surfels. This is shown in Fig. 8.3. The way particles are advected across the sliding mesh interface is very similar to the wall treatment described in the previous paragraphs. The gathering step is performed on all surfels, both internal and external. Then a modified surfel collision step is done, but here Eq. 8.11 uses the velocity vector and not the tangential velocity vector, preserving the momentum normal to the interface. In the internal domain, the velocity is computed in the rotating reference frame. The information that needs to cross the interface is interpolated by a projected area weight ξ. This is also shown in Fig. 8.3, where the particles from the top external surfel are split between the two surfels that overlap with it using ξ on the left side and $1 - \xi$ on the right, which is conservative. Finally, the streaming step is performed in the internal and external domains.

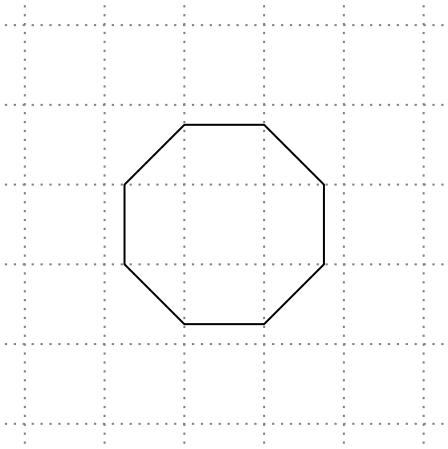

(a) Starting position

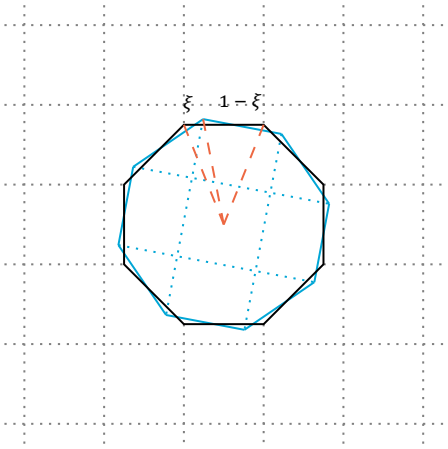

(b) Rotated position (rotating reference frame in blue), with the dashed orange lines representing how the particles that reach the top surfel of the external mesh are split between the two internal mesh surfels that overlap with it

Figure 8.3: Sliding mesh approach, with the background lattice (dotted grey lines) and reference frame interface surfels (solid lines).

Advantages of the LBM over traditional Navier-Stokes are mostly related to the simple and computationally inexpensive mathematics of the method. Collision operators are fully local, which is highly advantageous for simulations using large computer clusters and GPUs. The advection step does require neighbor information, but only adjacent cells are used, while the low dissipation in the method is similar to high order traditional schemes [18], which require several neighbors of given cells. With these advantages, the LBM can be orders of magnitude faster than high-fidelity Navier-Stokes solvers, while the explicit time marching scheme allows for the capturing of high frequency flow phenomena [19]. Additionally, the Cartesian meshes typically associated with the LBM, allow for very complex geometries to be included in simulations [20] with little effort from the user side.

8.2. The Ffowcs Williams-Hawkings Approach

While CFD approaches can be sufficient to compute pressure fluctuations (i.e., noise) in arbitrary locations, numerical dissipation usually plays a big role if the acoustic source (e.g., an aircraft flying over an urban community) is distant from the acoustic target (e.g., a person on the ground). Hence, it would be beneficial to calculate local pressure fluctuations on an acoustic source using CFD, while propagating such sources to a distant target using a different method, not requiring a mesh between the two locations. This is the standard practice in computational aeroacoustics (CAA) when it is coupled to CFD and it uses the Ffowcs Williams-Hawkings (FW-H) analogy, which can be coupled to the LBM [21].

The FW-H approach [22] takes a data surface near the acoustic sources and

propagates that noise to arbitrary points in space. The data surfaces can coincide with the solid walls or be placed arbitrarily around them, which are known as the solid and permeable approaches, respectively. Mathematically, the data surfaces are defined with the variable f, which is positive outside the surface and negative inside. The formulation is based on a rearrangement of the Navier-Stokes equations. Here we focus on one of the time-domain formulations, but frequency-domain formulations are also available [23] (as will be shown in Chapter 12). The FW-H equation is:

$$\left(\frac{1}{c^2}\frac{\partial^2}{\partial t^2} - \frac{\partial^2}{\partial x_i \partial x_i}\right)[p'H(f)] = \frac{\partial}{\partial t}[Q_n \delta(f)] - \frac{\partial}{\partial x_i}[L_i \delta(f)] + \frac{\partial^2}{\partial x_i \partial x_j}\left[T_{ij} H(f)\right] \tag{8.18}$$

where c is the speed of sound, p' is the pressure fluctuation, t is time, H is the Heaviside function, equal to unity outside the data surface and zero inside of it, and δ is the Dirac delta function, the derivative of H, equal to unity on the data surface and zero elsewhere. The index n indicates the term is computed normal to the data surface, while the indices i and j indicate the three spatial dimensions, as per indicial notation. The three leading terms in square brackets, Q_n, L_i, and T_{ij} represent the thickness, loading, and quadrupole sources, respectively. The thickness source is defined as:

$$Q_n = Q_i \hat{n}_i = [\rho_0 v_i + \rho(u_i - v_i)]\,\hat{n}_i \tag{8.19}$$

where $\hat{n}_i$ is the data surface normal vector, ρ is the instantaneous fluid density, ρ_0 is the freestream fluid density, such that $\rho = \rho_0 + \rho'$, v_i is the data surface velocity vector, and u_i is the fluid velocity vector. Neglecting the viscous stress tensor, the loading source is defined as:

$$L_i = L_{ij}\hat{n}_j = \left[p'\delta_{ij} + \rho u_i(u_j - v_j)\right]\hat{n}_j \tag{8.20}$$

where δ_{ij} is the Kronecker delta, or in this case, a 3×3 matrix with ones in the main diagonal and zeros in the other positions. The quadrupole source term is the Lighthill stress tensor, which once again ignoring the viscous stress tensor is:

$$T_{ij} = \rho u_i u_j + p'\delta_{ij} + c^2 \rho' \delta_{ij} \tag{8.21}$$

While the thickness and loading sources are defined on the data surfaces, as they are multiplied by the Dirac function, making them zero everywhere else, the quadrupole sources are volumetric and are typically neglected on most numerical formulations. For solid data surfaces this means that quadrupole sources are not captured at all, while for permeable data surfaces, this means quadrupole sources outside the surface are neglected, as the Heaviside function sets the quadrupole term to zero inside the data surfaces. This is acceptable if the region inside the permeable data surface is large enough to capture the relevant quadrupole effects,

such as shocks. The FW-H equation is often solved using the Farassat 1A [24, 25] formulation and an advanced time approach [26]. The result of formulation 1A is:

$$
\begin{aligned}
4\pi p' = &\int \frac{\frac{\partial Q_i}{\partial \tau}\hat{n}_i + Q_i\frac{\partial \hat{n}_i}{\partial \tau}}{r(1-M_i\hat{r}_i)^2}dS + \int \frac{Q_n\left[r\frac{\partial M_i}{\partial \tau}\hat{n}_i + c_0(M_i\hat{r}_i - M^2)\right]}{r^2(1-M_i\hat{r}_i)^3}dS \\
&+ \frac{1}{c_0}\int \frac{\frac{\partial L_i}{\partial \tau}\hat{r}_i}{r(1-M_i\hat{r}_i)^2}dS + \int \frac{L_i\hat{r}_i - L_iM_i}{r^2(1-M_i\hat{r}_i)^2}dS \\
&+ \frac{1}{c_0}\int \frac{L_i\hat{r}_i\left[r\frac{\partial M_i}{\partial \tau}\hat{r}_i + c_0(M_i\hat{r}_i - M^2)\right]}{r^2(1-M_i\hat{r}_i)^3}dS
\end{aligned}
\tag{8.22}
$$

where all integrals are performed on the data surfaces at the emission time τ. The first two integrals are due to the thickness noise sources and the last three are due to the loading noise sources. Here, r is the scalar distance between source and target, which has a normalized vector form of $\hat{r}_i$, S is the surface, M_i is the Mach number vector of the source, with norm M, and c_0 is the freestream speed of sound. A review and derivation of Farassat formulation 1A can be found in [27]. The inclusion of convection effects in a wind tunnel modality, which is often used for validation cases and uses Farassat formulation 1C is described in [28].

For aeroacoustics of aircraft and rotors at subsonic Mach numbers, the FW-H formulation using solid data surfaces is commonly used, while applications including shocks or strong volumetric sources, such as jet noise, typically use the permeable formulation, to include quadrupole effects. However, recent studies have shown that the solid formulation often shows severe issues, hence its use should be carefully validated using direct noise measurements from the simulations [29].

8.3. Actuator Line Method

Here, the actuator line (AL) method is described. AL simulations apply blade element theory (BET) to CFD simulations. Hence, we start with a description of BET.

8.3.1. Blade Element Theory

BET is based on a 2D representation of rotor blades. Instead of considering the flow around the entire blade, cylindrical cuts centered around the rotor axis are made along the radius and airfoil sections are calculated. For a given blade section with incoming axial flow U_a, the rotation of the blade introduces a tangential flow velocity U_t in the airfoil reference frame. Adding these two velocities leads to a relative velocity vector U_r, with an angle relative to the rotor plane of ϕ. The airfoil, which is rotated relative to the rotor plane with a twist angle θ will then be under an angle of attack α which is $\alpha = \phi - \theta$ in the case of a turbine and $\alpha = \theta - \phi$ in the case of a propeller. The airfoil then generates a drag force D, aligned with U_r and a lift force L, perpendicular to U_r. These forces can be projected to be aligned with the rotor coordinate system, leading to an axial force F_a, or thrust, and a tangential force F_t, which is associated with the rotor torque. These vectors and angles are shown in Figure 8.4.

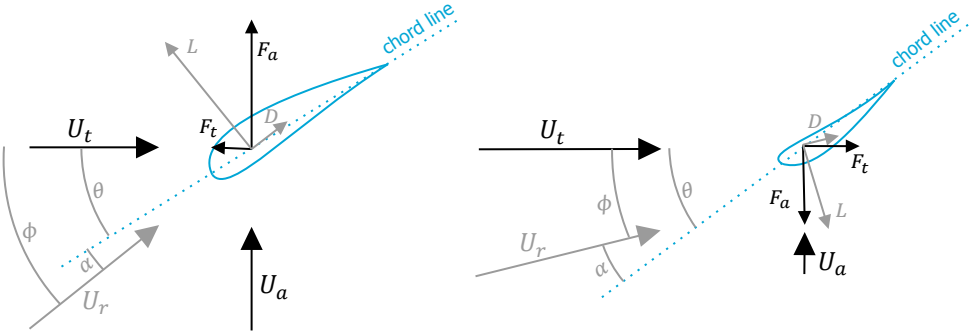

Figure 8.4: Vectors and angles involved in 2D flow around the section of a turbine (left) and propeller (right) blades.

Note that U_a does not need to equal the freestream velocity and U_t does not need to equal the local kinematic velocity. The blades and wakes create a disturbance in the flow and this can be accounted for when using BET. Note also that with BET a complex 3D problem, i.e., the flow around rotor blades, is reduced to a combination of a few dozen simple 2D problems, i.e., the flow around an arbitrary number of radial stations. BET is essential for blade element momentum theory, lifting line, actuator line, and some actuator disk models.

The assumption of 2D flow along blades of BET breaks down near tips and roots, where the flow becomes 3D and tip/root vortices play a large role. Additionally, BET was developed to be used with blade element momentum theory, which works based on actuator disks with an infinite number of blades, which is not representative of wind turbines. This can be accounted for using corrections based on the Prandtl tip losses. A popular method [30] is based on the Glauert formulation, which multiplies L and D of each section by a function F, reducing the forces along the blades based on the local section radius r.

$$F_{tip} = \frac{2}{\pi}\cos^{-1}\left(e^{-g\frac{B(R_{tip}-r)}{2r\sin(\phi)}}\right) \tag{8.23}$$

where B is the number of blades, R_{tip} is the tip radius, and g is a correction function:

$$g = e^{-0.125(B\lambda-21)} + 0.1 \tag{8.24}$$

where $\lambda = \Omega R_{tip}/U_\infty$ is the tip-speed ratio, Ω is the rotor angular velocity, U_∞ is the freestream velocity, and the numerical values are empirical. In order to apply F to the root, a very similar equation is used:

$$F_{root} = \frac{2}{\pi}\cos^{-1}\left(e^{-g\frac{B(r-R_{root})}{2r\sin(\phi)}}\right) \tag{8.25}$$

where R_{root} is the root radius. In practical terms, F reduces the forces on blade sections to zero at the tip and root, while having small effects near the blade center.

In order to keep the exponential under unity, ϕ must be assumed positive. Negative values could occur in case of strong turbulence or an oscillating rotor. The correction factor g can be used to tune results to better match experimental values of a specific rotor. Other corrections for the root vortex have been proposed [31], with a certain degree of empiricism being employed to match wind turbine data.

8.3.2. Actuator Line Implementation

The AL method [32] combines the lifting line method with CFD, by using BET based on the local flow quantities provided by the CFD solver, and applying the airfoil forces on the CFD simulation as body forces. The main motivation for the AL is that much coarser meshes can be used, as solid walls are removed from the simulation. From the vectors shown in Fig. 8.4 one obtains:

$$F_a = \frac{1}{2}\rho U_r^2 \Delta r c \left[C_l(\alpha)\cos(\phi) + C_d(\alpha)\sin(\phi)\right] \tag{8.26}$$

$$F_t = \frac{1}{2}\rho U_r^2 \Delta r c \left[C_l(\alpha)\sin(\phi) - C_d(\alpha)\cos(\phi)\right] \tag{8.27}$$

where C_l and C_d are the lift and drag coefficients respectively, which are typically measured or calculated for a given airfoil shape and Reynolds number and provided in a table as a function of α, Δr is the length of the current blade section, and c is the airfoil chord. Projection of the BET forces onto the CFD mesh is done with the classical 3D-Gaussian distribution:

$$\vec{F}_{AL}(\vec{x}) = -\vec{F}_{BET}\frac{1}{\epsilon^3\pi^{3/2}}e^{-\frac{\|\vec{x}-\vec{x}_0\|^2}{\epsilon^2}} \tag{8.28}$$

where $\vec{F}_{AL}$ is the body force to be applied in the CFD simulation at the coordinate $\vec{x}$, $\vec{F}_{BET}$ is the force obtained in the BET step, or the vector sum of F_a and F_t, $\vec{x}_0$ is the position where $\vec{F}_{BET}$ is applied (the corresponding airfoil quarter chord), and ϵ is the Gaussian width or smearing factor, a projection parameter which determines the size of the spherical region where the body forces are applied.

This smearing of the forces causes the trailing vortices from the blades to effectively have a core, instead of following the inviscid behavior of idealized vortices. This causes the induction on nearby blade sections to be reduced, leading to inaccuracies, in particular near the blade tips. A typical method to solve this is using tip corrections [30] as in BET, by multiplying $\vec{F}_{AL}(\vec{x})$ by F_{tip} and F_{root}. However, these corrections have no physical meaning in AL, as they were initially intended to correct for the finite number of blades in a turbine. In recent years, smearing corrections derived from attempting to make AL into a method consistent with actuator line were achieved [33].

References

[1] J. H. Ferziger and M. Perić, *Computational Methods for Fluid Dynamics*, 3rd ed. (Springer Berlin, 2002).

[2] H. Chen, C. Teixeira, and K. Molvig, *Digital physics approach to computational fluid dynamics: Some basic theoretical features,* International Journal of Modern Physics C **08**, 675 (1997).

[3] S. Succi, *The Lattice Boltzmann Equation: For Fluid Dynamics and Beyond*, Numerical Mathematics and Scientific Computation (Clarendon Press, 2001).

[4] P. L. Bhatnagar, E. P. Gross, and M. Krook, *A model for collision processes in gases. I. Small amplitude processes in charged and neutral one-component systems,* Physical Review **94**, 511 (1954).

[5] H. Fan, R. Zhang, and H. Chen, *Extended volumetric scheme for lattice boltzmann models,* Physical Review E **73**, 066708 (2006).

[6] E. Fares, B. Duda, A. F. P. Ribeiro, and B. König, *Scale-resolving simulations using a lattice Boltzmann-based approach,* CEAS Aeronautical Journal **9**, 721 (2018).

[7] H. Chen and C. Teixeira, *H-theorem and origins of instability in thermal lattice Boltzmann models,* Computer Physics Communications **129**, 21 (2000).

[8] S. Chapman, T. Cowling, D. Burnett, and C. Cercignani, *The Mathematical Theory of Non-uniform Gases: An Account of the Kinetic Theory of Viscosity, Thermal Conduction and Diffusion in Gases*, Cambridge Mathematical Library (Cambridge University Press, 1990).

[9] H. Chen, S. Chen, and W. H. Matthaeus, *Recovery of the Navier-Stokes equations using a lattice-gas Boltzmann method,* Physical Review A **45**, R5339 (1992).

[10] Z. Guo, C. Zheng, and B. Shi, *Discrete lattice effects on the forcing term in the lattice Boltzmann method,* Physical Review E **65**, 046308 (2002).

[11] A. Anagnost, A. Alajbegovic, H. Chen, D. Hill, C. Teixeira, and K. Molvig, *Digital physics^{TM} analysis of the morel body in ground proximity,* SAE transactions , 306 (1997).

[12] D. Casalino, G. Romani, R. Zhang, and H. Chen, *Lattice-Boltzmann calculations of rotor aeroacoustics in transitional boundary layer regime,* Aerospace Science and Technology **130**, 107953 (2022).

[13] D. Casalino, G. Romani, L. M. Pil, and R. Colombo, *Sensitivity of laminar separation noise from a rotor to inflow turbulence,* in *AIAA AVIATION Forum* (2023).

[14] Q. Zou and X. He, *On pressure and velocity boundary conditions for the lattice Boltzmann BGK model,* Physics of Fluids **9**, 1591 (1997).

[15] H. Chen, C. Teixeira, and K. Molvig, *Realization of fluid boundary conditions via discrete boltzmann dynamics,* International Journal of Modern Physics C **09**, 1281 (1998).

[16] Y. Li, *An improved volumetric LBM boundary approach and its extension for sliding mesh simulation*, Ph.D. thesis, Iowa State University (2012).

[17] R. Zhang, C. Sun, Y. Li, R. Satti, R. Shock, J. Hoch, and H. Chen, *Lattice boltzmann approach for local reference frames,* Communications in Computational Physics **9**, 1193 (2011).

[18] G. Brès, F. Pérot, and D. Freed, *Properties of the lattice Boltzmann method for acoustics,* in *15th AIAA/CEAS Aeroacoustics Conference (30th AIAA Aeroacoustics Conference)* (2012).

[19] E. Manoha and B. Caruelle, *Summary of the LAGOON solutions from the benchmark problems for airframe noise computations-III workshop,* in *21st AIAA/CEAS Aeroacoustics Conference* (2015).

[20] M. R. Khorrami, B. Konig, E. Fares, A. F. P. Ribeiro, M. Czech, and P. A. Ravetta, *Airframe noise simulations of a full-scale large civil transport in landing configuration,* in *AIAA AVIATION FORUM* (2021).

[21] G. Brès, F. Pérot, and D. Freed, *A Ffowcs Williams - Hawkings solver for lattice-Boltzmann based computational aeroacoustics,* in *16th AIAA/CEAS Aeroacoustics Conference* (2010).

[22] J. E. Ffowcs Williams and D. L. Hawkings, *Sound generation by turbulence and surfaces in arbitrary motion,* Philosophical Transactions of the Royal Society of London. Series A, Mathematical and Physical Sciences **264**, 321 (1969).

[23] D. P. Lockard, *An efficient, two-dimensional implementation of the Ffowcs Williams and Hawkings equation,* Journal of Sound and Vibration **229**, 897 (2000).

[24] F. Farassat and G. Succi, *A review of propeller discrete frequency noise prediction technology with emphasis on two current methods for time domain calculations,* Journal of Sound and Vibration **71**, 399 (1980).

[25] K. S. Brentner, *Prediction of helicopter rotor discrete frequency noise: A computer program incorporating realistic blade motions and advanced acoustic formulation*, Technical Memorandum 87721 (National Aeronautics and Space Administration, 1986).

[26] D. Casalino, *An advanced time approach for acoustic analogy predictions,* Journal of Sound and Vibration **261**, 583 (2003).

[27] F. Farassat, *Derivation of Formulations 1 and 1A of Farassat*, Technical Memorandum 214853 (National Aeronautics and Space Administration, 2007).

[28] A. Najafi-Yazdi, G. A. Brès, and L. Mongeau, *An acoustic analogy formulation for moving sources in uniformly moving media,* Proceedings of the Royal Society A: Mathematical, Physical and Engineering Sciences **467**, 144 (2011).

[29] A. F. P. Ribeiro, M. R. Khorrami, R. Ferris, B. Koenig, and P. A. Ravetta, *Lessons learned on the use of data surfaces for Ffowcs Williams-Hawkings calculations: Airframe noise applications,* in *28th AIAA/CEAS Aeroacoustics Conference* (2022).

[30] W. Z. Shen, R. Mikkelsen, J. N. Sørensen, and C. Bak, *Tip loss corrections for wind turbine computations,* Wind Energy **8**, 457 (2005).

[31] J. N. Sørensen, K. Nilsson, S. Ivanell, H. Asmuth, and R. F. Mikkelsen, *Analytical body forces in numerical actuator disc model of wind turbines,* Renewable Energy **147**, 2259 (2020).

[32] J. N. Sørensen and W. Z. Shen, *Numerical modeling of wind turbine wakes,* Journal of Fluids Engineering **124**, 393 (2002).

[33] A. R. Meyer Forsting, G. R. Pirrung, and N. Ramos-García, *A vortex-based tip/smearing correction for the actuator line,* Wind Energy Science **4**, 369 (2019).

9

Implementation of a Sliding Mesh Actuator Line Method

Better the devil you know than the devil you don't.

Proverb

Simulating entire wind farms with an actuator line model requires significant computational effort, especially if one is interested in wake dynamics and wants to resolve the tip vortices. Hence, there is a need to explore unconventional approaches for this kind of simulation. In this chapter, the actuator line method is implemented within a lattice-Boltzmann flow solver, combined with a sliding mesh approach. Lattice-Boltzmann solvers have advantages in terms of performance and low dissipation, while the sliding mesh allows for local refinement of the blade and tip vortices. This methodology is validated on a well-documented case, the NREL Phase VI rotor and the local refinement is demonstrated on the NREL 5MW rotor. Results show good agreement with reference Navier-Stokes simulations. Advantages and limitations of the sliding mesh approach are identified.

Parts of this chapter have been published in Wind Energy (2023) [1], co-written with Claudia Muscari.

9.1. Introduction

The climate crisis caused the European Union and the member states to consider net zero greenhouse gas emissions as a legally binding target for 2050 [2]. While wind energy is mature enough to help substantially with such ambitious plans, we still have margins of improvements from all perspectives. We can make better use of the favourable sites available for wind plant installation with effective layout and control of the plant itself. Turbines can be made more durable and to have a longer operational life through the use of better materials, which would also reduce the environmental impact of discarding the turbine components. A detailed and clear report on these points can be found in the work of Veers et al. [3]. Any technical progress requires the support of data which can be obtained via experiments and/or numerical simulations. For wind energy applications, given the large Reynolds numbers and the multiple length scales involved, not only is direct numerical simulation infeasible but also large eddy simulation (LES) on fully resolved geometries is too computationally demanding to be used extensively.

In a seminal work published in 2002 [4], the actuator line (AL) model is first presented. Computational fluid dynamics (CFD) is used with LES as the turbulence closure, and the presence of the turbine is accounted for by solving the blade element theory (BET) equations for discrete blade radial sections, where the computed lift and drag is projected onto the flow field as a momentum source along rotating blade lines. In the following two decades, this hybrid approach has become the go-to high fidelity method when dealing with wind turbine wakes and wind farms simulations, mostly using Navier-Stokes (NS) solvers.

The BET step needs only airfoil polars and a locally sampled velocity as input. This velocity should simultaneously account for the deceleration caused by the rotor induction and ignore the blade-local flow effects. One possibility is to sample locally at the AL point (local sampling). Physically this would be justified by potential flow theory: the AL point is the center of the bound vortex cross-section where the effect of the bound vortex itself is null. Potential flow theory, however, does not hold for the conditions in which wind turbines operate and it surely does not hold when using kernel functions different from the classic isotropic Gaussian one. Alternatives have been discussed such as integral sampling [5], Lagrangian sampling [6] and the effective velocity model [7].

The BET forces are computed along lines aligned with each blade. They are applied to the momentum equation as source terms by projecting the line forces into volumetric body force surrounding each line. The most common choice is then to use a three-dimensional Gaussian projection function that is isotropic and fixed in width along the blade span. This makes the resultant body-force field around an actuator line appear as a cylindrical cloud surrounding the line. More advanced functions lead to a distribution that more closely resembles an actual blade [5]. Several studies have demonstrated the model's reliability in a number of different conditions,[5, 8, 9] however result quality is still strongly dependent on the method used to sample the incoming velocity, the characteristics of the chosen projection function, and the quality of the tabulated data.

Recently, particular effort has gone into reducing the number of tuning param-

eters on AL and making choices based on a better understanding of the physics involved. An important contribution was made by Shives and Crawford [10], relating the width of the Gaussian projection function to the chord length. Respecting such requirements leads to much finer meshes than traditionally used by AL, hence increasing the computational cost of the simulations. This opens opportunities for alternative CFD approaches and meshing strategies.

The lattice-Boltzmann method (LBM) [11] can reproduce the same physics as the NS equations [12], while presenting substantial advantages in performance and numerical dissipation. LBM-based solvers have been shown to perform unsteady simulations orders of magnitude faster than NS-based ones [13], while displaying low-dissipation characteristics equivalent to high order methods [14]. Due to these advantages, some effort has been made in developing LBM-based AL models [15, 16]. However, as traditionally LBM is used for isothermal simulations, this limits the use of these methods, as thermal effects are critical for an accurate description of the atmospheric boundary layer [17].

In this work, we perform the first AL implementation into a state-of-the-art LBM solver that is able to handle thermal effects [18], local mesh refinement, and complex terrain, which we henceforth refer to as AL-LBM, in an attempt to address the limitations outlined in the previous paragraph. The commercial LBM solver PowerFLOW is used.

Standard AL simulations are performed with constant refinement on the entire rotor disk, as the forces rotate with the rotor, while the mesh remains static. While a static mesh is advantageous for its simplicity, a sliding mesh approach would allow for local refinement around the rotor blades [5]. Hence, another novel contribution of this work, is the use of a sliding mesh for the AL simulations [19], which has potential to improve the efficiency of advanced AL models [5]. The objectives of this work are to validate the AL-LBM implementation we have developed and to demonstrate the advantages and disadvantages of the sliding mesh approach for AL simulations in general.

9.2. Methods

9.2.1. Navier-Stokes Solver

For almost all CFD problems the reference model is some convenient expression of the NS equations. Each model comes with a level of empiricism and simplifications that have to be taken into account when making the other choices and analyzing the results. In particular, for wind energy, we consider an incompressible NS formulation. Force terms can be added to the right side of the equations, in order to model gravity, Coriolis effects, and other body forces. These equations are usually solved using the finite volume method [20]. Most of the CFD codes simulating horizontal axis wind turbines wakes rely on LES, meaning that they simulate the large scales and model the small ones. The effect of the large scale momentum flux caused by the action of the small or unresolved scales is represented by the subgrid-scale Reynolds stress. The models used to approximate it are called subgrid-scale (SGS) or sub filter-scale models [21] and most of these models work by adding an eddy

viscosity to the fluid viscosity in the momentum equations.

We use NS results in this work as validation to our LBM simulations through comparison with SOWFA [17], a set of libraries, solvers and boundary conditions specific to wind energy applications, based on the OpenFOAM® finite volume CFD software. SOWFA is open source and inherits the capabilities of OpenFOAM, allowing for relatively inexpensive wind turbine simulations by providing AL and actuator disk solvers, thus making simple, Cartesian grids that are accurate enough to run the simulations on. SOWFA's AL implementation is widely used in the community and is considered state-of-the-art. The AL solver is based on a pressure-implicit with splitting of operators (PISO) algorithm [22]. PISO is well suited for simulations where the time step is controlled by external factors and temporal accuracy is important, as in LES. In such cases, the assumption of slow variation over non-linearity holds and the cost of momentum assembly and solution can be safely avoided. SOWFA can also be coupled with FAST, NREL's aero-servo-elastic tool.

We use the typical settings for SOWFA taken from the provided examples, which include a second order backwards Euler time discretization and an interpolation scheme equivalent to second order central differences for pressure and velocity, while fluxes use a Rhie-Chow-like formulation [23]. The SGS model is a one equation turbulence kinetic energy-based model.

9.2.2. Lattice-Boltzmann Solver with a Sliding Mesh

Our LBM computations are conducted with PowerFLOW, a commercial CFD code. It employs a $k-\epsilon$ RNG turbulence model [24] with a swirl model [25], which reduces the eddy viscosity in the presence of resolved flow structures, an approach called very large eddy simulation (VLES). This LBM-VLES approach has been validated on numerous simulations of vortical flows [26, 27]. A Cartesian mesh is used, which is convenient for comparisons to SOWFA, as the same mesh topology can be employed in both solvers. A unique capability of PowerFLOW is in the handling of very complex geometry [28], which will be useful for future onshore wind turbine simulations with complex terrain. This is done with the concept of surface elements, or surfels [29]. Other features relevant to wind farm simulations are the ability to simulate complex buoyancy effects, by using a finite difference thermal solver [30], and the ability to use a sliding mesh.

A sliding mesh [19] is used to rotate the AL in LBM. The sliding mesh allows the blades to always be in the same location relative to the surrounding cells, making the local velocity sampling more stable, as long as aeroelastic effects are not present. With the sliding mesh, local refinement can also be put on the blades and the tip vortex if needed, without having to refine the entire rotor disk. LBM is solved using explicit time schemes, leading to very small time steps. However, implicit solvers like SOWFA are often limited in their time step when using AL in order to avoid that the blade tip moves by more than one element in a single time step. This could potentially be mitigated with the sliding mesh, which could allow for larger time steps in implicit solvers.

Sliding meshes also present some disadvantages. Depending on the methods used, some degree of interpolation in the interface between the static and rotating

cells is needed, leading to some dissipation of the flow structures in that region. Another issue is that the the rotor must fall in a cylindrical rotating region, separate from the tower, which can be challenging when simulating cases with very small tower clearance. Finally, a sliding mesh adds some computational cost to any simulation, which may or may not be compensated by coarsening the elements between the blades.

9.2.3. Actuator Line Method

The AL model used in this study was implemented with the user defined equations and scripting capabilities of PowerFLOW, which usually models blades as solid walls [31]. Henceforth, we refer to this as AL-LBM. Velocity sampling on the actuator points is achieved by averaging values of the cells within a user-defined radius (which we set as equal to the smearing factor ϵ) around the corresponding airfoil quarter-chord.

The explicit time marching scheme uses much smaller time steps than OpenFOAM, about 30 times for the same grid size. Hence, we choose not to update the body forces at every time step. As the body forces are applied in the rotating reference frame, the conversion from the tangential direction to the vertical and horizontal directions is done in the first timestep and does not need to be updated, hence if the flow is steady, the body forces remain constant over time. This is in contrast with a static mesh approach, where even steady forces need to be updated frequently, to reflect on the changes in azimuthal position.

Another difference between LBM and NS is that LBM is almost always compressible, even if weakly for most codes. AL codes such as SOWFA are typically based on the incompressible NS equations, meaning that they are limited to low Mach numbers. The methodology implemented in this work could be used for cases with stronger compressibility effects, although the literature on using AL for compressible flows is scarce (the only applications in aerospace to the authors' knowledge are for low Mach numbers [32, 33]) and such applications would need to be validated.

9.3. Validation: NREL Phase VI Wind Turbine

For our validation we consider the SOWFA example case based on the NREL Phase VI rotor [34], a 10 m diameter turbine with two blades. The rotor is simulated here without the nacelle and tower for simplicity. Tip corrections are also omitted. Simulations are conducted with uniform incoming free-stream velocity $U_\infty = 7$ m/s. The fluid density ρ is set to 1.23 kg/m^3 and the free-stream pressure p_∞ is set to one atmosphere in PowerFLOW and zero gauge pressure in SOWFA. The sides of the domain use free slip walls and a pressure outlet boundary condition is employed at the end of the domain. Simulations use the same domain size. The turbine rotates at 71.9 RPM and 60 points per blade are used to describe the actuator line. Simulations are run for 20 seconds of physical time and results are averaged over the last 5 seconds.

The sliding mesh interface in PowerFLOW is placed at a distance of 3.04ϵ away from the rotor disk, which is where the exponential the Gaussian distribution re-

duces to $1/10000$. The value of ϵ was set to $0.035D$ [5], where D is the rotor diameter. As these simulations are using coarse meshes, the tip vortices are resolved with approximately 5 elements across their diameter. This caused some dissipation of the vortices as they crossed the sliding mesh interface. Hence, we refined the LBM grid around the downstream face of the sliding mesh to avoid dissipation. This extra refinement is likely not needed for finer meshes, but is the main drawback in the sliding mesh approach. Everywhere else in the domain, the two meshes are identical, with a cell size of $D/100$ in most of the domain including the rotor wake, growing by factors of 2 up to a final cell size of $D/6.25$ in the outer edges of the simulation volume.

Figure 9.1 shows instantaneous AL-LBM results on a slice that is on the rotor plane. Velocity magnitude and the computational grid are shown, where the sliding mesh interface can be seen as the circle around the rotor. This image was captured with the rotor at an azimuth of 25° and is zoomed in to allow for the grid lines to be distinguished.

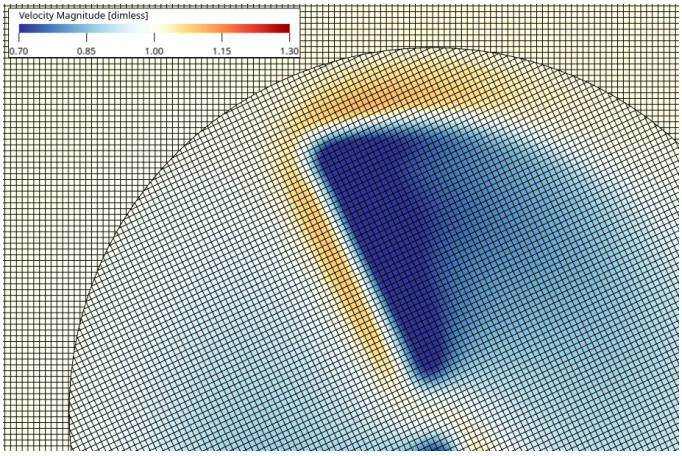

Figure 9.1: Slice on rotor plane showing an example of the computational grid and sliding mesh interface on the AL-LBM. Colors show velocity magnitude divided by U_∞.

Isosurfaces of the Q criterion [35] from the AL-LBM and SOWFA simulations are shown in Figures 9.2 and 9.3, respectively. Results are very similar, with some differences in the breakup of the blade root vortices and small artifacts appearing around the sliding mesh. In both cases, the simulations are able to preserve the tip vortices as long as the fine mesh resolution of $D/100$ is maintained.

The thrust obtained with AL-LBM is 2% higher than in NS, while the torque is 5% higher. Given the differences in the velocity sampling between the two methods, we consider this good agreement. A breakdown of the forces is shown in Figures 9.4 and 9.5, where the axial and tangential forces along the blades are shown for the SOWFA and AL-LBM cases. Here, R is the rotor radius. While minor differences are present, we consider the codes to be in good agreement.

A quantitative comparison of the wake is shown in Figure 9.6, where the mean

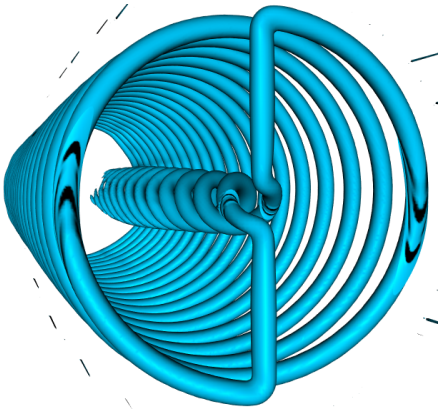

Figure 9.2: AL-LBM isosurfaces of $Q = 5$ s^{-2}.

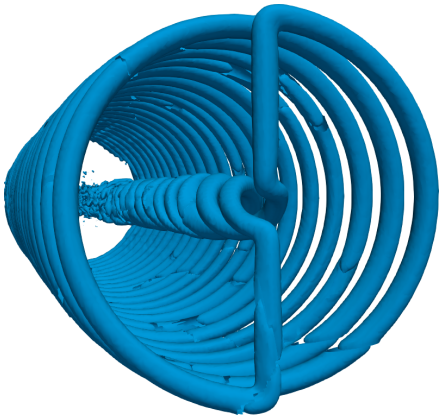

Figure 9.3: SOWFA isosurfaces of $Q = 5$ s^{-2}.

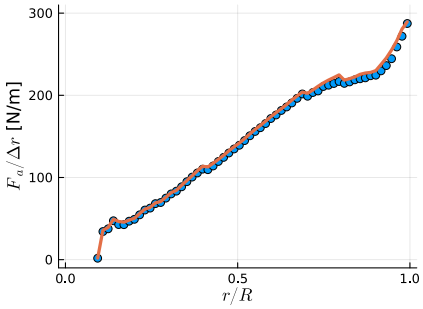

Figure 9.4: Axial force per unit span over blade radius. SOWFA results shown as blue circles, AL-LBM results as orange lines.

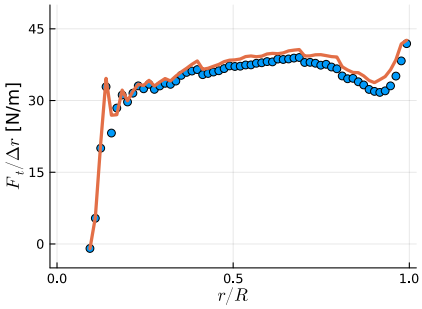

Figure 9.5: Tangential force per unit span over blade radius. SOWFA results shown as blue circles, AL-LBM results as orange lines.

pressure (p) coefficient $Cp = (p - p_\infty)/(0.5\rho U_\infty^2)$, and the mean and variance of the streamwise (u), horizontal (v), and vertical (w) components of velocity are shown. Results are computed on a vertical line 10 m (about one diameter) downstream of the rotor. Results are in excellent agreement, with minor variations in some of the quantities, mostly near the root vortices. The AL-LBM simulations were conducted with merely 6 BET steps to update the body forces in the first few seconds of physical time. After that, velocities on the sampling points converged to a steady state and more couplings between BET and CFD became unnecessary. This would not be possible if the rotor were tilted, if strong tower effects were present, or if the incoming flow were turbulent.

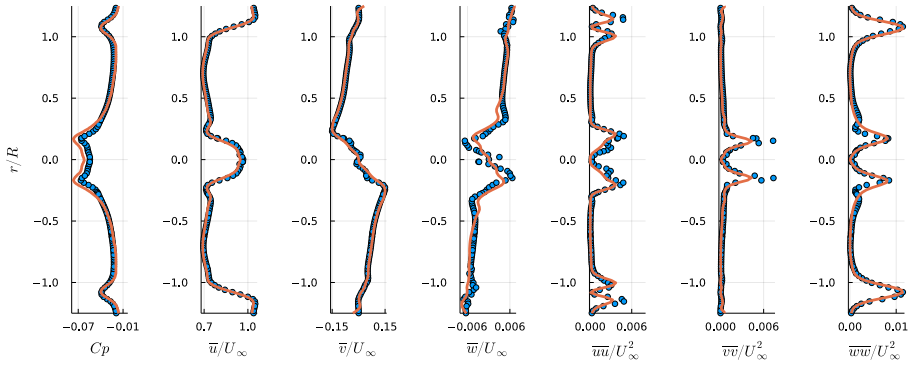

Figure 9.6: Pressure and velocity profiles along a vertical line 10 m downstream of the rotor. SOWFA results shown as blue circles, AL-LBM results as orange lines.

9.4. Refining the Blades: NREL 5MW Wind Turbine

We now move on to a finer mesh around the blades, to demonstrate the advantage of the sliding mesh. In AL simulations it is often preferred to minimize the size of ϵ in order not to artificially extend the radius of the blades. This requires either mesh refinement or more advanced tip corrections [36]. Non isotropic projection functions have also been proposed [5], where ϵ is a fraction of the local airfoil chord and thickness. As ϵ tends to be at least twice the local cell size [37], these non isotropic models require much finer meshes than originally envisioned with AL. With the sliding mesh, we can refine the blades without refining the entire rotor, which we demonstrate in this section.

We use the SOWFA example case based on the NREL 5 MW rotor [38], a 126 m diameter turbine with three blades. Again, we make a few simplifications by removing the tower, the nacelle, the tilt and precone angles, and the controller. These can be included in future simulations. Tip and root corrections are added with $g = 1$. Simulations are conducted with uniform incoming free-stream velocity $U_\infty = 8$ m/s. The turbine rotates at 9.16 RPM and 40 points per blade are used to describe the actuator line. We set ϵ to have the same size as the previous simulation relative to the finest cell size, i.e., 3.5 times the finest cell. Other settings are the same as used in Section 9.3.

For the computational mesh we start with the rotor and wake resolved with cubic cells of side $D/100$, as in Section 9.3. We use two approaches to refine this case: rotor refinement and blade refinement. For rotor refinement, we refine every cell within a distance of 3.04ϵ from the rotor disk. This is illustrated in Figure 9.7. For blade refinement, we refine cells at a distance of 3.04ϵ from the lines that represent the blades, as illustrated in Figure 9.8. In both cases, we quadruple the refinement near the body forces, leading to a local cell size of $D/400$. Compared to the starting point, the two approaches correspond to increasing the cell count in the simulation by 5% for rotor and 0.4% for blade refinement.

While the cell count increases do not seem excessive at a first glance, one must

recall that usually AL simulations have their time step limited to avoid having the blade skip a cell in the simulation. A sliding mesh approach does not necessarily suffer from this limitation and even if certain implementations have a limit on the rotation allowed in a single timestep on the sliding mesh interface, such region can be at a much coarser resolution than the blades. While rotor refinement increases the cell count by 5%, the associated time step reduction in a typical NS AL solver would mean quadrupling the number of time steps. Hence, for this particular example, an AL simulation using an implicit NS solver with a sliding mesh would be 4.2 times cheaper than the stationary mesh approach, the first using blade refinement and the latter rotor refinement.

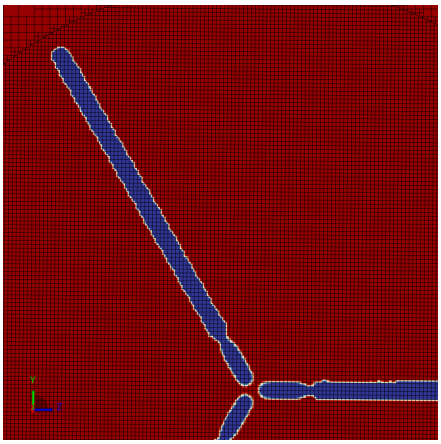

Figure 9.7: Rotor refined mesh. Actuator line shown in blue. Every other grid line drawn in black.

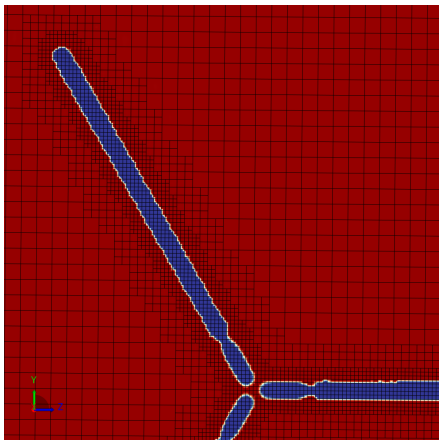

Figure 9.8: Blade refined mesh. Actuator line shown in blue. Every other grid line drawn in black.

In the case of LBM, simulations use explicit time marching schemes, with very small time steps that would avoid the blade skipping a cell. However, local time stepping is typically employed. The finest cells are updated every time step, with the next level being updated every 2 time steps, the next level every 4, then 8, and so on. In this simulation, the cells with size $D/400$ are hence updated 4 times more often than the cells with size $D/100$. This means the finest cells are expensive relative to the other cells and, in this particular case, the rotor refinement is about 23% more expensive than the blade refinement, even though the difference in the two approaches in terms of total cell count is only 6%.

These costs are summarized in Table 9.1. The conclusion is that, given a sliding mesh implementation that does not change the simulation cost substantially, the time savings of using such an approach over the typical static meshes can be significant, if finer resolution on the blades is desired. This is more true for NS than LBM, due to the small timesteps inherent to most explicit LBM solvers.

Cases with rotor and blade refinement were simulated in AL-LBM and are shown in Figures 9.9 and 9.10, respectively. Instantaneous isosurfaces of λ_2 [39] are shown, with remarkably similar results, given the chaotic nature of the flow. The

Table 9.1: Ratio of computational costs associated with simulations using a static mesh with rotor refinement (Static Rotor) and a sliding mesh with blade refinement (Sliding Blade).

	$\frac{\text{Static Rotor}}{\text{Sliding Blade}}$ (ratio)
Number of cells	1.05
Number of timesteps	4
CPU time (implicit NS)	4.2
CPU time (explicit LBM)	1.23

higher tip speed ratio and number of blades on the NREL 5MW rotor compared to the NREL Phase VI rotor make the tip vortices interact earlier, creating complex wake structures [40]. Differences can be seen between the two simulations, with small secondary structures in the rotor plane, in the inner half of the rotor radius, being better resolved in the rotor refined case. However, these differences are small and the tip and hub vortices are very similar in the two simulations. For both cases, the cell size increases by a factor of 4 as soon as the vortices leave the blade or disk refined regions. Therefore, the tip vortices in Figures 9.9 and 9.10 have a substantially larger radius than the bound vortices that represent the blades.

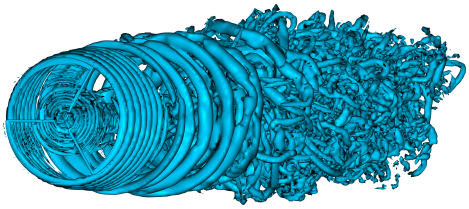

Figure 9.9: Isosurfaces of $\lambda_2 = -5D^2/U_\infty^2$. Rotor refined case in AL-LBM.

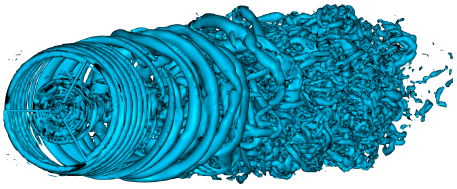

Figure 9.10: Isosurfaces of $\lambda_2 = -5D^2/U_\infty^2$. Blade refined case in AL-LBM.

The thrust and torque obtained with the two methods exhibit excellent agreement. The thrust of the blade refined case is 0.4% higher than the rotor refined case, while the torque is 1% higher. A breakdown of the axial and tangential forces is shown in Figures 9.11 and 9.12. The forces are almost indistinguishable, indicating the methods provide results that are consistent with each other.

Finally, we again look at a vertical profile one diameter downstream of the rotor and compare pressure and velocity components. We observe excellent agreement between the rotor and blade refined simulations, with only minor differences in some of the peak variance values near the hub. This demonstrates the capability of the sliding mesh to perform local refinement in AL simulations without appreciable accuracy loss, with the aforementioned substantial reductions in run time.

9.5. Conclusions

In this work, we demonstrated the AL-LBM implementation and compared the results with a reference NS code, with good agreement between the solutions being observed. The LBM approach often presents performance advantages over

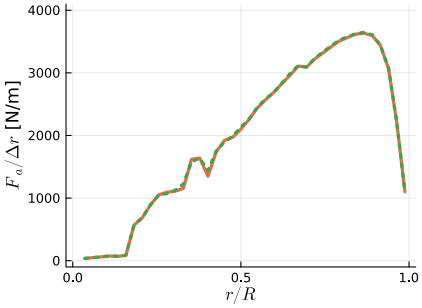

Figure 9.11: Axial force per unit span over blade radius. AL-LBM rotor refined results as orange lines, AL-LBM blade refined results as green dotted lines.

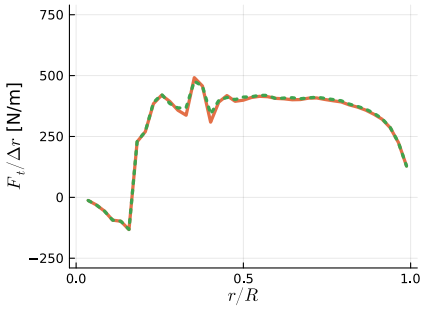

Figure 9.12: Tangential force per unit span over blade radius. AL-LBM rotor refined results as orange lines, AL-LBM blade refined results as green dotted lines.

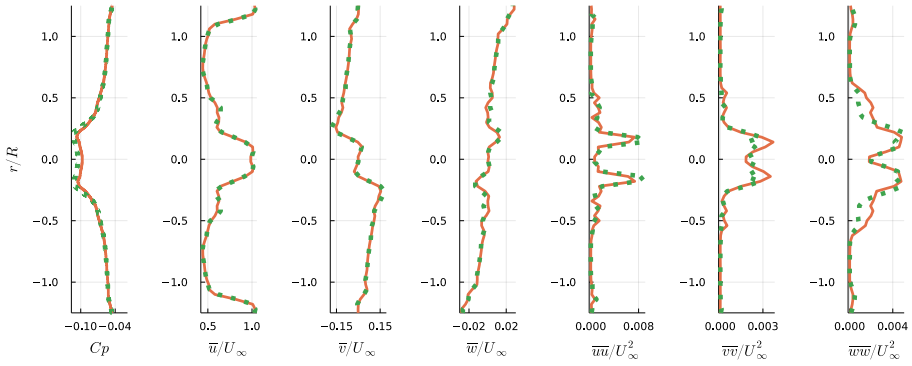

Figure 9.13: Pressure and velocity profiles along a vertical line 126 m downstream of the rotor. AL-LBM rotor refined results as orange lines, AL-LBM blade refined results as green dotted lines.

9

unsteady NS solvers, as demonstrated by other studies [13, 16]. Here, we implemented the AL method in a state of the art solver which can include thermal effects, hence being a potential replacement for NS simulations of wind farms, as the atmospheric boundary layer can be properly modeled. Our main focus was on the impact the sliding mesh in AL simulations, which we believe is a first in the literature. The advantages of the sliding mesh are:

- The mesh can be refined around the blades and tip vortices, while keeping most of the rotor disk at a coarse resolution. We demonstrated that refining the blades can be dramatically more efficient than refining the full rotor in a simulation with a sliding mesh, while providing the same results.
- The body forces do not have to be updated at every time step, which can lead to some computational cost being saved by skipping the BET steps. For

rotors in non-homogeneous flows, the update frequency has to be high, but for homogeneous conditions, few (fewer than 10) updates to the body forces seems sufficient to obtain converged results.

- The sampling stage of the AL algorithm is always done in the same cells of the CFD simulation (in rigid cases), which can improve fluctuations induced from interpolation of the velocity field and can simplify the implementation of the algorithm.
- The sampling always occurring in the same cells also means that the CFD solver only needs to search for the cells that correspond to the actuator lines once, at the start of the simulation. Performing this search at every timestep and within a parallel computing framework can be a bottleneck in AL codes.
- For implicit solvers, the time step can potentially be increased. In traditional AL simulations, the time step is limited so the blade does not travel more than one cell in one time step, which can be mitigated with a sliding mesh, in particular when cells are refined around the blades and coarsened before reaching the interface between rotating and fixed reference frames.

The sliding mesh also has some drawbacks, such as:

- The sliding mesh interface introduces challenges in terms of parallel computing, as the neighbors of the cells change over time. This and the calculation of the flow variables across the interface can increase the computational time.
- The interface between rotating and fixed reference frames can introduce some dissipation or numerical artifacts, depending on the implementation and grid resolution.
- With traditional AL implementations, the Gaussian body forces are allowed to come very close to each other, as with small tower clearance for wind turbines. A sliding mesh approach would require that every object represented by a body force is at a distance of twice the influence length of the body forces (here taken as 3.04ϵ). Hence, small tower clearance or simulations of multiple adjacent rotors can be a challenge. Being able to refine the blades means that the value of ϵ can also be reduced, potentially reducing the impact of this limitation.

Assuming the computational savings and losses when using a sliding mesh on a traditional AL setup cancel out, for typical cases with coarse blades one would likely not benefit tremendously from using a sliding mesh approach. On the other hand, when resolving the blades more finely, the advantages of blade refinement over rotor refinement are substantial. One could potentially achieve the same gains using adaptive mesh refinement, but the cost and complexity of adding it to a simulation are a significant drawback when compared to a sliding mesh approach.

The implementation used in this work can easily be extended to include improvements to the AL method, such as a non-spherical projection of the body forces.

Future work can include the atmospheric boundary layer in stable, neutral, and unstable conditions, including complex terrain. Then, simulation of wind farms can be achieved taking full advantage of the LBM solver used in this work.

References

[1] A. F. P. Ribeiro and C. Muscari, *Sliding mesh simulations of a wind turbine rotor with actuator line lattice-Boltzmann method,* Wind Energy **27**, 1115 (2024).

[2] S. Bouckaert, A. F. Pales, C. McGlade, U. Remme, B. Wanner, L. Varro, D. D'Ambrosio, and T. Spencer, *Net Zero by 2050: A Roadmap for the Global Energy Sector*, Report (International Energy Agency, 2021).

[3] P. Veers, K. Dykes, E. Lantz, S. Barth, C. L. Bottasso, O. Carlson, A. Clifton, J. Green, P. Green, H. Holttinen, *et al.*, *Grand challenges in the science of wind energy,* Science **366**, eaau2027 (2019).

[4] J. N. Sørensen and W. Z. Shen, *Numerical modeling of wind turbine wakes,* Journal of Fluids Engineering **124**, 393 (2002).

[5] M. J. Churchfield, S. J. Schreck, L. A. Martinez, C. Meneveau, and P. R. Spalart, *An advanced actuator line method for wind energy applications and beyond,* 35th Wind Energy Symposium (2017), 10.2514/6.2017-1998.

[6] S. Xie, *An actuator-line model with lagrangian-averaged velocity sampling and piecewise projection for wind turbine simulations,* Wind Energy **24**, 1095 (2021).

[7] P. Schito and A. Zasso, *Actuator forces in cfd: Rans and les modeling in openfoam,* Journal of Physics: Conference Series **524**, 012160 (2014).

[8] W. Z. Shen, W. J. Zhu, and J. N. Sørensen, *Actuator line/navier–stokes computations for the mexico rotor: comparison with detailed measurements,* Wind energy **15**, 811 (2012).

[9] R. J. Stevens, L. A. Martínez-Tossas, and C. Meneveau, *Comparison of wind farm large eddy simulations using actuator disk and actuator line models with wind tunnel experiments,* Renewable energy **116**, 470 (2018).

[10] M. Shives and C. Crawford, *Mesh and load distribution requirements for actuator line CFD simulations,* Wind Energy **16**, 1183 (2013).

[11] H. Chen, C. Teixeira, and K. Molvig, *Digital physics approach to computational fluid dynamics: Some basic theoretical features,* International Journal of Modern Physics C **08**, 675 (1997).

[12] H. Chen, S. Chen, and W. H. Matthaeus, *Recovery of the Navier-Stokes equations using a lattice-gas Boltzmann method,* Physical Review A **45**, R5339 (1992).

[13] E. Manoha and B. Caruelle, *Summary of the LAGOON solutions from the benchmark problems for airframe noise computations-III workshop,* in *21st AIAA/CEAS Aeroacoustics Conference* (2015).

[14] G. Brès, F. Pérot, and D. Freed, *Properties of the lattice Boltzmann method for acoustics,* in *15th AIAA/CEAS Aeroacoustics Conference (30th AIAA Aeroacoustics Conference)* (2012).

[15] S. Rullaud, F. Blondel, and M. Cathelain, *Actuator-line model in a lattice Boltzmann framework for wind turbine simulations,* Journal of Physics: Conference Series **1037**, 022023 (2018).

[16] H. Asmuth, H. Olivares-Espinosa, and S. Ivanell, *Actuator line simulations of wind turbine wakes using the lattice Boltzmann method,* Wind Energy Science **5**, 623 (2020).

[17] M. J. Churchfield, S. Lee, J. Michalakes, and P. J. Moriarty, *A numerical study of the effects of atmospheric and wake turbulence on wind turbine dynamics,* Journal of Turbulence **13**, N14 (2012).

[18] S. Chen, H. Liu, and C. Zheng, *Numerical study of turbulent double-diffusive natural convection in a square cavity by les-based lattice boltzmann model,* International Journal of Heat and Mass Transfer **55**, 4862 (2012).

[19] R. Zhang, C. Sun, Y. Li, R. Satti, R. Shock, J. Hoch, and H. Chen, *Lattice boltzmann approach for local reference frames,* Communications in Computational Physics **9**, 1193 (2011).

[20] J. H. Ferziger and M. Perić, *Computational Methods for Fluid Dynamics*, 3rd ed. (Springer Berlin, 2002).

[21] J. Smagorinsky, *General circulation experiments with the primitive equations: I. the basic experiment,* Monthly Weather Review **91**, 99 (1963).

[22] R. I. Issa, *Solution of the implicitly discretised fluid flow equations by operator-splitting,* Journal of computational physics **62**, 40 (1986).

[23] C. M. Rhie and W. L. Chow, *Numerical study of the turbulent flow past an airfoil with trailing edge separation,* AIAA Journal **21**, 1525 (1983).

[24] V. Yakhot, S. A. Orszag, S. Thangam, T. B. Gatski, and C. G. Speziale, *Development of turbulence models for shear flows by a double expansion technique,* Physics of Fluids A: Fluid Dynamics **4**, 1510 (1992).

[25] E. Fares, B. Duda, A. F. P. Ribeiro, and B. König, *Scale-resolving simulations using a lattice Boltzmann-based approach,* CEAS Aeronautical Journal **9**, 721 (2018).

[26] R. Ferris, M. Sacks, D. Cerizza, A. F. P. Ribeiro, and M. R. Khorrami, *Aeroacoustic computations of a generic low boom concept in landing configuration: Part 1 - aerodynamic simulations,* in *AIAA AVIATION FORUM* (2021).

[27] A. F. P. Ribeiro, *Unsteady analysis of ground vortex ingestion with LBM-VLES,* in *AIAA SCITECH Forum* (2022).

[28] M. R. Khorrami, B. Konig, E. Fares, A. F. P. Ribeiro, M. Czech, and P. A. Ravetta, *Airframe noise simulations of a full-scale large civil transport in landing configuration,* in *AIAA AVIATION FORUM* (2021).

[29] H. Chen, C. Teixeira, and K. Molvig, *Realization of fluid boundary conditions via discrete boltzmann dynamics,* International Journal of Modern Physics C **09**, 1281 (1998).

[30] B. Bonnal, E. Vanoli, A. Placko, and S. Combébias, *Methodology for Simulation of Soak-Back in a Helicopter Engine Bay Using Lattice Boltzmann Method,* in *Turbo Expo: Power for Land, Sea, and Air* (2020).

[31] D. Casalino, W. C. van der Velden, and G. Romani, *A framework for multi-fidelity wind-turbine aeroacoustic simulations,* in *28th AIAA/CEAS Aeroacoustics 2022 Conference* (2022).

[32] T. C. A. Stokkermans, N. van Arnhem, T. Sinnige, and L. L. M. Veldhuis, *Validation and comparison of rans propeller modeling methods for tip-mounted applications,* AIAA Journal **57**, 566 (2019).

[33] R. Merabet and E. Laurendeau, *Actuator line method for helicopter rotors computations in various flight conditions,* CASI AERO 2021 (2021).

[34] M. Hand, D. Simms, L. Fingersh, D. Jager, J. Cotrell, S. Schreck, and S. Larwood, *Unsteady Aerodynamics Experiment Phase VI: Wind Tunnel Test Configurations and Available Data Campaigns*, Tech. Rep. TP-500-29955 (NREL, 2001).

[35] Y. Dubief and F. Delcayre, *On coherent-vortex identification in turbulence,* Journal of Turbulence **1**, N11 (2000).

[36] K. O. Dağ and J. N. Sørensen, *A new tip correction for actuator line computations,* Wind Energy **23**, 148 (2020).

[37] N. Troldborg, *Actuator line modelling of wind turbine wakes,* PhD Thesis, Technical University of Denmark (2009).

[38] J. Jonkman, S. Butterfield, W. Musial, and G. Scott, *Definition of a 5-MW reference wind turbine for offshore system development,* Technical Report TP-500-38060 (2009).

[39] J. Jeong and F. Hussain, *On the identification of a vortex,* Journal of Fluid Mechanics **285**, 69 (1995).

[40] M. Felli, G. Guj, and R. Camussi, *Effect of the number of blades on propeller wake evolution,* Experiments in Fluids **44**, 409 (2008).

10

Blade-Resolved and Actuator Line Simulations of Rotor Wakes

People don't want to live longer.
They want more memories.
And really, how do you get more memories?
It's doing novel, interesting things.

Jimmy Carr

This chapter focuses on high-fidelity numerical simulations of a rotor wake, with a focus on the tip vortices and their stability. Blade-resolved and actuator line lattice-Boltzmann simulations are performed on a baseline rotor, as well as a case with asymmetries. The asymmetry has the purpose of destabilizing the tip vortices to enhance wake recovery and hence the performance of potential downstream turbines. Several limitations in the actuator line method are highlighted, and we show the potential of addressing these limitations with a so-called "preset" actuator line, where the forces are extracted from blade-resolved simulations or an analytical model. Simulations agree well with experimental results and leapfrogging is captured, even with a coarse actuator line simulation. The asymmetric rotor is shown to improve power in the far-wake by 12%.

Parts of this chapter have been submitted for publication in Computers & Fluids (2024) [1].

10.1. Introduction

The near wake of a wind turbine is formed by helical vortices shed from the tips and roots of the rotor blades [2]. These coherent vortices can cause increased fatigue loading on downstream turbines within a wind farm and delay wake recovery by blocking mixing between the low-speed flow inside the wake and the free-stream flow outside [3]. This delayed wake recovery limits the minimum allowable spacing between turbines within a wind farm, reducing the amount of power available for a given area. In existing wind farms, wakes can lead to power losses of up to 40% [4]. Inducing early tip vortex breakdown could help mitigate these detrimental wake effects by enhancing mixing between wake and free-stream and by reducing the amount of coherent vortical structures in the flow.

Tip vortices are subject to various instabilities due to their helical geometry, which can cause them to break down. Since the work of Widnall [5] and Gupta & Loewy [6], it is known that helical vortex systems are inherently unstable. Certain types of deformations are naturally amplified by a mechanism of pairing between successive loops of the helical vortices. These instabilities have been identified as one of the first steps in the deconstruction of the wake of a rotor and its return to equilibrium with the external flow. The instabilities fall into two categories: short-wave and long-wave instabilities [7]. Short-wave instabilities are characterized by perturbations within the vortex core, whereas long-wave instabilities involve displacement of the entire vortex. Long-wave instabilities, which are the focus of the current investigation, lead to pairing between adjacent vortex loops and leapfrogging, where the upstream loop rolls up around and passes in front of the downstream loop. This pairing has been shown to play a significant role in tip vortex breakdown [2, 8].

Recent laboratory experiments and numerical simulations by the authors have shown that tip vortex instabilities can be excited, and hereby accelerate their destruction, by adding particular disturbances (Sarmast et al. [9], Sørensen et al. [10], Quaranta et al. [11], Ramos-García et al. [12], Abraham & Leweke [13]). Among these unstable disturbances are those that can be generated by an asymmetry of the rotor. An intentional asymmetry can be created on the rotors of wind turbines, and in particular those of the first row facing the wind in a wind farm, in order to accelerate the development of the natural instabilities of the vortex system of the wake. This asymmetry may be in the form of an extension or a different pitch setting of one of the blades, or the addition of a flap at the end of a blade, or different flaps on each of the three blades. These devices can be passive or active, oscillating at a suitably chosen frequency to excite the unstable deformations of the vortices.

This work focuses on simulating configurations of a symmetric and an asymmetric rotor by means of high-fidelity numerical simulations. A computational fluid dynamics (CFD) lattice-Boltzmann method (LBM) [14] code is used to perform blade-resolved and actuator line [15] simulations of a rotor, which are validated with experimental data. The LBM has been successfully coupled with the actuator line method by various groups to simulate wind turbines [16–19] and tidal turbines [20, 21]. Blade-resolved simulations are expected to be very accurate, but unfea-

sible for simulation of full wind farms, which is where the less costly actuator line simulations can contribute, as they are typically orders of magnitude faster than blade-resolved simulations. Both methods are validated with experiments, with an emphasis on highlighting the limitations of the actuator line method for our test case.

10.2. Experimental Setup and Flow Conditions

The experiments used for model validation in the current study were conducted in a recirculating free-surface water channel with a test section of dimensions 150 cm $\times$ 38 cm $\times$ 50 cm. A three-bladed rotor was mounted on a shaft with a 1.5 cm diameter, which extends 96 cm downstream to a gearbox connecting the shaft to a stepper motor outside of the water. The rotor has a radius of $R = 9$ cm and the blade cross-sections are NACA2414 airfoils. The tip chord is $c_{tip} = 2.3$ cm, yielding a tip chord-based Reynolds number of $Re = 2\pi f R c_{tip}/\nu \approx 40,000$, where f is the rotation frequency and ν is the fluid kinematic viscosity. Each blade can be detached from the hub individually, enabling the replacement of one or two blades with a slightly modified version to introduce rotor asymmetry. A sketch of the experiment is shown in Fig. 10.1. The chord c and twist θ distributions of the rotor blade over the radius r are shown in Fig. 10.2.

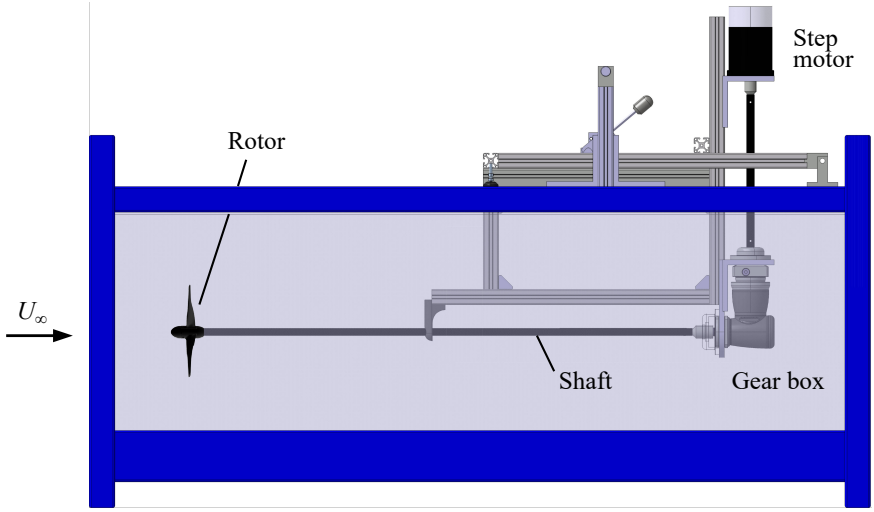

Figure 10.1: Experimental setup.

The rotor was operated at a tip speed ratio of $\lambda = 2\pi f R/U_\infty = \Omega R/U_\infty = 3$, with a free-stream flow speed of $U_\infty = 56$ cm/s and where Ω is the rotor angular velocity. Blade deformation was not deemed substantial and all simulations in this work assume undeformed blades. To visualize the helical tip vortices, fluorescent dye was applied to the blade tips before the rotor was lowered into the water. Once the rotor was submerged and spinning, LED panels were used to illuminate

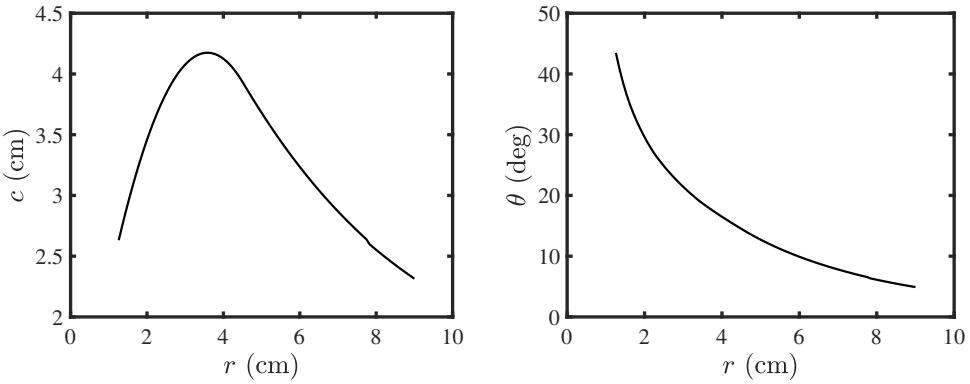

(a) Chord distribution

(b) Twist distribution

Figure 10.2: Description of the blade geometry.

the test section, causing the dye entrained in the tip vortices to fluoresce. Particle image velocimetry was also conducted at two resolutions, 0.88 mm and 0.16 mm, to capture the whole wake and tip vortex velocity fields, respectively. Additional details about the experiment are provided in [13] and the rotor geometry is provided as a supplement in [1].

10.3. Numerical Methods

10.3.1. Lattice-Boltzmann Flow Solver

In this work, the commercial LBM code PowerFLOW is used. The tool has been used extensively for aerodynamics of attached and separated flows [22–25] rotor aerodynamics [26–30], and vortical flows [31, 32]. Turbulence modelling is achieved with a $k-\epsilon$ RNG model [33], with the eddy viscosity being reduced depending on local flow properties [34], which is referred to as very large eddy simulation (VLES).

10.3.2. Actuator Line Tip Corrections

Actuator line (AL) simulations (described in Chapter 8) without any special tip treatments tend to have non-physical force distributions near blade tips. Because of this, tip corrections used in blade element momentum theory are often employed in AL, even if these tip corrections were originally designed to compensate for the infinite-number-of-blades assumption in the momentum theory, which is not an assumption of the AL method. A common tip correction is the Glauert one [35], where G, a function of the radial position r, normalized as $\chi = r/R$, and the flow angle ϕ, is defined as:

$$G = \frac{2}{\pi} cos^{-1}\left(e^{-\frac{B(1-\chi)}{2\chi \sin(\phi)}}\right) \tag{10.1}$$

where B is the number of blades. The root region can use the same correction (replacing $(R-r)$ with $(r-\delta)$, where δ is the radius where the blade lifting sur-

face starts), but alternative formulations for the root correction g have also been proposed [36]:

$$g = 1 - e^{-a(\chi R/\delta)^b} \tag{10.2}$$

where a and b are empirical constants. Using these methods, G and g are multiplied by the forces along the blades, giving the force distributions a more physical behavior.

A more physically meaningful justification for the issues near blade tips in AL is related to the smearing factor [37]. This smearing of the forces causes the trailing vortices from the blades to effectively have a core, instead of following the inviscid behavior of idealized vortices. This causes the induction on nearby blade sections to be reduced, leading to inaccuracies, in particular near the blade tips. In recent years, smearing corrections derived from attempting to make AL into a method consistent with lifting line were achieved. In this work, simulations are performed using the smearing correction of Meyer Forsting et al. [38]. This correction compensates for the smearing of the forces from the vortices produced by the actuator line by combining a near-wake model of the trailed vorticity with the Lamb–Oseen viscous core model and coupling it with the AL model.

10.4. Case Setup

Simulations are conducted in a domain representing the water tunnel used in the experiments. This allows for potential blockage or wall proximity effects to be accounted for. However, the boundary layer on the tunnel walls is assumed to be small and is neglected, by means of free-slip walls in the simulations. A velocity boundary condition is used on the upstream face of the simulation domain and a pressure boundary condition is used on the downstream face, both with constant values in space and time, meaning freestream turbulence is neglected. The experiments were conducted in a water tunnel at low velocities, meaning the flow is incompressible, and hence, Reynolds number matching is important, while the Mach number is less critical. Hence, we simulate the flow assuming air as the fluid, meaning the ideal gas law is used, with the fluid density of air $\rho = 1.23$ kg/m^3, ambient pressure of one atmosphere, and specific gas constant $R = 287$ J/(kgK). However, the viscosity needs to be modified to match the Reynolds number of the experiments, thus ensuring the same physics are being resolved. Hence, we use a fluid viscosity of $\nu = 2\pi f R c_{tip}/Re = 9.75\times10^{-7}$. We then modify the speed of sound so that the freestream Mach number is 0.02, instead of the experimental 3.7×10^{-4}. This is still well within the incompressible range, while providing a timestep that is over 50 times larger than the experimental Mach number would provide (see Eq. 8.7), greatly reducing the simulation cost. Thus, the fluid properties used in the simulation do not correspond to an existing fluid, but ensure Reynolds and Mach numbers that are compatible with reproducing the physics in the experiments.

The blade-resolved simulations are done with the first cell size chosen so that the dimensionless distance of the first cell center to the wall $y^+ < 5$, avoiding the use of wall functions, which is possible with the Cartesian mesh due to the low

Reynolds number of this case. The tip vortex region is resolved with cubic cells of side $R/45$. A sliding mesh is placed around the blades at a distance of $R/9$. The shaft and hub are included in both the blade-resolved and AL simulations. Cases are initialized with free-stream pressure and velocity. All cases are run for 10 full rotor revolutions.

A radial plane showing the volume mesh used in the blade-resolved simulations is shown in Fig. 10.3. The sliding mesh interface is sketched as the thick black line. Adjacent resolution levels always change cell size by a factor of two. Besides refinement near the blade surface, to achieve the aforementioned y^+ values, the mesh is refined in the wake of the rotor in regions where the tip vortices are expected to be present, i.e. in a cylinder behind the blade roots and in a hollow cone section behind the blade tips. In these regions, the cell size is $R/225$. The baseline mesh for the AL simulations is nearly identical to the one shown in Fig. 10.3, but without the small refinement regions near the blades and coarsened by a factor of two.

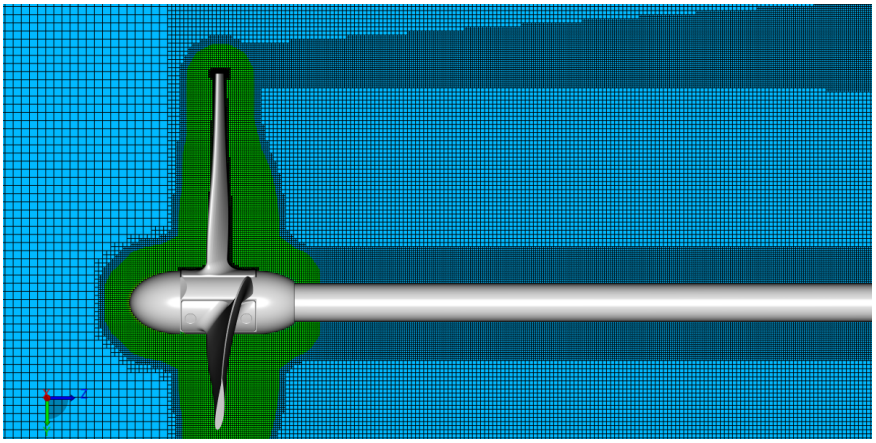

Figure 10.3: Slice of the mesh used in the blade-resolved simulations. Every second line shown. Blue region shows the inertial reference frame, green region is inside the sliding mesh interface.

When mean results are presented, simulations are time-averaged over one rotor rotation and spatially averaged over the azimuth, by taking planes every $5°$ around the circumference of the domain. Instantaneous results are phase-averaged with 20 samples, by taking planes in the blade reference system over one third of a rotation period. These time and phase-averaging approaches are done to achieve the smoothness seen in the experimental results, which were time or phase-averaged over many turbine rotations.

The smearing factor ϵ is a user-defined aspect of AL, with different authors using a wide range of values. Shives and Crawford [39] found the requirements $\epsilon/c \approx 0.25$ and $\epsilon/\Delta > 4$ to be necessary, where c is the airfoil chord and Δ the local mesh size. Churchfield et al. [40] found $\epsilon/D = 0.035$ to be an adequate ratio, where D is the rotor diameter. Dağ & Sørensen [37] tested ϵ/Δ equal to 3 and 5 and found both

to be adequate when using a smearing correction. Kleine et al. [41] found that, for non-planar wings, $\epsilon/\Delta = 7$ produced substantially lower errors than $\epsilon/\Delta = 3.5$.

For our fine AL simulations, if the mesh matches the blade-resolved resolution, we use $\epsilon = 2.8$ mm, which is roughly equal to the blade thickness. This was done in an attempt to match the tip vortex radius obtained in the blade-resolved simulations. This value for ϵ corresponds to $\epsilon/c = 0.12$ at the blade tip, $\epsilon/\Delta = 7$, and $\epsilon/D = 0.016$. On the fine mesh, we set $\Delta = D/225$ in an attempt to resolve the tip vortex with the same resolution as in the blade-resolved simulations. When we change the mesh resolution, we preserve $\epsilon/\Delta = 7$, meaning the baseline AL cases use $\epsilon = 5.6$ mm. All AL cases use 43 actuator points along each blade.

10.5. Results for the Baseline Rotor

10.5.1. Validation of Blade-Resolved Simulation

We begin by performing a validation of the blade-resolved simulations. We do this because we will use the axial force along the blades to validate the AL simulations, and these forces are not available in the experiments. Hence, we must first make sure the blade-resolved simulations are capturing the same thrust distribution as the experiments, then we can use these numerical results as a reference. This comparison is done by examining the mean axial velocity $\bar{u}$ in the wake of the rotor, which by momentum theory, is directly related to the thrust distribution.

Figure 10.4 shows a comparison of $\bar{u}$ along radial (r) lines at several different axial positions (z). The lines are shifted along the horizontal axis for clarity, but the values all start at zero on the bottom of the plots. Excellent agreement between simulations and experiments is achieved for this quantity, giving us confidence that the axial loading on the blades is well captured in the blade-resolved simulations. Further results of the blade-resolved simulations are shown in Section 10.5.3.

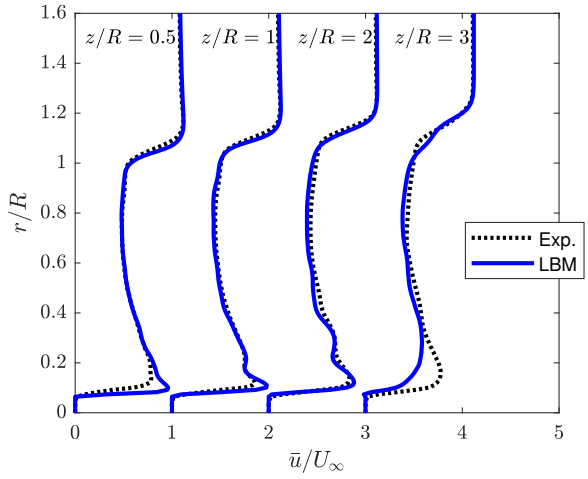

Figure 10.4: Time and azimuthal-averaged axial velocity at different radial lines. Dotted black lines are experimental data, blue lines are blade-resolved simulations.

10.5.2. Validation of the Actuator Line Simulations

We now focus on the AL simulations and attempt to match the axial force distribution on the blades from the blade-resolved case. We start by comparing the blade-resolved axial force distribution with AL simulations with different tip mesh resolutions. The AL simulations are performed on a mesh that is two times coarser than the blade-resolved case, which is still quite fine for AL ($\Delta = R/112.5$), and a coarse mesh, coarsened by a factor of two ($\Delta = R/56.25$). Force distributions are shown in Fig. 10.5 and the thrust coefficients ($C_T = T/(0.5\rho U_\infty^2)$, where T is the integrated thrust) are shown in Table 10.1. The baseline AL results show substantially less thrust than the reference blade-resolved simulations. As indicated by the coarse mesh results, the thrust slightly improves by coarsening the mesh. This is consistent with the findings of Nathan et al. [42] and Meyer Forsting and Troldborg [43], who demonstrated that as the grid resolution increases, AL tends to produce lower torque for the same ϵ/Δ. In order to increase the forces acting on the blades, either the mesh needs to be coarsened or ϵ needs to be larger. Neither of these options is adequate for our purposes, as both would lead to thicker tip vortices.

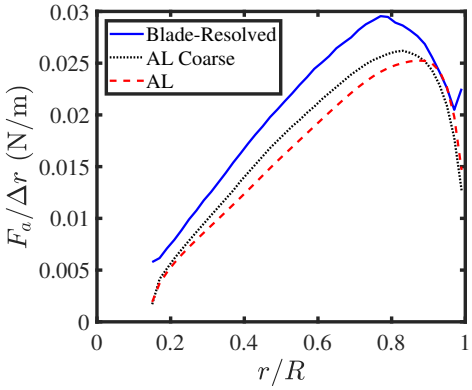

Figure 10.5: Axial forces along the blades. Blade-resolved simulations compared to different actuator line resolutions.

10

Table 10.1: Thrust coefficient for each case, along with relative error compared to blade-resolved case.

	C_T	Error
Blade-resolved	0.96	
Actuator line coarse	0.83	14%
Actuator line	0.78	19%

Potential reasons for the discrepancy of AL and blade-resolved simulations are numerous. The AL simulations use 2D airfoil data for the NACA2414 airfoil at a Reynolds number (Re) of 30,000, which were obtained using XFOIL [44]. This is a popular airfoil for scaled models, as it is known for having good aerodynamic behavior at low Re. However, this behavior was originally studied for Re starting at $60,000$ [45] and the tip Re for this turbine is $40,000$, which leads to large flow

separations according to XFOIL. The very low Re encountered throughout the blade radius led to massive separations in the blade-resolved simulations. Hence, some inaccuracies are to be expected from the AL cases.

Figure 10.6 shows instantaneous surface streamlines from the blade-resolved simulation, demonstrating the 3D flow features. On the pressure side, there is some curvature towards the blade root or tip throughout most of the blade, while on the suction side a large flow separation is present and the streamlines are mostly pointing towards the tip. The images are colored by the pressure coefficient $Cp = (p - p_\infty)/q_\infty$, where p is the static pressure, q the dynamic pressure, and ∞ denotes a free-stream quantity. This massively separated flow makes the AL simulations unreliable for two reasons: first, obtaining polars for separated flows is difficult and depends on Re, meaning highly accurate data would be needed for many angles of attack and Re to represent the entire blade properly. Second, blade element theory, which AL relies on, assumes that the flow around the blades is locally 2D.

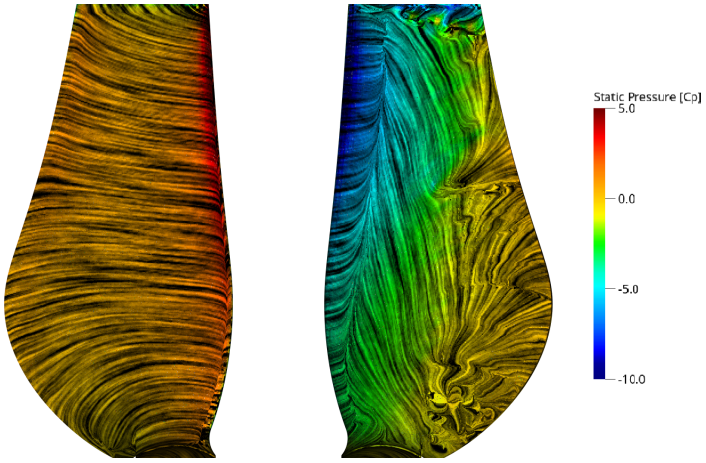

(a) Pressure side (b) Suction side

Figure 10.6: Line integral convolution showing instantaneous surface streamlines colored by pressure coefficient on a blade.

Another issue is that the blade in this study has low aspect-ratio, which is a problem for AL and lifting line. Corrections for low aspect-ratio blades have been proposed [46], but are not used here. These issues put into question the capabilities of AL for our test case and we investigate the potential for AL accuracy further in the next section.

10.5.3. Preset Actuator Line Simulations

As discussed in the previous section, AL has fundamental limitations linked to separated flows. Additionally, likely because of the velocity sampling in the simulation, results can be sensitive to the mesh and the smearing factor sizes [39]. In this section, we verify what the best possible result out of an AL simulation can be for our test case, removing the limitations highlighted in the previous section.

Hence, we employ what we refer to as "preset AL". The blades are still modelled as lines composed of Gaussian blobs applying body forces to the CFD simulations. We use the same mesh as the blade-resolved simulations and $\epsilon = 2.8$ mm, which is roughly equal to the blade thickness. This resolution is consistent with the blade-resolved simulations. However, instead of computing the forces based on sampling the local velocity and using blade element theory, we simply extract the forces on the blades of a blade-resolved simulation and apply them on the preset AL case, with no feedback or table look-ups. No tip or smearing corrections are needed, removing another source of uncertainty. With this method, no assumption of attached 2D flow is made and the only simplification of the rotor in the simulation is that the blades are modelled as actuators instead of walls. The forces are extracted from the blade-resolved simulations by integrating the pressure and friction on the blade surface within rings of constant radii, centered on the locations where the AL body forces are applied.

A second preset AL, which we refer to as "analytical preset AL" only employs thrust and power coefficients as input, whereas the force distribution along the blades is obtained from an analytical model [36]. This model assumes a constant circulation Γ along the blade, with normalized form γ:

$$\gamma = \frac{\Gamma}{4\pi R U_\infty} \tag{10.3}$$

From momentum theory, the thrust coefficient is:

$$C_T = 2a_1\gamma^2 + 4\lambda a_2 \gamma \tag{10.4}$$

where a_1 and a_2 are defined as:

$$a_1 = \int_0^1 \frac{g^2 G^2}{\chi} d\chi \tag{10.5}$$

$$a_2 = \int_0^1 g G \chi d\chi \tag{10.6}$$

where G and g are defined in Eqs. 10.1 and 10.2. For g we use $a = 1.256$ and $b = 2$ [47] and for G we assume the tangential induction is negligible, hence $U_t = \Omega r$ and we can compute the sine term in Eq. 10.1 as:

$$\frac{1}{\sin(\phi)} = \sqrt{1 + \frac{\lambda^2 r^2 U_\infty^2}{R^2 U_a^2}} \tag{10.7}$$

Solving Eq. 10.4 for γ we obtain:

$$\gamma = \frac{-4\lambda a_2 + \sqrt{16\lambda^2 a_2^2 + 8a_1 C_T}}{4a_1} \tag{10.8}$$

The average axial flow velocity at the rotor disk U_a is calculated using momentum theory as:

$$U_a = \frac{U_\infty C_P}{4\lambda a_2 \gamma} \tag{10.9}$$

where $C_P = Q\Omega/(0.5\rho\pi R^2 U_\infty^3)$ is the power coefficient, with Q as the rotor torque. With an initial value of U_a, one can compute Eq. 10.1, update the value of γ, recompute Eq. 10.9, and after a few iterations converge on a value for U_a and γ. Finally, the axial force distribution F_a and tangential force distribution F_t can be computed as:

$$F_a = \frac{\pi R \rho U_\infty^2 g G}{B} \gamma \left(\frac{2\lambda r}{R} + \frac{\gamma R g G}{r} \right) \tag{10.10}$$

$$F_t = \frac{\pi R \rho U_\infty^2 g G}{B} \left(\frac{C_P}{2\lambda a_2} \right) \tag{10.11}$$

Hence, F_a is a function of γ, which depends on C_T, and F_t is a function of C_P.

This analytical approach is more general-purpose than the preset AL, as the amount of information required before conducting the simulation is greatly reduced from full force distributions to C_T and C_P. The drawback is that the force distribution along the blade is not fully correct, but as is shown in Fig 10.7, it is very close to the blade-resolved results.

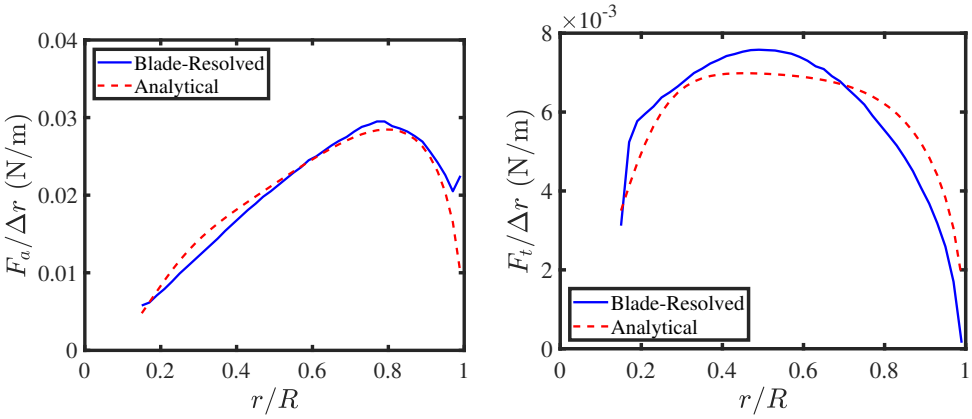

(a) Axial force (b) Tangential force

Figure 10.7: Forces along the blades. Blade-resolved simulations compared to analytical model.

Both preset AL approaches used here assume a fixed force on each blade section over time, meaning these approaches are limited to cases where the flow around the blades does not change over time. Hence, in cases with atmospheric boundary layers, rotor yaw, rotor tilt, or freestream turbulence, the use of the preset AL approaches as they are used here would lead to severe accuracy concerns.

The resulting velocity fields are shown in Fig. 10.8, where we can see the preset AL and blade-resolved results match each other and experimental data very well,

with minor difference in the wake of the blade root. The analytical AL results are also in good agreement with the experiments, with differences mostly confined to the wake of the blade root ($r/R < 0.5$). The standard AL results (here using the coarse mesh) show much weaker tip vortices, barely visible using the same color range as the other cases. The lower thrust seen in Fig. 10.5 is also noticeable here, with the deceleration behind the rotor being less pronounced in the AL case. The blade-resolved case shows a deceleration of the flow near $r/R = 0.1$ and $z/R = 3$ due to the root vortex bursting, which either does not occur in the other case or occurs at a later point. This explains the differences in Fig. 10.4 near the root of the most downstream line.

Similar results can be seen in Fig. 10.9, where the radial component of the velocity is shown for each case. The experiments, blade-resolved simulations, and preset AL simulations once again show excellent agreement. The blade-resolved simulations seems to capture the root vortex more accurately than the preset AL, as evidenced by the contours in $1 < z/R < 2$ and $0 < r/R < 0.5$. The analytical AL results ara again very close to the reference cases, with differences mostly in the blade root wake. The coarse AL case clearly has much weaker tip vortices than the other cases.

A notable feature of the experiments and blade-resolved case is that the tip vortex starts becoming misaligned around $z/R = 3$. This is the beginning of the long-wave instability that leads to leapfrogging. For a perfectly symmetric rotor, this should not happen. In the experiments, the presence of very small asymmetries introduced during rotor assembly ($\sim 0.001R$) can lead to these instabilities, while in the simulations the asymmetry due to having a Cartesian mesh (instead of an axisymmetric mesh) could be the main trigger for leapfrogging. Flow separation around the blades and the chaotic nature of the associated turbulence could also be the source of the instabilities. The AL cases, with their very smooth velocity distributions and more simple wake structure do not exhibit any long-wave instabilities.

While the velocity fields for the blade-resolved and preset AL cases look almost identical in the wake of the rotor, the flow around the real blades has strong separations, which lead to some differences. Figure 10.10 shows the phase-averaged azimuthal velocity, which shows that the wake from the blades is much more visible in the preset AL case. This quantity is not available in the experimental data set. Note the vertical green lines in the blue region of the near wake ($0.2 < z/R < 1.5$). The wakes of the AL blades behave in a steady fashion, while the turbulence in the blade-resolved case causes diffusion, making the wake more difficult to visualize. Overall, using AL leads to higher swirl in the wake.

Finally, we examine the tip vortex itself. Figure 10.11 shows the phase-averaged rotation velocity v_θ around the tip vortex center, measured in a plane rotated $60°$ in the azimuthal direction, downstream of one of the blades. We only focus on the experiments, blade-resolved simulations, and preset AL, as the standard AL simulations produced tip vortices that were clearly too weak, as the thrust distributions indicate, and the analytical preset AL results are very similar to the preset AL. Experimental results are available in low resolution (0.88 mm), which is the resolution

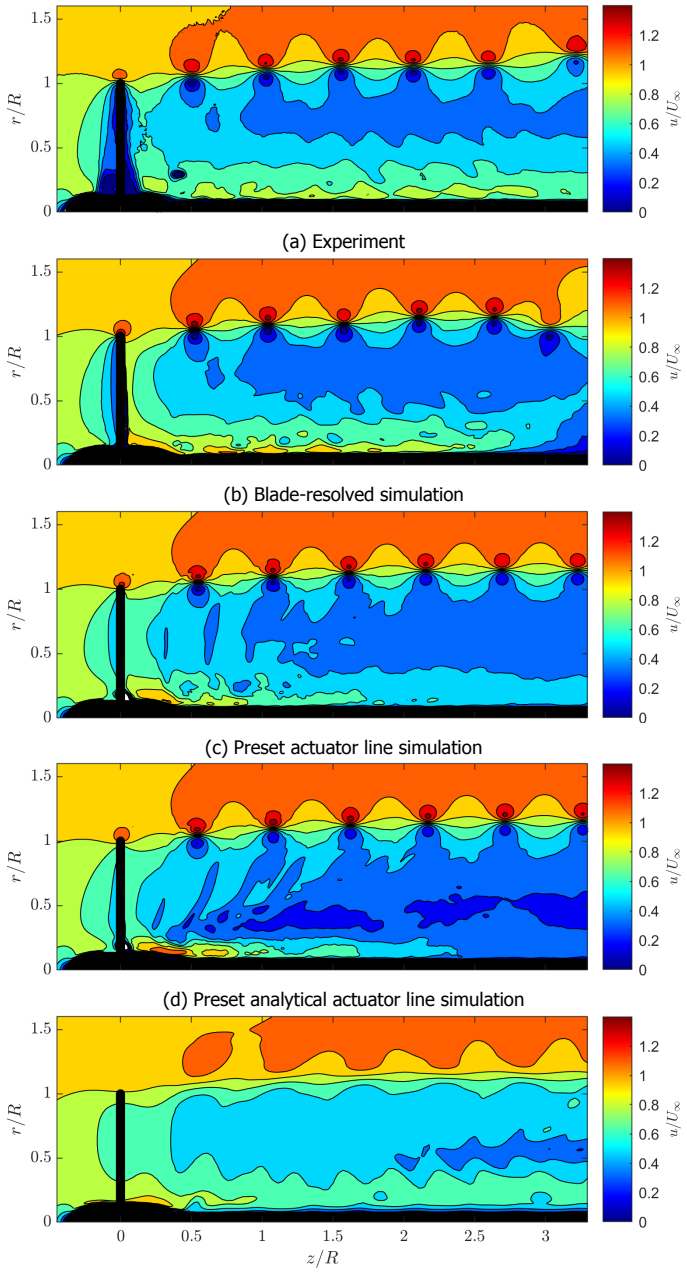

(a) Experiment

(b) Blade-resolved simulation

(c) Preset actuator line simulation

(d) Preset analytical actuator line simulation

(e) Coarse standard actuator line simulation

Figure 10.8: Phase-averaged axial velocity on a $z-r$ plane.

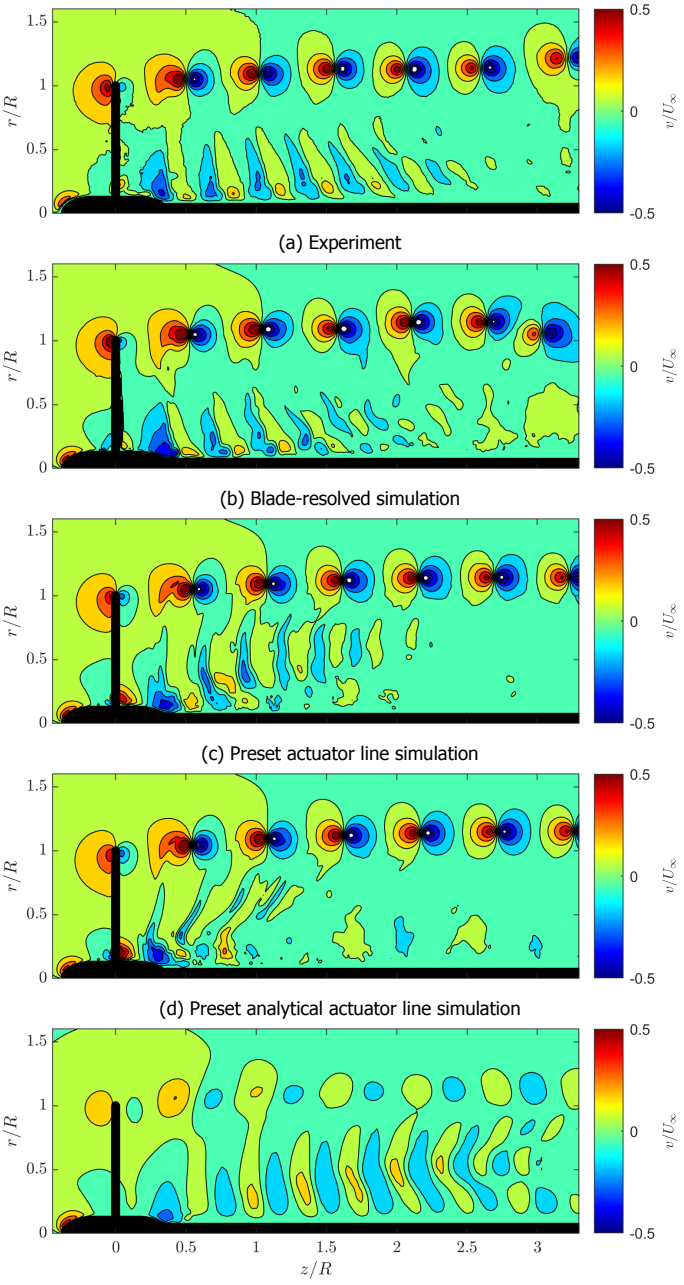

(a) Experiment

(b) Blade-resolved simulation

(c) Preset actuator line simulation

(d) Preset analytical actuator line simulation

(e) Coarse standard actuator line simulation

Figure 10.9: Phase-averaged radial velocity on a $z-r$ plane.

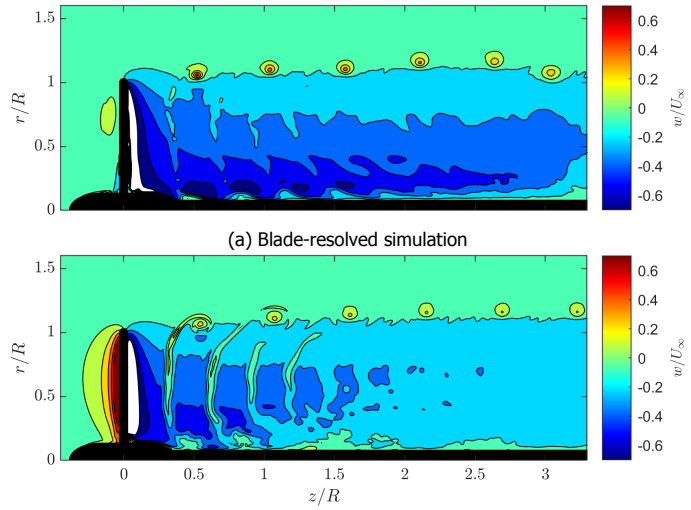

(a) Blade-resolved simulation

(b) Preset actuator line simulation

Figure 10.10: Phase-averaged azimuthal velocity on a $z-r$ plane.

used in the PIV shown in the previous sections, and high resolution (0.16 mm), where the field of view was reduced to a small area around the tip vortex location. The difference between the two experimental curves indicates how difficult it is to capture the vortex core accurately. The preset AL and blade-resolved simulations agree very well with each other, even in terms of the vortex radius (i.e., the value of r corresponding to the maximum value of v_θ), indicating the choice of ϵ is adequate. Both simulations match the velocities induced by the vortex outside of the laminar core for $r > 8$ mm. This agreement means that the vortex circulation is well captured by the simulations, which is consistent with the axial and radial velocity agreement shown in Figs. 10.8 and 10.9. The cell size in the simulations is 0.4 mm, which is too large to capture the core size measured in the experiments (about 1.5 mm). For short-wave instabilities, matching the vortex core is important, whereas for long-wave instabilities, matching the circulation should be enough.

10.6. Asymmetric Rotor Simulations

10.6.1. Validation with Experiments

Here, we simulate cases where one of the blades of the rotor is modified, in order to promote wake instability and earlier recovery. We focus on a case from previous work [13]: extending the radius of one blade by 4.1% ($R = 9.37$ cm). The extended blade geometry is provided as a supplement to this work. The helical vortex system from the experiments, blade-resolved simulation, preset AL simulation, and coarse AL simulation are shown in Fig. 10.12. The blade-resolved simulations show strong short-wave instabilities in the tip vortex, while also capturing secondary flow structures around the tip vortex, which begin near the blade, where

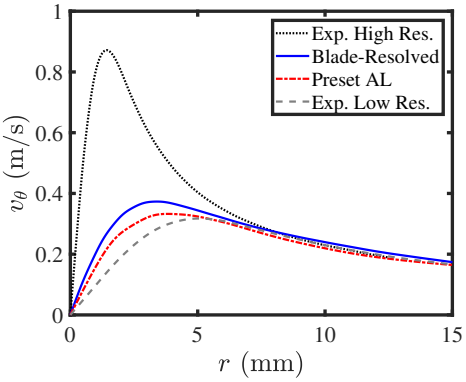

Figure 10.11: Tangential velocity around the tip vortex core.

massive flow separation occurs. These secondary structures, or turbulent worms [48], are not visible in the experiments, which may be due to the dye being entrained only in the primary tip vortex. They have been shown to occur in reality, but are only numerically captured via blade-resolved, scale-resolved simulations [49]. The coarse AL results have a much thicker tip vortex, due to the low resolution and high ϵ. All cases capture the leapfrogging that occurs in the helical wake due to the asymmetric rotor.

The distance z_L from the rotor plane where leapfrogging, or the swapping of axial positions between two adjacent vortex loops, occurs was measured for each case. It is compared to experimental data [13] in Table 10.2. In both simulation and experiment the leapfrogging location was determined visually as the point where two successive loops have the same axial coordinate. As previously discussed, small imperfections in simulations and experiments lead to leapfrogging in experiments and blade-resolved simulations of the symmetric rotor. The AL simulations are much less turbulent than the blade-resolved ones, with effectively steady flow around the fictitious blades. Hence, in AL leapfrogging does not occur, whereas in blade-resolved simulations and in experiments it occurs at similar locations for reasons that could be coincidental.

10

Table 10.2: Streamwise position z_L/R where leapfrogging occurs for each case.

	Baseline	Extended
Experiment [13]	4.09	2.73
Blade-resolved	4.1	2.9
Preset actuator line	No	3.1
Actuator line	No	3.7

When one blade is extended, the asymmetry introduces a disturbance in the helical vortex system that leads to leapfrogging. The blade-resolved simulations capture leapfrogging within 6% of experimental values, whereas the AL simulations overshoot the leapfrogging location by 14% for the preset case and 36% for the

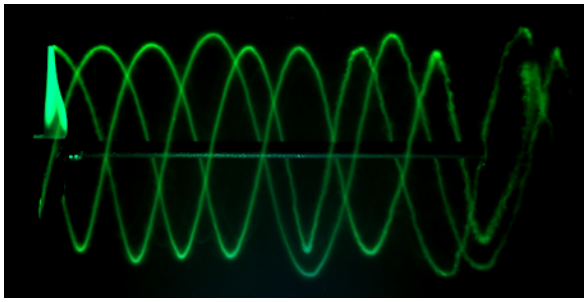

(a) Experimental results, dye visualization [13]

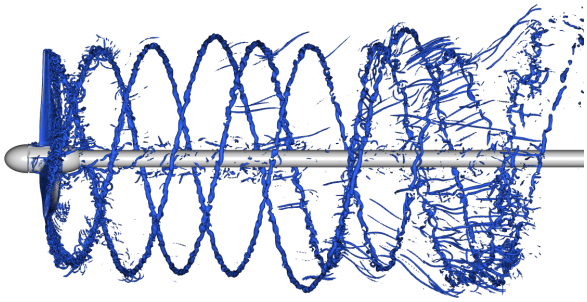

(b) Blade-resolved simulation, isosurface of $\lambda_2 = -300R^2/U_\infty^2$

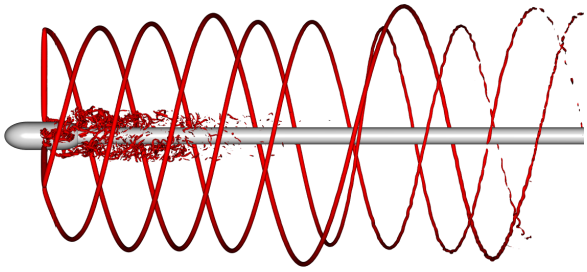

(c) Preset actuator line simulation, isosurface of $\lambda_2 = -300R^2/U_\infty^2$

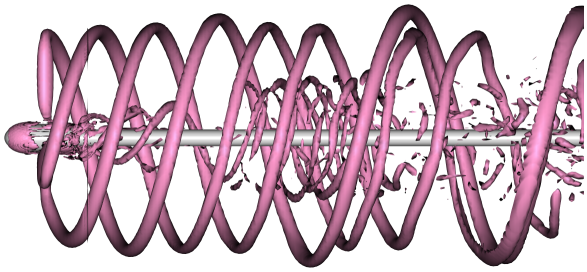

(d) Coarse standard actuator line simulation, isosurface of $\lambda_2 = -5R^2/U_\infty^2$

Figure 10.12: Visualization of tip vortex for extended blade case.

coarse AL case. The steady nature of the vortex system in AL is likely responsible for stabilizing the helical vortex system. Hence, AL is unsuitable for predicting the exact location of tip vortex instability, but can likely still be used for wind farm studies, where the exact instability location is less relevant than the far-wake mixing.

10.6.2. Far-Wake Analysis

We now go beyond the experiments, which were limited to the near-wake, and move on to simulating the far-wake, in order to investigate the potential wake-recovery benefits of the asymmetric rotor. We extend the simulation domain downstream, in order to examine the wake up to a distance of $14R$ of the rotor. Simulations are conducted with the preset AL method, in order to save on computational time, and the shaft is removed. The tip vortices for the baseline and asymmetric rotor are shown in Fig. 10.13. In spite of the smooth vortices of AL, the asymmetric case eventually develops instabilities, near $z/R = 6.5$. This is likely due to small asymmetries in the flow introduced by the Cartesian mesh and potential short-wave instabilities, which are not axisymmetric. The asymmetric rotor still leads to leapfrogging in under half the distance ($z_L/R = 3.1$), meaning it is still likely to lead to better wake recovery.

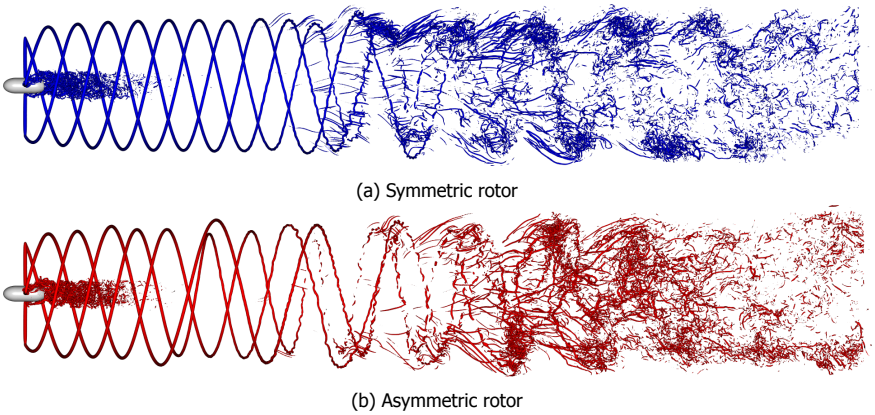

(a) Symmetric rotor

(b) Asymmetric rotor

Figure 10.13: Visualization of tip vortex for extended domain cases. Preset AL, isosurface of $\lambda_2 = -200R^2/U_\infty^2$.

The power available for a wind turbine is proportional to u^3. This allows us to estimate the available power for wind turbines downstream of our rotor, normalized by the power available to our rotor:

$$\text{Available Power} = \frac{\int u^3 \mathrm{d}A}{\int U_\infty^3 \mathrm{d}A} \tag{10.12}$$

where A refers to the area of a disk of radius R perpendicular to, and centered on, the rotor axis, at several z/R locations. The results of this analysis are shown in Fig. 10.14. At a distance of $14R$, the asymmetric rotor allows for 12% more power to reach a potential wind turbine, in spite of the longer blade leading to slightly

more thrust than the symmetric rotor. This demonstrates the potential of the tip extension for far-wake recovery in a wind farm.

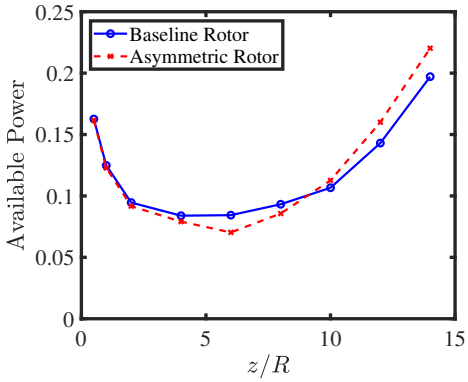

Figure 10.14: Available power in the wake of the rotor.

10.7. Conclusions and Outlook

Blade-resolved and actuator line lattice-Boltzmann simulations of a small three-bladed rotor, operating as a wind turbine, were shown in this work. Simulations were validated with experimental data, showing a remarkable agreement for the blade-resolved simulations. The actuator line was shown to have moderate dependence on the mesh resolution. Coarsening the mesh improves the actuator line thrust generation, but also necessarily makes the tip vortices thicker.

Preset actuator line simulations, where the body forces are copied from the blade-resolved simulations, with no feedback from the flow velocity or look-up tables, are conducted. These preset simulations show excellent agreement with blade-resolved simulations and experiments, which leads to the conclusion that it is possible to model this case with actuator line, but the 2D assumptions, airfoil data, and sampling introduce substantial errors. The preset actuator line simulations, using the same tip vortex resolution as the blade-resolved case, used one fifth of the computational resources. It was shown that having the thrust and power of the turbine is sufficient to produce accurate preset actuator line simulations, by using an analytical model to compute the force distributions along the blades.

Tip vortex instability was examined and we found short-wave instabilities in the blade-resolved simulations, which were not visible in the experiments. Long-wave instabilities leading to leapfrogging were found when the rotor was made asymmetric by extending one blade radially. All simulations were able to capture the leapfrogging caused by the asymmetric rotor, with the preset and standard actuator line cases predicting the location of leapfrogging less accurately than the blade-resolved simulations.

Finally, the effects of rotor asymmetry on the far-wake were investigated by using preset actuator line simulations with a longer domain than was available in

the experiments. The wake recovery introduced by early leapfrogging led to an increase of 12% in the available power for a downstream turbine perfectly aligned with the rotor, at a distance of 7 rotor diameters.

Future work will focus on simulating different asymmetric rotor configurations, focusing on the effects of vortex instability on wake recovery over long distances. The effect of free-stream turbulence will also be investigated.

References

[1] A. F. P. Ribeiro, T. Leweke, A. Abraham, J. N. Sørensen, and R. F. Mikkelsen, *Blade-resolved and actuator line simulations of rotor wakes,* Computers & Fluids **287**, 106477 (2025).

[2] J. N. Sørensen, *Instability of helical tip vortices in rotor wakes,* Journal of Fluid Mechanics **682**, 1– (2011).

[3] L. E. M. Lignarolo, D. Ragni, F. Scarano, C. J. Simão Ferreira, and G. J. W. Van Bussel, *Tip-vortex instability and turbulent mixing in wind-turbine wakes,* Journal of Fluid Mechanics **781**, 467 (2015).

[4] J. C. Y. Lee and M. J. Fields, *An overview of wind-energy-production prediction bias, losses, and uncertainties,* Wind Energy Science **6**, 311 (2021).

[5] S. E. Widnall, *The stability of a helical vortex filament,* Journal of Fluid Mechanics **54**, 641– (1972).

[6] B. P. Gupta and R. G. Loewy, *Theoretical analysis of the aerodynamic stability of multiple, interdigitated helical vortices,* AIAA Journal **12**, 1381 (1974).

[7] T. Leweke, H. U. Quaranta, H. Bolnot, F. J. Blanco-Rodríguez, and S. L. Dizès, *Long- and short-wave instabilities in helical vortices,* Journal of Physics: Conference Series **524**, 012154 (2014).

[8] M. Felli, R. Camussi, and F. Di Felice, *Mechanisms of evolution of the propeller wake in the transition and far fields,* Journal of Fluid Mechanics **682**, 5 (2011).

[9] S. Sarmast, R. Dadfar, R. F. Mikkelsen, P. Schlatter, S. Ivanell, J. N. Sørensen, and D. S. Henningson, *Mutual inductance instability of the tip vortices behind a wind turbine,* Journal of Fluid Mechanics **755**, 705 (2014).

[10] J. N. Sørensen, R. F. Mikkelsen, D. S. Henningson, S. Ivanell, S. Sarmast, and S. J. Andersen, *Simulation of wind turbine wakes using the actuator line technique,* Philosophical Transactions of the Royal Society A: Mathematical, Physical and Engineering Sciences **373**, 20140071 (2015).

[11] H. U. Quaranta, M. Brynjell-Rahkola, T. Leweke, and D. S. Henningson, *Local and global pairing instabilities of two interlaced helical vortices,* Journal of Fluid Mechanics **863**, 927– (2019).

[12] N. Ramos-García, A. Abraham, T. Leweke, and J. N. Sørensen, *Multi-fidelity vortex simulations of rotor flows: Validation against detailed wake measurements,* Computers & Fluids **255**, 105790 (2023).

[13] A. Abraham and T. Leweke, *Experimental investigation of blade tip vortex behavior in the wake of asymmetric rotors,* Experiments in Fluids **64**, 109 (2023).

[14] H. Chen, C. Teixeira, and K. Molvig, *Digital physics approach to computational fluid dynamics: Some basic theoretical features,* International Journal of Modern Physics C **08**, 675 (1997).

[15] J. N. Sørensen and W. Z. Shen, *Numerical modeling of wind turbine wakes,* Journal of Fluids Engineering **124**, 393 (2002).

[16] S. Rullaud, F. Blondel, and M. Cathelain, *Actuator-line model in a lattice Boltzmann framework for wind turbine simulations,* Journal of Physics: Conference Series **1037**, 022023 (2018).

[17] H. Asmuth, H. Olivares-Espinosa, and S. Ivanell, *Actuator line simulations of wind turbine wakes using the lattice Boltzmann method,* Wind Energy Science **5**, 623 (2020).

[18] H. Schottenhamml, A. Anciaux-Sedrakian, F. Blondel, A. Borras-Nadal, P.-A. Joulin, and U. Rüde, *Evaluation of a lattice Boltzmann-based wind-turbine actuator line model against a Navier-Stokes approach,* in *Journal of Physics: Conference Series*, Vol. 2265 (IOP Publishing, 2022) p. 022027.

[19] A. F. P. Ribeiro and C. Muscari, *Sliding mesh simulations of a wind turbine rotor with actuator line lattice-Boltzmann method,* Wind Energy **27**, 1115 (2024).

[20] M. Grondeau, S. Guillou, P. Mercier, and E. Poizot, *Wake of a ducted vertical axis tidal turbine in turbulent flows, LBM actuator-line approach,* Energies **12**, 4273 (2019).

[21] S. Watanabe and C. Hu, *Lattice Boltzmann simulations for multiple tidal turbines using actuator line model,* Journal of Hydrodynamics **34**, 372 (2022).

[22] A. F. P. Ribeiro, D. Singh, B. Konig, and E. Fares, *On the stall characteristics of iced wings,* in *55th AIAA Aerospace Sciences Meeting* (2017).

[23] B. König, D. Singh, A. Ribeiro, and E. Fares, *Lattice-boltzmann simulations at the corners of the flight envelope,* 54th 3AF International Conference on Applied Aerodynamics (2019).

[24] C. L. Rumsey, J. P. Slotnick, and A. J. Sclafani, *Overview and summary of the third AIAA high lift prediction workshop,* Journal of Aircraft **56**, 621 (2019).

[25] B. Konig, B. M. Duda, and G. M. Laskowski, *Lattice Boltzmann simulations for the 4th AIAA high-lift prediction workshop using PowerFLOW,* in *AIAA AVIATION Forum* (2022).

[26] S. D. Lucas-Bodas, J. Narbona-Gonzalez, V. Ossorio-Contreras, J. Jose, Guerra-Crespo, D. E. Funes-Sebastian, and L. P. Ruiz-Calavera, *Experimental validation of numerical prediction of wing-propeller aerodynamic interaction,* 32nd Congress of the International Council of the Aeronautical Sciences (2021).

[27] W. van der Velden, G. Romani, and D. Casalino, *Validation and insight of a full-scale S-76 helicopter rotor using the lattice-Boltzmann method,* Aerospace Science and Technology **118**, 107007 (2021).

[28] D. Casalino, W. C. van der Velden, and G. Romani, *A framework for multi-fidelity wind-turbine aeroacoustic simulations,* in *28th AIAA/CEAS Aeroacoustics 2022 Conference* (2022).

[29] G. Romani, E. Grande, F. Avallone, D. Ragni, and D. Casalino, *Performance and noise prediction of low-Reynolds number propellers using the lattice-Boltzmann method,* Aerospace Science and Technology **125**, 107086 (2022).

[30] A. F. P. Ribeiro, R. Duivenvoorden, and D. Martins, *High-fidelity simulations of propeller-wing interactions in high-lift conditions,* in *AIAA AVIATION Forum* (2023).

[31] A. F. P. Ribeiro, *Unsteady analysis of ground vortex ingestion with LBM-VLES,* in *AIAA SCITECH Forum* (2022).

[32] R. Ferris, M. Sacks, D. Cerizza, A. F. P. Ribeiro, and M. R. Khorrami, *Aeroacoustic computations of a generic low boom concept in landing configuration: Part 1 - aerodynamic simulations,* in *AIAA AVIATION FORUM* (2021).

[33] V. Yakhot, S. A. Orszag, S. Thangam, T. B. Gatski, and C. G. Speziale, *Development of turbulence models for shear flows by a double expansion technique,* Physics of Fluids A: Fluid Dynamics **4**, 1510 (1992).

[34] E. Fares, B. Duda, A. F. P. Ribeiro, and B. König, *Scale-resolving simulations using a lattice Boltzmann-based approach,* CEAS Aeronautical Journal **9**, 721 (2018).

[35] W. Z. Shen, R. Mikkelsen, J. N. Sørensen, and C. Bak, *Tip loss corrections for wind turbine computations,* Wind Energy **8**, 457 (2005).

[36] J. N. Sørensen, K. Nilsson, S. Ivanell, H. Asmuth, and R. F. Mikkelsen, *Analytical body forces in numerical actuator disc model of wind turbines,* Renewable Energy **147**, 2259 (2020).

[37] K. O. Dağ and J. N. Sørensen, *A new tip correction for actuator line computations,* Wind Energy **23**, 148 (2020).

[38] A. R. Meyer Forsting, G. R. Pirrung, and N. Ramos-García, *A vortex-based tip/smearing correction for the actuator line,* Wind Energy Science **4**, 369 (2019).

[39] M. Shives and C. Crawford, *Mesh and load distribution requirements for actuator line CFD simulations,* Wind Energy **16**, 1183 (2013).

[40] M. J. Churchfield, S. J. Schreck, L. A. Martinez, C. Meneveau, and P. R. Spalart, *An advanced actuator line method for wind energy applications and beyond,* 35th Wind Energy Symposium (2017), 10.2514/6.2017-1998.

[41] V. G. Kleine, A. Hanifi, and D. S. Henningson, *Simulating airplane aerodynamics with body forces: Actuator line method for nonplanar wings,* AIAA Journal **61**, 2048 (2023).

[42] J. Nathan, C. Masson, and L. Dufresne, *Near-wake analysis of actuator line method immersed in turbulent flow using large-eddy simulations,* Wind Energy Science **3**, 905 (2018).

[43] A. R. M. Forsting and N. Troldborg, *Generalised grid requirements minimizing the actuator line angle-of-attack error,* Journal of Physics: Conference Series **1618**, 052001 (2020).

[44] M. Drela, *XFOIL: An analysis and design system for low Reynolds number airfoils,* in *Low Reynolds Number Aerodynamics*, edited by T. J. Mueller (Springer Berlin Heidelberg, Berlin, Heidelberg, 1989) pp. 1–12.

[45] M. S. Selig, C. A. Lyon, P. Giguere, C. P. Ninham, and J. J. Guglielmo, *Summary of Low-Speed Airfoil Data, Volume 2* (SoarTech Publications, 1996).

[46] J. N. Sørensen, K. O. Dag, and N. Ramos-García, *A refined tip correction based on decambering,* Wind Energy **19**, 787 (2016).

[47] J. M. Delery, *Aspects of vortex breakdown,* Progress in Aerospace Sciences **30**, 1 (1994).

[48] N. M. Chaderjian, *Advances in rotor performance and turbulent wake simulation using des and adaptive mesh refinement,* in *Seventh International Conference on Computational Fluid Dynamics (ICCFD7)* (2012).

[49] P. Weihing, M. Cormier, T. Lutz, and E. Krämer, *The near-wake development of a wind turbine operating in stalled conditions – part 1: Assessment of numerical models,* Wind Energy Science **9**, 933 (2024).

11

Propeller-Wing Interactions in High-Lift Conditions

Technique is no substitute for power.

Ben Moon

The recent increased interest in distributed propulsion and electric vertical take-off and landing vehicles have made propeller wake interactions with the aircraft more relevant. The interaction between high-lift wings and propeller slipstreams are still not fully understood and several research efforts are being carried out to improve that knowledge. Lattice-Boltzmann, very large eddy simulations of a propeller-wing-flap configuration are conducted in this chapter. The simulations are validated with experimental data, with very good agreement of surface static pressure, surface shearlines, and wake total pressure. The complex separation patterns on the flap and their interaction with the slipstream of the propeller are well captured. The effects of grid resolution and laminar-to-turbulent transition are demonstrated. With the simulations validated, they are used to better understand the flow field of this configuration. We find that the angle of attack has a strong effect on how the slipstream is split over the wing, that the tip vortices wrap around the wing leading-edge instead of being cut by it, and that increased circulation stabilizes the tip vortices on the suction side, while making the tip vortices on the pressure side more unstable.

Parts of this chapter have been published in AIAA Aviation (2023) [1], co-written with Ramon Duivenvoorden.

11.1. Introduction

With the recent boom in the electric vertical take-off and landing (eVTOL) market and the interest in hydrogen-powered short-haul aircraft, distributed propulsion has become an important academic and industrial topic. Several institutions are investigating aircraft with large numbers of propellers on their wings, such as the NASA X-57 [2]. Extensive fundamental studies on propeller installation effects have been conducted at the Delft University of Technologu (TUD), focusing on tip mounted propellers [3], interaction between multiple propellers [4], distributed propulsion [5] and propeller-wing interaction in high-lift conditions [6]. The latter provides a challenging case for numerical methods, with highly complex and interactive flow fields featuring dominant viscous effects.

In this work, recent experimental results from TUD [6] are used to validate numerical simulations of interactions between a propeller and a wing with a deployed flap. The lattice-Boltzmann method (LBM) [7] is used as an alternative to the Navier-Stokes (NS) equations [8]. This method is particularly suited for high-fidelity simulations of wakes, as it offers low-dissipation characteristics equivalent to high order methods [9], while being orders of magnitude faster than traditional computational fluid dynamics (CFD) solvers [10].

11.2. Numerical Methods

Our LBM computations are conducted with PowerFLOW, a commercial CFD code. A sliding mesh [11] is used to rotate the propeller. Validations of the approach used here that are relevant to this work include vortical flows [12], rotors [13], tracks [14], wings in stall conditions [15], and a propeller-mounted high-lift wing [16].

11.3. Test Case Description

The geometry used in this work is a straight wing based on the NLF-Mod22(B) airfoil [17], with a nested chord $c = 300$ mm, a span of 1.248 m, and a Fowler flap with 30% of the full airfoil chord. The wing is equipped with a TUD-XPROP-S reference propeller [5, 18], with a diameter $D = 203.2$ mm and a blade pitch at 70% of the radius of 30°. The propeller is installed 173.5 mm ($\approx 0.858D$) from the leading-edge, with the axis of rotation angled $5°$ with respect to the wing chord line. The flow conditions are freestream velocity $U_\infty = 30$ m/s, resulting in $Re \approx 600{,}000$, and a propeller advance ratio of $J = U_\infty/(Dn) = 0.8$, where n is the rotational speed in rotations per second.

11.3.1. Experimental Setup

The experimental data used for validation in this paper were obtained in the Low Turbulence Tunnel at the TUD. The cross-section of the octagonal test section measures 1.25 m high by 1.8 m wide and is slightly divergent to compensate for the wall boundary layer. The wing was mounted vertically, clamped between both walls, with the flap attached the main element using 6 brackets. The main element of the wing model was tripped by a zigzag-strip, while the flap was left to transition

naturally.

The experimental data set includes pressure tap measurements, total pressure in the wake plane, and oil flow visualizations. The pressure taps were located in two chord-wise rows positioned at $y = 0.7R$ on either side of the nacelle. A wake rake of total pressure probes on a traverse mechanism was used to capture total pressure in the wake, one chord downstream of the nested flap trailing-edge, with a resolution of 10 mm in spanwise and 3 mm in vertical directions. Oil flow visualization was achieved using a solution of UV-luminescent material in a light paraffin oil, taking images while wind was on after the oil had been allowed to transport sufficiently. Further details on the experimental setup are detailed in [6]. Table 11.1 summarizes the configurations and data points from the experiment which are considered for validation in this paper. Here, δ_f is the flap deflection angle, dx is the flap overlap with the main element, and ds is the gap between the flap and the main element leading-edge.

Table 11.1: Overview of experimental configurations used for validation.

δ_f [°]	ds [c]	dx [c]	U_∞ [m/s]	J [-]
0	-	-	30	0.8
15	0.02	0.08	30	0.8
30	0.03	0	30	0.8

Pressure tap measurements were taken at angles of attack α between -5 and 18° for the flap nested configuration, and up to 14° for the flap deployed configurations. Oil flow visualisations were taken for $\alpha = 0$ and 10° for the flap nested configuration, and $\alpha = 0$, 5, 8 and 10° for the flap deployed configurations. Wake rake measurements were taken at the same angles as the oil flow, with the exclusion of $\alpha = 5$° for the flap deployed configurations.

11.3.2. Numerical Setup

Simulations are run with PowerFLOW 6-2021-R7, using the subsonic isothermal solver, as the freestream Mach number is 0.088 and the tip Mach number due to the propeller rotation is 0.35. A Cartesian mesh is used, with cubic cells ranging from 0.03 mm on the propeller blades leading-edges to 61 mm far from the wing. An average y^+ of 40 was used on the wing. A large refinement cylinder with cell size of 0.96 mm was placed around the propeller wake, to avoid numerical dissipation up to the experimental measurement plane. A refinement region, with cell size of 0.48 mm, was placed near the flap upper surface, to capture separation effects and the shear layer from the main element trailing-edge. A plane showing the mesh setup is shown in Fig. 11.1, where the outline of the sliding mesh interface, which is 10 mm from the blades and spinner, can also be seen.

The mesh dimensions given in the previous paragraph are for the baseline mesh used throughout this study. This can also be referred to as the medium resolution cases. Two additional setups are used, to check for grid independence of the results. These are the coarse and fine cases, which have cells that are 1.25 times larger and smaller than the medium case, respectively. Due to the nature of the Cartesian

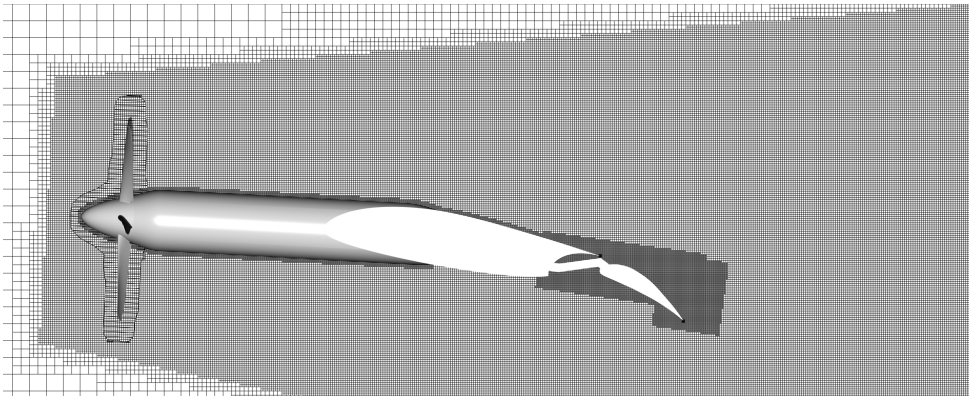

Figure 11.1: Center plane of the wing showing the mesh used in the simulations. Every other line shown for clarity.

mesh, that means that the ratio of the number of cells from coarse to medium and from medium to fine is about two.

The simulations are setup similar to previous works on wing sections [19, 20]. The wind tunnel walls are included to account for blockage effects, but are simulated as free slip walls. Hence the additional blockage effects due to the side walls boundary layers are neglected. These effects can be included if needed, but it is often challenging to do so exactly [21]. The side walls boundary layers effects on the wing root vortex are also neglected. Unless stated otherwise, the surfaces of the propeller and wing are modelled as fully turbulent. The boundary conditions used in the upstream and downwind faces of the numerical wind tunnel are a velocity inlet and a pressure outlet, respectively.

11.4. Validation of Numerical Results

In this Section, we perform a thorough comparison with experimental data, before moving on to conducting a detailed analysis of the flow in Section 11.5.

11.4.1. Propeller Thrust

The reference thrust coefficient of the TUD-XPROP-S propeller is $T_c = T/(q_\infty A) = 1.05$, where T is the thrust force, $q_\infty = 0.5\rho_\infty U_\infty^2$ is the freestream dynamic pressure, ρ_∞ is the freestream air density, and A is the propeller rotor plane area. This was measured for the isolated propeller at $\alpha = 0°$. We can use this as an approximate reference for our simulations and concurrently verify if the propeller thrust achieved in CFD is grid convergent. The values of T_c for the three resolutions simulated at $\delta_f = 30°$, $\alpha = 8°$ are shown in Table 11.2. The reason for this specific flap and wing angle settings are that we also use the same simulations to perform a resolution study on the wing aerodynamics (see Section 11.4.2), and this is the case with the most complex aerodynamics.

Grid convergent behavior is observed, with the difference between the fine and

Table 11.2: Propeller thrust for different grid resolutions at $\delta_f = 30°$, $\alpha = 8°$ and experimental value for isolated propeller at $\alpha = 0°$.

Resolution	T_c
Coarse	1.032
Medium	1.039
Fine	1.042
Experiment	1.05

medium grids being over two times smaller than the difference from medium to coarse. The value of T_c is within 1% of the reference for the isolated propeller, which we consider adequate.

11.4.2. Wing Pressure Distribution

Pressure coefficient $Cp = (p - p_\infty)/q_\infty$, where p is the static pressure and p_∞ is the freestream static pressure, are computed on two planes on either side of the propeller. The two Cp cut locations, named up-going and down-going, are on planes at 70% of the propeller radius (71.12 mm), on either side of the propeller axis. We select the highest flap deflection and angle of attack in our simulations, to perform a resolution study of Cp, as this should be a challenging case and would indicate the resolution is adequate for the other cases. The results of this study are shown in Fig. 11.2.

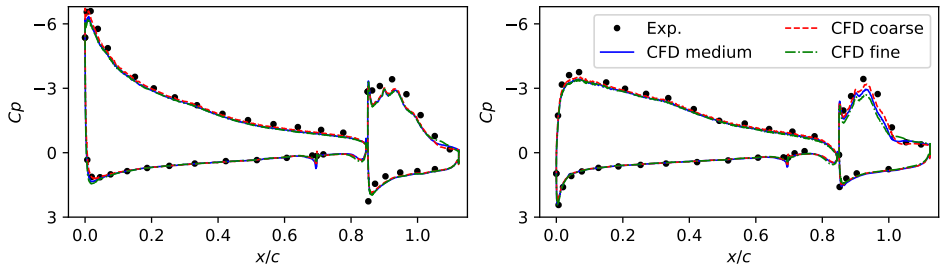

(a) Up-going wing side (b) Down-going wing side

Figure 11.2: Effect of grid resolution on pressure coefficient along the wing chord for $\delta_f = 30°$, $\alpha = 8°$.

The smooth body separation over the flap is slightly affected by the resolution, in particular on the down-going side, but the results do not change substantially with increase in grid resolution. Hence, we use the medium resolution throughout this study.

While the main element of the wing was tripped in the experiments, the flap was not. At such low Reynolds numbers (600,000 based on the clean wing chord), substantial regions of laminar flow can occur and laminar separation bubbles were observed on the flap in the experiments. To verify the sensitivity to such effects, we conducted simulations using a transition model [22] on the flap. This made the flap leading-edge laminar and the results of this are shown in Fig. 11.3. The pressure

cuts show a small delay in the flap separation, improving the pressure distribution on the flap, and also the suction peak on the main element of the wing. Using a more advanced transition treatment, capable of accurately capturing separation bubbles [23] could lead to further improvements.

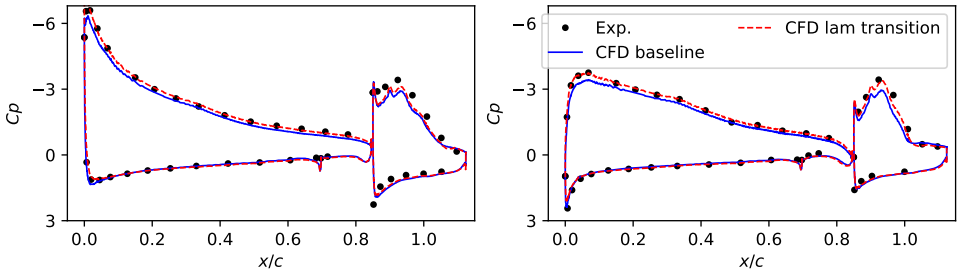

(a) Up-going wing side

(b) Down-going wing side

Figure 11.3: Effect of laminar to turbulent transition on pressure coefficient along the wing chord for $\delta_f = 30^\circ$, $\alpha = 8^\circ$.

Although the results with the transition model show a slight improvement over the fully turbulent simulation, the differences are small enough that we set the remaining cases to fully turbulent, to avoid any uncertainties associated with using a transition model for a high-lift configuration [24]. This also facilitates the grid resolution study, as transition models have been shown to be sensitive to the mesh [25].

Results for various values of α and δ_f can be seen in Fig. 11.4. All configurations results show very good agreement with experiment. As δ_f increases, the simulations show discrepancies compared to experiments in the suction peaks, which as shown in Fig. 11.3, is connected to laminar to turbulent transition. In all simulations the additional total pressure generated by the propeller is well captured, as the Cp values at the stagnation points agree with experimental values.

11.4.3. Surface Oil Flow

Oil flow measurements allow us to compare the flow features of the experiments with simulations. In particular, 3D flow separations and the footprint of the slipstream can be assessed. Top views of the experimental oil flow visualization are shown in the top rows of Figs. 11.5 and 11.6, and compared to surface shear lines from the simulations in the bottom rows. The CFD results also show streamwise shear force C_{fx}, normalized by q_∞ to assist in visualizing regions near flow separation. Note that the experimental oil flow images show some effect of gravity, turning the oil towards the up-going blade side, as the wing was mounted vertically in the wind tunnel. This effect is mostly present in areas with low surface shear.

Figures 11.5 and 11.6 are also annotated to show specific areas of interest. Blue boxes are used to draw attention to several flow structures that match very well between the experimental oil flow and the simulated surface shear. Red boxes show differences between simulations and experiments. Figures 11.5a and 11.5d

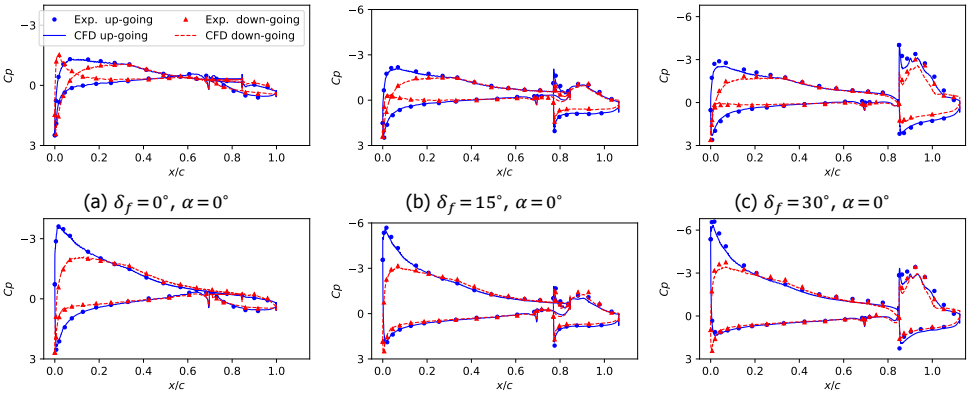

(a) $\delta_f = 0°$, $\alpha = 0°$ (b) $\delta_f = 15°$, $\alpha = 0°$ (c) $\delta_f = 30°$, $\alpha = 0°$

(d) $\delta_f = 0°$, $\alpha = 8°$ (e) $\delta_f = 15°$, $\alpha = 8°$ (f) $\delta_f = 30°$, $\alpha = 8°$

Figure 11.4: Pressure coefficient along the wing chord on the up-going and down-going blade sides of the propeller for different flap angles δ_f and angles of attack α.

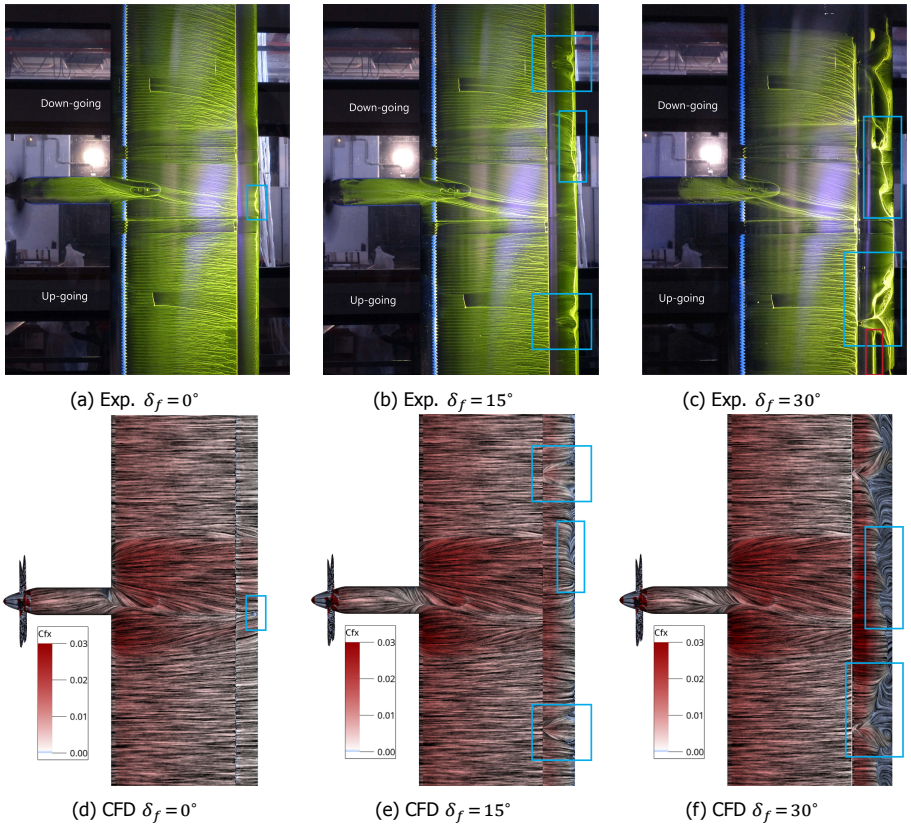

(a) Exp. $\delta_f = 0°$ (b) Exp. $\delta_f = 15°$ (c) Exp. $\delta_f = 30°$

(d) CFD $\delta_f = 0°$ (e) CFD $\delta_f = 15°$ (f) CFD $\delta_f = 30°$

Figure 11.5: Surface shear lines, represented by oil flow in the experiment and colored by streamwise skin friction coefficient in simulations at $\alpha = 0°$.

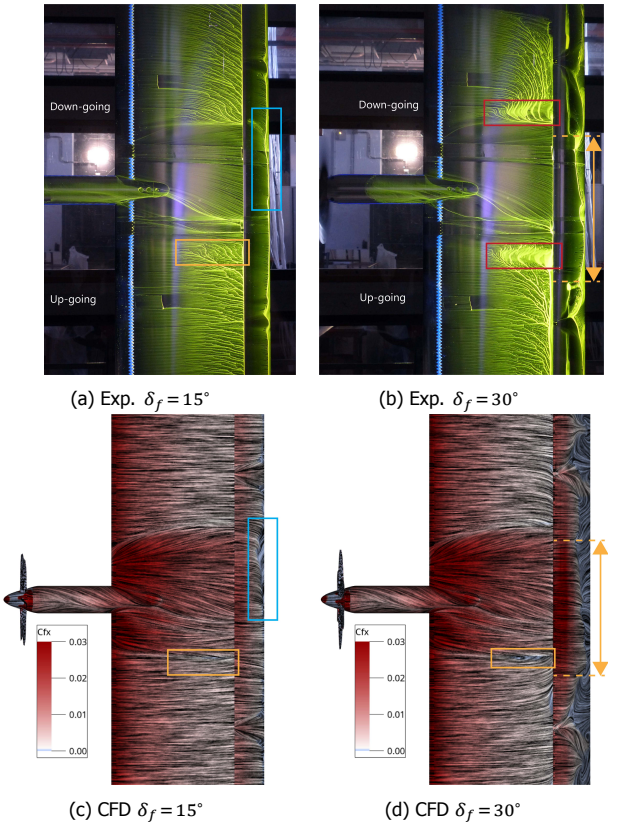

(a) Exp. $\delta_f = 15°$ (b) Exp. $\delta_f = 30°$

(c) CFD $\delta_f = 15°$ (d) CFD $\delta_f = 30°$

Figure 11.6: Surface shear lines, represented by oil flow in the experiment and colored by streamwise skin friction coefficient in simulations at $\alpha = 8°$.

both show a slight separation due to nacelle vortex structure. With flaps deployed, the interference of the flap brackets on the flap flow is clearly visible in both experiment and simulation. The local separation on the flap is also captured well by the simulations, where the flow structures near the center of the flap span in Fig. 11.5c and Fig. 11.5f are particularly of note. They also show the presence of the laminar separation bubble on the flap (marked in red in Fig. 11.5c), which is not present in the simulation and has some effect on the flap separation.

At $\alpha = 8°$ (Fig. 11.6), the major flow structures, such as the effect of flap brackets and the crossflows directly behind the nacelle, are again captured well. The separated areas on the main element are captured by the simulation, but seem under-predicted (marked with orange boxes). They only occur on the up-going blade side in the simulation, while Fig. 11.6b shows clear signs of separation on the main element on the down-going blade side as well. The area of the flap that is affected by the slipstream also seems slightly larger in the oil flow images, although this cannot be fully judged from these images alone. Nonetheless, overall the

simulations shear lines agree well with experimental oil flow visualization, which is very challenging to achieve in numerical simulations with smooth body separations [24].

11.4.4. Total Pressure Wake Plane

Total pressure coefficient $Cp_T = (p_T - p_\infty)/q_\infty$, where $p_T = p + q$, $q = 0.5\rho U^2$, ρ is the local air density, and U is the local velocity magnitude, is computed on a plane one chord downstream of the nested flap trailing-edge at $\alpha = 0$. Experimental results are shown on the top rows of Figs. 11.7 and 11.8, while the simulations are shown in the bottom rows. The horizontal lines represent the wing leading-edge and flap trailing-edge, while the circles indicate the propeller position.

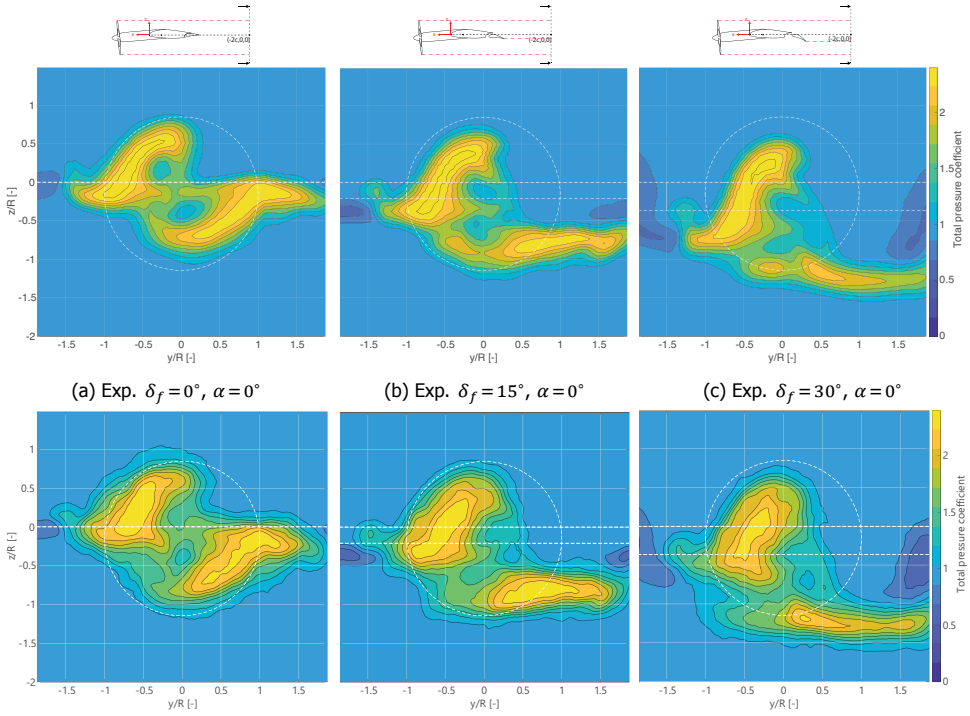

(a) Exp. $\delta_f = 0°$, $\alpha = 0°$ (b) Exp. $\delta_f = 15°$, $\alpha = 0°$ (c) Exp. $\delta_f = 30°$, $\alpha = 0°$

(d) CFD $\delta_f = 0°$, $\alpha = 0°$ (e) CFD $\delta_f = 15°$, $\alpha = 0°$ (f) CFD $\delta_f = 30°$, $\alpha = 0°$

Figure 11.7: Total pressure coefficient planes in the wake of the wing.

The flow features of the propeller wake being cut by the wing and the slipstream on the upper surface moving to the down-going side, while the slipstream on the lower surface moves to the up-going side are well captured by the simulations. The vortices that appear as blue circles near the center of the images are also well captured, with small differences that increase with α and δ_f. The "inverted-T" shape that appears at $\alpha = 8°$ is also captured by the simulations, with some differences (at least in part) due to the slightly different flap separations. Again, overall the

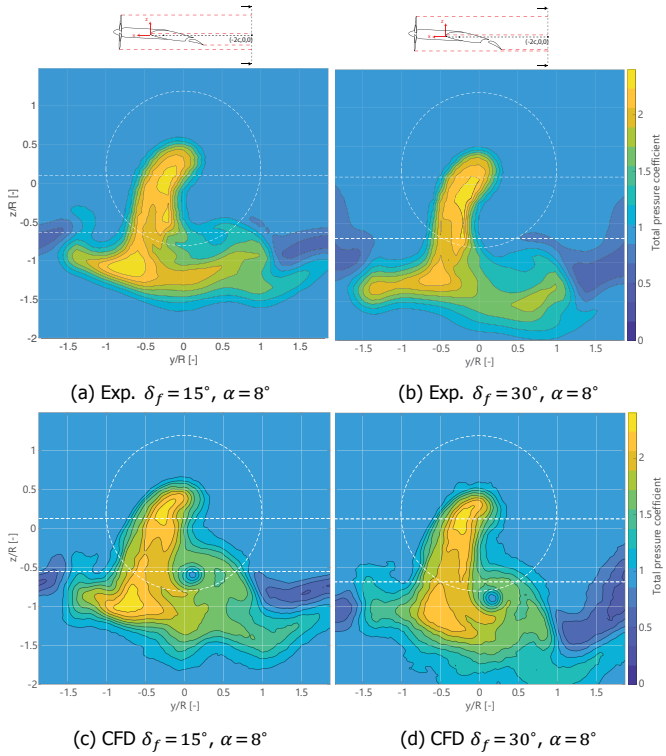

(a) Exp. $\delta_f = 15°$, $\alpha = 8°$ (b) Exp. $\delta_f = 30°$, $\alpha = 8°$

(c) CFD $\delta_f = 15°$, $\alpha = 8°$ (d) CFD $\delta_f = 30°$, $\alpha = 8°$

Figure 11.8: Total pressure coefficient planes in the wake of the wing. Experimental results from [6].

simulations and experiments agree well. Matching the slipstream in a downstream location such as this would be very challenging with traditional NS solvers, due to the dissipation of the tip vortices.

11.5. Flow Analysis

The close match of the simulations with the experimental results also offers the opportunity to use the simulations to further investigate the flow. Taking advantage of the full domain time-accurate data available from the simulation, we are able to quantify the slipstream shear and reflect on the off-the-surface structure of the slipstream.

11.5.1. On-the-surface slipstream trajectory

Figure 11.9 shows the spanwise distribution of skin friction coefficient $Cf = F/q_\infty$, where F is the amplitude of the force vector acting on the wing surface, on the main element of the wing for different chordwise stations. Solid lines correspond to the upper surface of the wing, while dashed lines show the same station on the lower surface. Positive y/R corresponds to the down-going blade side. The slipstream edges, highlighted with markers, can be identified from the substantial change in

skin friction due to the presence of the slipstream. Plotting the positions of the markers in Fig. 11.9 illustrates the on-the-surface translation of the slipstream edge as it moves along the wing. This is shown in Fig. 11.10.

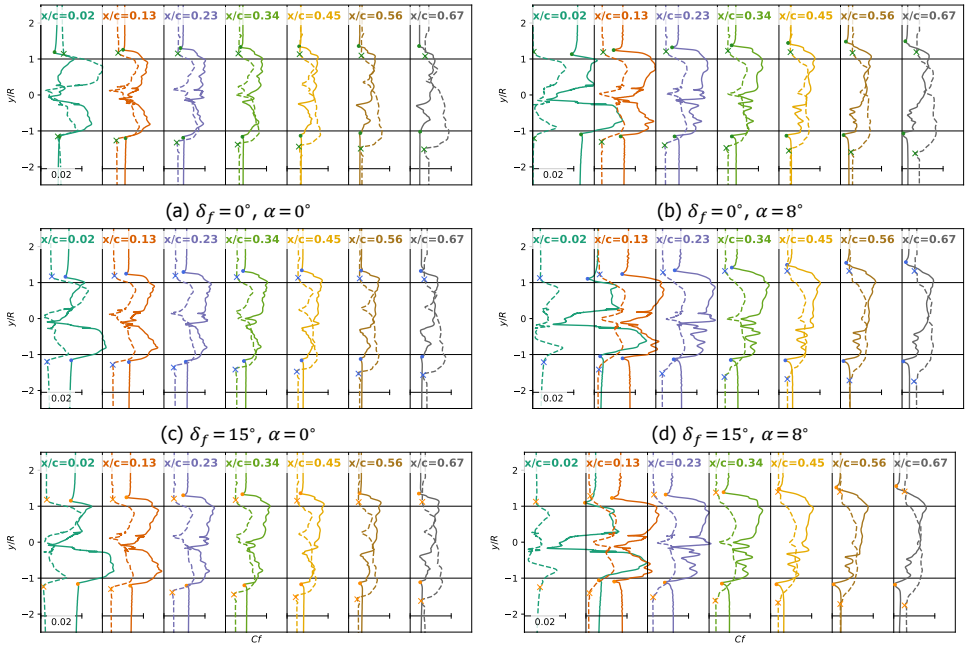

Figure 11.9: Spanwise skin friction distributions for various chordwise positions. Dashed lines are on the lower surface of the wing, solid lines are on the upper surface. Markers show the approximate edges of the slipstreams. Marker colors correspond to the lines in Fig. 11.10

Several observations are shared between all configurations. Close to the leading-edge of the wing the slipstream-affected area is slightly wider for $\alpha = 0°$ than for $\alpha = 8$. This is caused by the different trajectory of the slipstream between disk and wing leading-edge due to the angle of attack. At $\alpha = 8°$ the wing intersects the slipstream at a lower part, where the slipstream is less wide. We can also see that the slipstream-affected area is generally wider than one propeller diameter at $x/c = 0.02$. This is a function of the balance between propeller thrust coefficient (and associated slipstream contraction) and the nacelle width (and associated slipstream displacement). Furthermore, it depends on the intersection position of the wing as a result of propeller position, inclination, and wing angle of attack.

For all presented cases, we can see a slight divergence of the slipstream affected area between $x/c = 0.02$ and $x/c = 0.13$. This is particularly apparent on the upper surface. This leading-edge expansion is also noted in the experiment by Duivenvoorden et al. [6]. We attribute this to a vortex imaging effect of the tip vortices bending around the leading-edge, which is also described by Thom [26]. Rather than being cut at the leading-edge, as suggested by Veldhuis [27], the tip vortex

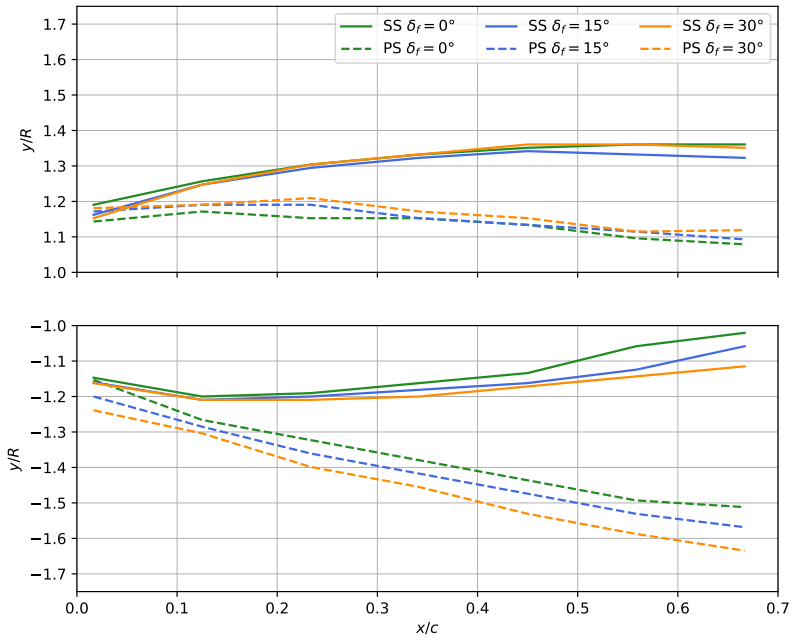

(a) $\alpha = 0°$

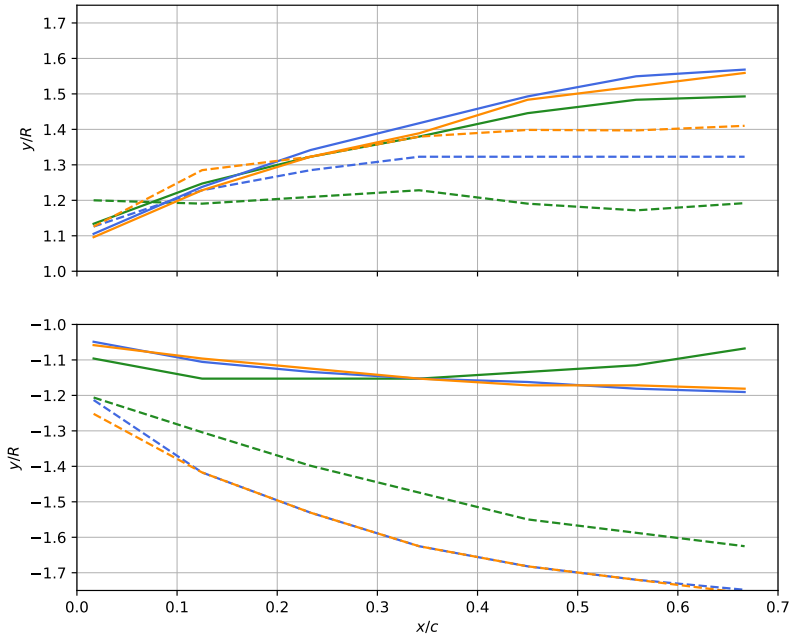

(b) $\alpha = 8°$

Figure 11.10: Spanwise evolution of propeller wake size on wing. Solid lines represent the suction side (SS) of the wing, dashed lines the pressure side (PS).

remains intact and stretches around the wing leading-edge. This is clearly visible in Fig. 11.11 and follows experimental flow visualisations of propeller-rudder interaction performed by Felli et al. [28, 29]. Due to image vortex effects on the wing surface, this tip vortex will self-induce away from the centerline. As the tip vortices move downstream, the stretched portion loses strength of even disintegrates and the expansion effect disappears.

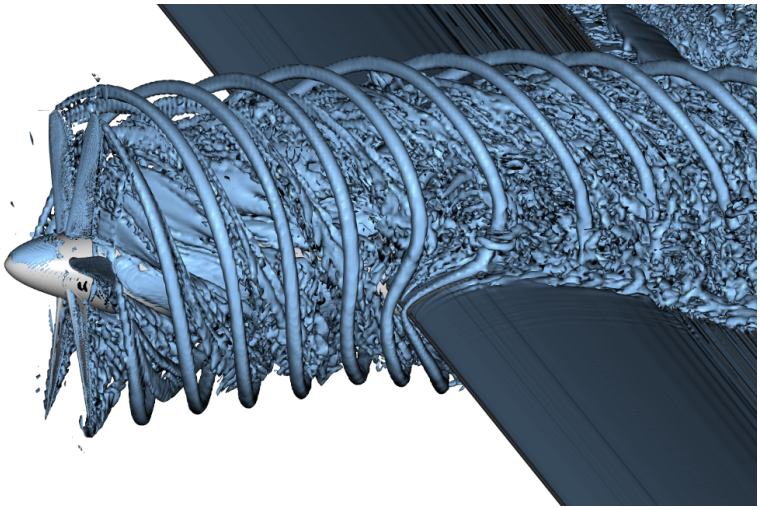

Figure 11.11: Isosurfaces of instantaneous $\lambda_2 = -5U_\infty^2/c^2$ for $\delta_f = 30°$, $\alpha = 8°$, showing the tip vortex wrapping around the leading-edge.

Figure 11.10 also clearly illustrates the shearing effect between the slipstream portions passing either side of the wing and how this effect is compounded with other factors. On the up-going blade side, the lower surface slipstream edge clearly moves away from the propeller axis, while the upper surface slipstream edge moves toward the axis, but to a lesser extent due to the shear being counteracted by the initial leading-edge expansion. On the down-going blade side, the upper surface slipstream edge clearly moves away from the axis, while the lower surface moves very little. As the slipstream moves downstream on the wing, the slipstream edge on the down-going blade side of the lower surface becomes difficult to distinguish exactly. The amount of shear clearly increases at higher α.

Deploying the flap and increasing angle of attack both show to have an expansion effect on the slipstream, most evident from the upper surface up-going blade side slipstream edge. Figures 11.9a, 11.9c, 11.9e and 11.9b all clearly show an initial movement away from the axis between $x/c = 0.02$ and $x/c = 0.13$, followed by movement towards the axis up to $x/c = 0.67$. For Figs. 11.9d and 11.9f the latter no long occurs and the slipstream edge continues to move away slightly. Overall, the slipstream thus both shears and expands as it moves over the main element.

Finally, the skin friction coefficient distributions in Fig. 11.9 show that increasing both angle of attack and flap deflection cause the effect of the slipstream on the

lower surface skin friction to become dissipated. We attribute this to the effect of interactions between tip vortices on the slipstream development and the dependency on slipstream deflection.

11.5.2. Tip vortex interaction

Figure 11.12 shows side views of the vortical slipstream structures as they pass the wing for various angles of attack and flap deflections. In Fig. 11.12a the tip vortices initially remain concentrated, but start to interact around the wing mid-chord and break down into larger structures by the time the slipstream reaches the trailing-edge. Increasing the angle of attack increases the wing circulation, thus increasing velocity on the upper side and maintaining separate flow structures further downstream. On the lower side, the flow decelerates, causing tip vortices to interact sooner. This is similar to the effect of increasing the number of blades [30] or decreasing the advance ratio.

Deploying the flap has a similar effect. Distinct tip vortex structures are maintained further downstream on the upper side and on the lower side interaction occurs further upstream. With the addition of increased angle of attack these effects are amplified, inducing tip vortex interactions nearly at the leading-edge of the lower side. As no concentrated tip vortices reach the flap, the interaction of the slipstream with the flap will be different from the main element. For instance, there will be no stretching of the vortex leading to self-induced expansion.

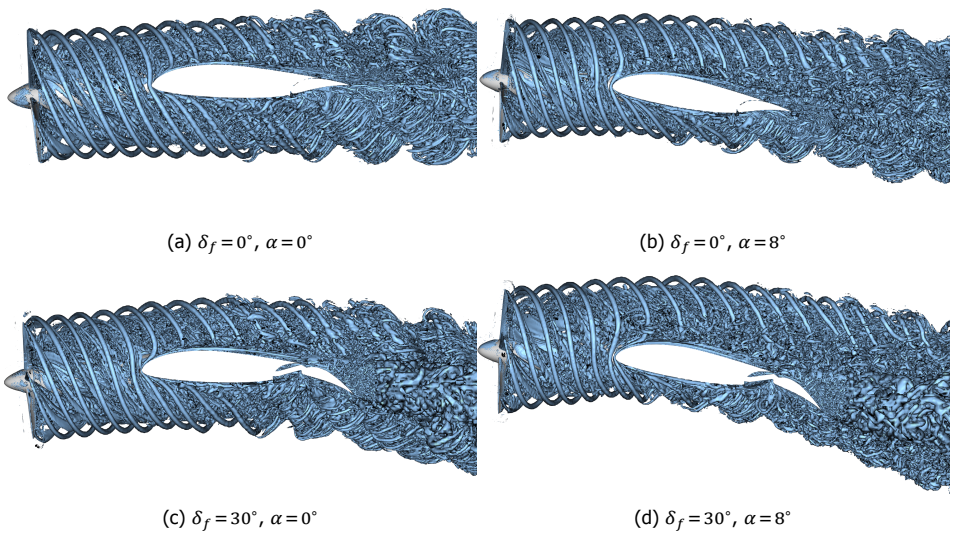

(a) $\delta_f = 0°$, $\alpha = 0°$ (b) $\delta_f = 0°$, $\alpha = 8°$

(c) $\delta_f = 30°$, $\alpha = 0°$ (d) $\delta_f = 30°$, $\alpha = 8°$

Figure 11.12: Isosurfaces of instantaneous $\lambda_2 = -5U_\infty^2/c^2$, illustrating how angle of attack and flap deflection affect slipstream evolution and instability.

11.5.3. Slipstream deformation

Both the skin friction distributions of Fig. 11.9 and the tip vortex interactions shown in Fig. 11.12 show how much the slipstream shape is distorted as it passes over the wing. The ”inverted-T” shape of the slipstream in the wing wake starts developing early on the wing, not just in the wake of the wing. This is visualized in Fig. 11.13a, showing slices of the total pressure coefficient Cp_T at various streamwise positions for the case with $\delta_f = 15^\circ$ and $\alpha = 8^\circ$. Only $Cp_T > 1.2$ is visualized to highlight the slipstream. The figure clearly shows that the ”inverted-T” shape is the result of deformation across the entire wing chord. The stem of this ”T” develops from a minor deformation at the wing leading-edge, combined with contraction of the slipstream. The lower half expands significantly, likely due to the spanwise pressure gradient and the tip vortex interactions and associated break-down.

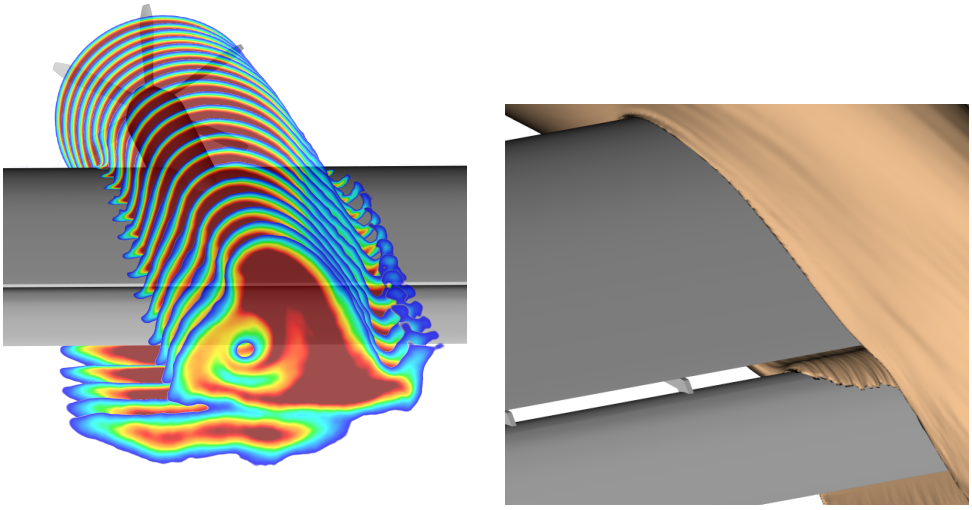

(a) Slices of total pressure coefficient (>1.2), (b) Isosurfaces of $C_{p,T} = 1.2$,

Figure 11.13: Visualisation of the slipstream deformation as it moves along the wing based on (time-averaged) total pressure coefficient $C_{p,T}$ for the $\delta_f = 15^\circ$, $\alpha = 8^\circ$ case.

The extent of the shearing effect of both slipstream halves as they pass the wing is also clearly visualized in Fig. 11.13a. The flap thus encounters very different flows depending on the spanwise station. This varies from being only immersed in the portion of the slipstream that passes the lower half of the main element to being fully immersed in the slipstream or only having the slipstream pass it off-the-surface. For most spanwise stations, the total pressure varies strongly in the vertical direction. By taking an isosurface of the mean total pressure, shown in Fig. 11.13b, we can also see that a portion of the slipstream will pass through the slot and over the flap suction surface.

11.6. Conclusions and Outlook

The conclusions we can draw from this work are:

- LBM simulations show very good agreement with experimental measurements on both qualitative and quantitative aspects.
- Wake development is captured to an impressive level considering the usual difficulty of numerical methods with numerical dissipation and diffusion.
- Quantification of the slipstream edge trajectory showed a combination of shearing and expanding effects, the balance of which dictates spanwise variation of flow on the flap.
- Slipstream trajectory change due to angle of attack can have a significant effect on the spanwise area of the wing that intersects the slipstream.
- Tip vortices are stretched around the leading-edge rather than cut by it, leading to slipstream expansion through image vortex mechanisms.
- Angle of attack and flap deflection have significant effect on tip vortex evolution by affecting vortex-vortex interactions, leading to instabilities.

Future work will focus on further analysis of slipstream deformation and flap interaction, potentially including multiple propellers.

References

[1] A. F. P. Ribeiro, R. Duivenvoorden, and D. Martins, *High-fidelity simulations of propeller-wing interactions in high-lift conditions,* in *AIAA AVIATION Forum* (2023).

[2] K. A. Deere, J. K. Viken, S. Viken, M. B. Carter, M. Wiese, and N. Farr, *Computational analysis of a wing designed for the X-57 distributed electric propulsion aircraft,* in *35th AIAA Applied Aerodynamics Conference* (2017).

[3] T. Sinnige, R. Nederlof, and N. van Arnhem, *Aerodynamic performance of wingtip-mounted propellers in tractor and pusher configuration,* in *AIAA AVIATION FORUM* (2021).

[4] T. C. A. Stokkermans, D. Usai, T. Sinnige, and L. L. M. Veldhuis, *Aerodynamic interaction effects between propellers in typical evtol vehicle configurations,* Journal of Aircraft **58**, 815 (2021).

[5] R. de Vries, N. van Arnhem, T. Sinnige, R. Vos, and L. L. Veldhuis, *Aerodynamic interaction between propellers of a distributed-propulsion system in forward flight,* Aerospace Science and Technology **118**, 107009 (2021).

[6] R. R. Duivenvoorden, N. Suard, T. Sinnige, and L. L. M. Veldhuis, *Experimental investigation of aerodynamic interactions of a wing with deployed fowler flap under influence of a propeller slipstream,* (2022).

[7] H. Chen, C. Teixeira, and K. Molvig, *Digital physics approach to computational fluid dynamics: Some basic theoretical features,* International Journal of Modern Physics C **08**, 675 (1997).

[8] H. Chen, S. Chen, and W. H. Matthaeus, *Recovery of the Navier-Stokes equations using a lattice-gas Boltzmann method,* Physical Review A **45**, R5339 (1992).

[9] G. Brès, F. Pérot, and D. Freed, *Properties of the lattice Boltzmann method for acoustics,* in *15th AIAA/CEAS Aeroacoustics Conference (30th AIAA Aeroacoustics Conference)* (2012).

[10] E. Manoha and B. Caruelle, *Summary of the LAGOON solutions from the benchmark problems for airframe noise computations-III workshop,* in *21st AIAA/CEAS Aeroacoustics Conference* (2015).

[11] R. Zhang, C. Sun, Y. Li, R. Satti, R. Shock, J. Hoch, and H. Chen, *Lattice boltzmann approach for local reference frames,* Communications in Computational Physics **9**, 1193 (2011).

[12] A. F. P. Ribeiro, *Unsteady analysis of ground vortex ingestion with LBM-VLES,* in *AIAA SCITECH Forum* (2021).

[13] D. Casalino, W. C. van der Velden, and G. Romani, *A framework for multi-fidelity wind-turbine aeroacoustic simulations,* in *28th AIAA/CEAS Aeroacoustics 2022 Conference* (2022).

[14] A. F. P. Ribeiro, M. Murayama, Y. Ito, K. Yamamoto, and T. Hirai, *Effect of slat tracks and inboard slat tip geometry on airframe noise,* in *28th AIAA/CEAS Aeroacoustics Conference* (2022).

[15] B. König, D. Singh, A. Ribeiro, and E. Fares, *Lattice-boltzmann simulations at the corners of the flight envelope,* 54th 3AF International Conference on Applied Aerodynamics (2019).

[16] S. D. Lucas-Bodas, J. Narbona-Gonzalez, V. Ossorio-Contreras, J. Jose, Guerra-Crespo, D. E. Funes-Sebastian, and L. P. Ruiz-Calavera, *Experimental validation of numerical prediction of wing-propeller aerodynamic interaction,* 32nd Congress of the International Council of the Aeronautical Sciences (2021).

[17] L. Boermans and P. Rutten, *Two-dimensional aerodynamic characteristics of airfoil NLF-MOD22 with fowler flap*, Technical Report (Delft University of Technology, 1995).

[18] N. van Arnhem, R. de Vries, T. Sinnige, and L. Veldhuis, *TUD-XPROP-S propeller geometry,* (2022).

[19] A. F. P. Ribeiro, D. Casalino, and E. Fares, *Lattice-boltzmann simulations of an oscillating NACA0012 airfoil in dynamic stall,* in *Advances in Fluid-Structure Interaction*, edited by M. Braza, A. Bottaro, and M. Thompson (Springer International Publishing, 2016) pp. 179–192.

[20] A. F. P. Ribeiro, D. Singh, B. Konig, and E. Fares, *On the stall characteristics of iced wings,* in *55th AIAA Aerospace Sciences Meeting* (2017).

[21] B. Konig, B. M. Duda, and G. M. Laskowski, *Lattice Boltzmann simulations for the 4th AIAA high-lift prediction workshop using PowerFLOW,* in *AIAA AVIATION Forum* (2022).

[22] B. M. Duda, E. Fares, R. Kotapati, Y. Li, I. Staroselsky, R. Zhang, and H. Chen, *Capturing laminar to turbulent transition within the LBM based CFD solver PowerFLOW,* AIAA Scitech Forum (2019), 10.2514/6.2019-1832.

[23] D. Casalino, G. Romani, R. Zhang, and H. Chen, *Lattice-Boltzmann calculations of rotor aeroacoustics in transitional boundary layer regime,* Aerospace Science and Technology **130**, 107953 (2022).

[24] C. L. Rumsey, J. P. Slotnick, and A. J. Sclafani, *Overview and summary of the third AIAA high lift prediction workshop,* Journal of Aircraft **56**, 621 (2019).

[25] J. Carnes and J. G. Coder, *Benchmarking the Langtry-Menter transition model using OVERFLOW for the AIAA transition modeling workshop,* in *AIAA AVIATION Forum* (2022).

[26] A. D. Thom, *Analysis of Vortex-Lifting Surface Interactions*, Ph.D. thesis, University of Glasgow (2011).

[27] L. Veldhuis, *Propeller wing aerodynamic interference*, PhD dissertation, Delft University of Technology (2005).

[28] M. Felli, F. Di Felice, G. Guj, and R. Camussi, *Analysis of the propeller wake evolution by pressure and velocity phase measurements,* Experiments in Fluids **41**, 441 (2006).

[29] M. Felli and M. Falchi, *Propeller tip and hub vortex dynamics in the interaction with a rudder,* Experiments in Fluids **51**, 1385 (2011).

[30] M. Felli, G. Guj, and R. Camussi, *Effect of the number of blades on propeller wake evolution,* Experiments in Fluids **44**, 409 (2008).

12

Trailing-Edge Noise of a Full Wind Turbine with Serrations

How do you eat an elephant? One bite at a time.

Proverb

Numerical simulations of a wind turbine blade with and without trailing-edge serrations are validated with full-scale field test of a 130 m diameter onshore wind turbine. Simulations focus on trailing-edge noise and are conducted on extruded airfoil sections of the blade using the lattice-Boltzmann method and very large eddy simulations, which are then propagated to the far-field using the Ffowcs Williams-Hawkings approach, simulating the rotation of the sections and the noise of the entire rotor. Far-field noise spectra at two mean wind speeds are used for validation, with the sound power level of the simulations being within 2.5 dB of field test and the total noise reductions attributed to the serrations being captured within 0.6 dB.

Parts of this chapter have been published in AIAA/CEAS Aeroacoustics (2024) [1].

12.1. Introduction

With the recent increased focus on renewable energies, wind energy is becoming even more relevant. While offshore installations are growing, the vast majority of operating turbines worldwide are onshore, where noise is key for the acceptance of wind energy. The maximum noise a wind turbine can produce can be a limiting factor in its energy output.

In this chapter, we perform scale-resolved simulations of sections of a wind turbine blade. While airfoil noise can be computed with semi-empirical methods [2], the addition of complex geometries, such as trailing-edge serrations makes this difficult. We then use a process to extrapolate the noise from these sections to the entire wind turbine and propagate this noise to the far-field, taking the rotation of the blades into account [3]. These simulations are carried out for a baseline blade without add-ons and the same blade with added trailing-edge serrations, designed to reduce the trailing-edge noise. These simulations are validated with experimental data from field tests on a full-scale wind turbine.

The work conducted here builds upon the work of [3], where a framework for wind turbine noise simulations was developed and validated with other numerical data. This framework consists of low-fidelity simulations using blade element momentum theory (BEMT) and semi-analytical airfoil noise models, a mid-fidelity approach using computational fluid dynamics (CFD) simulations of airfoil sections that are combined to generate the noise of the entire turbine, and a high-fidelity approach where the entire turbine is simulated in CFD. As the low-fidelity approach is not suitable for complex blade geometries including serrations and the high-fidelity approach is still too computationally expensive for industrial use, here we focus on the mid-fidelity approach. For the first time, we apply it to a full-scale industrial case with experimental data.

The lattice-Boltzmann method (LBM) [4] is used as an alternative to the Navier-Stokes (NS) equations [5]. This method is particularly suited for high-fidelity simulations of aeroacoustics, as it offers low-dissipation characteristics equivalent to high order methods [6], while being orders of magnitude faster than traditional NS CFD solvers [7].

12.2. Methodology

12.2.1. Fluid Solver

The Lattice-Boltzmann method, as described in Chapter 8 is used in this work. Our LBM computations are conducted with PowerFLOW, a commercial CFD code. It employs a k–ϵ RNG turbulence model [8] with a swirl model [9], which reduces the eddy viscosity in the presence of resolved flow structures, an approach called very large eddy simulation (VLES). Laminar to turbulent transition can be modelled with an algebraic model [10] or, with enough grid resolution, simulated by resolving the boundary layer [11]. Validations of the approach used here that are relevant to this work include unsteady airfoil aerodynamics [12], stall of complex wing sections [13], and applications to airfoil trailing-edge noise using direct numerical simulations [14], implicit large eddy simulations [15], and VLES [16].

12.2.2. Noise Propagation

Numerical approaches can successfully compute pressure fluctuations, i.e., noise, at arbitrary locations of the computational domain. However, it is typically prohibitively expensive to compute the noise propagation from the source region to the microphone locations. Therefore, integral methods based on the acoustic analogy are used to extrapolate the noise from the near-field flow fluctuations to far-field locations. In this work, we adopt a Ffowcs Williams & Hawkings (FW-H) frequency-domain formulation [17] with integration of the pressure field on the surface of the blades.

The FW-H analogy [18] is based on the usage of generalized derivatives to rearrange the flow governing equations satisfied outside a surface S in the form of a non-homogeneous wave equation with terms at the right-hand-side treated as source terms. An auxiliary variable f is used, which is equal to zero on S, positive outside S, and negative inside S. The formulation used in this work is derived by recasting the NS equations in the form of a convected wave equation for the perturbation density $\rho' = \rho - \rho_\infty$ (i.e. a prime is used to denote a perturbation quantity relative to the free-stream conditions, denoted by the subscript $_\infty$.), which reads:

$$\begin{aligned}&\left(\frac{1}{c_\infty^2}\frac{\partial^2}{\partial t^2} + M_i M_j \frac{\partial^2}{\partial x_i \partial x_j} + \frac{2M_i}{c_\infty}\frac{\partial^2}{\partial x_i \partial t} - \frac{\partial^2}{\partial x_i \partial x_i}\right)\left[H(f)c_\infty^2 \rho'\right] \\ &= \frac{\partial^2}{\partial x_i \partial x_j}\left[T_{ij}H(f)\right] - \frac{\partial}{\partial x_i}\left[F_i \delta(f)\right] + \frac{\partial}{\partial t}\left[Q\delta(f)\right]\end{aligned} \tag{12.1}$$

where t is time, $M_i = U_i/c_\infty$ is the time-averaged Mach number component corresponding to a fluid free-stream velocity U_i and a free-stream speed of sound c_∞, the subscripts i and j indicate Cartesian coordinates (indicial notation), $H(f)$ is the Heaviside function, which is unity where $f > 0$ and zero for $f < 0$. The derivative of the Heaviside function is the Dirac delta function $\delta(f)$, which is zero for $f \neq 0$, but yields a finite value when $f = 0$. The source terms T_{ij}, F_i, and Q take into account the noise generation due to non-linear coupling of velocity fluctuations and non-isentropic flow perturbations in the outer volume, the effect of pressure loading on S and momentum flux across it, and the effect of fluid displacement across S, respectively.

Here we use a frequency-domain (ω) formulation instead of the time-domain approach described in Section 8.2. By applying the Fourier transform $\hat{g}(\omega) = \int_{-\infty}^{\infty} g(t)\exp(-\mathrm{i}\omega t)\mathrm{d}t$ to all terms of Eq. 12.1, we obtain the final form of the frequency-domain FW-H acoustic analogy equation built upon a convected Helmholtz wave operator, which reads:

$$\begin{aligned}&\left(k^2 - M_i M_j \frac{\partial^2}{\partial x_i \partial x_j} - 2\mathrm{i}kM_i \frac{\partial}{\partial x_i} + \frac{\partial^2}{\partial x_i \partial x_i}\right)\left[H(f)c_\infty^2 \hat{\rho}'\right] \\ &= -\frac{\partial^2}{\partial x_i \partial x_j}\left[\hat{T}_{ij}H(f)\right] + \frac{\partial}{\partial x_i}\left[\hat{F}_i \delta(f)\right] - \mathrm{i}\omega\left[\hat{Q}\delta(f)\right]\end{aligned} \tag{12.2}$$

where $k = \omega / c_\infty$ is the acoustic wave number.

An integral solution of this non-homogeneous wave equation is sought by convolution with the free-space Green's function $G(X_i, Y_i)$, which describes the acoustic field at a fixed point X_i due to a non-moving Dirac source (a pulse) located in Y_i. This function is a solution of the convected wave equation and can be computed in time domain and then converted to the frequency domain with a Fourier transform. When limited to subsonic conditions, this Green's function can be expressed as:

$$G(X_i, Y_i) = -\frac{\exp\left(-\mathrm{i}\frac{k}{\beta^2}\left(\sqrt{M_r^2 + \beta^2 \left\|X_i - Y_i\right\|^2} - M_r\right)\right)}{4\pi\sqrt{M_r^2 + \beta^2 \left\|X_i - Y_i\right\|^2}} \tag{12.3}$$

where $M_r = M_i(X_i - Y_i)$ and $\beta^2 = 1 - \|M_i\|^2$. Finally, integrating by parts, exploiting the properties of the Dirac function, and knowing that X_i is outside the integration surface, the following integral solutions is obtained:

$$\begin{aligned} c_\infty^2 \hat{\rho}'(X_i, \omega) = &-\int_{f>0} \hat{T}_{ij}(Y_i, \omega) \frac{\partial^2 G(X_i, Y_i)}{\partial x_i \partial x_j} \mathrm{d}V \\ &-\int_{f=0} \hat{F}_i(Y_i, \omega) \frac{\partial G(X_i, Y_i)}{\partial x_i} \mathrm{d}S \\ &-\int_{f=0} \mathrm{i}\omega \hat{Q}(Y_i, \omega) G(X_i, Y_i) \mathrm{d}S \end{aligned} \tag{12.4}$$

where V is the volume outside S.

In the present study we aim at computing the noise generated by turbulent flow past the rotating blades of a wind turbine. Thanks to the large difference existing between the rotation period and the time scales of turbulent flow motion, it is convenient to compute the noise spectra for a discrete number of blade positions along one revolution at the corresponding relative microphone locations, by using the integral solution of the frequency-domain FW-H equation, which implicitly assumes that no relative motion exists between source and receiver, and by neglecting the mean-flow convective effects. Due to the low Mach number of the convected turbulence, we can neglect the direct contribution of turbulence by performing the integration on the physical surface of the blade, thus dropping the volume integral. The fluid velocity is zero on the solid surface, making Q constant and $\hat{Q}$ zero, leading to:

$$\hat{p}'(X_i, \omega) = -\int_{f=0} \hat{p}(Y_i, \omega)\, n_i \frac{\partial G(X_i, Y_i)}{\partial x_i} \mathrm{d}S \tag{12.5}$$

where p is pressure, we have assumed that $p' = c_\infty^2 \rho'$ in the far-field, and $F_i = p\, n_i$ on the surface of the blade, with $n_i = \partial f / \partial x_i$ denoting the outward normal unit vector.

Recent studies have shown that performing an integration on the solid surface of a body and dropping the volume integral outside the surface, can lead to significant inaccuracy issues, also for low Mach number cases, and hence it should be adopted with caution [19]. In the presence of sheared flows past complex geometries, as for instance the landing gear of an aircraft, errors are a combination of modelling and numerical errors. The first ones are due to the fact that, for acoustic wavelengths comparable to the characteristic scale of mean-flow variations in the presence of shear, the sound refraction effects, which are accounted for by the volume integral, cannot be neglected. This error would mostly affect the high-frequency spectrum. Moreover, in the presence of large vortical structures convected over long distances, the cumulative effect of noise contribution due to turbulence is not negligible. This error would mostly affect the low frequency spectrum for microphones located in a relatively near-field. The numerical errors, instead, are mostly related to the accuracy of the surface integral in the presence of abrupt variations of the surface normal over distances smaller than the acoustic wavelength. For the case of low Mach number turbulent flow past the blade of a wind turbine, the main error would be related to the occurrence of a coherent unsteady flow motion in the wake in the presence of separation. Therefore, for airfoil trailing edge noise calculations, a solid data surface FW-H formulation is the standard practice [14–16] and hence we select it for this work due to its simplicity and robustness.

12.2.3. Wind Turbine Noise Model

Although it is possible to simulate full wind turbines with PowerFLOW using the actuator line method [20] or by directly simulating the blades [21], simulations including trailing-edge noise of a full-scale turbine would be prohibitively expensive in an industrial environment. Simply performing airfoil section simulations is also not sufficient, as it has been shown [22] that the noise reduction for an airfoil section in a wind tunnel does not correspond to the noise reduction seen in field tests of wind turbines. Hence, we use an approach that uses simulations of airfoil sections, but that predicts the noise these section would produce on a real wind turbine [3, 21, 23].

The process starts with extracting sectional geometric information from a triangularized blade geometry by means of the SIMULIA® toolkit *Opty∂B*®. Then, the BEMT simulations of the wind turbine aerodynamics carried out, either with the included BEMT tool, or with a third-party code. In this case, the BEMT calculations were performed using GE internal codes. The aerodynamic polars used by the BEMT calculation can come from an external source or be computed by means of a 2D viscous panel method, similar to [24]. From BEMT, we obtain the sectional flow velocity $\vec{U}_\infty$ angle of attack α, and laminar to turbulent transition locations of airfoil sections along the blades. Then, the sectional blade coordinates are used to create an extruded blade section used to carry out 2.5D flow simulations, i.e. 3D flow simulations with a constant airfoil section. The spanwise length s of the sections are chosen to be around 10% of the local chord c, while also being an integer multiple of the serration wavelength λ_s. A sketch of an airfoil section with serrations is shown in Fig. 12.1.

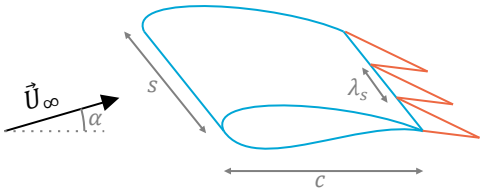

Figure 12.1: Sketch of the airfoil sections simulated in this work.

The choice of blade sections depends on the noise generated by the blade and the variation of the serrations. For the turbine configuration used in this study, there are five different serration geometries near the blade tips, starting at about 80% of the blade radius. We simulate two additional inboard sections, near 60 and 70% of the radius, ignoring the first half of the radius, as its contribution to the overall noise is negligible.

If a leading-edge protection tape is placed on the blade, the edges of the tape are assumed to cause transition and these locations are used instead of the 2D viscous panel method. Zig-zag transition trips are placed on the desired locations to trigger a turbulent boundary layer in the simulations. The height of these trips are made to be as small as possible, so that they do not generate excessive self-noise and do not lead to flow separations, but are able to trigger a turbulent boundary layer.

Simulations are run for 5 to 25 flow passes, depending on the radial section, on a coarse grid, in order to obtain a statistically converged flow field. The results of these coarse simulations are then used as initial conditions for the fine simulations. This process reduces the cost of the transient time substantially, with the circulation on the airfoil section changing little with the finer mesh.

Once the simulation for all the blade sections are concluded, the solid FW-H surfaces are used to compute the far-field noise using *Opty∂B*-FWHFREQ. This is done in the frequency domain, on a ring of microphones that correspond to the different relative positions between the blade section and the certification microphone. The noise of each section is scaled to account for the associated extent of the blade span, shown in Fig. 12.2. More details about the employed aeroacoustic methodology can be found in [3].

12.3. Test Case Description

The TIADE (Turbine Improvements for Additional Energy) [25] wind turbine is a full-scale, 130 m diameter onshore wind turbine, built and instrumented by GE Vernova (Onshore Wind & LM Wind Power) and TNO. It is part of a project that aims at developing and validating innovative wind turbine blade improvements, such as blade add-ons, to boost the performance of wind turbines.

Field noise measurements and data processing are carried out according to the IEC standard 61400-11 edition 3.0 [26]. A microphone is placed approximately 200 m downwind of the rotor. Noise data with turbine running and also background

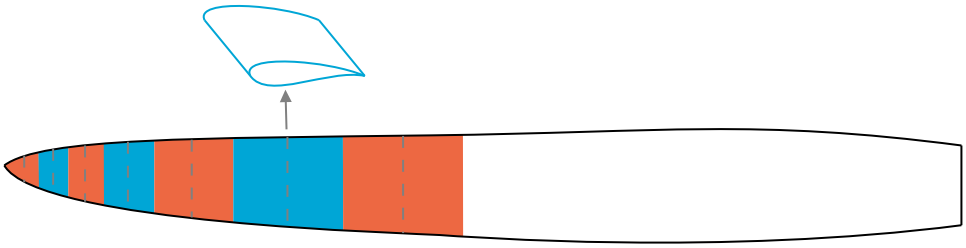

Figure 12.2: Sketch of a blade, where the dashed grey lines are the simulated airfoil sections and the blue and orange regions represent the strips of the blade where the airfoil sections are used. The inboard half of the blade is ignored.

noise are collected through an extended period. The data are then synchronised with turbine operation data such as power, blade pitch angle and rotor RPM and then processed to compute the apparent sound power level (Lwa) and its third-octave band spectra as a function of the hub height wind speed. Moreover, to further reduce the uncertainty and day-to-day variation of the field measurement, during the TIADE measurement campaign, data from multiple tests of the identical configuration are combined and energy-averaged.

We use field data measured at two mean wind speeds, 10 and 13 m/s. Trailing edge noise was estimated to be the dominant noise source for the TIADE wind turbine, with separation noise, turbulent inflow noise, and tip vortex noise all being negligible for the purposes of this validation.

We compare far-field noise data captured downstream of the turbine, near ground level. The noise metric we use in this work is the apparent sound power level:

$$L_{wa} = L_v - 6 + 10\log_{10}(4\pi R^2) \tag{12.6}$$

where L_v is the sound power level, corrected for background noise and converted to dBA, the factor of 6 is to remove ground reflection effects, and R is the distance between the tower hub and the microphone, with the logarithm term in the equation being present to make it independent of the measurement distance, barring atmospheric absorption effects.

Simulations are run with PowerFLOW, using the subsonic isothermal solver, as the tip Mach number is approximately 0.25. A Cartesian mesh is used, with cubic cells ranging from about 0.2 to 60 mm. An average y^+ of 30 was used, which is compatible with the wall model used. The setup is consistent with previous publications on 2.5D trailing-edge noise [16].

12.4. Results

12.4.1. Dilatation Fields

Figs. 12.3 and 12.4 show the dilatation field on the middle span of the most outboard airfoil section. With low frequency sampling, where the frequencies being captured are up to 1 kHz, the trailing-edge noise dominates over all other sources. At high frequency sampling, capturing beyond the grid cut-off, noise from the trip can be seen, although at lower levels than trailing-edge noise. The trip noise appears to be present above frequencies of 2 kHz, which is at the edge of the range of interest for this work.

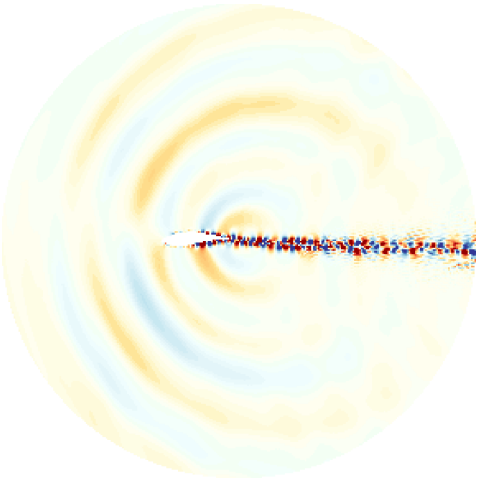

Figure 12.3: Dilatation field based on low frequency sampling.

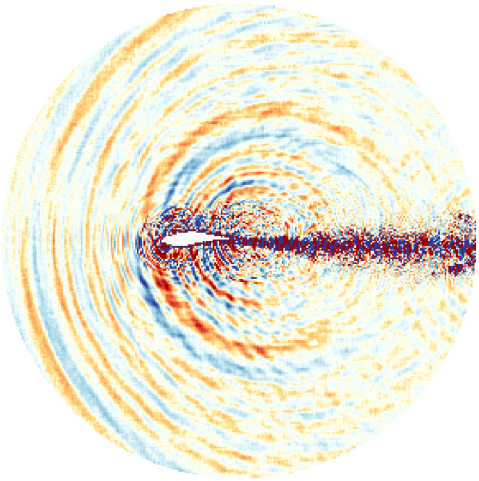

Figure 12.4: Dilatation field based on high frequency sampling.

12.4.2. Noise Contribution per Section

Fig. 12.5 shows the noise contribution of virtual rings on the rotor plane. Each ring is associated with a blade section, simulated in 2.5D. Results are shown for the baseline turbine and the case with serrations. The five sections on the right are the ones that are modified in the case with serrations, hence the other sections are identical for both cases. The section further to the left is within the first half of the blade and has a negligible contribution to overall noise and is ignored throughout this work. This type of analysis is useful to understand which sections are worth optimizing for noise and how much of the blade needs to be simulated for total noise to be within the desired accuracy.

Further observations can be made on Fig. 12.5. First, increasing radius, noise emissions increase. However there is turning point as closer to the tip, noise emissions are reduced. This is in line with what is stated in literature [27]. Second, after retrofitting the blade with serrations, noise levels are substantially reduced for each of the sections. However, serrations seem more effective further away from the blade tip. Third, noise levels in the sections with serrations drop below the most

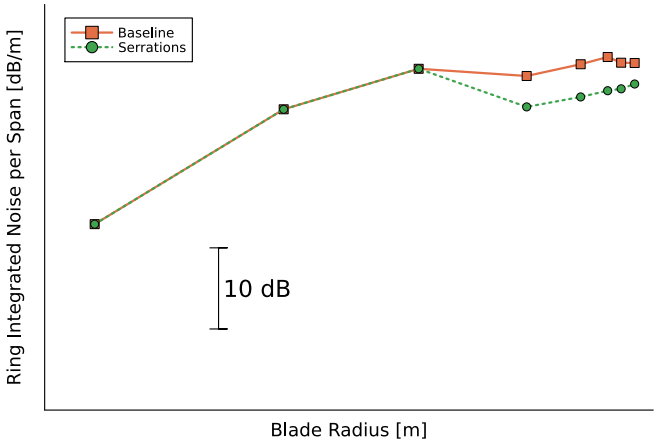

Figure 12.5: Noise contribution of rotor rings associated with each airfoil section to the far field noise, normalized by span.

outboard section without serrations, suggesting that extending the serrations in the inboard direction could further reduce noise in this turbine.

12.4.3. Far-Field Noise Spectrum

The far-field noise spectra for the baseline case at 10 m/s are shown in Fig. 12.6. Field test data and simulations are shown. Results agree well, given the uncertainties associated with field test data, e.g. the lack of control over the incoming flow velocity and background noise. Note that, based on analysis done with semi-empirical methods, the dominant noise source for this turbine at these frequencies is trailing-edge noise, with other sources being negligible.

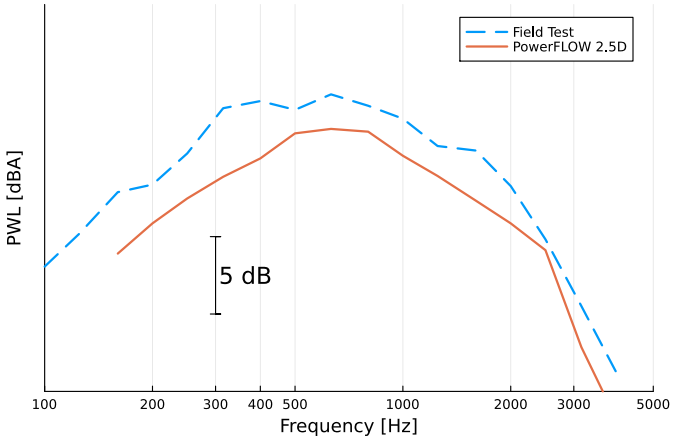

Figure 12.6: Far-field microphone noise levels on 3rd Octave bands.

The impact of the serrations, i.e. the difference between the noise spectra for the cases with and without trailing-edge serrations is shown in Fig. 12.7. A small shift in frequencies is observed, which is not understood at the moment, but overall numerical results agree very well with field tests.

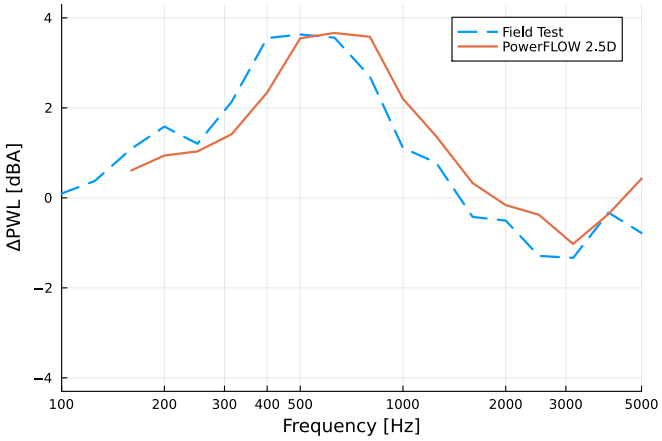

Figure 12.7: Noise reduction due to serrations in the far-field microphone on 3rd Octave bands..

12.4.4. Integrated Noise Levels

For design loops and certification purposes, a single-value integrated noise metric is critical. In Table 12.1 we compare the integrated noise levels for the simulations and experiments. The accuracy of the simulations is considered satisfactory, especially given the uncertainties associated with field tests.

Table 12.1: Comparison between simulations and experimental data.

$\vec{U}_\infty$	10 m/s	13 m/s
Total noise without serrations L_{wa}, Exp.-Sim.	2.5 dBA	2.1 dBA
Serration effect on noise ΔL_{wa}, Exp.-Sim.	-0.3 dBA	-0.6 dBA

12.4.5. Computational Cost

Another important metric for the simulations are the cost. In order to make the process industrially relevant, the run times need to be within the limitations of a design process. The cost for computing the total noise of the turbine, including all seven airfoils sections was about 100 kCPUh, which can be done fairly easily in one day, by running all simulations concurrently and on about 1000 cores. For the quantification of the noise reduction due to the serrations, only the outboard sections need to be simulated, as the inboard is the same for the baseline blade and the blade with serrations. The inboard sections have lower freestream velocities and longer chords, and hence require more physical time to reach statistical

convergence. With this, the cost is substantially reduced by focusing on the blade tips, and the cost per turbine becomes about 55 kCPUh, or 110 kCPUh to calculate ΔL_{wa}.

12.5. Conclusions and Outlook

This paper showed validation of a recently developed mid-fidelity computational fluid dynamics framework for trailing-edge noise, including serrations effects. Field data from a full-scale wind turbine were used as reference and we found the agreement on the serration delta to be satisfactory and in line with industrial requirements for blade design, from an aeroacoustics point of view. To our knowledge, this is the first publication of scale-resolved simulations of serration effects, including validation with field test data. With the methods used herein, trailing-edge noise alleviation can be designed with fewer expensive field tests and with accuracy that is higher than simple wind tunnel models, as rotation effects are included.

Future work will include leading-edge, or turbulent inflow noise. Full 3D simulations of the TIADE turbine are also planned.

Acknowledgements

The TIADE project was partially funded by the Netherlands Enterprise Agency (RVO) and the Netherlands Organization for Applied Scientific Research (TNO).

References

[1] A. F. P. Ribeiro, W. C. van der Velden, D. Casalino, and G. Wang, *Aeroacoustic simulations of a wind turbine: Validation with field tests, including trailing-edge serrations,* in *30th AIAA/CEAS Aeroacoustics Conference* (2024).

[2] T. F. Brooks, P. D. Pope, and M. A. Marcolini, *Airfoil self-noise and prediction*, Reference Publication 89N25673 (National Aeronautics and Space Administration, 1989).

[3] D. Casalino, W. C. van der Velden, and G. Romani, *A framework for multi-fidelity wind-turbine aeroacoustic simulations,* in *28th AIAA/CEAS Aeroacoustics 2022 Conference* (2022).

[4] H. Chen, C. Teixeira, and K. Molvig, *Digital physics approach to computational fluid dynamics: Some basic theoretical features,* International Journal of Modern Physics C **08**, 675 (1997).

[5] H. Chen, S. Chen, and W. H. Matthaeus, *Recovery of the Navier-Stokes equations using a lattice-gas Boltzmann method,* Physical Review A **45**, R5339 (1992).

[6] G. Brès, F. Pérot, and D. Freed, *Properties of the lattice Boltzmann method for acoustics,* in *15th AIAA/CEAS Aeroacoustics Conference (30th AIAA Aeroacoustics Conference)* (2012).

[7] E. Manoha and B. Caruelle, *Summary of the LAGOON solutions from the benchmark problems for airframe noise computations-III workshop,* in *21st AIAA/CEAS Aeroacoustics Conference* (2015).

[8] V. Yakhot, S. A. Orszag, S. Thangam, T. B. Gatski, and C. G. Speziale, *Development of turbulence models for shear flows by a double expansion technique,* Physics of Fluids A: Fluid Dynamics **4**, 1510 (1992).

[9] E. Fares, B. Duda, A. F. P. Ribeiro, and B. König, *Scale-resolving simulations using a lattice Boltzmann-based approach,* CEAS Aeronautical Journal **9**, 721 (2018).

[10] B. M. Duda, E. Fares, R. Kotapati, Y. Li, I. Staroselsky, R. Zhang, and H. Chen, *Capturing laminar to turbulent transition within the LBM based CFD solver PowerFLOW,* AIAA Scitech Forum (2019), 10.2514/6.2019-1832.

[11] D. Casalino, G. Romani, R. Zhang, and H. Chen, *Lattice-Boltzmann calculations of rotor aeroacoustics in transitional boundary layer regime,* Aerospace Science and Technology **130**, 107953 (2022).

[12] A. F. P. Ribeiro, D. Casalino, and E. Fares, *Lattice-boltzmann simulations of an oscillating NACA0012 airfoil in dynamic stall,* in *Advances in Fluid-Structure Interaction*, edited by M. Braza, A. Bottaro, and M. Thompson (Springer International Publishing, 2016) pp. 179–192.

[13] A. F. P. Ribeiro, D. Singh, B. Konig, and E. Fares, *On the stall characteristics of iced wings,* in *55th AIAA Aerospace Sciences Meeting* (2017).

[14] A. F. P. Ribeiro, D. Casalino, E. Fares, and M. Choudhari, *Direct Numerical Simulation Of An Airfoil With Sand Grain Roughness On The Leading Edge*, Technical Memorandum TM-2016-219363 (NASA, 2016).

[15] G. Romani, D. Casalino, and W. van der Velden, *Numerical analysis of airfoil trailing-edge noise for straight and serrated edges at incidence,* AIAA Journal **59**, 2558 (2021).

[16] F. Avallone, W. C. P. van der Velden, D. Ragni, and D. Casalino, *Noise reduction mechanisms of sawtooth and combed-sawtooth trailing-edge serrations,* Journal of Fluid Mechanics **848**, 560 (2018).

[17] D. P. Lockard, *An efficient, two-dimensional implementation of the Ffowcs Williams and Hawkings equation,* Journal of Sound and Vibration **229**, 897 (2000).

[18] J. E. Ffowcs Williams and D. L. Hawkings, *Sound generation by turbulence and surfaces in arbitrary motion,* Philosophical Transactions of the Royal Society of London. Series A, Mathematical and Physical Sciences **264**, 321 (1969).

[19] A. F. P. Ribeiro, M. R. Khorrami, R. Ferris, B. Koenig, and P. A. Ravetta, *Lessons learned on the use of data surfaces for Ffowcs Williams-Hawkings calculations: Airframe noise applications,* in *28th AIAA/CEAS Aeroacoustics Conference* (2022).

[20] A. F. P. Ribeiro and C. Muscari, *Sliding mesh simulations of a wind turbine rotor with actuator line lattice-Boltzmann method,* Wind Energy **27**, 1115 (2024).

[21] W. C. van der Velden, D. Casalino, and G. Romani, *Full-scale serrated wind turbine trailing edge noise certification analysis based on the lattice-boltzmann method,* AIAA SCITECH 2023 Forum (2023), 10.2514/6.2023-0970.

[22] S. Oerlemans, M. Fisher, T. Maeder, and K. Kögler, *Reduction of wind turbine noise using optimized airfoils and trailing-edge serrations,* AIAA Journal **47**, 1470 (2009).

[23] W. C. van der Velden and D. Casalino, *Towards digital noise certification of serrated wind turbines,* 25th AIAA/CEAS Aeroacoustics Conference (2019), 10.2514/6.2019-2646.

[24] M. Drela, *XFOIL: An analysis and design system for low Reynolds number airfoils,* in *Low Reynolds Number Aerodynamics*, edited by T. J. Mueller (Springer Berlin Heidelberg, Berlin, Heidelberg, 1989) pp. 1–12.

[25] GE, *GE renewable energy and TNO to test new research on blade tip improvements aimed at reducing levelized cost of energy (LCOE) of offshore wind power,* (2021), accessed: March 24 2023.

[26] International Electrotechnical Commission, *Wind turbines – part 11: Acoustic noise measurement techniques,* IEC 61400-11 **3rd ed.** (2012).

[27] S. Oerlemans, P. Sijtsma, and B. Mendez Lopez, *Location and quantification of noise sources on a wind turbine,* Journal of Sound and Vibration **299**, 869 (2007).

13

Inflow Turbulence Distortion Effects on Airfoil Noise

Mathematicians aren't people who find maths easy;
they're people who enjoy how hard it is.

Matt Parker

The interaction of grid-generated turbulence with airfoils of different thicknesses is investigated, leading to a deeper understanding of the influence of the airfoil geometry on the near-field flow and on the far-field pressure fluctuations. Experimentally validated lattice-Boltzmann simulations are used to analyze the flow properties in the leading-edge (LE) vicinity. The analysis shows that momentum is transferred from the streamwise to the transverse velocity for the thin airfoil and to the spanwise velocity for the thick airfoil. This mechanism changes with the increase in the airfoil thickness, resulting in a higher concentration of vortices near the LE oriented in the transverse direction. Thick airfoils are shown to have noise directivity patterns significantly different from theory at higher frequencies, radiating noise upstream of the LE, due to turbulence distortion.

Parts of this chapter have been published in Physics of Fluids **35** (11), p. 115112 (2023) [1], co-written with Fernanda L. dos Santos.

13.1. Introduction

Flow-induced noise negatively impacts people and wildlife [2–5], being a relevant problem to the sustainable development of ships, aircraft engines, and wind turbines. Leading-edge (LE) noise is an important low-frequency sound production mechanism [6], occurring in situations such as blade interaction with the wake generated by a ship hull, a stator crossing the wake generated by a rotor, or the atmospheric boundary layer impinging on a wind turbine blade. The phenomenon is caused by fluctuations in the incoming flow impinging on the LE of the blades, leading to wall pressure fluctuations (WPF) and hence noise radiation to the far field. LE noise is relevant for noncavitating marine applications since low-frequency sound waves can propagate over large distances due to higher sound speed in water compared to air and low sound absorption [7, 8], harming marine animals that depend on sound for communication, mating, searching for prey, and avoiding predators [4, 5]. Therefore, understanding the LE noise mechanism is crucial to developing accurate noise prediction methods and technologies to mitigate LE noise production. The typical nomenclature used for LE noise, which we use throughout this work, is shown in Fig. 13.1, where the origin of the coordinate system is considered at the airfoil LE at mid-span.

The blade geometry is a critical parameter for the LE noise generation [9–14]. Among the airfoil geometrical parameters, the airfoil LE region has the most significant influence on this noise source [13, 15, 16]. The airfoil camber is reported to have a small effect on the radiated LE noise [9, 10, 17]. The angle of attack also has negligible influence in the LE noise generation [9, 10, 17, 18]. Moreau et al. [10] found that LE noise is insensitive to changes in the angle of attack from zero to $15°$. Gill et al. [13] and Hainaut et al. [15] used computational aeroacoustics (CAA) to study the main airfoil geometrical parameters influencing LE radiated noise. Gill et al. [13] considered single-frequency harmonic gusts interacting with the LE of symmetric airfoils of different thicknesses and LE nose diameters. Hainaut et al. [15] considered two-component synthetic turbulence and investigated the inflow turbulence interaction with the LE of symmetric airfoils of several LE nose diameters, chord lengths, thicknesses, and maximum thickness locations. Gill et al. [13] showed that the airfoil maximum thickness and LE nose diameter affect the radiated noise, resulting in lower sound power levels as these parameters increase, mainly for high frequencies. Paruchuri [17] came to the same conclusion in an experimental study. Hainaut et al. [15] observed the same trend for an observer position normal to the airfoil. Hainaut et al. [15] showed that the location of maximum thickness also influences the LE noise, resulting in higher noise levels for high frequencies as the location of maximum thickness shifts downstream. They investigated the effect of the chord length on LE noise by keeping the geometry upstream of the maximum thickness the same and changing the geometry downstream of this location. They reported that the chord length did not affect the LE noise and concluded that the LE noise is only influenced by the geometry forward of the position of the maximum thickness.

According to Gill et al. [13] and Hainaut et al. [15], the mechanism responsible for the effect of the airfoil geometry on the LE noise is the distortion of the

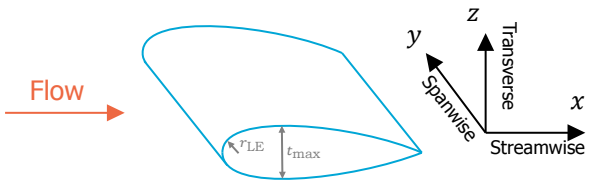

Figure 13.1: Nomenclature used throughout the paper, where r_{LE} is the leading-edge radius and $t_{\max}$ is the airfoil maximum thickness.

inflow turbulence as it approaches the LE. Gill et al. [13] attributed this turbulence distortion to the velocity gradients in the LE stagnation region, which resulted in a larger stagnation region for airfoils with a larger thickness. However, the specific mechanism responsible for the turbulence distortion near an airfoil LE has not been extensively investigated yet [19, 20]. According to the rapid distortion theory (RDT) developed by Hunt [21], the mechanism responsible for the turbulence distortion in the stagnation region of a cylinder depends on the ratio of the cylinder radius r to the turbulence integral length scale Λ_f [22]. This dependence is assumed to also occur in the case of turbulence-airfoil interaction because, according to Mish and Devenport [23], the inflow distortion produced by an airfoil in the region sufficiently close to the stagnation point is similar to that produced by a cylinder with a radius equal to the airfoil LE radius. According to the RDT, for $\Lambda_f \gg r$, the governing physical mechanism of the turbulence distortion is the flow blockage imposed by the cylinder [21, 22]. This yields a momentum transfer between the streamwise and the upwash velocity (z-direction) as the flow approaches the cylinder LE along the stagnation streamline. As a result, the root-mean-square (RMS) of the streamwise velocity fluctuations u_{rms} decreases, and the RMS of the transverse velocity fluctuations w_{rms} increases close to the body LE, whereas the RMS of the spanwise velocity fluctuations v_{rms} remains constant. For $\Lambda_f \ll r$, the turbulence distortion is caused by the mean velocity field, which stretches and rotates vortex lines, resulting in the distortion of the vorticity field and consequent change of the turbulent velocities [21, 22]. In that case, the opposite behavior is observed: the u_{rms} and the w_{rms} values increase and decrease, respectively, close to the body LE.

Recent experimental studies [24–27] have focused on LE noise and turbulence distortion for airfoils. However, in experiments, measuring the noise of an airfoil under homogeneous grid-generated turbulence is challenging because the noise created by the grid is often comparable to the LE noise. Also, measuring and analyzing the turbulence distortion very close to the LE is difficult because not all flow properties can be measured simultaneously at several locations. Furthermore, the measurement itself may be intrusive and can modify the flow it aims to measure. In this context, numerical studies can complement experimental investigations because they result in the complete and simultaneous flow field, allowing a more in-depth analysis of the turbulence distortion phenomenon.

Numerical simulations of freestream turbulence impinging on an airfoil LE have historically been carried out assuming inviscid flow, using vortex methods [28, 29]

or Euler-based methods [30–32]. Although LE noise caused by interaction with blade wakes, e.g., a rotor-stator configuration, has been studied in depth with high-fidelity computational fluid dynamics (CFD) [33], LE noise due to interaction with a wind/water-like turbulence spectrum, as experienced by wind turbines and ship propellers, has rarely been directly simulated with such methods [34, 35]. These high-fidelity simulations allow the inclusion of potential boundary layer effects on LE noise and any interaction with flow separations and trailing-edge noise. For the specific case of the turbulence distortion mechanism, this phenomenon has been investigated numerically by Gill et al. [13] and Hainaut et al. [15], where they investigated one- and two-dimensional disturbances, respectively, interacting with airfoil geometries. However, according to Gill et al. [13], studying the turbulence distortion for a realistic turbulent inflow containing three-dimensional disturbances is paramount because the turbulence may be deformed differently than one-dimensional or two-dimensional disturbances. Thus, high-fidelity simulations of realistic inflow turbulence interacting with airfoils can yield valuable results to investigate the turbulence distortion phenomenon, complementing the experimental investigations.

The current study investigates the turbulence distortion for different airfoil geometries numerically. The main objective is to deepen our understanding of the inflow turbulence distortion mechanism near the LE of airfoils. A secondary objective is to understand the effects of airfoil thickness on the turbulence distortion phenomenon, including the pressure fluctuations on the airfoil surface and in the far field. Both objectives are achieved using a realistic turbulent inflow containing three-dimensional, broadband disturbances. In this work, the lattice-Boltzmann method (LBM) is used. The numerical methodology is first validated by comparing the numerical results of grid-generated turbulence with experimental data available in the literature. Throughout this work, we use the word "grid" to refer to the turbulence generation device in the wind tunnel and "mesh" as the set of elements that discretize the fluid domain in the simulation. We perform simulations of the grid-generated turbulence interacting with a National Advisory Committee for Aeronautics (NACA) 0008 airfoil to validate the flow properties near the LE with experimental data. After validating the simulation method, we investigate the turbulence distortion mechanism for two airfoils, a NACA 0008 and a NACA 0018, based on the flow field near the LE region. Subsequently, we analyze the simulated spectrum of the WPF and far-field noise of the airfoils, comparing these results with the predictions of semi-analytical models and experimental data when available. Finally, we investigate the thickness effects on the far-field noise directivity pattern for different frequencies.

13.2. Numerical Methods

A brief summary of the numerical methods used in this work is given in this Section. Detailed information on the flow solver and noise propagation approach is given in the references.

13.2.1. Fluid Solver

In the last two decades, the LBM [36] has become a viable alternative to perform high-fidelity simulations. Unlike the classic simulations based on Navier-Stokes (NS) equations, instead of using continuum mechanics as the foundation to describe fluid flow, the LBM uses statistical mechanics, considering the fluid as particles that interact with each other and the boundary conditions.

The method uses the particle distribution function $\varphi(\vec{x}, \vec{c}, t)$, which represents the probability that particles at position $\vec{x}$ and time t have velocity $\vec{c}$. Discretizing space into a numerical mesh, time into a finite timestep Δt, and the velocity space into a finite number of possible velocities (i.e., using a discrete velocity method [37]), the discrete Boltzmann equation can be numerically solved [38], leading to the Lattice-Boltzmann equation. Eddy viscosity can be added to the fluid viscosity in the particle collision model if turbulence modeling is used. With φ computed, fluid properties can be extracted from its moments, and pressure is calculated based on the ideal gas law.

A key feature of the LBM is that fluid advection is achieved by directly moving particle density functions from one cell to another without using costly and dissipative interpolation functions. The collision step accounts for the interaction between particles with different velocities in the same cell. This is usually computed with the Bhatnagar-Gross-Krook (BGK) [39] approximation, which only depends on simple mathematics based on local quantities, making it computationally inexpensive and well-suited for parallelization, unlike the derivatives in the NS equations.

The LBM computations are conducted with PowerFLOW, a commercial CFD code, which is able to handle very complex geometries [40] by using a Cartesian mesh and the concept of surface elements, or surfels [41]. Due to the Cartesian mesh, a wall model is necessary, which is done similarly to NS solvers by employing the log-law and pressure gradient corrections [42]. In addition, the solver is usually run using very large eddy simulations (VLES), which allow for a hybrid approach of Reynolds-averaged Navier-Stokes (RANS) and large eddy simulations (LES) [43]. Here, we are interested in resolved turbulence, mainly the free-stream turbulence; therefore, we avoid turbulence modeling strategies away from the walls. Hence, the LBM simulations are conducted as coarse direct numerical simulations (DNS) or implicit LES (ILES), meaning that the numerical dissipation of the numerical method and mesh act as a sub-grid scale model [44]. This was achieved by multiplying the eddy viscosity by zero in the simulations included herein.

The LBM can formally reproduce the physics of the weakly compressible NS equations [45], depending on the discretization of the velocity space [46], equilibrium distribution function [47], and collision model [39], while presenting potential advantages in terms of computational performance and numerical dissipation. For aeroacoustics in particular, LBM exhibits low-dissipation characteristics equivalent to high-order methods [48], while the explicit and simple mathematics of the algorithm can make it substantially faster than NS methods [49] when small timesteps are used. For aerodynamics, the performance advantage can be reduced [50], especially as NS solvers can use larger timesteps [51]. Some relevant applications of the LBM for this paper are simulations of the wake of a cylinder impinging on another

cylinder in an open jet wind tunnel [52], unsteady airfoil aerodynamics [53], and applications to airfoil trailing-edge noise using DNS [54], ILES [55], and VLES [56].

13.2.2. Noise Propagation

Numerical approaches can successfully compute pressure fluctuations, i.e., noise, in arbitrary locations of the computational domain. However, it is prohibitively expensive to represent the propagation of the noise sources to the targets, i.e., microphones, with high resolution. Therefore, acoustic analogies are powerful tools for predicting far-field noise based on near-field pressure fluctuations. Therefore, this paper adopts the Ffowcs Williams-Hawkings (FW-H) acoustic analogy coupled to the LBM [57].

The FW-H analogy [58] considers a surface near the acoustic sources to propagate the aeroacoustic noise to arbitrary points in space. The surfaces can coincide with solid walls or be placed arbitrarily around them, yielding approaches dubbed as solid or permeable, respectively. The formulation is based on a rearrangement of the Navier-Stokes equations and is often solved by neglecting viscous terms and quadrupole sources outside the surface, using the Farassat 1A [59, 60] formulation, and an advanced time approach [61]. For details on the Farassat formulation 1A, see Farassat [62].

Recent studies have shown that the solid formulation often shows severe issues, particularly with complex flows and geometries, and hence should be adopted with caution [63]. However, the permeable formulation is deemed particularly challenging for the objectives of this study. This conclusion is based on the observation that the upstream turbulence yields hydrodynamic fluctuations on the permeable data surface that would be computed as acoustic noise in the far-field microphones. Hence, we use the solid formulation, which has been used successfully for airfoil trailing-edge noise in the past [54–56].

13.3. Amiet Theory for Leading-Edge Noise

This section briefly describes the Amiet model for LE noise and WPF because they are used to predict the WPF and far-field noise spectra for the cases investigated in this study. The reader is referred to Amiet [64] and de Santana [65] for a detailed derivation of the following expressions.

13.3.1. Far-Field Noise Model

Amiet [64] proposed a semi-analytical model to predict the far-field noise generated by the interaction of a turbulent uniform inflow. The approach considers a flat plate of infinitely large span and negligible thickness, therefore, neglecting important effects present in airfoils of realistic geometry. The model assumes a stationary observer and frozen turbulence and is formulated in the Fourier domain. The one-sided power spectral density (PSD) of pressure fluctuations observed in the far field at position (x_o, y_o, z_o) for a flat plate of chord c and span d as a function of f is:

$$G_{pp}(x_o, y_o, z_o, f) = 4\pi^2 \left(\frac{2\pi f z_o \rho(c/2)}{c_\infty \sigma^2} \right)^2 \bar{u}_\infty \frac{d}{2} \left| \mathcal{L}(x_o, K_x, K_y) \right|^2 \Phi_{ww}(K_x, K_y) \quad (13.1)$$

where $\sigma^2 = x_o^2 + (1-M^2)(y_o^2 + z_o^2)$, $K_x = 2\pi f/\bar{u}_\infty$, and $K_y = (2\pi f y)/(c_\infty \sigma)$. $\mathcal{L}$ is the aeroacoustic transfer function. Its formulation and derivation are shown in pages 155, 166, and 168 of the work by de Santana [65]. The main input for the Amiet prediction model is the transverse turbulence spectrum Φ_{ww}, which is discussed in Section 13.3.3.

13.3.2. Wall-Pressure Fluctuation Model

In the derivation of the far-field noise model, Amiet [64] defines the two-sided cross-PSD of the surface pressure jump. Paterson and Amiet [18] show that the cross-PSD of the WPF is derived from the surface pressure jump, i.e., Eq. 18 in Paterson and Amiet [18]. From this equation, the one-sided auto-PSD at the chordwise position x as a function of f is computed as:

$$G_{qq}(x,f) = 8\pi\bar{u}_\infty(\pi\rho)^2 \int_0^\infty \Phi_{ww}(K_x,k_y) g(x,K_x,k_y) g^*(x,K_x,k_y) \mathrm{d}k_y \tag{13.2}$$

where k_y is the spanwise wavenumber. The airfoil response function g is determined from Mish and Devenport [66], and g^* refers to the complex conjugate of the function g.

13.3.3. Inflow Turbulence Spectrum Models

Different models exist to represent the inflow turbulence spectrum. Two formulations for Φ_{ww} are used in this research: the traditional von Kármán turbulence spectrum and the RDT-based turbulence spectrum. These two formulations are discussed in the following sections. They are determined by integrating the energy spectrum function $E(k)$. A detailed derivation of this formulation is given in Glegg and Devenport [67] for the von Kármán spectrum and in de Santana et al. [26] and dos Santos et al. [25] for the RDT-based spectrum.

Von Kármán Turbulence Spectrum

The inflow turbulence spectrum of the z-direction velocity is usually assumed to be represented by the two-dimensional von Kármán turbulence spectrum:

$$\Phi_{ww}^{\mathrm{vK}}(k_x,k_y) = \frac{4}{9\pi}\frac{u_{\mathrm{rms}}^2}{k_e^2}\frac{(k_x/k_e)^2 + (k_y/k_e)^2}{[1+(k_x/k_e)^2+(k_y/k_e)^2]^{7/3}} \tag{13.3}$$

where k_x is the streamwise wavenumber and k_e is the wavenumber scale of the largest eddies [67]:

$$k_e = \frac{\sqrt{\pi}}{\Lambda_f}\frac{\Gamma(5/6)}{\Gamma(1/3)} \tag{13.4}$$

The von Kármán one-dimensional inflow turbulence spectrum for the streamwise velocity $\Phi_{uu}(k_x)$ is useful as a reference to validate the experimental and numerical spectra. This turbulence spectrum is given as:

$$\Phi_{uu}^{\mathrm{vK}}(k_x) = \frac{2}{\sqrt{\pi}} \frac{\Gamma(5/6)}{\Gamma(1/3)} \frac{u_{\mathrm{rms}}^2}{k_e} \left[1 + \left(\frac{k_x}{k_e}\right)^2\right]^{-5/6} \tag{13.5}$$

It is clear from this equation that the von Kármán spectrum follows a -5/3 power law in k_x at high frequencies.

RDT-Based Turbulence Spectrum

To account for the turbulence distortion, de Santana et al. [26] proposed a modification to the turbulence energy spectrum based on the asymptotic results of the RDT developed by Hunt [21] for turbulent flow around two-dimensional bluff bodies. In the proximity of an upstream cylinder wall, the decay of the one-dimensional turbulence energy spectrum $\Phi_{ww}(k_x)$ tends asymptotically to a -10/3 power law at high frequencies. De Santana et al. [26] proposed an energy spectrum formulation that results in an expression for $\Phi_{ww}(k_x)$ that follows this -10/3 power law at high frequencies. The resulting turbulence spectrum is given as [26]:

$$\Phi_{ww}^{\mathrm{RDT}}(k_x, k_y) = \frac{91}{36\pi} \frac{u_{\mathrm{rms}}^2}{k_e^2} \frac{(k_x/k_e)^2 + (k_y/k_e)^2}{[1 + (k_x/k_e)^2 + (k_y/k_e)^2]^{19/6}} \tag{13.6}$$

The one-dimensional inflow turbulence spectrum for the streamwise velocity is [25]:

$$\Phi_{uu}^{\mathrm{RDT}}(k_x) = \frac{91}{36\sqrt{\pi}} \frac{\Gamma(5/3)}{\Gamma(19/6)} \frac{u_{\mathrm{rms}}^2}{k_e} \left[1 + \left(\frac{k_x}{k_e}\right)^2\right]^{-5/3} \tag{13.7}$$

It is clear that the one-dimensional wavenumber for the streamwise velocity $\Phi_{uu}(k_x)$ follows a -10/3 power law at high frequencies as $\Phi_{ww}(k_x)$ shown by Hunt [21].

In this study, Eqs. (13.3) and (13.6) are used as input in the Amiet models (Eqs. (13.1) and (13.2)). Equation (13.5) is compared to the velocity spectrum obtained from the simulation results and is present as a function of frequency f. Thus:

$$\Phi_{uu}(f) = (2\pi/\tilde{u}_\infty)\Phi_{uu}(K_x) \tag{13.8}$$

13.4. Setup Description

13.4.1. Wind Tunnel Reference Case

The case studied in this work corresponds to an open-jet setup of a turbulent inflow impinging on an airfoil LE. The setup corresponds to the open test section of the Aeroacoustic Wind Tunnel of the University of Twente, an open-jet, closed-circuit facility with contraction with a ratio of 10:1. After the contraction, the flow enters a closed test section and subsequently an open test section. The generated uniform flow has turbulence intensity below 0.08% [68]. An anechoic chamber of 6 m × 6 m × 4 m encloses the test region. The test section dimensions are

0.7 m × 0.9 m (height x width). The airfoil is mounted vertically on the open test section, which consists of horizontal side plates; see Fig. 13.2.

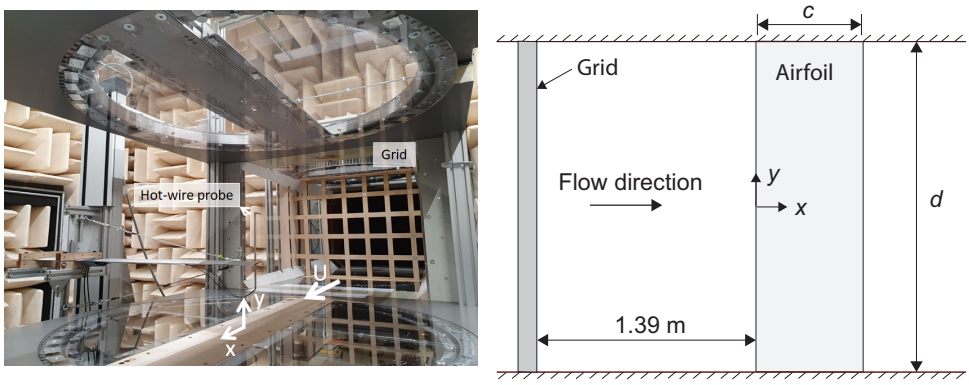

Figure 13.2: Wind tunnel setup with the grid installed in the closed test section and the hot-wire probe used to characterize the turbulent flow generated by the grid.

The turbulent inflow is generated by a mono-planar rectangular grid placed in the closed test section at 1.39 m upstream of the airfoil LE; see Fig. 13.2. The bar width is 32 mm, and the gaps are 109.5 mm, resulting in a porosity of 60%. The turbulent flow generated by the grid was characterized experimentally using hot-wire anemometry by dos Santos et al. [24]. The turbulence generated by the simulation is compared with the experimental results in dos Santos et al. [24] to validate the simulation. To do so, a simulation with an empty test section, i.e., without the airfoil, was performed.

The grid-generated turbulent inflow at the stagnation line of a NACA 0008 airfoil was evaluated by dos Santos et al. [25]. They measured the streamwise velocity at the stagnation streamline of the airfoil using hot-wire anemometry for streamwise positions $x/r_{\mathrm{LE}} \in [-100, -1.8]$, with $x = 0$ at the LE position. They also measured the WPF along the airfoil chord, with the first measurement at $x/c = 0.0007$. These experimental data sets are compared with the simulation results for a Reynolds number based on the airfoil chord of $500{,}000$.

13.4.2. Numerical Case Setup

The airfoils NACA 0008 and NACA 0018 are used in this study to investigate the influence of the airfoil geometry on the turbulence distortion mechanism and radiated LE noise. Experimental data for the NACA 0008 airfoil is available in the literature [25] for validation. Table 13.1 shows the airfoil main geometrical parameters, namely, chord c, LE radius r_{LE}, airfoil maximum thickness t_{max}, chordwise position of the maximum thickness x_{tmax}, and span d. As the thickness in the LE region is the most critical parameter for the LE noise, two airfoils from the same family but with relatively different thicknesses were chosen.

The open jet wind tunnel was reproduced in the simulations for better comparisons with experimental data. The experimental anechoic chamber was replaced

Table 13.1: Geometric parameters of the airfoils used in this research.

Airfoil	c [mm]	r_{LE}/c [-]	$t_{\max}/c$ [-]	x_{tmax}/c [-]	d/c [mm]
NACA 0008	300	0.007	0.08	0.3	2.3
NACA 0018	300	0.036	0.18	0.3	2.3

with a large cubic domain of side $200c$ with sponge zones, which are regions of high viscosity, to avoid reflections. An inlet of uniform constant velocity of about 25 m/s was placed $1.6D_H$ upstream of the turbulence grid, where D_H is the wind tunnel hydraulic diameter. In the far field, atmospheric pressure is defined as the boundary condition. Figure 13.3 shows the spanwise vorticity and the open jet setup. Note that the computational mesh was coarsened outside the jet shear layer and downstream of the airfoil trailing-edge. This can be noticed by the non-physical turbulence dissipation downstream of the airfoil. The coordinate system is shown in Fig. 13.3, with the streamwise component of the flow being parallel to the x-axis direction, the spanwise direction parallel to the y-axis, and the transverse component parallel to z-axis. The origin of the coordinate system is considered at the airfoil LE position at mid-span. Figure 13.3 also displays the turbulence decay from the start of the open test section to the airfoil LE.

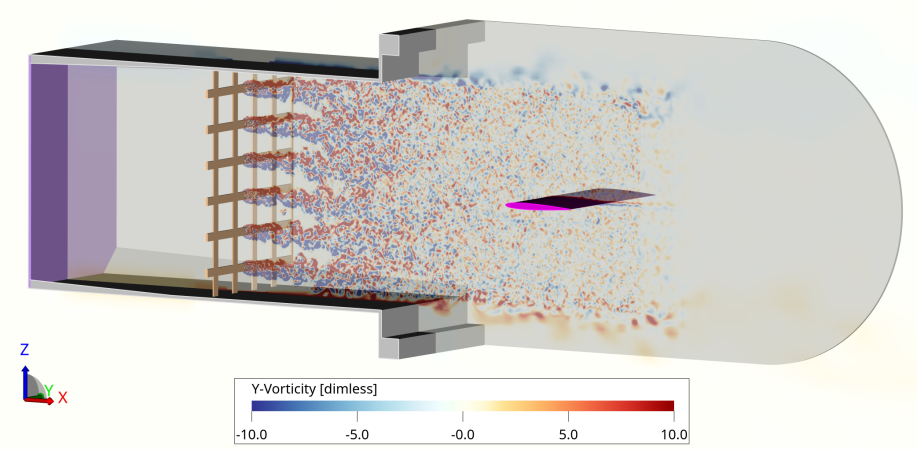

Figure 13.3: Slice showing spanwise vorticity, along with the open test section. The sidewall closer to the viewer's side is hidden for clarity.

The computational mesh was kept at a constant resolution, with a cell size of 0.0373 $\Lambda_{f,\mathrm{LE}}$, in most of the test section, from the near wake of the turbulence grid to the airfoil. This was shown to preserve the turbulence spectrum up to frequencies above 1 kHz, which is adequate for the scales of interest in this study. The local time step in this region was equivalent to 276 kHz, far exceeding time resolution requirements for the turbulence structures around 1 kHz. The mesh was further refined near the grid to capture the relevant geometrical features, with about 22 cells over the edge of the grid, transitioning to about 60 cells over the grid bar

width, doubling that cell size in the near wake of the grid, and doubling the cell size again in the bulk of the flow, between the grid and airfoil. The mesh and the instantaneous spanwise vorticity field near the grid are shown in Fig. 13.4.

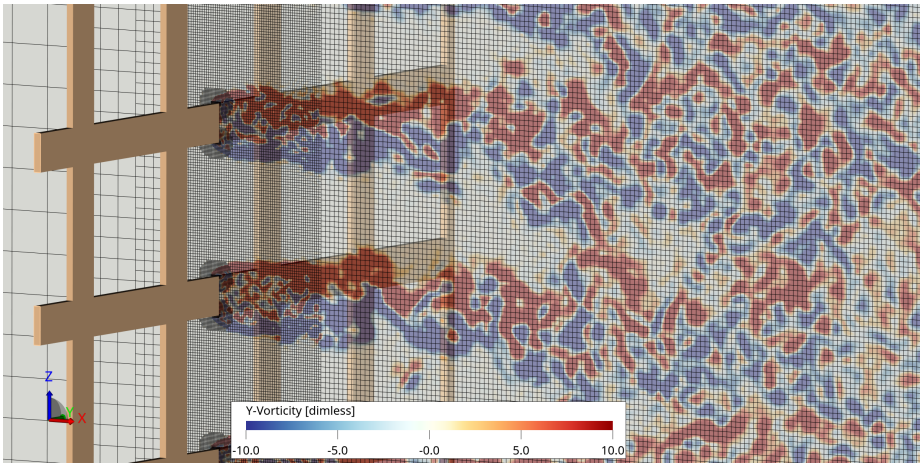

Figure 13.4: Computational mesh near the turbulence grid. Every second mesh line is shown for clarity.

Near the airfoil LE, two levels of mesh refinement were added so that the gradients in flow quantities, such as velocity and velocity fluctuations, could be properly measured near the stagnation point. The average y^+ value on the surface of the airfoil was about 40, which is compatible with the wall model used. The airfoil trailing-edge is refined by three levels relative to the freestream mesh to resolve the trailing-edge thickness with two elements. This is sufficient, based on previous experience, due to the use of the wall model. The airfoil boundary layer was refined by one level to capture the airfoil geometry adequately. However, the boundary layer was not fully resolved in the simulations. This decision is supported by the fact that the boundary layer mainly affects trailing-edge noise, having a minor influence on LE noise. The mesh and the instantaneous spanwise vorticity field near the airfoil are shown in Fig. 13.5. On the right side of the image, coarsening of the mesh can be observed past the region of interest.

Three cases are shown throughout this work: one without an airfoil, one with the NACA 0008, and one with the NACA 0018. The simulation without the airfoil was performed to mirror the experimental approach, where the turbulence was characterized with an empty test section [24] before studying the effects of the presence of the airfoil [25]. The number of cells in the domain was 300 million. The simulations were run for 2 s of physical time (over 160 flow passes, based on c), with the first 0.2 s being dismissed as the initial transient. The flow coming from the inlet takes about 0.07 s to reach the airfoil, meaning the flow goes over the airfoil for about 0.13 s (11 flow passes) during the initial transient. This initial transient was selected based on the convergence of the mean velocity towards a constant value at the target airfoil LE location by taking windows of 0.1 s. The simulation duration was chosen based on the statistical convergence of the mean and root-

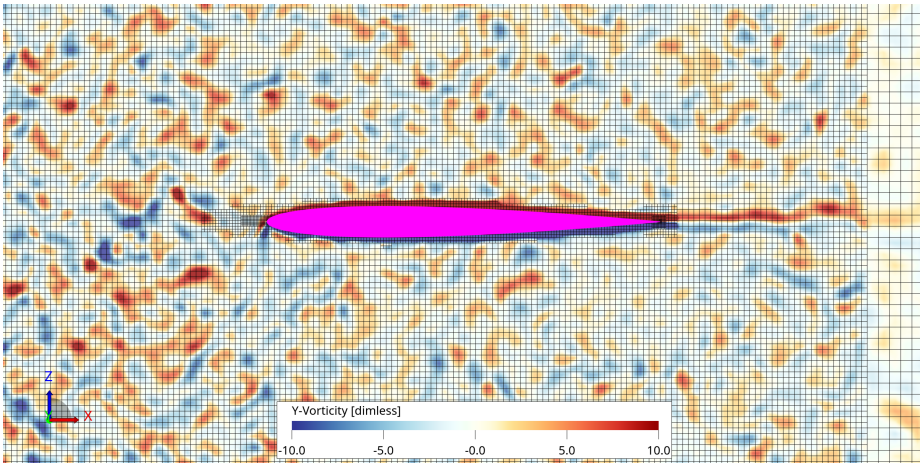

Figure 13.5: Computational mesh near the airfoil. Every second mesh line is shown for clarity.

mean-square (RMS) of the velocity fluctuations, turbulence spectrum, turbulence length scale, wall pressure spectrum on the airfoil LE region, and far-field noise. Out of these quantities, the turbulence length scale seems to be the most sensitive to the simulation duration. While other quantities showed small variations by comparing the signal for $0.2 - 1.2$ s to $0.2 - 2.0$ s, the length scale for the empty tunnel case near the target airfoil LE at various values of z had a scatter of over 14 mm for the shorter run time and 8 mm for the longer run time, corresponding to 35 and 20% of the mean, respectively. This is associated with the uncertainties in calculating the length scale, which will be covered in Section 13.5.2. While a longer run time would further reduce this uncertainty, we chose 2 s as the total run time because the far-field noise was unaffected. Simulations took about $50,000$ CPU hours on 280 cores, which corresponds to about one week of wall-clock time.

13.4.3. Mesh Resolution Effects

A concise mesh resolution study is discussed in this section to verify the consistency of the numerical results. This study is performed by coarsening the mesh for the case with the NACA 0008 airfoil by a linear factor of 1.25, meaning that number of cells is almost halved for the coarse case, and verifying the comparability of the velocity and WPF spectra for the cases of fine and coarse meshes.

The analysis starts by verifying whether the mesh affects the freestream turbulence, which is shown in Fig. 13.6. The power spectral density (PSD) of the streamwise and transverse velocity components at $x = -30r_{\mathrm{LE}}$, i.e., in the freestream, is measured for the coarse and fine meshes. In this paper, the PSD of the velocity components (Φ_{uu} and Φ_{ww}), WPF (G_{qq}), and far-field pressure fluctuations (G_{pp}) are estimated using Welch's method [69]. The spectral level is shown in decibels, where the reference values were 1 m/s for Φ_{uu} and Φ_{ww}, and 20 μPa for G_{qq} and G_{pp}. Hanning windows were used, with an overlap of 50%. The results shown in

Fig. 13.6 match well for $f < 1000$ Hz, with the only notable difference being the numerical cut-off of the coarse mesh appearing earlier, as expected. In Section 13.5.1, it is shown that the cut-off frequency for the simulation is at approximately 2 kHz.

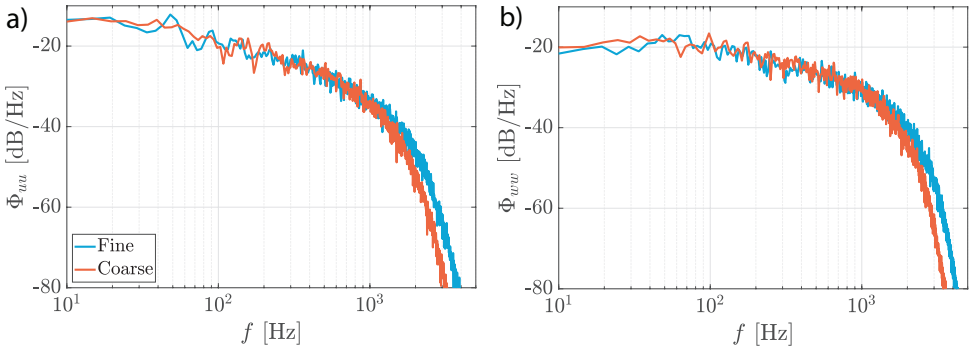

Figure 13.6: PSD of the streamwise (a) and transverse (b) velocities at $x = -30r_{\mathrm{LE}}$ for the case with the NACA 0008 airfoil for simulations with a fine and a coarse mesh (number of cells almost halved).

Next, the WPF spectra for the two meshes are compared, which is an indicator of the sensitivity of the mesh near the airfoil. Results are shown in Fig. 13.7. Some minor differences of up to $2-3$ dB are seen around 70 Hz for $x/c = 0.0035$, which correspond to the small differences seen in Fig. 13.6 for the same frequency range. For the other frequencies, the results overlap, which is not entirely expected. As the coarse mesh has a noticeable earlier cut-off near 1500 Hz, one could expect the results above this frequency to be very different for the two meshes and to decay quickly toward zero. However, the high frequencies of the WPF spectrum do not seem to correspond directly to the high frequencies of the velocity spectrum in the freestream spectrum because the level of Φ_{uu} is effectively zero at 5000 Hz (Fig. 13.6a). This will be discussed further in Section 13.5.6.

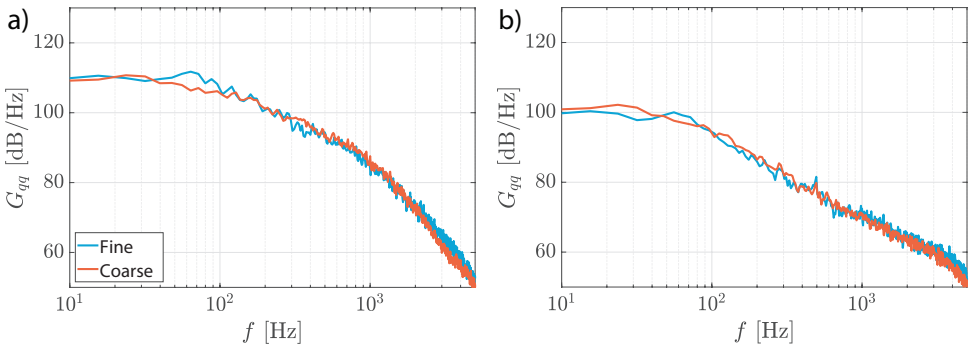

Figure 13.7: PSD of the WPF on the NACA 0008 surface at $x/c = 0.0035$ (a) and $x/c = 0.1$ (b) for simulations with a fine and a coarse mesh (number of cells almost halved).

The differences shown in Figs. 13.6 and 13.7 are considered to be acceptable.

Thus, the results from this study are considered to be grid converged up to nearly 2000 Hz.

13.5. Results

13.5.1. Validation of the Freestream Turbulence

This section compares the numerical results to the experimental data available in the literature [24] for the grid-generated turbulence without the airfoil present in the test section.

The numerical and experimental spectra of the streamwise velocity u and the transverse velocity w are shown in Fig. 13.8. The von Kármán turbulence spectrum is also included in these figures because this formulation is often used as input for LE noise calculations and is representative of isotropic turbulence. These spectra are determined at $x = 0$, which is the location where the airfoil LE would be. The level and frequency of the experimental spectrum are scaled to consider the minor differences in mean velocity between the experimental and numerical results. The frequency f is scaled as the Strouhal number based on Λ_f and $\bar{u}$. The spectral level of Φ_{uu} (or Φ_{ww}) is scaled by analyzing Eqs. 13.4, 13.5, and 13.8. The final scaling for the frequency and level of the experimental spectrum is:

$$f_{\text{Exp.,scaled}} = f_{\text{Exp.}} \frac{\bar{u}_{\text{Num.}}}{\bar{u}_{\text{Exp.}}} \frac{\Lambda_{f\text{Exp.}}}{\Lambda_{f\text{Num.}}}, \tag{13.9}$$

$$\Phi_{\text{Exp.,scaled}} = \Phi_{\text{Exp.}} \frac{\bar{u}_{\text{Exp.}}}{\bar{u}_{\text{Num.}}} \frac{\Lambda_{f\text{Num.}}}{\Lambda_{f\text{Exp.}}} \frac{u^2_{\text{rms,Num.}}}{u^2_{\text{rms,Exp.}}}. \tag{13.10}$$

The streamwise experimental spectrum (Φ_{uu}) matches the von Kármán spectrum well in the entire frequency range, whereas the streamwise numerical spectrum slightly overpredicts the energy levels for $300 < f < 2000$ Hz; see Fig. 13.8a. For the transverse velocity spectrum (Φ_{ww}), both experimental and numerical spectra have higher spectral levels than predicted by the von Kármán turbulence spectrum; see Fig. 13.8b. The von Kármán model was developed for an isotropic turbulent flow; thus, the difference between the experimental/numerical spectrum with the von Kármán spectrum for the transverse velocity indicates some level of anisotropy in the turbulence. As observed for Φ_{uu}, the numerical spectrum Φ_{ww} has higher energy levels than the experimental one for $300 < f < 2000$ Hz. The numerical spectra (Φ_{uu} and Φ_{ww}) decay rapidly for frequencies above 2 kHz, which is the numerical cut-off of the simulations. In general, a reasonable agreement between the numerical, experimental, and von Kármán spectra is observed for frequencies up to 2 kHz.

Figure 13.9 compares the numerical and experimental results of the RMS of the streamwise and transverse velocity fluctuations and the longitudinal length scale along the streamwise direction at mid-span and $z = 0$. These quantities are normalized by the values extracted at the LE location without the airfoil, i.e., $u_{\text{RMS,LE}}$, $w_{\text{RMS,LE}}$, and $\Lambda_{f,\text{LE}}$. The numerical results for the RMS of the velocity fluctuations follow a similar decay as the experimental results; see Figs. 13.9a and 13.9b. The

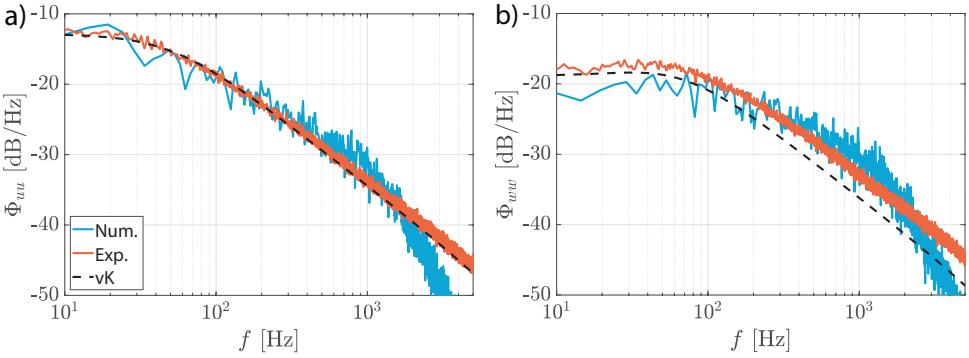

Figure 13.8: PSD of the streamwise (a) and transverse (b) velocities at $x = 0$ (target LE location) for the case without the airfoil. Num. - numerical results, Exp. - experimental results [24], vK - von Kármán spectrum.

numerical integral length scale has a similar tendency as the experimental length scale for $-100 < x < 0$; see Fig. 13.9c. However, a significant discrepancy is observed for $-400 < x < -200$ mm. Section 13.5.2 discusses the reason for this mismatch. We conclude from comparing the numerical and experimental results that the numerical turbulence presents similar trends as the experimental turbulence, except for the integral length scale.

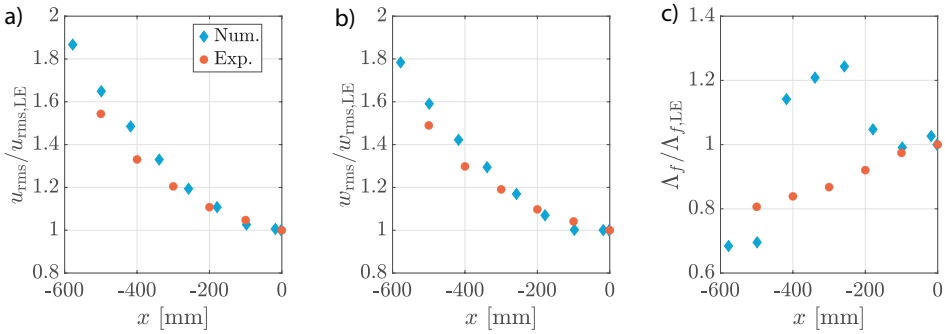

Figure 13.9: RMS of the velocity fluctuations and longitudinal length scale at mid-span and $z = 0$ along the streamwise direction. Num. - numerical results, Exp. - experimental results [24].

13.5.2. Integral Length Scale Determination

The longitudinal integral length scale Λ_f is a statistical parameter that quantifies the streamwise dimension of the largest turbulent structures present in the turbulent flow. This parameter is computed following the method proposed by Hinze [70]. This method was also used by dos Santos et al. [24] to compute the integral length scale from hot-wire measurements, which are used to validate the numerical results. In this method, the turbulence time scale is determined as the time when

the autocorrelation of the streamwise velocity reaches zero for the first time. In light of Taylor's frozen turbulence hypothesis [71], the longitudinal integral length scale is computed considering that the turbulence is convected with the mean flow velocity at the measurement location, which according to Pope [72], provides accurate results. According to Lin [73], this hypothesis is valid when $u_{\mathrm{rms}}^2 \ll \bar{u}^2$. For the results discussed in this paper, u_{rms}^2 was two orders of magnitude smaller than $\bar{u}^2$, making this hypothesis valid.

In Fig. 13.9c, the abrupt increase and decrease in the integral length at $x = -258$ mm and $x = -418$ mm, respectively, are attributed to the method used to determine the integral length scale. To clarify this, the autocorrelation of the streamwise velocity is analyzed for the locations $x = -498$ mm and $x = -418$ mm; see Fig. 13.10. The autocorrelation for $x = -418$ mm oscillates close to zero but does not cross zero as quickly as the autocorrelation for $x = -498$ mm. Thus, the time scale determined from the first-zero crossing for $x = -418$ mm is longer than the time scale at $x = -498$ mm, resulting in a larger integral length scale for $x = -418$ mm. The autocorrelations for the numerical data for $-100 < x < 0$ mm and $-600 < x < -498$ mm present the oscillatory behavior close to zero to a much lesser extent than the data for $-418 < x < -258$ mm, showing a better agreement with the experiments; see Fig. 13.9c. The experimental integral length scale in Fig. 13.9c continuously increases with the streamwise position, indicating that the numerical results are likely more susceptible to this effect because the numerical data were obtained for a relatively shorter time (2 s signal length) than the experimental data (30 s signal length). Thus, the numerical values for Λ_f should be considered with a substantial margin of uncertainty. There are other methods to determine the integral length scale, e.g., by fitting an exponential curve to the autocorrelation data, by considering the time scale as the time period needed for the autocorrelation to decrease to $1/e$ [74], or by integrating the correlation of streamwise velocity in the streamwise direction [72]. These methods were analyzed in this research. However, these approaches also did not result in consistent values and tendencies of the longitudinal integral length scale for all data points used. Thus, we decided to compute the integral length scale based on the traditional calculation method proposed by Hinze [70].

Figure 13.11 shows the streamwise and transverse (Λ_g) integral length scales for the simulations. The transverse integral length scale is calculated by integrating the correlation of the transverse velocity in the z-direction, as discussed by Pope [72]. Experimental results for the transverse integral length scale with the streamwise position are not available. For isotropic turbulence, it is expected that $\Lambda_f \approx \Lambda_g$. Figure 13.11 shows that the turbulence generated numerically results in $\Lambda_f \approx 2\Lambda_g$ at the LE, indicating that the turbulence is not isotropic at the LE, confirming what is discussed in relation to Figs. 13.8a and 13.8b. Petrikat et al. [34] performed LES simulations of a grid generating turbulence. They observed that the grid-generated turbulence resulted in $\Lambda_f \approx 2\Lambda_g$, which agrees with the results of the current study at the LE location.

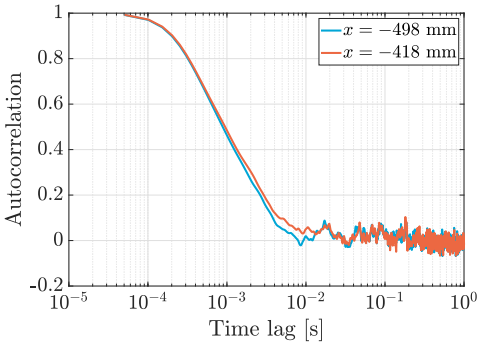

Figure 13.10: Autocorrelation of the numerical streamwise velocity fluctuations at two streamwise positions at mid-span and $z = 0$.

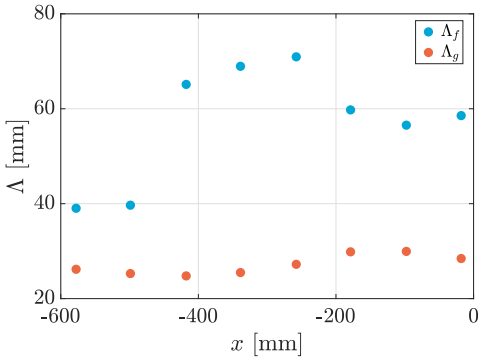

Figure 13.11: Streamwise and z-direction integral length scales. Numerical data.

13.5.3. Influence of Airfoil on the Inflow Turbulence

This section investigates the turbulence distortion due to the presence of the airfoil. First, the numerical results are compared with the available experimental data [25]. Subsequently, the numerical results of the turbulence in the vicinity of the airfoils are analyzed in detail.

Figure 13.12 shows the numerical and experimental results of mean streamwise velocity $\bar{u}$, RMS of the streamwise velocity fluctuations u_{rms}, and integral length scale Λ_f along the stagnation line of the NACA 0008 airfoil. These values are normalized by their freestream quantities, which are extracted at $x/r_{\mathrm{LE}} = -30$, because the experiments were conducted at a slightly different freestream velocity as the velocity used in the simulation (26.5 m/s in experiments, 25 m/s in simulations). The streamwise distance x is normalized with the LE radius of the airfoil. Figure 13.12a shows the decay of $\bar{u}$ as the stagnation point is approached, resulting in a zero velocity at the stagnation point, as expected. A good agreement between the simulation and the experimental data is observed for the mean velocity. Figure 13.12b shows that the experimental u_{rms} reasonably agrees with the simulation results. The experimental u_{rms} values slightly increase for $x/r_{\mathrm{LE}} > -1$, which likely occurs because the hot-wire probe used to perform the measurements was not precisely at the stagnation line. Figure 13.12c shows a good agreement between the numerical and experimental integral length scale. It is important to mention that the behavior of the autocorrelation discussed in Section 13.5.2 is not observed for the results shown in Fig. 13.12c. This means that the autocorrelation for the streamwise positions shown in Fig. 13.12c crossed zero quickly, resulting in a smooth decay of the integral length scale as the LE position is approached. The integral length scale was computed using different methods, as discussed in Section 13.5.2, presenting the same trend observed in Fig. 13.12c. Therefore, the results in Fig. 13.12 indicate that the simulated flow near the LE agrees with the experimental observations well. As the experimental data are limited in proximity to the airfoil LE due to the difficulty in performing these measurements, the numerical data can give new insights into

the turbulence distortion phenomenon for airfoils.

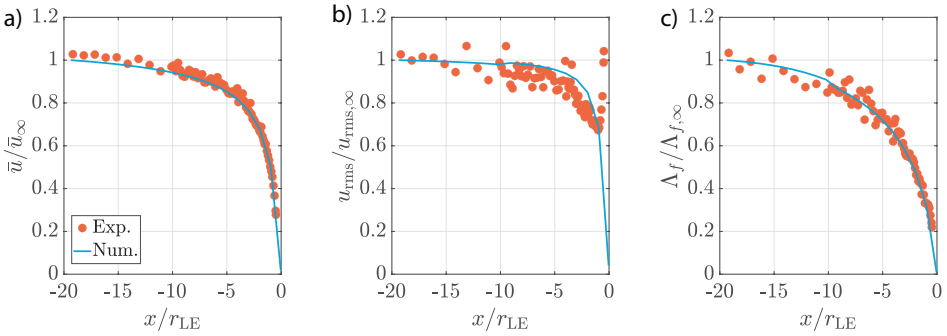

Figure 13.12: Flow quantities at the stagnation line of the NACA 0008 airfoil at mid-span. Average streamwise velocity (a), RMS of the streamwise velocity fluctuations (b), and longitudinal integral length scale (c). Num. - numerical results, Exp. - experimental results [25].

Figure 13.13a shows the numerical results of RMS values of the streamwise, spanwise, and transverse velocity components (u, v, and w, respectively) at the NACA 0008 stagnation streamline. We observe that u_{rms} tends to zero but does not reach it at the wall due to the sampling being off-body, the coarse mesh on the boundary layer, and the use of wall functions. The component associated with LE noise, w_{rms}, increases substantially near the LE. The spanwise component v_{rms} is less affected by the NACA 0008 airfoil. The changes in the RMS quantities for Fig. 13.13b near $x/r_{\mathrm{LE}} = -5$ and -2 are due to jumps in resolution of the Cartesian grid, which allow for higher frequencies to be resolved, particularly in an ILES scheme. They do not appear in Fig. 13.13a because they are outside the range of the figure due to the normalization of the x-axis by the r_{LE}.

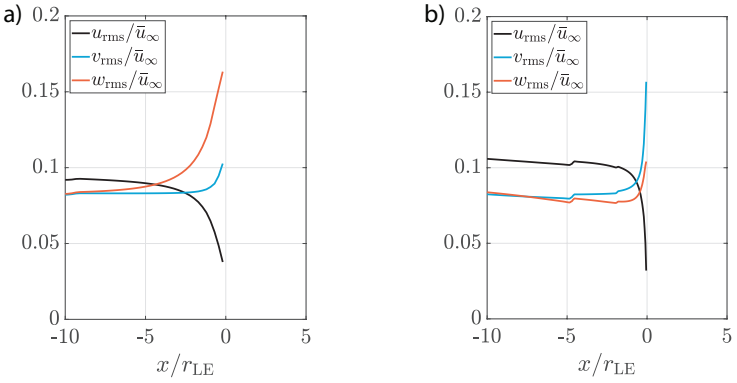

Figure 13.13: Numerical results of the turbulence intensity of the three velocity components at mid-span along the stagnation streamline for the NACA 0008 (a) and NACA 0018 (b) airfoils.

We perform the same analysis for the NACA 0018 airfoil in Fig. 13.13b. Note that scaling the x-axis with r_{LE} does not lead to similar curves for both airfoils, which fact

we will address later in this work. Although the trends of the streamwise velocity fluctuations for the NACA 0018 are to a certain extent similar to the NACA 0008 results, noticeable differences are seen for the v_{rms} and w_{rms} results. Contrary to the results for the NACA 0008, the spanwise turbulence intensity for the NACA 0018 increases near the LE more considerably than the transverse velocity.

To understand the different trends in spanwise and transverse velocities near the LE of the NACA 0008 and NACA 0018, the transverse (z-direction) vorticity is analyzed. Figure 13.14 shows the transverse vorticity in the range $\pm 15\bar{u}_\infty/c$ for the NACA 0008 and NACA 0018. The thicker airfoil leads to vortical structures that wrap around the LE, distorting the incoming turbulence and accumulating transverse vortices in front of the LE. In LE noise theory, the transverse flow fluctuations associated with spanwise vortices are the main noise source for LE noise [64]. Figure 13.14 shows that for a thicker airfoil, spanwise flow fluctuations associated with transverse vortices dominate the flow near the LE and just upstream of it. This figure shows an arbitrary spanwise location where the accumulation of transverse vortices happens for both airfoils. However, the vortices upstream of the NACA 0018 LE are larger and stronger. In addition, we observed that such behavior is very common along the span of the NACA 0018 and is fairly rare along the span of the NACA 0008.

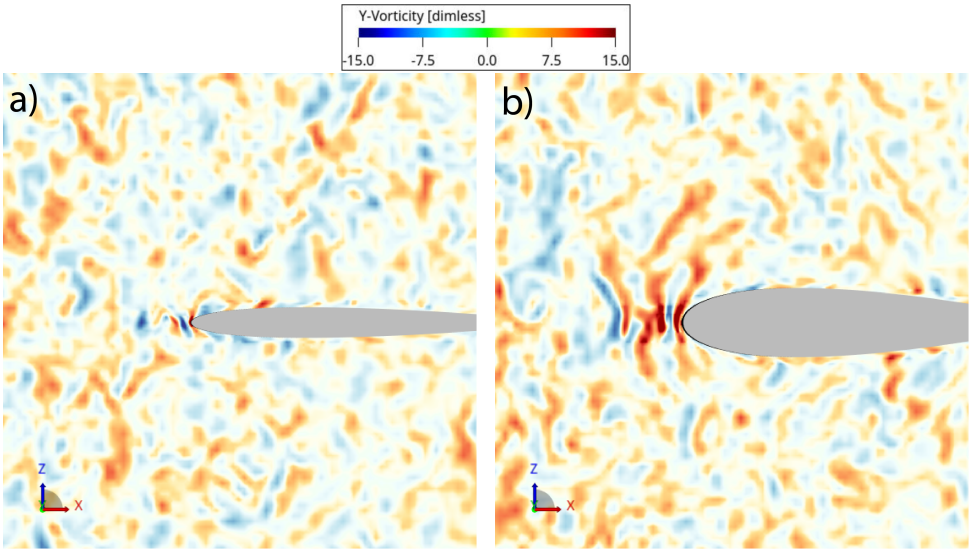

Figure 13.14: Slice in the x-z plane of the instantaneous transverse vorticity near the LE of the NACA 0008 (a) and NACA 0018 (b). Numerical data.

The vortices in the transverse direction that impinge on the airfoil LE and wrap around it are difficult to visualize in three dimensions in the fluid due to the background turbulence. Typical isosurfaces that are often used to visualize vortices of high-fidelity simulations [75] do not allow us to isolate vortices close to the surface easily and that bend, changing from having transverse to streamwise vorticity.

Hence, it is more practical to visualize these vortices indirectly by analyzing their footprint on the airfoil surface. This is done in Fig. 13.15, where the spanwise surface skin friction is shown in the range $\pm 0.002 q_\infty$, where q_∞ is the freestream dynamic pressure. The red and blue streaks correspond to positive and negative forces, respectively. We can see stronger spanwise forces acting on the LE region of the NACA 0018 airfoil compared to the NACA 0008. The red and blue streaks running from the LE up to about 30% of the chord are due to the vortices wrapping around the NACA 0018 LE. This occurs with a lower intensity and on a smaller extension of the chord length for the NACA 0008. This is likely associated with the NACA 0008 sharper LE, which splits the incoming vortices due to the smaller stagnation region.

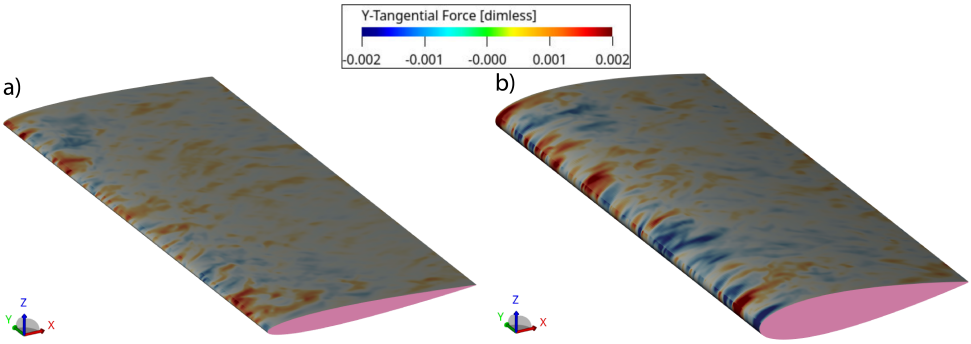

Figure 13.15: Instantaneous spanwise skin friction for the NACA 0008 (a) and NACA 0018 (b). Numerical data.

According to the RDT for cylinders, the turbulence distortion effects depend on the ratio Λ_f/r, where r is the cylinder radius [21, 22]. Considering the LE radius as characteristic length, this ratio is $\Lambda_f/r_{\mathrm{LE}} = 27.2$ for the NACA 0008 and $\Lambda_f/r_{\mathrm{LE}} = 5.3$ for the NACA 0018, where the Λ_f is considered as the value at the LE without the airfoil. The results in the stagnation line for the NACA 0008 (Fig. 13.13a) are consistent with the RDT calculations for $\Lambda_f \gg r$ [21, 22]: u_{rms} decreases as the stagnation point is approached because of the blockage imposed by the airfoil, whereas w_{rms} increases due to the momentum transfer. Meanwhile, v_{rms} is not expected to change according to the RDT. Even though this component remains mostly constant in the stagnation line of the NACA 0008, it slightly increases close to the airfoil LE. These results show that the turbulence distortion mechanism observed for a cylinder for $\Lambda_f \gg r$ is also observed for an airfoil when this ratio is respected. For the NACA 0018, the trend expected from the RDT asymptotic results is also observed but to a lesser degree: the transverse velocity fluctuations increase as the LE is approached, whereas the spanwise component increases comparatively more; see Fig. 13.13b. This change in trend occurs because the NACA 0018 LE radius is more comparable to the integral length scale, where the RDT asymptotic results for $\Lambda_f \gg r$ start to be invalid. Thus, the turbulence distortion mechanism observed for the NACA 0018 is different than that for the NACA 0008.

Figure 13.16 shows the streamwise, transverse, and spanwise spectra at stream-

wise positions along the stagnation line of the NACA 0008 airfoil. The spectral level of Φ_{uu} decreases as the stagnation point is approached, whereas the level of Φ_{ww} increases, especially for frequencies below 200 Hz. Higher frequencies seem less affected by the presence of the airfoil. The levels for Φ_{vv} show very little change, as expected, since the main momentum transfer occurs between the streamwise and transverse velocity components. The level decrease in Φ_{uu} and the level increase in Φ_{ww} confirm the momentum transfer from the streamwise component to the transverse component, which is responsible for the turbulence distortion, agreeing with the previous discussion. These results also show that the momentum transfer is concentrated in the large turbulence scales, i.e., low frequencies. The medium-length scales, i.e., mid-frequency range, are mainly unaffected by the turbulence distortion. According to the energy cascade theory and the Kolmogorov hypotheses, the outer flow parameters, i.e., mean flow field and pressure gradient, affect only the large scales and, as the energy is transferred from the large to the small scales, all the information about the geometry of the large scales, i.e., mean flow field and boundary conditions, is lost [72]. This observation suggests that the mean flow does not affect the mid-frequency range. Additionally, Gill et al. [13] attribute the turbulence distortion in the stagnation region of an airfoil to the velocity gradients present in this region. Thus, it is reasonable that the mid-frequency range is not affected by the turbulence distortion because the mean flow field does not impact this frequency range. Furthermore, the effect of the turbulence distortion for frequencies higher than 2 kHz can not be analyzed because this is the cut-off frequency of the simulation. Similar tendencies for the velocity spectra are observed for the NACA 0018, which correspond to the tendencies presented in Fig. 13.13b. Hence, the corresponding graphs are omitted here for brevity.

Next, the scaling of the main flow quantities in the stagnation line with airfoil geometrical parameters is investigated. Figure 13.17a shows the mean streamwise velocity at the stagnation line with the streamwise position scaled with the airfoil maximum thickness. $\Delta\bar{u}$ is the difference between the mean streamwise velocity for the cases with and without the airfoils. We scaled the vertical axis to achieve values between zero and unity. The best scaling of the mean velocity is obtained when the horizontal axis is normalized by the airfoil maximum thickness $t_{\max}$. According to Gill et al. [13], the turbulent inflow is distorted due to a pressure gradient in the stagnation area, which depends on the airfoil geometry in the LE region. As the airfoil maximum thickness is the largest dimension blocking the flow field, resulting in the stagnation region, it is reasonable that the velocity scales with this dimension. The scaling of Λ_f is shown in Fig. 13.17b, where the curves for both airfoils overlap when the streamwise coordinate is scaled by the airfoil LE radius r_{LE}. The integral length scale curves are smoothed to avoid the discontinuities in Λ_f for the case of the NACA 0018, as those seen in Fig. 13.11, which introduces a certain degree of uncertainty regarding the scaling. The vertical axis is scaled to result in values between zero and unity, which is done by: using $\Delta\Lambda_f$, i.e., the difference between Λ_f for the cases with and without the airfoils, adding $\Lambda_{f,0}$, which is Λ_f at $x=0$ for the case without the airfoils, and dividing each curve by a reference value taken arbitrarily at $x/r_{\mathrm{LE}}=-10$. Figure 13.17c shows the u_{rms} values at the stagnation

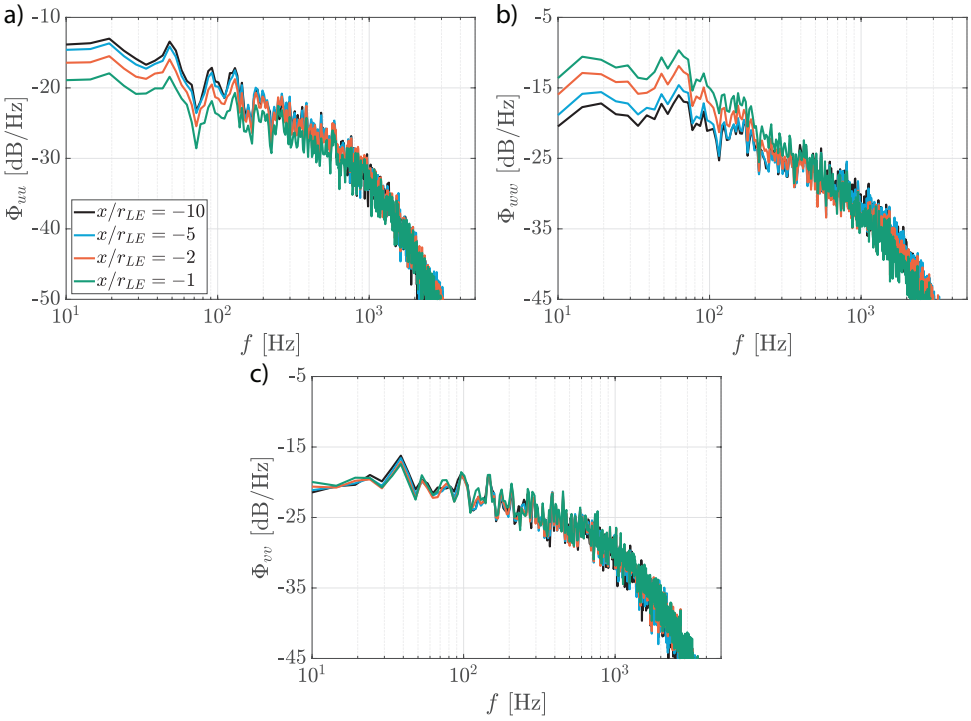

Figure 13.16: PSD of the numerical streamwise (a), transverse (b), and spanwise (c) velocity fluctuations along the stagnation line of the NACA 0008 at mid-span .

line of the airfoils. Contrary to the mean velocity and length scale, the u_{rms} curves do not require any scaling of the streamwise coordinate to collapse. The vertical axis is scaled with the value of u_{rms} at the arbitrary reference point of -6 mm. Similar behavior is observed for w_{rms}; see Fig. 13.17d. For this case, the vertical axis is scaled with the value of w_{rms} at the arbitrary reference point of $x = -10.5$ mm and the maximum value of w_{rms} since $w_{\mathrm{rms,max}}$ changes considerably from one airfoil to the other. Note that the location of maximum thickness for both airfoils is at the same chordwise position; hence, it is possible that u_{rms} scales with x/x_{tmax} or x/c. Finally, Fig. 13.17e shows the v_{rms} scaling, which seems to scale with x/r_{LE}. The reference location used to normalize v_{rms} is $x/r_{\mathrm{LE}} = -4$, as this quantity seems to start changing dramatically only very close to the LE. For the NACA 0008 airfoil, more points are likely needed to capture the peak value of v_{rms}, but both airfoils show a strong growth in v_{rms} around $x/r_{\mathrm{LE}} = -2$ and, initially, the growth rates seem comparable. Figure 13.17 shows that different flow quantities scale differently near the stagnation point, with the results for u_{rms} and Λ_f being particularly important for noise predictions using the RDT-based turbulence spectrum since the main inputs for this formulation are u_{rms} and Λ_f near the LE.

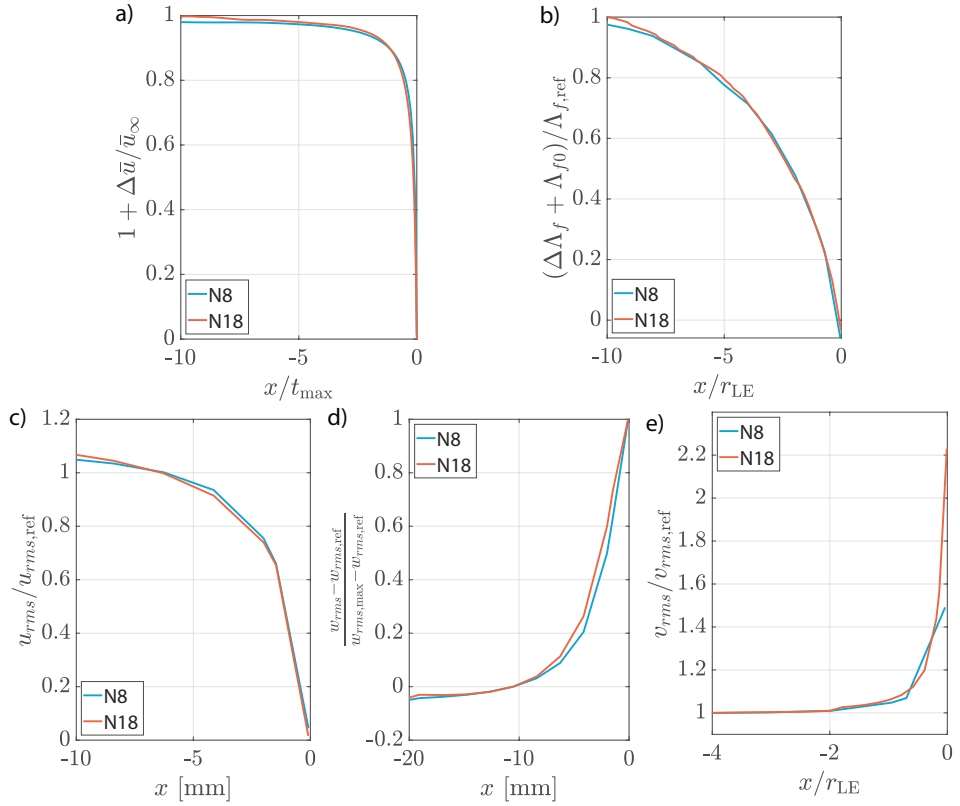

Figure 13.17: Flow quantities at the stagnation line of the airfoils at mid-span normalized by different parameters. Average velocity (a), integral length scale (b), RMS of the streamwise (c), transverse (d), and spanwise (e) velocity fluctuations. Numerical data.

13.5.4. Wall Pressure Spectra

We evaluate the behavior of the WPF near the NACA 0008 LE in Fig. 13.18. Six curves are shown: the experimental measurements ("Exp."), the numerical results ("Num."), the Amiet prediction using the von Kármán spectrum with input $\bar{u}$, u_{rms}, and Λ_f from either the experiments ("Amiet(vK)-Exp.") or the simulations ("Amiet(vK)-Num.") extracted at the LE location without the airfoil, and the Amiet prediction using the RDT spectrum with input the $\bar{u}$, u_{rms}, and Λ_f from either the experiments ("Amiet(RDT)-Exp.") or the simulations ("Amiet(RDT)-Num.") extracted at the LE location without the airfoil. At $x/c = 0.0035$, in Fig. 13.18a, we observe a near constant shift of about 10 dB between Amiet(vK)-Num. and the numerical spectrum for frequencies below 30 Hz, whereas the experimental data are close to the numerical results. Between 300 Hz and 1000 Hz, the Amiet(vK) predicts WPF spectral levels between the numerical and experimental levels. The experimental spectrum at $x/c = 0.0035$ is less reliable than at positions further downstream due to the difficulty of calibrating the microphones because of the high curvature of

the airfoil LE at this position. Amiet(RDT) does not approximate the numerical and experimental spectra. However, the decay observed for the numerical spectrum for $f > 1$ kHz is similar to that of the Amiet(RDT)-Num. This frequency range is close to the simulation cut-off frequency; therefore, these results may not be reliable. Similar results are observed for the NACA 0018; hence, results for this geometry are omitted for brevity. The WPFs at this chordwise position, i.e., $x/c = 0.0035$, are due to the direct impingement of the turbulent inflow on the surface because the boundary layer is barely developed yet.

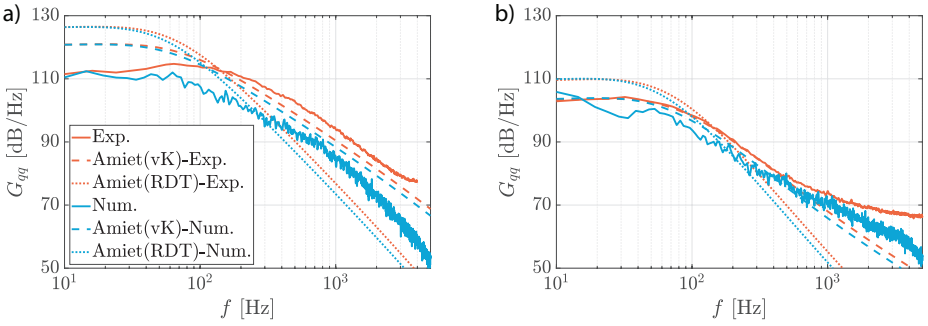

Figure 13.18: PSD of the WPF on the NACA 0008 surface at $x/c = 0.0035$ (a) and $x/c = 0.10$ (b) at mid-span. Num. - numerical results, Exp. - experimental results [25], Amiet prediction - Eq. 13.2.

In Fig. 13.18b, at $x/c = 0.10$, the discrepancies between numerical, experimental, and Amiet(vK) spectra are smaller than at $x/c = 0.0035$. We observe a near-constant shift between the numerical and experimental spectra, which is expected because of a slight difference in freestream velocity for these cases. This shift is comparable to the corresponding differences between the Amiet curves Amiet(vK)-Exp. and Amiet(vK)-Num. The Amiet prediction Amiet(vK) agrees with the experimental and numerical spectra reasonably well up to 500 Hz. For frequencies above approximately 500 Hz, the experimental spectrum changes slope, which is attributed to the boundary layer influence on the WPF. The simulation does not capture this, as the coarsely resolved, wall-modeled flow does not resolve the small fluctuations inside the boundary layer. According to previous research [76, 77], the freestream turbulence penetrates the boundary layer when the turbulence length scale of the free stream is significantly larger than the length scale in the boundary layer. This phenomenon influences the length scales in the boundary layer differently. Dogan et al. [76] showed that the freestream turbulence penetrates the outer part of the boundary layer, and for sufficiently high turbulence levels, it can penetrate up to locations very close to the wall, i.e., up to the small scales, resulting in a modulation of these scales. The results in Fig. 13.18b indicate that the freestream turbulence penetrates the boundary layer and induces the pressure fluctuations for $f < 500$ Hz. This is stated for two reasons. First, the Amiet theory only considers the impingement of the turbulent inflow on the surface, not accounting for the boundary layer development, and there is a good agreement between the Amiet prediction Amiet(vK) and the numerical and experimental spec-

tral curves for $f < 500$ Hz. Second, the spectral decay at $x/c = 0.10$ in the range $100 < f < 500$ Hz for both numerical and experimental spectra follows a similar decay as that at $x/c = 0.0035$ in the range $200 < f < 1000$ Hz for the numerical data and $200 < f < 3000$ Hz for the experimental data, which is due to the direct impingement of the turbulent inflow. For $f > 500$ Hz, the WPF spectral levels are associated with the boundary layer because the penetration of the freestream turbulence is more difficult to occur for the smaller length scales in the boundary layer, and it only causes a modulation of these scales [76]. Furthermore, the Amiet(vK) curves are much closer to the corresponding experimental and numerical spectra than the Amiet(RDT) data for $f > 500$ Hz, indicating that the turbulence distortion effect does not play a major role downstream from the LE, with the WPF at this location being mostly affected by the freestream turbulence and the boundary layer development. As we will see later in Section 13.5.5, $x/c = 0.0035$ is a region of very high gradients of the pressure fluctuations, while $x/c = 0.10$ has a less steep gradient. Hence, small differences in probe placement or turbulence decay can lead to larger errors closer to the LE. This justifies the larger discrepancies between experimental and numerical spectra at $x/c = 0.0035$.

Considering that the larger discrepancy between the Amiet(vK) prediction and the simulation/experiment at $x/c = 0.0035$ is related to the turbulence distortion effects, which are mostly concentrated in the LE region, the prediction of the WPF might be improved by using the distorted turbulence parameters as input to the Amiet prediction. As discussed in the previous section, the turbulence parameters used as input to the Amiet model change considerably in the LE vicinity. Hence, we verify the behavior of the WPF prediction considering as input the turbulence parameters extracted close to the LE, i.e., the distorted turbulence parameters. We extract the turbulence input parameters at the stagnation line at $x/r_{\mathrm{LE}} = -2$ for the NACA 0008 and at $x/r_{\mathrm{LE}} = -1$ for the NACA 0018. Different locations were used so that Amiet's prediction presented the best agreement with the numerical results for frequencies below 30 Hz. It is important to highlight that $\Lambda_{f,\infty} >> r_{\mathrm{LE}}$ for the NACA 0008 airfoil and $\Lambda_f \approx r_{\mathrm{LE}}$ for the NACA 0018 airfoil, which might be the reason why different locations are needed to obtain more accurate WPF predictions since the ratio $\Lambda_{f,\infty}/r_{\mathrm{LE}}$ dictates the mechanism responsible for the turbulence distortion [21]. The results are shown in Figs. 13.19 and 13.20 for the NACA 0008 and the NACA 0018, respectively. Figure 13.19 shows a better agreement of the Amiet(vK) prediction with the numerical and experimental spectra, mainly for frequencies below 30 Hz. For both airfoils, the difference between Amiet(vK)-Num. and numerical spectra was reduced from about 11 dB to less than 1 dB at 10 Hz when accounting for the turbulence distortion in the input parameters for the model. For Amiet(RDT)-Num., the differences were reduced from about 15 dB to 5 dB. For frequencies $f > 600$ Hz, a better agreement of the numerical spectra occurs with the Amiet(RDT)-Num. These results indicate that the disagreement of the Amiet prediction for positions close to the LE is most probably due to the turbulence distortion effects since the WPF is affected by this phenomenon. They also show that the turbulence parameters used as input to the model have to be representative of the turbulent flow in the region of interest. Thus, for a position close to the airfoil

LE where the turbulence distortion is relevant, the distorted turbulence parameters near the position of interest should be used as input to the Amiet model for the WPF. However, the freestream turbulence parameters should be used as input for a position away from the LE where the turbulence distortion is negligible. Furthermore, the spectral level and main hump are sensitive to the turbulence input parameters, mainly the integral length scale. For example, the level difference in prediction of the Amiet(vK)-Num. for the cases where the inputs were the freestream values and the distorted values is around 10 dB for $f = 30$ Hz.

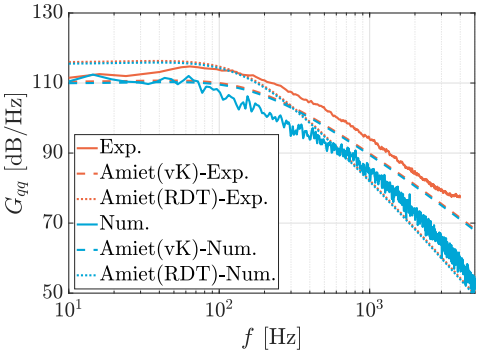

Figure 13.19: PSD of the WPF on the NACA 0008 surface at $x/c = 0.0035$ and mid-span using as input to the prediction the turbulence parameters extracted at $x/r_{\mathrm{LE}} = -2$. Num. - numerical results, Exp. - experimental results [25], Amiet prediction - Eq. 13.2.

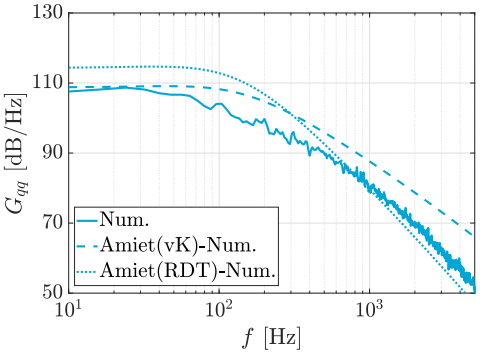

Figure 13.20: PSD of the WPF on the NACA 0018 surface at $x/c = 0.0035$ and mid-span using as input to the prediction the turbulence parameters extracted at $x/r_{\mathrm{LE}} = -1$. Num. - numerical results, Amiet prediction - Eq. 13.2.

13.5.5. Far-field Noise

Figures 13.21 and 13.22 show the far-field noise from the simulations and predicted using the Amiet model for different directivity angles. The numerical far-field pressure fluctuations were calculated using the FW-H method, considering probes located at different angles in an arc with a radius of 1.5 m centered at the airfoil mid-chord and mid-span. An angle of 180° corresponds to an upstream position of the airfoil LE, and an angle of 0° corresponds to a downstream position of the airfoil trailing-edge. The Amiet model is calculated for two cases: 1. using the von Kármán turbulence spectrum with input Λ_f and u_{rms} extracted at $x/r_{\mathrm{LE}} = 0$ without the airfoil, and 2. using the RDT-based turbulence spectrum with input Λ_f and u_{rms} extracted at $x/r_{\mathrm{LE}} = -2$ with the airfoil. The position of $x/r_{\mathrm{LE}} = -2$ is used because dos Santos et al. [25] showed that more accurate noise predictions are obtained when the turbulence input parameters are extracted at this position.

We can observe in Fig. 13.21 humps that begin around $f \approx 1$ kHz. These are due to the interference between the noise emitted at the LE and the noise scattered over the trailing-edge. The CFD and von Kármán Amiet results are very similar in the frequencies and amplitudes of these humps, but some differences appear, as is evident at $\theta = 30°$. These differences are linked to the fact that Amiet theory

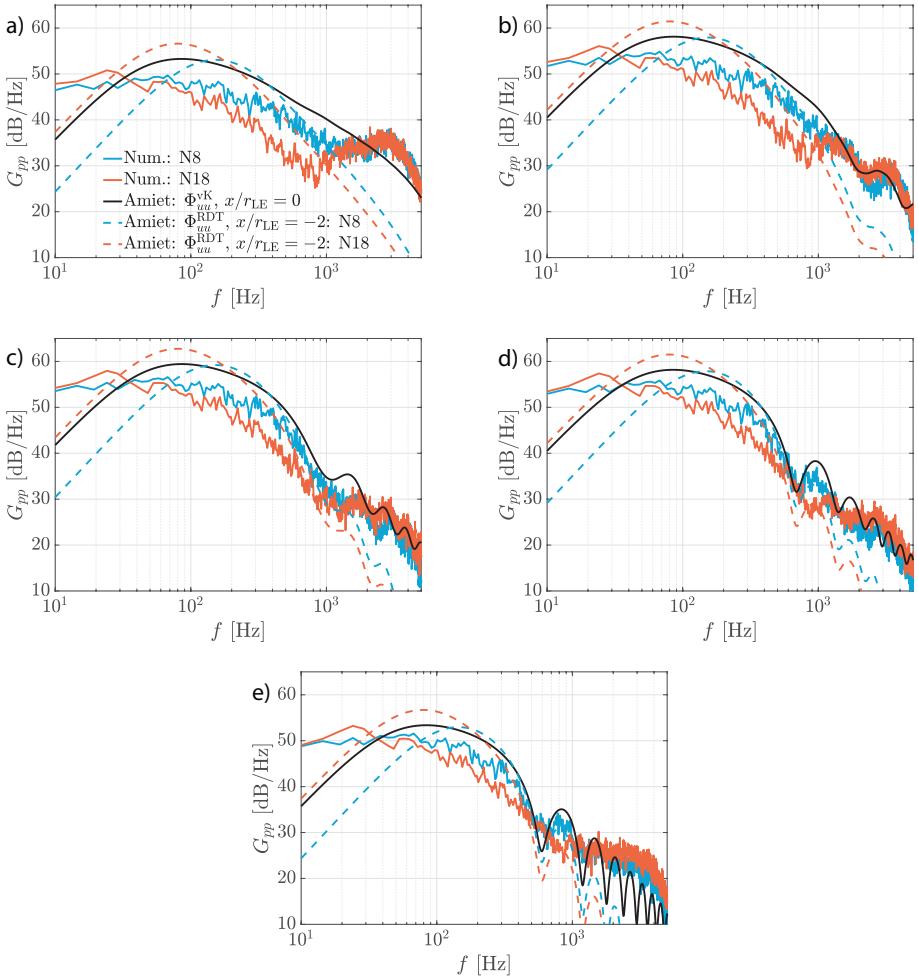

Figure 13.21: PSD of the far-field noise for the NACA 0008 and NACA 0018 airfoils from the Amiet model and from the numerical results for directivity angles of 30° (a), 60° (b), 90° (c), 120° (d), and 150° (e).

assumes a flat plate. The results for the NACA 0018 airfoil are consistently further away from the Amiet results than the NACA 0008, which is compatible with the explanation of the differences coming mostly from the airfoil thickness. Analytical models tend to overpredict these humps, as the interference patterns occur without any dissipation or dispersion. Differences to Amiet results in the high-frequency humps have also been observed in experiments [25].

For low frequencies ($f < 100$ Hz), the noise generated by both airfoils is similar. Figure 13.22 shows that the directivity at $f = 100$ Hz roughly resembles the directivity of a dipole because the airfoil is a compact noise source at this frequency, i.e., the acoustic wavelength is much larger than the airfoil chord. All analytical noise

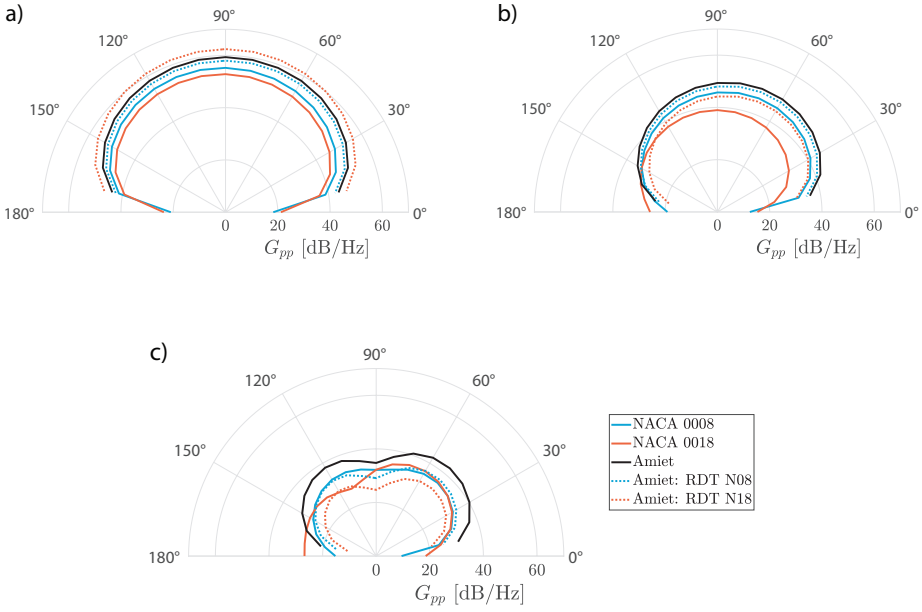

Figure 13.22: Far-field noise directivity for the NACA 0008 and NACA 0018 airfoils from the Amiet model and from the numerical results for 100 Hz (a), 500 Hz (b), and 1000 Hz (c).

predictions (using Amiet's theory) overestimate the noise for frequencies around 100 Hz and underestimate the noise for lower frequencies ($f < 30$ Hz).

For frequencies between 100 Hz and around 1 kHz, the NACA 0018 radiates lower noise levels than the NACA 0008, as expected [13, 15, 17]. The directivity pattern for $f = 500$ Hz (see Fig. 13.22) shows that the NACA 0018 generates higher or at least comparable noise levels to the NACA 0008 for upstream positions, i.e., observer angles between $180°$ and $150°$. However, as the observer angle decreases, the NACA 0018 generates lower noise levels than the NACA 0008, reaching a maximum difference of 10 dB at an angle of 30°. For this frequency ($f = 500$ Hz), the directivity pattern starts to deviate from a dipole because the airfoil is no longer a compact noise source. Regarding the noise prediction in the frequency range between 100 Hz and 1 kHz, it is clear that the prediction using the von Kármán model considerably overpredicts the noise, mainly for the thicker airfoil for observers localized at angles ranging from 30° to 120°; see Figs. 13.21 and 13.22. The noise prediction using the RDT-based spectrum also overpredicts the noise; however, it is closer to the numerical noise levels. Also, this noise prediction follows the trends of the numerical noise level; i.e., it predicts a lower noise level as the airfoil thickens. However, the RDT results do not predict the substantial change in the shape of the directivity pattern for $f = 500$ Hz for the NACA 0018 airfoil.

The noise radiated from both airfoils overlaps for higher frequencies ($f > 1$ kHz).

However, the simulation results are questionable for $f > 2$ kHz. The directivity pattern at $f = 1$ kHz in Fig. 13.22 shows that the NACA 0018 noise level is higher than the NACA 0008 for upstream positions. However, this shifts for angles smaller than $150°$, where the NACA 0018 produces lower noise levels. For angles smaller than $90°$, the noise produced by both airfoils is comparable. Again, the Amiet prediction using the von Kármán model overpredicts the noise for all observer angles, whereas the prediction based on the RDT model approximates the airfoil noise better. Note that the RDT-based spectrum only changes the noise levels and does not affect the directivity pattern. Hence, modifying the turbulence spectrum is insufficient to account for the airfoil geometry effect on the directivity, requiring modifications to the airfoil response function. The directivity pattern for the thicker airfoil changes considerably compared with the prediction, whereas the pattern for the NACA 0008 roughly follows the prediction. Thus, the airfoil geometry in the LE region affects both the noise level and the directivity pattern.

To understand the change in the directivity due to the airfoil geometry, we now investigate the pressure fluctuations in the vicinity of the airfoil LE. The pressure coefficient $Cp = (p - p_\infty)/q_\infty$ was computed in the simulations, and its RMS Cp_{rms} is used as a way to compare the integral of the noise spectra for the two airfoils. Results are shown in Fig. 13.23, where we can observe that the pressure fluctuations start at the same level at $x/c = 0$ for both airfoils. However, the NACA 0008 shows a rise in Cp_{rms} soon after the LE, followed by a sharp decrease. In contrast, the NACA 0018 shows a decay in fluctuations immediately, though at a lower rate.

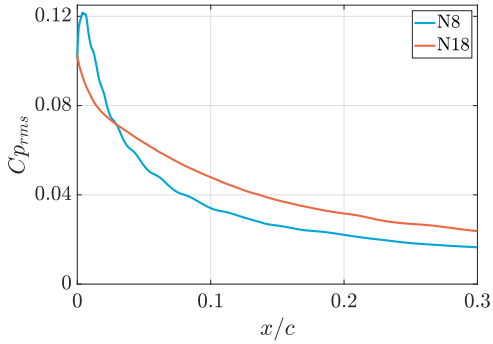

Figure 13.23: RMS of the pressure coefficient at mid-span over the airfoil chord near the LE for the NACA 0008 and NACA 0018 airfoils.

The off-body pressure fluctuations can be seen in Fig. 13.24. The discontinuities observed in Cp_{rms} near the wall, mainly observed for the NACA 0018, are visualization artifacts and do not correspond to refinement interfaces. The NACA 0018 has pressure fluctuations mainly concentrated in front of its LE, while the pressure fluctuations near the NACA 0008 LE have a cardioid shape. This agrees with the far-field noise directivity patterns of the two airfoils: while the thinner airfoil shape agrees with the Amiet theory with noise levels at $\theta = 180°$ being very low, the thicker airfoil radiates noise upstream. The difference in the pressure fluctuations near the LE for these airfoils is likely associated with the higher concentration of

transverse (z-direction) vortices that are observed just upstream of the NACA 0018 airfoil (Fig. 13.14), creating large spanwise velocity fluctuations.

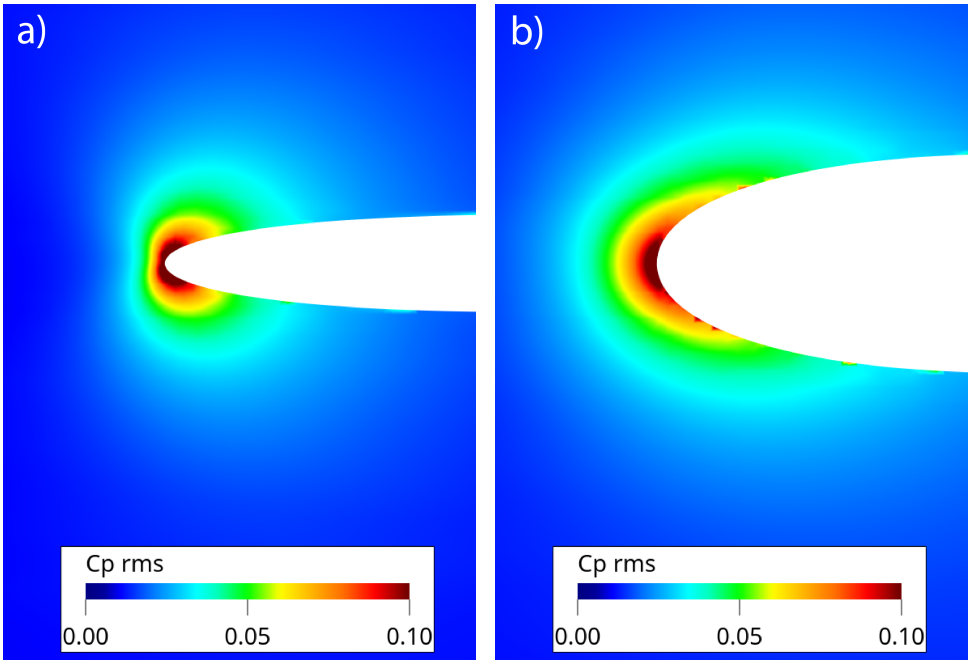

Figure 13.24: Slice showing standard deviation pressure on the central plane for the NACA 0008 (a) and NACA 0018 (b) airfoils.

13.5.6. Cut-Off Frequency Discrepancies

The numerical mesh used in the freestream to resolve the incoming flow turbulence was shown to resolve fluctuations up to about 2 kHz (e.g., Figs. 13.6 and 13.8). Even for the case without any airfoil, the mesh is refined near the target airfoil LE position, but this was a small refinement region (Fig. 13.5), and the turbulence measured in that area had a similar cut-off as in the freestream (Fig. 13.8). Hence, at the LE location, there should be effectively no turbulence for $f > 2$ Hz.

Despite this, throughout this work, the WPF (Figs. 13.7 and 13.18) and far-field noise (Fig. 13.21) did not show a clear cut-off around 2 kHz. Instead, the spectra for these quantities showed slopes between 2 and 5 kHz that followed similar trends to experiments and analytical methods (again, see Figs. 13.18 and 13.21). This is evidence that the WPF and associated far-field noise above 2 kHz are not associated with the incoming freestream turbulence at the same frequencies. A clear example of this is comparing Figs. 13.6 and 13.7. At 5 kHz, the freestream turbulence is effectively zero, while the WPF at that frequency follows the expected slope.

A potential explanation for this is that the turbulence at $f < 2$ kHz creates smaller structures near the wall, hence far-field noise at $f = 5$ kHz. This goes against Amiet

theory, where the noise is computed per frequency, meaning that far-field noise at 5 kHz only depends on the incoming turbulence spectrum at 5 kHz (see Eq. 13.1). This is surprising, and further research is needed to understand the reasons for this phenomenon.

13.6. Conclusions and Outlook

In this work, we conducted LBM numerical simulations of grid-generated turbulence in a wind tunnel and analyzed the effect of two airfoils on the turbulent inflow and the LE noise generated. The simulations match the experimental data available in the literature and noise predictions based on the Amiet model reasonably well. The detailed flow data obtained with the simulations give valuable insights into the physics of LE noise generation for real airfoils.

The velocity fluctuations in the stagnation line of the thin airfoil ($\Lambda_f \gg r_{\mathrm{LE}}$) follow the RDT trends for cylinders. In this case, momentum is transferred from the streamwise velocity component to mainly the transverse component as the LE is approached, resulting in a decrease in the RMS of the streamwise velocity, an increase in the transverse component, and the spanwise component remains mostly constant. The momentum transfer between the streamwise and the transverse velocity results in the increase in energy for the large scales in the transverse direction. A different trend is observed when the turbulence length scale is slightly larger than the airfoil LE radius, i.e., $\Lambda_f > r_{\mathrm{LE}}$. For this case, the spanwise velocity fluctuations also increase as the LE is approached, whereas the transverse velocity fluctuations increase to a lesser extent. These results indicate that a different mechanism occurs when the turbulence length scale starts to be comparable to the airfoil LE radius. Furthermore, there are significant differences between the aerodynamics of thin and thick airfoils. The flow around the thick airfoil studied in this work has a concentration of vortices near the LE oriented in the transverse direction, creating high-velocity fluctuations in the spanwise direction. This phenomenon is not seen for the thin airfoil, where the transverse velocity fluctuations dominate near the LE. Regarding the scaling of the turbulence parameters at the stagnation line, the mean streamwise velocity scales with the streamwise position normalized by the airfoil thickness. Normalizing the streamwise position with the airfoil LE radius results in the scaling of the turbulence length scale for positions close to the airfoil LE ($x/r_{\mathrm{LE}} > -10$). However, the RMS streamwise velocity does not require normalizing the streamwise position, indicating that u_{rms} does not depend on the airfoil maximum thickness and LE radius. These results show that different flow quantities scale differently near the stagnation point.

The WPF close to the airfoil LE is mainly caused by the impingement of the turbulent inflow on the surface because the boundary layer is barely developed yet. However, at $x/c = 0.10$, the low-frequency spectral level is attributed to freestream turbulence, whereas the higher frequencies are attributed to the WPF induced by the boundary layer. The Amiet theory overpredicts the WPF spectra for chordwise positions close to the LE ($x/c = 0.0035$) because the turbulence is distorted for these positions, which is not considered in the model. By using the turbulence parameters near the LE as input to the model, a good agreement between the

predicted WPF spectrum and the numerical spectrum is observed for low frequencies. For high-frequencies, the numerical spectrum follows the decay predicted by the RDT for positions near the LE ($x/c = 0.0035$). At $x/c = 0.10$, the turbulence distortion does not affect the WPF spectrum significantly.

Regarding the far-field LE noise, the directivity pattern changes as the airfoil thickness increase, mainly for mid and high frequencies. Thicker airfoils radiate higher noise levels upstream of the LE than thin airfoils due to the drastic change in the WPF distribution near the LE. This considerable change is associated with the transverse (z-direction) vortices that are observed for thick airfoils, creating large spanwise velocity fluctuations. The difference between the numerical and the Amiet predicted directivity patterns grows with airfoil thickness and frequency. Moreover, using the RDT-based turbulence spectrum is expected to improve the Amiet prediction for far-field noise of airfoils. However, this was not observed here. The prediction using the RDT spectrum shows improved trends for the LE noise decreasing with the airfoil thickness compared to the von Kármán spectrum. However, using the RDT spectrum only scales the directivity noise levels, preserving the incorrect directivity patterns. Thus, the change in directivity patterns due to the airfoil thickness must be considered in the airfoil response function. Another potential limitation of Amiet models is that they assume noise at a certain frequency depends on the incoming turbulence at the same frequency only. In our results, we observe WPF and far-field noise at expected levels for frequencies above what we resolve in the incoming turbulence. This should be a topic for further investigation.

As limitations in the Amiet models were shown for thick airfoils, numerical and experimental methods will continue to have value for applications including thick airfoils (such as those found in wind turbines) and less traditional applications, such as noise from complex LE shapes, which the current method is able to simulate [78]. This could be the case for highly eroded blades or to design airfoils with LE tubercles, which have been studied in various experiments due to their potential aerodynamic [79] and aeroacoustic [80, 81] advantages over traditional shapes. In this work, we did not seek to isolate LE radius effects from airfoil thickness effects, as done by other authors [13, 15]. Future studies could perform similar analyses as we conducted here while separating the effects of LE radius and airfoil thickness.

References

[1] A. F. P. Ribeiro, F. L. dos Santos, K. Venner, and L. D. de Santana, *Numerical study of inflow turbulence distortion and noise for airfoils,* Physics of Fluids **35**, 115112 (2023).

[2] K. Abrahamsen, *The ship as an underwater noise source,* Proceedings of Meetings on Acoustics **17**, 1 (2012).

[3] R. E. Kurt, H. Khalid, O. Turan, M. Houben, J. Bos, and I. H. Helvacioglu, *Towards human-oriented norms: Considering the effects of noise exposure on board ships,* Ocean Engineering **120**, 101 (2016).

[4] T. Götz, G. Hastie, L. Hatch, O. Raustein, B. Southall, M. Tasker, F. Thomsen,

J. Campbell, and B. Fredheim, *Overview Of The Impacts Of Anthropogenic Underwater Sound In The Marine Environment*, Tech. Rep. 441/2009 (OSPAR Convention (Convention for the Protection of the Marine Environment of the North-East Atlantic), 2009).

[5] M. C. Zwart, J. C. Dunn, P. J. K. McGowan, and M. J. Whittingham, *Wind farm noise suppresses territorial defense behavior in a songbird,* Behavioral Ecology **27**, 101 (2015).

[6] R. K. Amiet, *Noise due to turbulent flow past a trailing edge,* Journal of Sound and Vibration **47**, 387 (1976).

[7] J. S. Carlton, *Marine Propellers and Propulsion* (Butterworth-Heinemann, 2018).

[8] S. Merz, R. Kinns, and N. Kessissoglou, *Structural and acoustic responses of a submarine hull due to propeller forces,* Journal of Sound and Vibration **325**, 266 (2009).

[9] W. J. Devenport, J. K. Staubs, and S. A. L. Glegg, *Sound radiation from real airfoils in turbulence,* Journal of Sound and Vibration **329**, 3470 (2010).

[10] S. Moreau, M. Roger, and V. Jurdic, *Effect of angle of attack and airfoil shape on turbulence-interaction noise,* in *11th AIAA/CEAS Aeroacoustics Conference* (2005).

[11] J. Gershfeld, *Leading edge noise from thick foils in turbulent flows,* The Journal of the Acoustical Society of America **116**, 1416 (2004).

[12] S. Oerlemans and P. Migliore, *Aeroacoustic wind tunnel tests of wind turbine airfoils,* in *10th AIAA/CEAS Aeroacoustics Conference* (2004).

[13] J. Gill, X. Zhang, and P. Joseph, *Symmetric airfoil geometry effects on leading edge noise,* The Journal of the Acoustical Society of America **134**, 2669 (2013).

[14] J. Han, Y. Zhang, S. Li, W. Hong, and D. Wu, *On the reduction of the noise in a low-pressure turbine cascade associated with the wavy leading edge,* Physics of Fluids **35**, 095103 (2023).

[15] T. Hainaut, G. Gabard, and V. Clair, *A CAA study of turbulence distortion in broadband fan interaction noise,* in *22nd AIAA/CEAS Aeroacoustics Conference* (2016).

[16] L. J. Ayton and P. Chaitanya, *Analytical and experimental investigation into the effects of leading-edge radius on gust-aerofoil interaction noise,* Journal of Fluid Mechanics **829**, 780 (2017).

[17] C. Paruchuri, *Aerofoil geometry effects on turbulence interaction noise*, Ph.D. thesis, University of Southampton (2017).

[18] R. W. Paterson and R. K. Amiet, *Acoustic Radiation and Surface Pressure Characteristics of an Airfoil due to Incident Turbulence*, Contractor Report CR-2733 (NASA, 1976).

[19] A. Piccolo, R. Zamponi, F. Avallone, and D. Ragni, *Turbulence-distortion analysis for leading-edge noise-prediction enhancement,* in *AIAA AVIATION 2023 Forum* (2023).

[20] R. Zamponi, S. Satcunanathan, S. Moreau, D. Ragni, M. Meinke, W. Schröder, and C. Schram, *On the role of turbulence distortion on leading-edge noise reduction by means of porosity,* Journal of Sound and Vibration **485**, 115561 (2020).

[21] J. C. R. Hunt, *A theory of turbulent flow round two-dimensional bluff bodies,* Journal of Fluid Mechanics **61**, 625 (1973).

[22] R. E. Britter, J. C. R. Hunt, and J. C. Mumford, *The distortion of turbulence by a circular cylinder,* Journal of Fluid Mechanics **92**, 269 (1979).

[23] P. F. Mish and W. J. Devenport, *An experimental investigation of unsteady surface pressure on an airfoil in turbulence—Part 2: Sources and prediction of mean loading effects,* Journal of Sound and Vibration **296**, 447 (2006).

[24] F. L. dos Santos, L. Botero-Bolívar, C. H. Venner, and L. D. de Santana, *Modeling the turbulence spectrum dissipation range for leading-edge noise prediction,* AIAA Journal **60**, 3581 (2022).

[25] F. L. dos Santos, L. Botero-Bolívar, C. H. Venner, and L. D. de Santana, *Inflow turbulence distortion for airfoil leading-edge noise prediction for large turbulence length scales for zero-mean loading,* The Journal of the Acoustical Society of America **153**, 1811 (2023).

[26] L. D. de Santana, J. Christophe, C. Schram, and W. Desmet, *A rapid distortion theory modified turbulence spectra for semi-analytical airfoil noise prediction,* Journal of Sound and Vibration **383**, 349 (2016).

[27] L. Bowen, A. Celik, and M. Azarpeyvand, *A thorough experimental investigation on airfoil turbulence interaction noise,* Physics of Fluids **35**, 035123 (2023).

[28] S. A. L. Glegg and W. J. Devenport, *Panel methods for airfoils in turbulent flow,* Journal of Sound and Vibration **329**, 3709 (2010).

[29] M. J. Groom, B. Y. Zhou, and Q. Wang, *Efficient prediction of leading edge noise with a synthetic turbulence approach,* in *28th AIAA/CEAS Aeroacoustics Conference* (2022).

[30] J. Delfs, J. Yin, and X. Li, *Leading edge noise studies using CAA,* in *5th AIAA/CEAS Aeroacoustics Conference and Exhibit* (1999).

[31] C. Paruchuri, N. Subramanian, P. Joseph, C. Vanderwel, J. Turner, J. W. Kim, and B. Ganapathisubramani, *Broadband noise reduction through leading edge serrations on realistic aerofoils,* in *21st AIAA/CEAS Aeroacoustics Conference* (2015).

[32] M. Buszyk, C. Polacsek, R. Barrier, T. L. Garrec, and C. Bailly, *3D CAA methodology using synthetic turbulence to assess turbulence-cascade interaction noise emission and reduction from serrated airfoils,* in *AIAA AVIATION FORUM* (2021).

[33] D. Casalino, A. Hazir, and A. Mann, *Turbofan broadband noise prediction using the lattice boltzmann method,* AIAA Journal **56**, 609 (2018).

[34] S. A. Petrikat, R. Karve, and D. Angland, *Broadband leading edge interaction noise prediction using simulated grid turbulence,* in *AIAA/CEAS Aeroacoustics Conference* (2018).

[35] L. Trascinelli, L. Bowen, A. Piccolo, F. Avallone, R. Zamponi, D. Ragni, B. Zang, and B. Y. Zhou, *Numerical simulation of grid-generated turbulence interaction with a naca0012 airfoil,* in *AIAA AVIATION Forum* (2023).

[36] S. Succi, *The Lattice Boltzmann Equation: For Fluid Dynamics and Beyond*, Numerical Mathematics and Scientific Computation (Clarendon Press, 2001).

[37] L. Mieussens, *A survey of deterministic solvers for rarefied flows (Invited),* AIP Conference Proceedings **1628**, 943 (2014).

[38] P. J. Dellar, *An interpretation and derivation of the lattice boltzmann method using strang splitting,* Computers & Mathematics with Applications **65**, 129 (2013).

[39] P. L. Bhatnagar, E. P. Gross, and M. Krook, *A model for collision processes in gases. I. Small amplitude processes in charged and neutral one-component systems,* Physical Review **94**, 511 (1954).

[40] M. R. Khorrami, B. Konig, E. Fares, A. F. P. Ribeiro, M. Czech, and P. A. Ravetta, *Airframe noise simulations of a full-scale large civil transport in landing configuration,* in *AIAA AVIATION FORUM* (2021).

[41] H. Chen, C. Teixeira, and K. Molvig, *Realization of fluid boundary conditions via discrete boltzmann dynamics,* International Journal of Modern Physics C **09**, 1281 (1998).

[42] A. Anagnost, A. Alajbegovic, H. Chen, D. Hill, C. Teixeira, and K. Molvig, *Digital physics™ analysis of the morel body in ground proximity,* SAE transactions , 306 (1997).

[43] E. Fares, B. Duda, A. F. P. Ribeiro, and B. König, *Scale-resolving simulations using a lattice Boltzmann-based approach,* CEAS Aeronautical Journal **9**, 721 (2018).

[44] J. P. Boris, F. F. Grinstein, E. S. Oran, and R. L. Kolbe, *New insights into large eddy simulation,* Fluid Dynamics Research **10**, 199 (1992).

[45] H. Chen, S. Chen, and W. H. Matthaeus, *Recovery of the Navier-Stokes equations using a lattice-gas Boltzmann method,* Physical Review A **45**, R5339 (1992).

[46] P. J. Dellar, *Lattice Boltzmann algorithms without cubic defects in galilean invariance on standard lattices,* Journal of Computational Physics **259**, 270 (2014).

[47] G. Zhao-Li, Z. Chu-Guang, and S. Bao-Chang, *Non-equilibrium extrapolation method for velocity and pressure boundary conditions in the lattice Boltzmann method,* Chinese Physics **11**, 366 (2002).

[48] G. Brès, F. Pérot, and D. Freed, *Properties of the lattice Boltzmann method for acoustics,* in *15th AIAA/CEAS Aeroacoustics Conference (30th AIAA Aeroacoustics Conference)* (2012).

[49] E. Manoha and B. Caruelle, *Summary of the LAGOON solutions from the benchmark problems for airframe noise computations-III workshop,* in *21st AIAA/CEAS Aeroacoustics Conference* (2015).

[50] A. Aniello, D. Schuster, P. Werner, J. Boussuge, M. Gatti, C. Mirat, L. Selle, T. Schuller, T. Poinsot, and U. Rüde, *Comparison of a finite volume and two lattice boltzmann solvers for swirled confined flows,* Computers & Fluids **241**, 105463 (2022).

[51] A. F. P. Ribeiro and C. Muscari, *Sliding mesh simulations of a wind turbine rotor with actuator line lattice-Boltzmann method,* Wind Energy **27**, 1115 (2024).

[52] G. A. Brès, D. Freed, M. Wessels, S. Noelting, and F. Pérot, *Flow and noise predictions for the tandem cylinder aeroacoustic benchmark,* Physics of Fluids **24**, 036101 (2012).

[53] A. F. P. Ribeiro, D. Casalino, and E. Fares, *Lattice-boltzmann simulations of an oscillating NACA0012 airfoil in dynamic stall,* in *Advances in Fluid-Structure Interaction*, edited by M. Braza, A. Bottaro, and M. Thompson (Springer International Publishing, 2016) pp. 179–192.

[54] A. F. P. Ribeiro, D. Casalino, E. Fares, and M. Choudhari, *Direct Numerical Simulation Of An Airfoil With Sand Grain Roughness On The Leading Edge*, Technical Memorandum TM-2016-219363 (NASA, 2016).

[55] G. Romani, D. Casalino, and W. van der Velden, *Numerical analysis of airfoil trailing-edge noise for straight and serrated edges at incidence,* AIAA Journal **59**, 2558 (2021).

[56] F. Avallone, W. C. P. van der Velden, D. Ragni, and D. Casalino, *Noise reduction mechanisms of sawtooth and combed-sawtooth trailing-edge serrations,* Journal of Fluid Mechanics **848**, 560 (2018).

[57] G. Brès, F. Pérot, and D. Freed, *A Ffowcs Williams - Hawkings solver for lattice-Boltzmann based computational aeroacoustics,* in *16th AIAA/CEAS Aeroacoustics Conference* (2010).

[58] J. E. Ffowcs Williams and D. L. Hawkings, *Sound generation by turbulence and surfaces in arbitrary motion,* Philosophical Transactions of the Royal Society of London. Series A, Mathematical and Physical Sciences **264**, 321 (1969).

[59] F. Farassat and G. Succi, *A review of propeller discrete frequency noise prediction technology with emphasis on two current methods for time domain calculations,* Journal of Sound and Vibration **71**, 399 (1980).

[60] K. S. Brentner, *Prediction of helicopter rotor discrete frequency noise: A computer program incorporating realistic blade motions and advanced acoustic formulation*, Technical Memorandum 87721 (National Aeronautics and Space Administration, 1986).

[61] D. Casalino, *An advanced time approach for acoustic analogy predictions,* Journal of Sound and Vibration **261**, 583 (2003).

[62] F. Farassat, *Derivation of Formulations 1 and 1A of Farassat*, Technical Memorandum 214853 (National Aeronautics and Space Administration, 2007).

[63] A. F. P. Ribeiro, M. R. Khorrami, R. Ferris, B. Koenig, and P. A. Ravetta, *Lessons learned on the use of data surfaces for Ffowcs Williams-Hawkings calculations: Airframe noise applications,* in *28th AIAA/CEAS Aeroacoustics Conference* (2022).

[64] R. K. Amiet, *Acoustic radiation from an airfoil in a turbulent stream,* Journal of Sound and Vibration **41**, 407 (1975).

[65] L. D. de Santana, *Semi-analytical methodologies for airfoil noise prediction*, Ph.D. thesis, KU Leuven (2015).

[66] P. F. Mish and W. J. Devenport, *An experimental investigation of unsteady surface pressure on an airfoil in turbulence—Part 1: Effects of mean loading,* Journal of Sound and Vibration **296**, 417 (2006).

[67] S. Glegg and W. Devenport, *Aeroacoustics of Low Mach Number Flows* (Academic Press, London, UK, 2017).

[68] L. de Santana, M. P. J. Sanders, and C. H. Venner, *The UTwente aeroacoustic wind tunnel upgrade,* in *AIAA/CEAS Aeroacoustics Conference* (2018).

[69] P. Welch, *The use of fast Fourier transform for the estimation of power spectra: A method based on time averaging over short, modified periodograms,* IEEE Transactions on Audio and Electroacoustics **15**, 70 (1967).

[70] J. O. Hinze, *Turbulence* (McGraw-Hill, New York, USA, 1975).

[71] G. I. Taylor, *The spectrum of turbulence,* Proceedings of the Royal Society of London. Series A - Mathematical and Physical Sciences **164**, 476 (1938).

[72] S. B. Pope, *Turbulent Flows* (Cambridge University Press, Cambridge, United Kingdom, 2000) pp 182–263.

[73] C. C. Lin, *On Taylor's hypothesis and the acceleration terms in the Navier-Stokes equations,* Quarterly of Applied Mathematics **10**, 295 (1953).

[74] A. Trush, S. Pospisil, and H. Kozmar, *Comparison of turbulence integral length scale determination methods,* WIT Transactions on Engineering Sciences **128**, 113 (2020).

[75] A. F. P. Ribeiro, *Unsteady analysis of ground vortex ingestion with LBM-VLES,* in *AIAA SCITECH Forum* (2022).

[76] E. Dogan, R. E. Hanson, and B. Ganapathisubramani, *Interactions of large-scale free-stream turbulence with turbulent boundary layers,* Journal of Fluid Mechanics **802**, 79 (2016).

[77] L. Botero-Bolívar, F. L. dos Santos, C. H. Venner, and L. de Santana, *Increase of unsteady pressure at a trailing edge due to inflow turbulence,* AIAA Journal **60**, 6798 (2022).

[78] A. F. P. Ribeiro, D. Singh, B. Konig, and E. Fares, *On the stall characteristics of iced wings,* in *55th AIAA Aerospace Sciences Meeting* (2017).

[79] V. Demirci, M. Seyhan, and M. Sarioglu, *Investigation of aerodynamic performance of Clark-Y airfoil with more realistic tubercle model and internal slots,* Physics of Fluids **35**, 087109 (2023).

[80] R. I. A. Simanto, J.-W. Hong, K.-S. Kim, B.-K. Ahn, and S. Shin, *Experimental investigation on cavitation and induced noise of two-dimensional hydrofoils with leading-edge protuberances,* Physics of Fluids **34**, 124115 (2022).

[81] S. K. Singh and S. Narayanan, *On the reductions of airfoil-turbulence noise by curved wavy serrations,* Physics of Fluids **35**, 075140 (2023).

IV

Epilogue

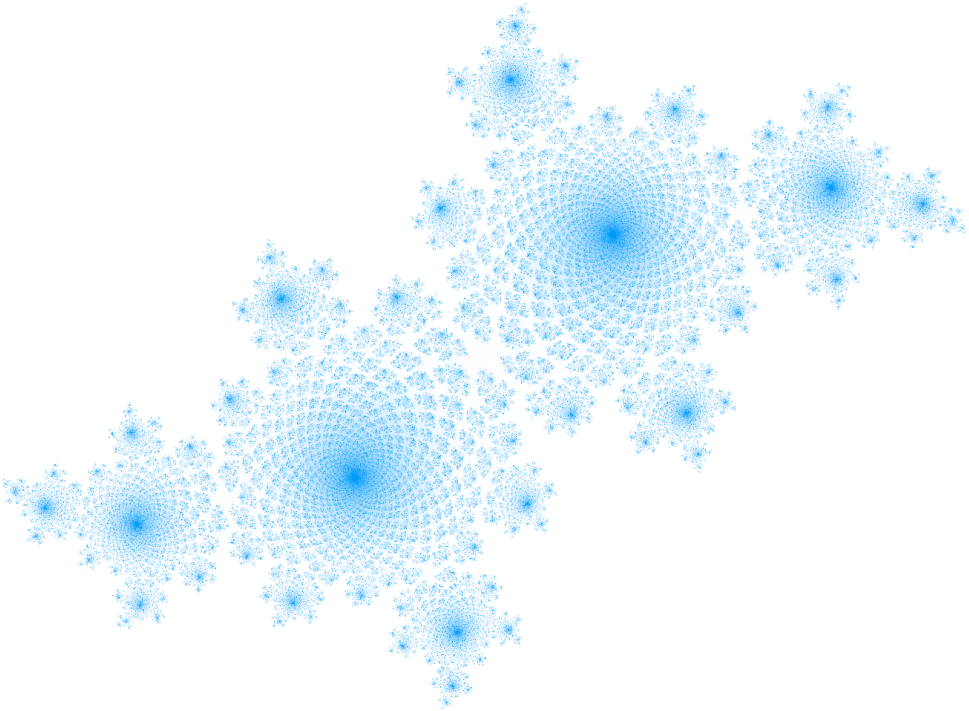

14

Conclusions and Outlook

You will someday die with items still on your list.

Tom Sachs

This chapter closes the thesis by focusing on the contributions made and suggestions for future work.

14.1. Contributions Of This Work

The work presented in the previous chapters was an attempt to contribute to the state-of-the-art of aerodynamics, aeroelasticity, and aeroacoustics. As per the thesis objectives, the methods and tools developed here were applied to a wide range of problems, which led to several findings, which are listed here.

In Chapter 2 the main numerical methods for an inviscid free wake panel method were described. Although no major new contributions were made, the work to summarize all the equations needed for a general purpose panel code, with arbitrary freestream conditions and body motion was quite substantial. The literature available for such methods is often incomplete, limited to specific cases, and inconsistent in terms of nomenclature and signs. Hence, this chapter can help future developers program their own codes.

Chapter 3 demonstrated the capabilities of the free wake panel code to solve many types of flow problems. The literature for dynamic cases (such as Theodorsen) often shows substantial differences between simulations and analytical results and we were able to achieve very accurate results, by employing a consistent formulation and proper discretization. The good results achieved for the NREL Phase VI turbine are also encouraging and, to the authors knowledge, the first use of such method to yield accurate results for this turbine.

Chapter 4 summarized results on floating offshore wind turbines simulations. The contributions here are: adding a different method to the pool of results for the UNAFLOW wind turbine, achieving the first experimentally validated numerical results for wake deformation due to surge motion, going beyond the UNAFLOW results to show when results become nonlinear, describing the nonlinear aerodynamics of sway and yaw motion, and quantifying the impact of wake motion on floating offshore wind turbine motion. The results from this chapter have been confirmed and expanded upon by other authors [1].

Chapter 5 showed results from aeroelastic simulations of a highly flexible wing. This was part of a contribution to the Aeroelastic Prediction Workshop, later summarized in [2], providing an alternative method to the pool of results, which mostly consisted of vortex lattice methods and doublet lattice methods. These simulations showed that the free wake panel method is capable of achieving very accurate flutter results, which could allow for simulations of more complex cases, where the aforementioned other methods would encounter accuracy issues. The results indicate that the second torsion mode of the wing plays a role in the limit cycle oscillations for the first flutter mode, which had not been identified in other publications. This chapter also includes the first numerical simulations of the Delft-Pazy wing under gusts, where we contribute to that database by proposing corrections to the experimental data. The results from this chapter have been confirmed and expanded upon by other authors [3].

Chapter 6 presented results of simulations of vertical axis wind turbines with blade and strut pitching, demonstrating the combined effects of these components for the first time. The benefits and limitations in using a free wake method for wind farm wake interaction were shown. The most meaningful contribution of this study was the demonstration that the tip vortices produced by the blades and struts can

potentially work together, injecting freestream flow into the wake in a very effective manner, while the vortices self-propel away from downstream turbines.

Chapter 7 summarized the potential use of free wake panel methods for preliminary design of aircraft including propeller-wing interaction effects. Detailed comparison to validated results of filament-based free wakes interacting with wings had not been shown in the literature. A mixed wake approach was developed and demonstrated, where the wing used a prescribed wake, while the propeller used a free wake, leading to a substantial reduction in computational time. The study demonstrated that, setting aside the well know limitations of inviscid approximations of boundary layers, filament-based free wakes can provide value in early design of aircraft, while including unsteady aerodynamics effects at a fraction of the cost of unsteady computational fluid dynamics.

Chapter 9 showed the implementation and verification of an actuator line method using a sliding mesh approach. This is the first time a sliding mesh was used with this method and the advantages and disadvantages of doing so were demonstrated and quantified.

Chapter 10 used the actuator line method developed in Chapter 9, along with blade-resolved simulations to investigate tip vortex instability in the wake of symmetric and asymmetric rotors. The first main contributions were on showing the potential of using preset actuator line simulations, using blade-resolved numerical results and an analytical model, to bypass the limitations of the traditional actuator line method in the presence of flow separations. Other contributions were the validation of the simulations with experimental data, the validation of the analytical model with blade-resolved results, and the first high-fidelity analysis of the blade extension effect in far-wake power recovery.

Chapter 11 showed high-fidelity simulations of a high-lift wing under the effects of a propeller slipstream. The simulations were thoroughly validated with experimental data, including the wing and the wake. The main novelty was the detailed analysis of wing effects on tip vortex deformation, instability, and slipstream shearing. Since the writing of this chapter, a new study using the same simulations was conducted in order to investigate slipstream deformation in more detail [4].

Chapter 12 focused on validation of a methodology for numerical prediction of trailing-edge noise for full wind turbines. For the first time, this method was validated with field data from a full-scale wind turbine, showing the potential for high-fidelity simulations to be used industrially for serration design on a full wind turbine.

Chapter 13 showed high-fidelity simulations of leading-edge noise and the effects of airfoil thickness on turbulence distortion, along with the associated pressure fluctuations on the airfoil surface and the far-field. The main contribution of this work was the detailed analysis of the turbulence characteristics very close to the airfoils leading-edges, demonstrating the energy transfer from the streamwise direction to the transverse and spanwise directions, depending on the airfoil thickness.

14.2. Applicability of the Methods

Part of the goal of this thesis was to understand the applicability of a free wake panel method and the high-fidelity lattice-Boltzmann code for complex problems in wind energy and aerospace. The conclusions of this endeavor are summarized here.

An inviscid free wake panel method was shown to be a useful tool for wind turbine simulations, in particular for offshore cases where the rotor movement plays a large role in the aerodynamics. The industrial relevance of this method is limited, as a fully inviscid scheme would not be used for design and extensions to blade element momentum theory can capture some unsteady effects well. A compromise would be to use lifting line simulations for these cases, which can include viscous effects in the airfoil data and dynamic stall models.

The panel method was also shown to be a useful tool for aircraft simulations with strong aeroelastic effects. In particular, doublet lattice methods and vortex lattice methods have limitations in their abilities to capture thickness effects and simulating realistic aircraft. The turnaround time for the panel method was also low enough that this seems like a tool that could be used for some verification stages of the design of highly flexible wings.

In the case of wake steering, it was shown that wind farm simulation are not accurate when done with a filament-based free wake method, as the wakes become entangled. However, design of specific wake steering approaches can be done with such a method. The advantages of using a panel method over computational fluid dynamics, namely the lack of a volume mesh, the lack of numerical disspation of vortices, the potential to easily include aeroelastic effects, and the shorter run time, make this a good application for industrial use.

The free wake panel method was also tested for propeller-wing interaction, where it was also demonstrated that, in spite the limitations of the inviscid approach, the interaction between the wing and slipstream was very well captured. Again, this does not necessarily make it an adequate design tool to be used in optimization, but a tool that can be used for intermediate design checks in early design phases.

The first use case tested on the high-fidelity lattice-Boltzmann solver was the actuator line method with a sliding mesh. Here it was shown that such a method is able to capture the same physics as traditional fixed-mesh Navier-Stokes solver, with some advantages when performing simulations on refined meshes. The lattice-Boltzmann simulations were shown to be very accurate for tip vortex instability studies, which is an active research topic.

Propeller-wing interaction was simulated very accurately with the lattice-Boltzmann solver. Again, the fact that the simulations are unsteady and relatively expensive compared to lower fidelity approaches make them more adequate for design checks rather than optimization, but this can improve over time. If the complex flow physics such as flap separations can only be properly captured with experiments and flight tests, then the numerical simulations performed are very cost-effective.

For trailing-edge noise and turbulence inflow noise, the lattice-Boltzmann solver was shown to be accurate and able to capture effects that lower fidelity approaches

cannot. This makes the tool compete with experimental methods instead of other numerical approaches, meaning that the cost comparison is not as simple. The results indicate that the tool should be used for design of noise reduction devices.

In summary, based on the work shown in this thesis the free wake panel method has potential today, where viscous effects do not dominate, unsteady effects are strong, aeroelasticity plays a role, and wakes are important. The lattice-Boltzmann method is relevant for cases where preserving wake is critical, complex flow separation occurs, traditional methods fail due to geometry or physics, and the interaction between lifting surfaces and turbulence plays a large role.

14.3. Suggestions for Future Work

The work done in this thesis was limited by time and scope. The tools and applications described here can be extended in the near future. Some of these extensions would be limited to new applications of the existing tools, while others would require efforts in software development.

- The most obvious improvement to the panel code is to include boundary layer effects, which would increase the applicability of the tool substantially. There are currently no perfect solutions for unsteady 3D boundary layer methods for panel codes and this will likely not come in the near future. Depending on the applications being focused on, streamline approaches that assume local 2D flow could be used and would be interesting for wind energy applications, in spite of their limitations. A cost-benefit trade-off must be made to ensure such simulations would not be too expensive compared to lifting line methods, which employ similar 2D assumptions at a much lower cost.

- The free wake used in this method is filament-based. For some applications, such as eVTOL aerodynamics, a vortex particle method could be more suitable. Combining the panel code developed in this thesis with existing free wake methods should not be too difficult and could open the door to other applications.

- The code performance of the free wake panel method could be much improved by using the fast multipole method and further GPU optimization.

- More advanced structural solvers such as Abaqus®, or an advanced multibody solver such as Simpack® could be coupled to the panel method, for more complex simulations. Stability and control simulations, including six degrees of freedom dynamics, could also be done and coupling such tools to the current method should not be too challenging.

- More complex aircraft models, including more geometric details, as well as more complex wind turbine cases, with more degrees of freedom (e.g. with flexible blades) could be performed. This could help perform such simulations in industrial environments in a more accurate way than current low fidelity methods, at a fraction of the cost of high-fidelity methods.

On the high-fidelity, viscous simulations side of this work, future studies could focus on:

- Performing leading-edge noise simulations using synthetic turbulence, in order to reduce the computational costs of these simulations.
- Using the actuator line method for installed propellers and validating such a method for compressibility effects.
- Performing wind turbine tip vortex instability studies in the presence of a turbulent atmospheric boundary layer.

References

[1] C. W. Schulz, S. Netzband, U. Özinan, P. W. Cheng, and M. Abdel-Maksoud, *Wind turbine rotors in surge motion: new insights into unsteady aerodynamics of floating offshore wind turbines (FOWTs) from experiments and simulations,* Wind Energy Science **9**, 665 (2024).

[2] M. Ritter, J. Hilger, A. F. P. Ribeiro, A. E. Öngüt, M. Righi, D. E. Raveh, A. Drachinsky, C. Riso, C. E. Cesnik, B. Stanford, P. Chwalowski, R. K. Kovvali, S. Duessler, K. C. Cheng, R. Palacios, J. P. dos Santos, F. D. Marques, G. R. R. Begnini, A. A. Verri, J. J. Lima, F. B. de Melo, and F. L. Bussamra, *Collaborative Pazy wing analyses for the third aeroelastic prediction workshop,* in *AIAA SCITECH 2024 Forum* (2024).

[3] S. Düssler, C. Mertens, and R. Palacios, *Effect of gust models on the response prediction of a very flexible wind tunnel wing model,* in *International Forum on Aeroelasticity and Structural Dynamics* (2024).

[4] R. Duivenvoorden, A. F. P. Ribeiro, T. Sinnige, and L. Veldhuis, *Slipstream deformation in propeller-wing-flap aerodynamic interaction,* submitted to Journal of Aircraft (2024).

Acknowledgements

First of all I thank my wife, who has been my life partner for so many years and supported me tremendously throughout my PhD. We started this living with one kid in Stuttgart, and now we finish it living with two kids in Munich. I couldn't have done it without you.

Thank you to my promotor Damiano, for being a great colleague since 2011, always willing to teach me, and for giving me the unique opportunity to conduct this PhD. My PhD was split between my day job at Dassault Systèmes, represented by the PowerFLOW simulations in the second half of the thesis, and my research activities for TU Delft, shown in the first half. Thank you to the various people at Dassault Systèmes and TU Delft who facilitated this PhD, by allowing me to do it in parallel to my work, with full trust and no bureaucracy. I must also thank my promotor Carlos, for all the valuable knowledge he shared with me during the PhD.

I am very grateful to the fellow PhD candidates I met, who became my co-authors. Claudia, a wonderful friend I met thanks to TU Delft who taught me what I needed to know about the actuator line method; Fernanda, a fantastic person to work with who taught me about leading-edge noise; Ramon, who shared his extensive knowledge on propeller-wing interactions and provided me with the open questions I tried to help answer; Erik, who let me be a part of his experimental campaign and was a pleasure to work with the whole time.

I am thankful for my colleagues in the Wind Energy group at TU Delft. I wish I could have spent more time with them, as they were a wonderful group of smart and kind people, who I am sure have brilliant careers ahead of them.

I am very grateful for the help of Massimo Gennaretti and Riccardo Giansante of Roma Tre University. Their expertise in panel methods helped me tremendously in achieving accurate results for dynamic cases. In particular, Massimo helped me integrate the far wake effects into the unsteady Bernoulli equation and I am very thankful for his teachings.

Thank you to Guannan Wang and Marc Canal from LM Wind Power for the fruitful collaboration on trailing-edge noise. Having access to data from field tests of a full-scale wind turbine was a privilege, and working with them was a pleasure.

I thank Scott Schreck for providing the experimental data for the NREL Phase VI wind turbine, Earl Duque for providing the surface mesh for the same turbine, and Felipe Miranda for providing the UNAFLOW experimental data.

For valuable feedback and assistance regarding the Pazy wing, I am grateful to Markus Ritter and Arik Drachinsky of the AePW Large Deflections Working Group. I also acknowledge the help of Philipp Drescher and Daniella Raveh, for providing the FEM results and information on the Pazy wing, respectively. I thank Cristina Riso for the beam model of the Pazy and Delft-Pazy wings. I am grateful to Christoph Mertens for the Delft-Pazy wind tunnel data and discussions on the gust results.

I am also very thankful for all the anonymous reviewers who gave me feedback on all the papers I wrote during my PhD. I was very fortunate to get many deep and valuable suggestions, along with numerous corrections and sometimes very critical feedback. All of this helped the quality of those papers and of this thesis tremendously. The help and feedback I received from my co-authors and colleagues is also very appreciated.

The coding done for this thesis was greatly assisted by the Julia Discourse community. Several open source Julia packages were essential for this work, such as CUDA.jl, KrylovKit.jl, IterativeSolvers.jl, Plots.jl, WriteVTK.jl, among others. In particular, Taylor McDonnell, the main developer of GXBeam.jl was instrumental for the aeroelasticity parts of this work.

Finally, I thank you, reader. Thank you for reading my thesis. Even if it was only a small part of it.

Curriculum Vitæ

André PINTO RIBEIRO

08-02-1986	Born in Porto Alegre, Brazil.

Professional Experience

2024–Present	Staff Engineer – Aeroacoustics and Installation Aerodynamics GE Aerospace, Munich, Germany.
2018–2024	Senior Specialist – Aerospace Dassault Systemes GmbH, Stuttgart, Germany.
2018	Technical Director – Airframe Exa GmbH, Stuttgart, Germany.
2015–2018	Technical Account Manager – Aerospace Exa GmbH, Stuttgart, Germany.
2014–2015	Team Leader – Aerospace Business Development Exa GmbH, Stuttgart, Germany.
2012–2014	Aerospace Application Engineer Exa GmbH, Stuttgart, Germany.
2011–2012	Aerospace Intern Exa GmbH, Stuttgart, Germany.
2010	Wind Turbine Aerodynamics Intern Elena Energia, Grenoble, France.

Education

2021–2024 PhD in Aerospace Engineering
Delft University of Technology
Thesis: Multi-Fidelity Numerical Methods for Aircraft and Wind Turbines: Aerodynamics, Aeroelasticity, and Aeroacoustics
Promotor: Prof. dr. D. Casalino
Promotor: Prof. dr. C. S. Ferreira

2010–2012 MSc in Mechanical Engineering
Universidade Federal do Rio Grande do Sul
Thesis: Computational Fluid Dynamics and Optimization Applied to Wind Turbines
Promotor: Prof. dr. A. M. Awruch
Co-Promotor: Prof. dr. H. M. Gomes

2004–2010 BSc in Civil Engineering
Universidade Federal do Rio Grande do Sul
Thesis: Aerodynamic Analysis of a Building Using Computational Fluid Dynamics
Promotor: Prof. dr. A. M. Awruch
Co-Promotor: Prof. dr. A. P. Petry

Awards

2019 Best Performers
Dassault Systemes

2013 Young Researcher Award
AIAA BANC-IV Workshop

2011 Young Researcher Award
International Conference on Wind Engineering

2010 Award for graduating at the top of the class
UFRGS

List of Publications

Journal Papers

13. R. Duivenvoorden, **A.F.P. Ribeiro**, T. Sinnige, L. Veldhuis, *Slipstream Deformation in Propeller-Wing-Flap Aerodynamic Interaction*, submitted to Journal of Aircraft (2025).

12. **A.F.P. Ribeiro**, T. Leweke, A. Abraham, J.N. Sørensen, R.F. Mikkelsen, *Blade-Resolved and Actuator Line Simulations of Rotor Wakes*, Computers & Fluids **287**, p. 106477 (2025).

11. E. Fritz, **A. Ribeiro**, K. Boorsma, C. Ferreira, *Aerodynamic characterisation of a thrust-scaled IEA 15 MW wind turbine model: Experimental insights using PIV data*, Wind Energy Science **9** (5), p. 1173-1187 (2024).

10. **A.F.P. Ribeiro**, C. Ferreira, D. Casalino, *On the Use of Filament-Based Free Wake Panel Methods for Preliminary Design of Propeller-Wing Configurations*, Aerospace Science and Technology **144**, 108775 (2024).

9. **A.F.P. Ribeiro**, C. Muscari, *Sliding mesh simulations of a wind turbine rotor with actuator line lattice-Boltzmann method*, Wind Energy **27** (11), p. 1115-1129 (2024).

8. **A.F.P. Ribeiro**, F.L. dos Santos, K. Venner, L.D. de Santana, *Numerical study of inflow turbulence distortion and noise for airfoils*, Physics of Fluids **35** (11), p. 115112 (2023).

7. **A.F.P. Ribeiro**, D. Casalino, C. Ferreira, *Free wake panel method simulations of a highly flexible wing in flutter and gusts*, Journal of Fluids and Structures **121**, p. 103955 (2023).

6. **A.F.P. Ribeiro**, D. Casalino, C.S. Ferreira, *Nonlinear inviscid aerodynamics of a wind turbine rotor in surge, sway, and yaw motions using a free-wake panel method*, Wind Energy Science **8** (4), p. 661-675, (2023).

5. **A.F.P. Ribeiro**, M.R. Khorrami, R. Ferris, B. König, P.A. Ravetta, *Lessons learned on the use of data surfaces for Ffowcs Williams-Hawkings calculations: Airframe noise applications*, Aerospace Science and Technology **135** (4), p. 108202 (2023).

4. E. Fares, B. Duda, **A.F.P. Ribeiro**, B. Koenig, *Scale-resolving simulations using a lattice Boltzmann-based approach*, CEAS Aeronautical Journal **9**, p. 721-733 (2018).

3. D. Casalino, **A.F.P. Ribeiro**, E. Fares, S. Noelting, *Lattice-Boltzmann Aeroacoustic Analysis of the LAGOON Landing-Gear Configuration*, AIAA Journal **52** (6), p. 1232-1248 (2014).

2. D. Casalino, **A.F.P. Ribeiro**, E. Fares, *Facing Rim Cavities Fluctuation Modes*, Journal of Sound and Vibration **333** (13), p. 2812-2830 (2014).

1. **A.F.P. Ribeiro**, A.M. Awruch, H.M. Gomes, *An airfoil optimization technique for wind turbines*, Applied Mathematical Modelling **36**, p. 4898-4907 (2012).

Technical Reports

1. **A.F.P. Ribeiro**, D. Casalino, E. Fares, M. Choudhari, *Direct Numerical Simulation of an Airfoil with Sand Grain Roughness on the Leading Edge*, NASA **TM-2016-219363** (2016).

Book Chapters

1. **A.F.P. Ribeiro**, D. Casalino, E. Fares, M. Choudhari, *Lattice-Boltzmann Simulations of an Oscillating NACA0012 Airfoil in Dynamic Stall*, In Braza, M., Bottaro, A., Thompson, M. ed. **Advances in Fluid-Structure Interaction**, Springer, p. 179-192 (2016).

Conference Papers

30. **A.F.P. Ribeiro**, A.M. Forsting, *Machine Learning Categorization of a Large CFD Data Set of Airfoil Leading-Edge Defects*, **International Conference on Computational Fluid Dynamics**, Kobe, Japan (2024).

29. **A.F.P. Ribeiro**, C.S. Ferreira, D. Casalino, *Vertical axis wind turbine wake steering by pitched struts and blades*, **The Science of Making Torque from Wind**, Florence, Italy (2024).

28. **A.F.P. Ribeiro**, W.C.P. van der Velden, D. Casalino, G. Wang, *Aeroacoustic Simulations of a Wind Turbine: Validation with Field Tests, Including Trailing-Edge Serrations*, **30th AIAA/CEAS Aeroacoustics Conference**, Rome, Italy (2024).

27. M. Ritter, J. Hilger, **A.F.P. Ribeiro**, A.E. Öngüt, M. Righi, D.E. Raveh, A. Drachinsky, C. Riso, C.E. Cesnik, B. Stanford, P. Chwalowski, R.K. Kovvali, S. Duessler, K.C. Cheng, R. Palacios, J.P. dos Santos, F.D. Marques, G.R. Ribeiro Begnini, A.A. Verri, J.J. Lima, F.B. de Melo, F.L. Bussamra, *Collaborative Pazy Wing Analyses for the Third Aeroelastic Prediction Workshop*, **AIAA SciTech Forum**, Orlando, USA (2024).

26. **A.F.P. Ribeiro**, R. Duivenvoorden, D. Martins, *High-Fidelity Simulations of Propeller-Wing Interactions in High-Lift Conditions*, **AIAA Aviation Forum**, San Diego, USA (2023).

25. **A.F.P. Ribeiro**, D. Casalino, C. Ferreira, *Free Wake Panel Method Simulations of a Highly Flexible Wing at Flutter*, **AIAA Aviation Forum**, Chicago, USA (2022).

24. **A.F.P. Ribeiro**, M. Murayama, Y. Ito, K. Yamamoto, T. Hirai, *Effect of Slat Tracks and Inboard Slat Tip Geometry on Airframe Noise*, **AIAA/CEAS Aeroacoustics Conference**, Southampton, UK (2022).

23. **A.F.P. Ribeiro**, M.R. Khorrami, R. Ferris, B. Konig, P.A. Ravetta, *Lessons Learned on the Use of Data Surfaces for Ffowcs Williams-Hawkings Calculations: Airframe Noise Applications*, **AIAA/CEAS Aeroacoustics Conference**, Southampton, UK (2022).

22. **A.F.P. Ribeiro**, D. Casalino, C.S. Ferreira, *Surging Wind Turbine Simulations with a Free Wake Panel Method*, **The Science of Making Torque from Wind**, Delft, Netherlands (2022).

21. **A.F.P. Ribeiro**, *Unsteady Analysis of Ground Vortex Ingestion with LBM-VLES*, **AIAA SciTech Forum**, online (2022).

20. M.R. Khorrami, P. Shea, C.S. Winski, P.A. Ravetta, **A.F.P. Ribeiro**, R. Ferris, M. Sacks, *Aeroacoustic Computations of a Generic Low Boom Concept in Landing Configuration: Part 3 - Aerodynamic Validation and Noise Source Identification*, **AIAA Aviation Forum**, online (2021).

19. **A.F.P. Ribeiro**, R. Ferris, M.R. Khorrami, *Aeroacoustic Computations of a Generic Low Boom Concept in Landing Configuration: Part 2 - Airframe Noise Simulations*, **AIAA Aviation Forum**, online (2021).

18. R. Ferris, M. Sacks, D. Cerizza, **A.F.P. Ribeiro**, M.R. Khorrami, *Aeroacoustic Computations of a Generic Low Boom Concept in Landing Configuration: Part 1 - Aerodynamic Simulations*, **AIAA Aviation Forum**, online (2021).

17. M.R. Khorrami, B. Konig, E. Fares, **A.F.P. Ribeiro**, M. Czech, P.A. Ravetta, *Airframe Noise Simulations of a Full-Scale Large Civil Transport in Landing Configuration*, **AIAA Aviation Forum**, online (2021).

16. E. Ozger, B. Koenig, **A.F.P. Ribeiro**, D. Cerizza, E. Fares, *Lattice-Boltzmann Simulations of Delta Wings — VFE-2 and SACCON*, **AVT-307 Research Symposium on Separated Flow: Prediction, Measurement and Assessment for Air and Sea Vehicles**, Trondheim, Norway (2019).

15. R. Ihi, **A.F.P. Ribeiro**, L. Santos, D. Silva, *Lattice Boltzmann Simulations of Flow Over an Iced Airfoil*, **SAE International Conference On Icing Of Aircraft, Engines, and Structures**, Minneapolis, USA (2019).

14. B. Koenig, D. Singh, **A. Ribeiro**, E. Fares,*Lattice-Boltzmann Simulations at the Corners of the Flight Envelope*, **3AF International Conference on Applied Aerodynamics**, Paris, France (2019).

13. **A.F.P. Ribeiro**, E. Fares, M. Choudhari, *DNS of Laminar to Turbulent Transition on NACA 0012 Airfoil with Sand Grain Roughness*, **International Conference on Computational Fluid Dynamics**, Barcelona, Spain (2018).

12. D. Singh, **A.F.P. Ribeiro**, B. Koenig, E. Fares,*Lattice Boltzmann Simulations of a Supersonic Cavity*, **AIAA Aviation Forum**, Denver, USA (2017).

11. **A.F.P. Ribeiro**, B. Konig, D. Singh, E. Fares, R. Zhang, P. Gopalakrishnan, A. Jammalamadaka, Y. Li, H. Chen, *Buffet Simulations with a Lattice-Boltzmann based Transonic Solver*, **AIAA SciTech Forum**, Grapevine, USA (2017).

10. **A.F.P. Ribeiro**, D. Singh, B. Konig, E. Fares, *On the Stall Characteristics of Iced Wings*, **AIAA SciTech Forum**, Grapevine, USA (2017).

9. B. Konig, **A.F.P. Ribeiro**, E. Fares, R. Zhang, P. Gopalakrishnan, Y. Li, *Extended Validation of a Transonic Lattice-Boltzmann Method on the Example of the NASA Common Research Model*, **Congress of the International Council of the Aeronautical Sciences**, Daejeon, South Korea (2016).

8. M. Terracol, T. Le Garrec, D-C. Mincu, E. Manoha, D. Casalino, **A.F.P. Ribeiro**, *Numerical simulations of LEISA2 high-lift configuration at ONERA*, **International Workshop Computational Experiment in AeroAcoustics**, Svetlogorsk, Russia (2016).

7. D. Casalino, **A.F.P. Ribeiro**, E. Fares, S. Noelting, A. Mann, F. Perot, Y. Li, P.-T. Lew, C. Sun, P. Gopalakrishnan, R. Zhang, H. Chen, K. Habibi, *Towards Lattice-Boltzmann Prediction of Turbofan Engine Noise*, **AIAA/CEAS Aeroacoustics Conference**, Atlanta, USA (2014).

6. A. Hazir, D. Casalino, R. Denis, **A.F.P. Ribeiro**, *Lattice-Boltzmann Simulation of the Aeroacoustic Properties of Round Cavities*, **AIAA/CEAS Aeroacoustics Conference**, Atlanta, USA (2014).

5. **A.F.P. Ribeiro**, D. Casalino, E. Fares, *Lattice-Boltzmann Simulations of an Oscillating NACA0012 Airfoil in Dynamic Stall*, **ERCOFTAC international symposium "Unsteady separation in fluid-structure interaction"**, Mykonos, Greece (2013).

4. D. Casalino, **A.F.P. Ribeiro**, E. Fares, *Facing Rim Cavities Fluctuation Modes*, **AIAA/CEAS Aeroacoustics Conference**, Berlin, Germany (2013).

3. **A.F.P. Ribeiro**, D. Casalino, E. Fares, S. Noelting, *CFD/CAA Analysis of the LAGOON Landing Gear Configuration*, **AIAA/CEAS Aeroacoustics Conference**, Berlin, Germany (2013).

2. **A.F.P. Ribeiro**, A.M. Awruch, H.M. Gomes, *An airfoil optimization technique for wind turbines*, **Brazilian Congress of Mechanical Engineering**, Natal, Brazil (2011).

1. **A.F.P. Ribeiro**, *Unsteady RANS modelling of flow past a rectangular 5:1 cylinder: investigation of edge sharpness effects*, **International Conference on Wind Engineering**, Amsterdam, Netherlands (2011).